TECHNISCHE UNIVERSITÄT MÜNCHEN

DOCTORAL THESIS

Unveiling the fundamental production mechanism of light nuclei using coalescence and femtoscopy

---

Author:
Maximilian Mahlein

Supervisor:
Prof. Dr. Laura Fabbietti

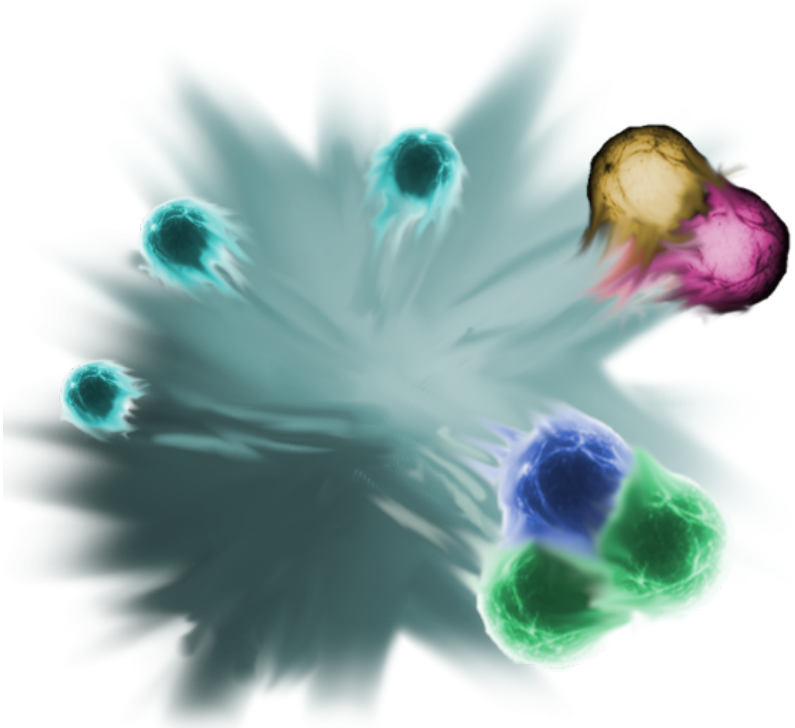

February, 2025

Technische Universität München
TUM School of Natural Sciences

Unveiling the fundamental production mechanism of light nuclei using coalescence and femtoscopy

Maximilian Mahlein

Vollständiger Abdruck der von der TUM School of Natural Sciences der Technischen Universität München zur Erlangung des akademischen Grades eines Doktors der Naturwissenschaften (Dr. rer. nat.) genehmigten Dissertation.

Vorsitz:	apl. Prof. Dr. Norbert Kaiser
Prüfende der Dissertation:	1. Prof. Dr. Laura Fabbietti
	2. Prof. Dr. Elisa Resconi
	3. Prof. Dr. Concettina Sfienti

Die Dissertation wurde am 27.02.2025 bei der Technischen Universität München eingereicht und durch die TUM School of Natural Sciences am 30.04.2025 angenommen.

Declaration of Authorship

I, Maximilian Mahlein, declare that this thesis titled, "Unveiling the fundamental production mechanism of light nuclei using coalescence and femtoscopy" and the work presented in it are my own. I confirm that:

- This work was done wholly or mainly while in candidature for a research degree at this University.
- I have not employed the services of an organization that provides dissertation supervisors in return for payment or that fulfills, in whole or in part, the obligations incumbent on me in connection with my dissertation.
- I have not submitted the dissertation, either in the present or a similar form, as part of another examination process.
- I have not yet been awarded the desired doctoral degree nor have I failed the last possible attempt to obtain the desired degree in a previous doctoral program.
- Where I have consulted the published work of others, this is always clearly attributed.
- Where I have quoted from the work of others, the source is always given. With the exception of such quotations, this thesis is entirely my own work.
- I have acknowledged all main sources of help.
- Where the thesis is based on work done by myself jointly with others, I have made clear exactly what was done by others and what I have contributed myself.

Signed:

Date:

Abstract

Unveiling the fundamental production mechanism of light nuclei using coalescence and femtoscopy

by Maximilian Mahlein

Light (anti)nuclei are of significant interest in nuclear and astroparticle physics, with implications ranging from fundamental hadron-hadron interactions to indirect Dark Matter searches. In the context of Dark Matter, a precise understanding of their formation mechanism is crucial for interpreting results from experiments such as GAPS and AMS-02. This thesis aims to definitively determine how light nuclei are formed.

Historically, two principal models—the Statistical Hadronization Model and the Coalescence Model—have been tested by comparing their nuclear yield predictions with experimental data. However, the diversity of their implementations has prevented a clear consensus. Here, a model-independent approach is introduced through femtoscopy, which investigates nuclear formation by analyzing momentum correlations between pions and deuterons. The detection of a distinct Δ resonance decay signature indicates that deuterons, and by extension all light nuclei, are produced via final state interactions occurring during or after the decay of short-lived resonances. Simple causality arguments thereby rule out thermal production mechanisms.

Building on these insights, a sophisticated coalescence model based on the Wigner Function Formalism is developed. When tested using the EPOS 3 event generator, the model successfully reproduces the deuteron spectra measured by the ALICE collaboration without introducing free parameters—provided that experimental inputs such as multiplicity, momentum distributions, emission source sizes, and nuclear wave functions are used. This model is further encapsulated within a custom Monte Carlo generator, ToMCCA, which extends predictions across the full energy and multiplicity range explored at the LHC with significantly improved statistical precision. Moreover, the coalescence approach is extended to A=3 (hyper)nuclei, including ^{3}He, ^{3}H, and $^3_\Lambda$H, marking the first event-by-event predictions that utilize realistic nuclear wave functions.

Overall, this work establishes a robust baseline for nuclear flux predictions by substantially reducing model uncertainties, thereby providing a solid foundation for future searches for new physics.

Zusammenfassung

Leichte (Anti-)Kerne sind von großem Interesse für die Kern- und Astroteilchenphysik, mit Implikationen, die von fundamentalen Hadron-Hadron-Wechselwirkungen bis hin zu indirekten Dunkle-Materie-Suchen reichen. Im Kontext der Dunklen Materie ist ein präzises Verständnis ihres Bildungsmechanismus entscheidend für die Interpretation von Ergebnissen experimenteller Projekte wie GAPS und AMS-02. Diese Dissertation verfolgt das Ziel, die Entstehung leichter Kerne eindeutig zu klären.

Historisch wurden zwei Modelle – das Statistische Hadronisierungsmodell und das Koaleszenzmodell – getestet, indem ihre Vorhersagen für Kernproduktionsraten mit experimentellen Daten verglichen wurden. Die Vielfalt ihrer Implementierungen hat jedoch eine eindeutige Schlussfolgerung verhindert. In dieser Arbeit wird daher ein modellunabhängiger Ansatz über die Femtoskopie eingeführt, der die Kernbildung durch die Analyse von Impulskorrelationen zwischen Pionen und Deuteronen untersucht. Der Nachweis eines charakteristischen Δ-Resonanzzerfalls belegt, dass Deuteronen – und damit auch alle anderen leichten Kerne – durch Endzustandswechselwirkungen gebildet werden, die während oder nach dem Zerfall kurzlebiger Resonanzen auftreten. Einfache Kausalitätsüberlegungen schließen damit thermische Produktionsmechanismen aus.

Aufbauend auf diesen Erkenntnissen wird ein verfeinertes Koaleszenzmodell entwickelt, das auf dem Wigner-Funktionsformalismus basiert. Getestet mit dem EPOS 3-Ereignisgenerator reproduziert das Modell erfolgreich die von der ALICE-Kollaboration gemessenen Deuteronspektren, ohne freie Parameter einzuführen – vorausgesetzt, experimentelle Eingangsgrößen wie Multiplizitäten, Impulsverteilungen, Emissionsquellengrößen und Kernwellenfunktionen werden verwendet. Dieses Modell wird in den maßgeschneiderten Monte-Carlo-Generator ToMCCA integriert, der die Vorhersagen über den gesamten Energie- und Multiplizitätsbereich des LHC mit deutlich verbesserter statistischer Präzision erweitert. Darüber hinaus wird der Koaleszenzansatz auf A=3 (Hyper-)Kerne, einschließlich ^{3}He, ^{3}H und $^{3}_{\Lambda}$H, ausgedehnt und liefert damit erstmals ereignisweise Vorhersagen unter Verwendung realistischer Kernwellenfunktionen.

Insgesamt etabliert diese Arbeit eine belastbare Grundlage für die Vorhersage von Kernflüssen, indem Modellunsicherheiten erheblich reduziert werden. Dadurch wird eine solide Basis für zukünftige Suchen nach neuer Physik geschaffen.

Acknowledgements

When I joined the group of dense and strange hadronic matter at TUM almost 6 years ago for my Master's thesis, I was a different person with a different view on life and what is important, hell, even a different last name. There are many people who helped me become the person I am today, probably too many to mention them all, but I will certainly try. Also, as most of you know, I'm not good at being nice to people. First and foremost, I want to thank Prof. Laura Fabbietti, my supervisor. We had our issues in the beginning. I was lazy and sloppy, but you saw something in me, something no one had seen before. So you invested blood, sweat, and tears into getting every piece of it out of me. Next is Laura Šerksnyte, who was my Master's thesis supervisor for most of the time and afterward became a dear friend. With your unapologetic honesty, you helped me on more occasions than you probably realize, even if I didn't want to hear it at the time. Luca Barioglio supervised the end of my Master's thesis and took over the early mentorship of my PhD. Working with you was always a pleasure with your clean and calm style in this work which can be hectic and messy at times. And you will always be good at math et merda (look at the name of the pdf file). When Luca left the group, Chiara Pinto became my mentor and dear friend. Your sunny nature and sharp tongue always strike a perfect balance (also you are tiny, which is honestly hilarious). Lastly, while writing this thesis, I was moved into a 2 person office with Bhawani, which was a blessing. I learned more about doing calculations and theory than in 6 years of university. Also, watching the chess world championship with you was a blast. Last but not least, my work husband Marcel Lesch. I don't think I have spent as much time in hotel rooms with a person as I have with you in the last few years. I can always be angry at things with you, be happy about things with you or just be braindead with you. I shall award you my last brain cell for your services! A quick rundown of people I haven't mentioned yet: Vale, you always have a sarcastic comment about the world, and honestly, that's beautiful. Dimi, ghetto_this ghetto_that... nothing is as permanent as a temporary solution. Anton, sorry for always crashing the Batch farm; a good system needs to be tested to its limits. Max, you have a score of 170, but you are masking it down to 120. Daniel, EPOS is indeed an **E**vil **P**iece **O**f **S**oftware. Emma, you won the race to the first thesis, but it was always nice knowing someone else is going through the same. Cindy, your weekly cat pictures always kept my morale up. Ante, we should keep our bets up remotely wherever we go. Berkin, I cherish the day you got your sparkle back; it lightens up the entire group.

Finally, I want to thank my family, especially my parents, who always supported me wherever I went, even when it was physics and not engineering. Also, a special thanks goes to the love of my life, my wife Mira, the mother of my unborn child. You always said that you wished you could help me but couldn't, but you made me a better person from day 1. You always had my back and always gave me a place where I was safe and could be myself. And that is honestly the greatest way to help somebody.

Contents

List of Figures

List of Tables

Chapter 1

Introduction

1.1 The goal of this work

The world around us, from the stars in the sky to the sheet of paper you are reading right now, is built upon structures governed by the fundamental forces of nature. At its basic level, matter consists of molecules that are held together by the electromagnetic force between electrons and atomic nuclei. These atomic nuclei themselves are made up of nucleons, protons and neutrons, which are constructed from the interaction between quarks, held together by the strong force, a force much stronger than any other force we have discovered. Indeed, at distances of 1 fm, the size of a proton, the strong force is about 100 times stronger than the electromagnetic force[1] and 10^{38} times stronger than the gravitational force[2]. Over the past century, fundamental theories that describe these forces have been developed and applied with astonishing accuracy. Many would consider general relativity, which describes the gravitational force as the warping of space-time, to be the "crown jewel" of physics, but in nuclear and particle physics, quantum electrodynamics (QED), which describes the electromagnetic interaction and quantum chromodynamics (QCD), which describes the strong force, reign supreme. It were those quantum field theories (QFTs) that allowed physicists to construct the Standard Model of particle physics, which has withstood every test given to it, even to this day. While the Standard Model accurately describes all fundamental particles, once these fundamental particles are combined into composite particles, entirely new and unexpected phenomena arise. As such, the study of hadrons, objects made out of quarks and gluons, is still a highly active field of research, especially the study of the interactions between them. A tool specialized for the study of interactions is the femtoscopy method. It can directly measure the effect of the interaction potential between two or more hadrons by investigating momentum correlations. Another approach is to study bound states of hadrons, such as nuclei, to constrain the interaction specifically between nucleons[3] and even hyperons[4]. This work aims to explore the formation of light (anti)nuclei[5] in high-energy collisions. Chapter 2 will introduce the commonly used nuclear production models, one of which will be discussed in more detail in Ch. 3. The femtoscopic method will be introduced in Sec. 2.2. Two different approaches will be used to understand nuclear production. The first approach will be the study of the femtoscopic correlation between pions[6] and nuclei,

[1] The ratio between the strong coupling constant and the electromagnetic constant at this range is $\alpha_S/\alpha \approx 1/(1/137)$

[2] The ratio between the gravitational force and coulomb force of a proton is $F_G/F_C = \frac{G}{k_e}\frac{m_p^2}{e^2} \approx 8.1 \cdot 10^{-37}$ and it is independent of the distance.

[3] Nucleons are objects made up of three quarks, either uud (Proton) or udd (Neutron).

[4] Hyperons are hadrons made up of three quarks, at least one of which has to be an s quark.

[5] In high-energy nucleonic reactions such as pp collisions at the LHC, the formation mechanism is assumed to be the same for matter and antimatter. Thus, in the following, the (anti) prefix will be dropped.

[6] Pions are hadrons with quark contents $u\bar{d}$ (π^+), $d\bar{u}$ (π^-) and $\frac{u\bar{u}-d\bar{d}}{\sqrt{2}}$ (π^0).

specifically deuterons in Ch. 4. Studying their momentum correlations reveals the dynamical evolution of nuclear formation and the special role of the pion in the formation process. The second approach discusses the modeling of nuclear formation via nucleon coalescence in Ch. 6 and Ch.7. The results from both studies agree with each other and leave only one conclusion: Nuclei are produced via the coalescence of nucleons due to final state interactions at a later time than all other hadrons.

1.2 The strong interaction

Nuclei are bound by the residual strong interaction, which arises as a manifestation of the fundamental strong interaction in multi-hadron systems. In order to understand the residual interaction, it is first necessary to examine the fundamental strong interaction at the level of quarks and gluons.

1.2.1 The fundamental strong force

In classical and quantum electrodynamics (QED), the electric charge is the quantity that determines the interaction strength between particles. More charges lead to stronger forces, and uncharged particles do not participate in the interaction at all. This concept can be extended to other interactions, and as such, in QCD, the strong interaction, the *color charge* plays the role of the electric charge. Quarks can be either *red*, *blue*, or *green*, while antiquarks can be *antired*, *antiblue*, or *antigreen*. This is conceptually different from electrodynamics, as QED only has one kind of charge that can be positive or negative, while QCD has three. The fundamental process of QCD is the gluon emission with accompanied color change (indicated in parentheses) with the corresponding Feynman diagram below (left diagram)

$$q(b) \rightarrow q(r) + g(b, \bar{r}). \tag{1.1}$$

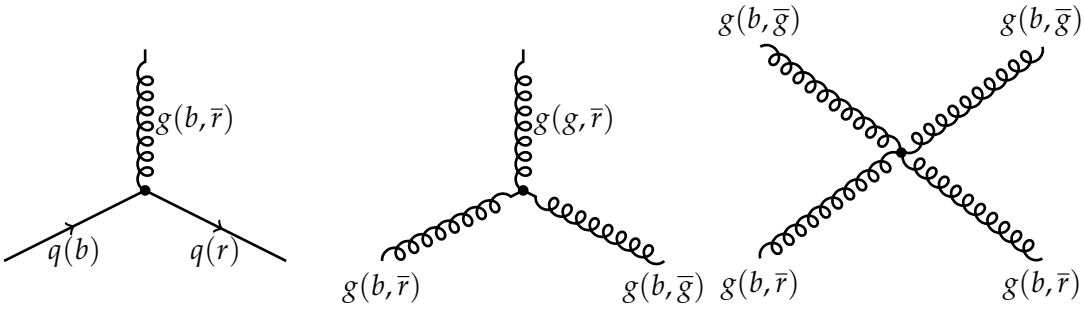

This equation shows that gluons carry two color charges, one positive and one negative, allowing them to interact with each other (middle and right diagram). In contrast, the photon in QED is neutral and cannot self-interact. This self-interaction in QCD leads to the *running of the coupling*, where the strong coupling constant α_S is not fixed but varies with the momentum transfer Q^2. A useful analogy comes from QED: in a dielectric medium, such as water (H_2O), a charged particle's electric field is screened by surrounding dipoles. The effect becomes weaker the further away the polarized molecules are. In QED, this effect is weak because the photon itself is not a dielectric medium, though it can create positron-electron pairs that contribute to screening. This causes the coupling constant to increase for large Q^2. This correlation results from the fact that a large Q^2 corresponds to a short distance, and the screening is diminished. In QCD, gluons can also couple to $q\bar{q}$ pairs (right diagram below), which causes the same kind of screening effect. However, unlike in QED, gluons also couple to other gluons, and gluon loops have to be included (left diagram). These gluon loops act as a source of new charge and amplify the charge effect, thus causing anti-screening.

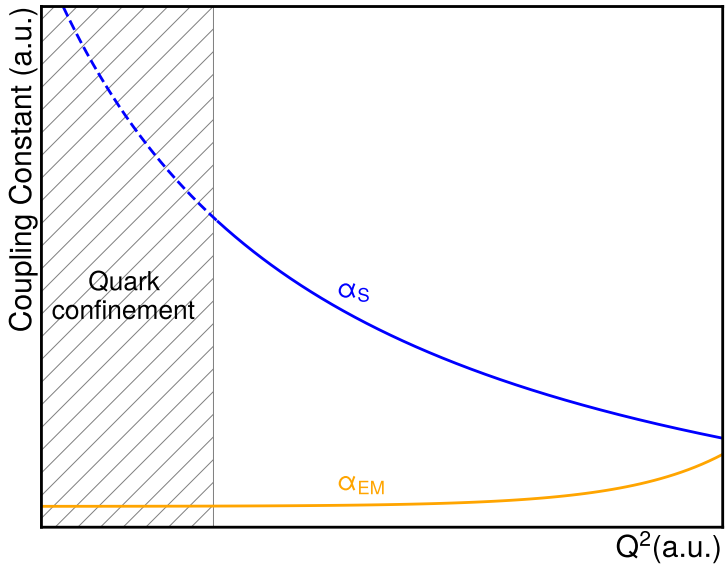

FIGURE 1.1: The strong (α_S) and electromagnetic (α_{EM}) coupling constants as a function of the momentum transfer Q^2. Below a certain threshold, quarks are bound by the strong interaction (*confinement*), while above this threshold, they are free (*asymptotic freedom*).

This latter effect turns out to be much stronger than the screening effect, and the strong coupling constant α_S decreases at high Q^2 (asymptotic freedom) and increases at low Q^2 (confinement), see Fig. 1.1. A first-order perturbation calculation yields

$$\alpha_S(Q^2) = \frac{12\pi}{(11N_c - 2n_f)\ln(Q^2/\Lambda^2_{QCD})}, \tag{1.2}$$

where $n_f = 6$ is the number of flavors and $N_c = 3$ the number of colors in the Standard Model. Q^2 is the momentum transfer and $\Lambda_{QCD} \approx 250$ MeV$/c$ is a free parameter, the so-called *QCD scale*. This free parameter was fitted to existing measurements, most importantly the strength of the coupling at $Q^2 = M_Z^2$ measured in decays of Z-bosons [30]. Since momentum transfer is inversely related to distance, quarks within a proton behave almost as free particles, but isolating a single quark requires an enormous amount of energy. This enormous energy barrier enforces quark confinement, ensuring that only color-neutral combinations - such as mesons and baryons - can exist as observable particles. Indeed, removing one quark requires enough energy to create a quark-antiquark pair as well as a new gluon. Figure 1.2 shows this gluon fragmentation, as the $q\bar{q}$ pair moves apart, a new $q\bar{q}$ pair is created at the breaking point. At very large energies, α_S becomes small, and the quarks and gluons are asymptotically free. This state of matter is called a *quark-gluon plasma* (QGP), and it is defined as a state in which quarks are no longer bound into hadrons. The study of the QGP is still an ongoing endeavor that has many implications for the early universe,

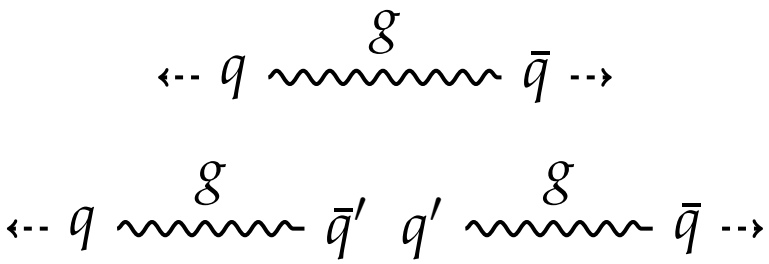

FIGURE 1.2: Creation of a $q\bar{q}$ pair as a result of two quarks moving away from each other. The large coupling at large distances causes the creation of two new quarks to be energetically favorable.

where such a state is predicted to have existed in the first 10^{-6}s as well as for high-energy particle collisions. The first indication of a QGP was found by the CERN SPS WA97 experiment at CERN in the year 2000 [31, 32] in Pb–Pb collisions at a center-of-mass energy of $\sqrt{s} = 17.3$ GeV and later confirmed in 2005 by the STAR, PHOBOS, BRAHMS and PHENIX experiments at the RHIC collider [33] in Au–Au collisions at $\sqrt{s} = 200$ GeV. Figure 1.3 shows the phase diagram of QCD with the QGP indicated as the phase to the top. The high-energy collisions at RHIC correspond to low baryon density and high temperature, while the CERN Pb–Pb collisions represent higher densities and lower temperatures. In both cases, a QGP can be created. Indeed, for larger baryon densities, the required temperature to form the deconfined phase drops. It is known that the transition between QGP and the confined hadronic matter is a smooth one at very low densities at a temperature of $k_B T \approx 155$ MeV and a transition of the first order at higher densities with a lower transition temperature. This indicates a critical point at the boundary between those two transitions. The exact location in the phase diagram is not yet known, but the Beam Energy Scan II (BES-II) program at RHIC has been conducted in an effort to determine it. The possibility of creating a QGP at large densities instead of high temperatures makes these studies also interesting for the understanding of neutron stars, as a QGP could be formed in their cores.

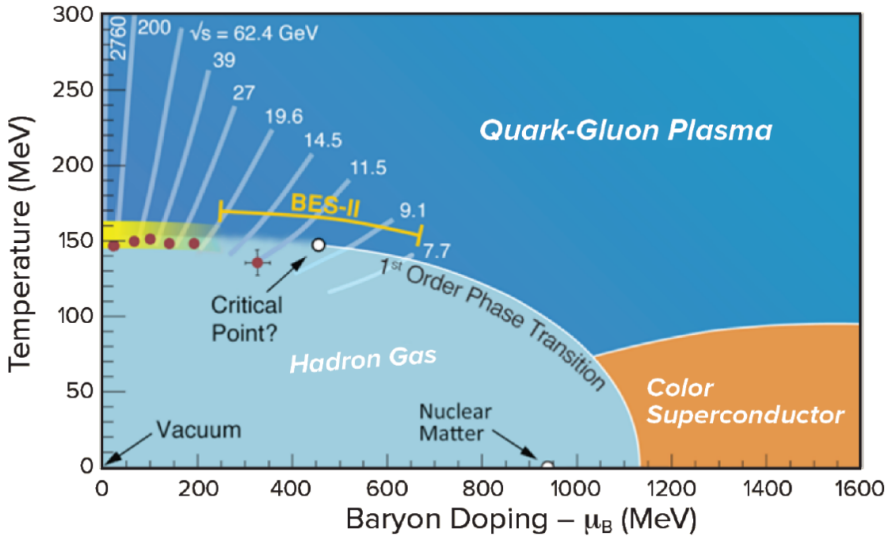

FIGURE 1.3: The QCD phase diagram. The lines are the trajectories traversed by the QGP droplets in the phase diagram for various different collision energies. Taken from [1].

1.2.2 The residual strong force

The strong interaction mediated by gluon exchange governs the structure of hadrons, such as nucleons and hyperons. However, these objects are color-neutral due to confinement, so they do not interact directly via QCD when viewed from afar (or very small Q^2). Only when interactions happen at a larger momentum scale, the QCD nature of baryons becomes apparent. This causes many highly non-trivial effects to occur, which can either be solved in an effective manner, such as chiral effective field theory, or numerically by using lattice QCD. Often, the interaction between particles is described using an interaction potential. For nucleons, an exemplary potential is shown in Fig. 1.4 (orange). It features a strong repulsion at short range and an attraction at intermediate to large distances. Note that the force is directly proportional to the first derivative of the potential

$$F(r) \propto -\frac{\mathrm{d}V}{\mathrm{d}r}, \tag{1.3}$$

so a positive slope indicates attraction and a negative slope indicates repulsion. It would

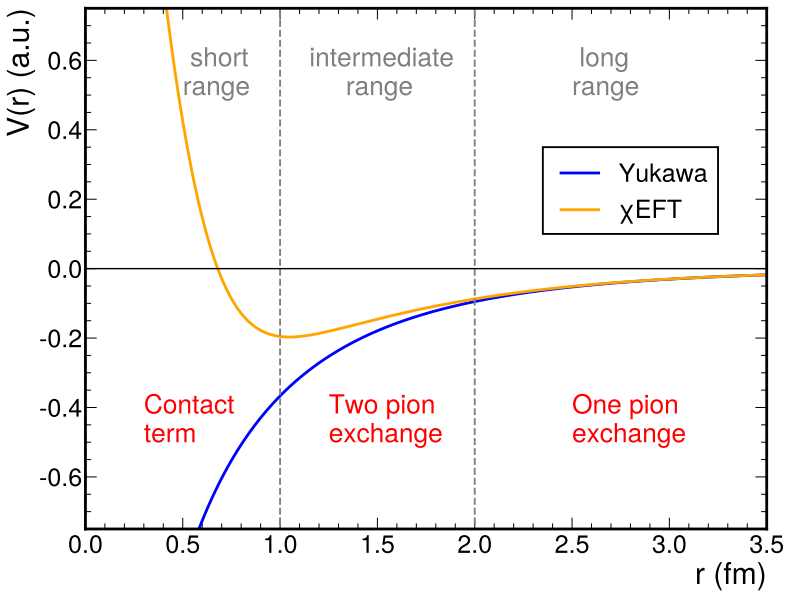

FIGURE 1.4: Sketches of the nuclear potential obtained from χEFT (orange) and the Yukawa meson exchange model (blue).

be reasonable to mark the strong repulsion at small distances down to Pauli blocking since quarks are fermions with $s = 1/2$. The two nucleons have the same types of quarks, but due to the color charge and spin combinatorics, it is possible to arrange the quarks in 12 different states, enough to not cause any blocking when looking at just two nucleons. The interaction must, however, be understood as a partonic effect due to the small distance. The real reason is the spin-spin coupling of quarks. The spin-spin potential between quarks i and j in the $\ell = 0$ state can be written as

$$V_{\mathrm{ss}}(i,j) \propto \alpha_s \sigma_i \cdot \sigma_j, \tag{1.4}$$

where $\sigma_{i,j}$ are the Pauli matrices for particle i and j, respectively. These describe the spin structure of the particle, and the scalar product between them indicates that parallel spins contribute positively (repulsively) and anti-parallel ones negatively (attractively). This has no connection to Pauli blocking since this also occurs for particles in, e.g., different color

states. This coupling only occurs for quarks with the same ℓ state. For this reason, it is energetically favorable to excite two quarks into an $\ell = 1$ state. This comes at a cost of energy and thus creates a repulsive potential. Indeed, there is an $8/9$ chance to find two quarks in a p state in the limit of two nucleons at exactly the same position ($r = 0$). Going to larger distances, the description using partonic degrees of freedom breaks down. While it is possible to describe a covalent bond between nucleons [34], where a quark is exchanged, similar to an electron in molecular bonds, due to the color charge, this effect is suppressed by a factor of $1/3$, and the resulting attraction is smaller than the measured one. This covalent bond model predicts at $r = 1$ fm a potential strength of $V_{\text{cov}} = -37$ MeV, compared to the $V_{\text{AV18}} \approx -55$ MeV predicted by modern effective potentials such as Argonne v_{18} [35].

The intermediate and long-range attraction is better described by meson exchange models, as shown in the Feynman diagram below.

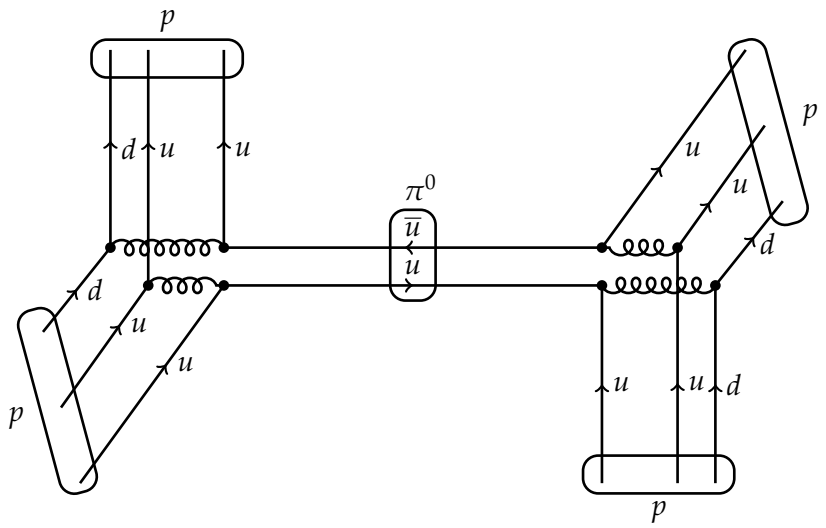

Here, a virtual meson takes on the role of the mediating particles instead of a gluon. The first example of such a model was developed by Hideki Yukawa [36] in which he proposed the existence of the pion as an exchange particle of the strong force. A simplified version of his derivation starts from the relativistic energy-momentum relation (with $\hbar = c = 1$)

$$E^2 = p^2 + m^2. \tag{1.5}$$

The Klein-Gordon equation can be obtained by quantizing this equation, i.e., replacing the energy with the Hamiltonian ($E \to i\,\partial/\partial t$) and the momentum with the momentum operator ($p \to -i\nabla$) and multiplying both sides by $i\Psi(\mathbf{x}, t)$

$$\frac{\partial^2}{\partial t^2}\Psi(\mathbf{x}, t) = (\nabla^2 - \mu^2)\Psi(\mathbf{x}, t), \tag{1.6}$$

where $\mu = \frac{m\hbar}{c}$ is the inverse range of the potential. Considering the static field limit ($\frac{\partial^2}{\partial t^2}\Psi(\mathbf{x}, t) \to 0$) and a spherically symmetric solution, one obtains

$$\frac{1}{r^2}\frac{\mathrm{d}}{\mathrm{d}r}\left(r^2\frac{\mathrm{d}\Psi(r)}{\mathrm{d}r}\right) - \mu^2\Psi(r) = 0. \tag{1.7}$$

A wave function that satisfies this equation is

$$\Psi(r) = \frac{\mathrm{e}^{-\mu r}}{r} \tag{1.8}$$

and a particularly simple ansatz for a potential that results from exchanging a particle is $V(r) = g\Psi(r)$, where g is an arbitrary constant. Choosing $g = -V_0/\mu$ results in the potential

$$V(r) = -V_0 \frac{e^{-\mu r}}{\mu r}, \tag{1.9}$$

which is the commonly known form of the Yukawa potential. This potential has the range of $1/\mu = \hbar/mc$, which is what one would expect from the Heisenberg uncertainty as the range of a particle with mass m; for the pion with $m_\pi \approx 140\ \mathrm{MeV}/c^2$ one obtains a range of 1.4 fm. This simplified derivation relies on the fact that the pion is a free particle, which, considering the density of atomic nuclei, can at best be an approximation. The resulting potential is shown in Fig. 1.4 (blue). It gives an adequate description of the long-range interaction denoted with *one pion exchange*, with diminishing quality in the intermediate range and a complete absence of the short-range repulsion. One important observation is the fact that the range decreases with increasing meson mass. In the intermediate range, the exchange of heavier mesons becomes possible, such as the $f_0(500)$. This meson has a mass of $400 - 800\ \mathrm{MeV}/c^2$ and decays into two pions. The exchange of these kinds of mesons can be modeled via *two pion exchange*, replacing the f_0 with two pions. In the short-range regime of the interaction, the exchange of even heavier vector mesons becomes possible, such as the ρ and the ω, with masses of $770\ \mathrm{MeV}/c^2$ and $782\ \mathrm{MeV}/c^2$, respectively. While these give a repulsive interaction, their effective coupling constants would need to be drastically increased in order to account for the strength of the central repulsion observed in experiments. Here, the structure of the nucleons should play a role, as discussed above. An approach that is successfully able to explain the entire range of the nuclear force is chiral effective field theory (χEFT). In this theory, only nucleons and pions exist as fundamental point-like objects. It describes the intermediate and long-range interaction via one- and two-pion exchange and the central part via direct interaction between the (fundamental) nucleons, so-called contact terms, and Pauli blocking. More information is given in Sec. 3.3.1.

1.3 Cosmic-ray antinuclei and implication for dark matter

Besides the study of fundamental nuclear interactions, nuclei, specifically their antimatter counterpart, have become a subject of interest in the field of astrophysics. The tentative observation of objects with a similar mass to helium nuclei and a doubly negative charge by the AMS-02 experiment has sparked a flurry of theoretical explanations for the origin of these antinuclei. Indeed, a very popular explanation is the creation of antinuclei in dark matter (DM) annihilation events. Dark matter is a form of matter that has only been observed due to its gravitational influence on galaxies and gravitational lensing. It also plays a key part in the current understanding of large structure formation in the early universe, where overdensities of DM lead to much faster galaxy formation than would normally be possible if only the visible matter was involved. DM thus allows our universe to form the intricate structure we see today in just 13 billion years. However, no DM particle has been directly observed, and its nature is still unknown. It can be assumed that the DM particle would only interact via gravity and the weak force, which makes it a so-called weakly interacting massive particle (WIMP). Under the WIMP assumption, DM particles could annihilate into standard model particles. They would create matter and antimatter particles in equal numbers, which is not true for the constituents of the rest of the galaxy, which is utterly dominated by matter particles. Such a source of antimatter in our galaxy could explain the measurements of antihelium by AMS-02, and even the definitive confirmation of one antinucleus would be incompatible with our current understanding without the inclusion of DM. Figure 1.5 shows the current state-of-the-art predictions in the case of antideuterons. The

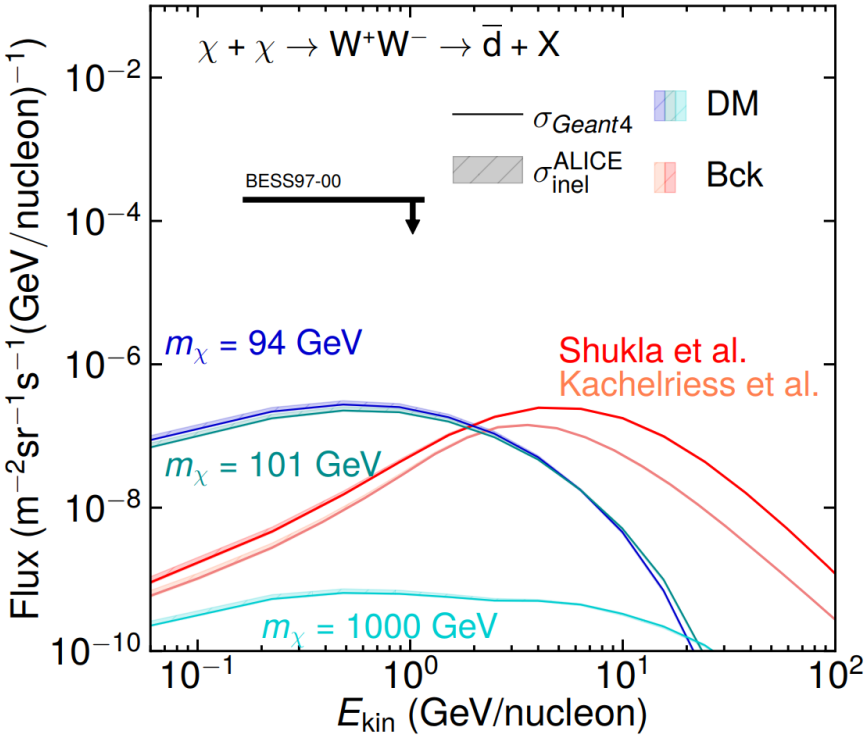

FIGURE 1.5: Deuteron flux predictions for the standard model background using two different parameterizations of the production cross-section [2, 3]. Also shown are the predictions of dark matter induced antideuteron flux for three different DM masses under the assumption that DM particles annihilate into W^+W^- boson pairs. Taken from [4].

background is described using two different parameterizations of the antideuteron production cross-section [2, 3]. This background contribution comes from high-energy cosmic rays (CRs) colliding with the interstellar medium (ISM) and creating antinuclei in the process. Such processes are well understood from collider experiments on Earth. The DM-induced signal is modeled under the assumption that the DM particles annihilate into W^+W^- boson pairs, which subsequently decay into standard model particles. It is very clear from Fig. 1.5 that at low kinetic energy, the expected signal from DM annihilations is dominant. This can be explained by the different kinematics of the production. In the background, high-energy CRs collide with the ISM, which is at rest. This creates particles very strongly boosted in the rest frame of the galaxy and results in an energy spectrum that is shifted to larger values. Since we assume that DM is approximately at rest (cold dark matter), the annihilation products will be produced with a much lower average kinetic energy. Figure 1.5 also shows that lower mass DM particles create a larger enhancement at low kinetic energies.

However, our current understanding of nuclear production is limited. The best predictions of antinuclear production in the galaxy, even from Standard Model processes only, use either simplified production models [2] or heavily simplified assumptions [3]. These simplifications lead to uncertainties of $^{+27}_{-42}$% and $\pm$20%, respectively, for the background and $^{+63}_{-70}$% for the DM contribution from production alone. If not even the background is properly understood, any interpretation of the current data, especially its interpretation as new physics, would not be possible. With the model developed in this work, a much higher precision of the background predictions could be achieved so that any signal beyond these predictions can be properly interpreted in future studies.

Another rather speculative avenue is the production of very heavy nuclei. Indeed, the

current models of kilonova explosions cannot account for the production of heavy elements, such as iron, that are observed in cosmic rays. If the nuclear production model can be arbitrarily extended to heavier masses, scenarios such as heavy element production in ultra-high cosmic ray collision could be studied.

Chapter 2

Theoretical considerations

2.1 Nuclei production models

The process by which nuclei are formed is still a topic of debate. It is surprising that these objects, which are bound by about 1 MeV/nucleon, can survive in the intense environment of a high-energy particle collision. In heavy ion collisions, temperatures can reach upwards of 150 MeV, leading to nuclei being described as 'Snowballs in Hell'. The survival problem and a detailed explanation of how they are formed can be addressed using three different families of phenomenological models: The statistical hadronization model (SHM), the kinetic approach, and the coalescence approach.

2.1.1 Statistcial hadronization model

The statistical hadronization model has been successfully applied to a large range of collision energies and systems to explain the abundances of all produced hadrons. The key concept of the SHM is that particles are produced by a statistical process, filling all available phase space from an excited region. Due to its close link to thermodynamics, it is also often referred to as thermal model. The final state conserves all quantum numbers of the initial state. Depending on the exact implementation, this is either done globally, i.e., in a grand canonical ensemble, or locally in a canonical ensemble. The grand canonical SHM is applicable only in central heavy ion collisions, while the canonical SHM (CSM) is applicable for all hadronic collisions, converging towards the grand canonical model for large event multiplicities and system sizes. Both of these models assume that nuclei are produced as compact colorless quark bags that only fully form once they have left the collision medium and subsequent hadronic cloud.

Grand canonical statistical hadronization model

A grand canonical ensemble in thermodynamics describes a system that is in thermodynamic equilibrium with a much larger reservoir. In the case of the SHM, the equilibrium is in energy, charges such as baryon number, strangeness, and electric charge. Since measurements, especially at the LHC and RHIC, are often performed in a finite rapidity window, the probed volume is much smaller than the entire collision system, and such an approximation is valid. This leads to a conservation of energy and charges only on average.

Grand canonical statistical hadronization model yields

In this section, the yields of particles in the grand canonical statistical hadronization model is calculated

$$\langle N_i \rangle^{th} = T\frac{\partial}{\partial \mu_i} \ln Z_i = \frac{VTg_i}{2\pi^2} \sum_{k=1}^{\infty} \frac{(\pm 1)^{k+1}}{k} \exp(\mu_i/T) m_i^2 K_2(km_i/T) \tag{2.1}$$

The grand canonical partition function for each hadron species i can be described as

$$\ln Z_i = \frac{Vg_i}{2\pi^2} \int_0^{\infty} \pm p^2 \mathrm{d}p \ln[1 \pm \exp(-(E_i - \mu_i)/T)] \tag{2.2}$$

with a + for fermions and a - for bosons. Further, $g_i = 2J_i + 1$ describes the Spin degeneracy factor, T is the temperature, and $E_i = \sqrt{p^2 + m_i^2}$ is the total energy. μ_i are the chemical potentials and ensure the conservation of baryon number, isospin, and strangeness. It is defined as

$$\mu_i = \mu_B B_i + \mu_{I_3} I_{3,i} + \mu_s S_i. \tag{2.3}$$

For measurements at mid-rapidity and LHC energies, the average baryon number, strangeness, and Isospin are 0. Finally, the total partition function of the system is given by the product of all particles:

$$Z = \prod_i Z_i \rightarrow \ln Z = \sum_i \ln Z_i. \tag{2.4}$$

Ref. [37] showed that doing a Taylor expansion of the natural logarithm and performing the momentum integral the partition function for a species i can be described as

$$\ln Z_i = \frac{VTg_i}{2\pi^2} \sum_{k=1}^{\infty} \frac{(\pm 1)^{k+1}}{k^2} \exp\left(\mu_i/T\right) m_i^2 K_2(km_i/T) \tag{2.5}$$

Where K_2 is the second modified Bessel function. From this partition function, the average number of particles from purely thermal production, $\langle N_i \rangle^{th}$, can be obtained with

$$\langle N_i \rangle^{th} = T\frac{\partial}{\partial \mu_i} \ln Z_i = \frac{VTg_i}{2\pi^2} \sum_{k=1}^{\infty} \frac{(\pm 1)^{k+1}}{k} \exp(\mu_i/T) m_i^2 K_2(km_i/T) \tag{2.6}$$

In addition to this direct production one also needs to take into account the contribution of heavier particles of species j feeding into particle species i

$$\langle N_i \rangle = \langle N_i \rangle^{th} + \sum_j \Gamma_{j\rightarrow i} \langle N_j \rangle^{th}, \tag{2.7}$$

where $\Gamma_{j\rightarrow i}$ is the branching ratio of species j decaying into particle species i.
This definition of particle yields, however, only holds in a gas of non-interacting hadrons and resonances, a so-called hadron resonance gas (HRG). This condition is only satisfied in a system with low density, where repulsive or attractive interactions can be neglected. To account for a repulsive interaction eigenvolume corrections of the van der Waals type can be implemented additionally [38]. Eq. 2.1 outlines the dependency of the particle yield on 5 crucial parameters: Temperature T, Volume V, and the three chemical potentials (μ_B, μ_S, μ_Q). Only two out of these five are constrained from the initial state of heavy ion collisions, μ_Q

is fixed by the isospin asymmetry of the initial state and $\mu_S = 0$ due to the vanishing net-strangeness of nuclei. μ_B is generally not constrained by the initial conditions, and only for mid-rapidity measurements at LHC energies can $\mu_B \simeq 0$ be fixed [39]. Finally, the dependence on the volume can be canceled by considering ratios of particle yields, which eventually only depend on the chemical freeze-out temperature of the system. The SHM can be used to predict the yields of hadrons going from pions to light nuclei. It is, in principle, surprising to see light nuclei in heavy ion collisions since the chemical freeze-out temperature is much higher than the binding energy of nuclei, which is of the order of MeV/nucleon. However, the thermal model is blind to the internal structure of hadrons and the hadron yields are the result of their distribution in phase space. A possible explanation on how light nuclei can survive the high temperatures of heavy ion collisions was developed in Ref. [5]: The expansion of the system after chemical freeze-out has to conserve entropy density, and it is the entropy conservation, and not the difference between the binding energy and temperature of the system, which governs the production yield in this case [5]. Figure 2.1 shows the thermal model fits to all light-flavoured hadrons measured in central (0-10%) Pb–Pb collisions at $\sqrt{s_{\rm NN}}$ = 2.76 TeV, including $A = 4$ (anti)nuclei and $A = 3$ (anti)hypernuclei, where one nucleon is replaced with a hyperon. For ^{3}He and ^{4}He the predictions of the yields, computed with the parameters obtained from the fit, are reported. The fits are performed with three different implementations of the thermal model: THERMUS 2.3 [40], GSI-Heidelberg [41], and SHARE 3 [42]. The models differ in the list of resonances included. Further, in SHARE, hadrons are assumed to be point-like, while THERMUS and GSI-Heidelberg take the hadron volume into account. For all models, the fit to the hadron yields gives a chemical freeze-out temperature $T_{\rm chem} \approx 156$ MeV, which interestingly coincides with the transition temperature obtained by Lattice QCD of $145 \leq T \leq 163$ MeV [43]. The measured yields of ^{4}He and $^4\overline{\rm He}$ agree within the uncertainties with a temperature between 137 MeV and 177 MeV, depending on the model. This means that light nuclei, from (anti)deuterons to (anti)^{4}He, are produced in statistical equilibrium at the same temperature as the other hadrons. Finally, from the fit of the particle abundances at lower energies, the

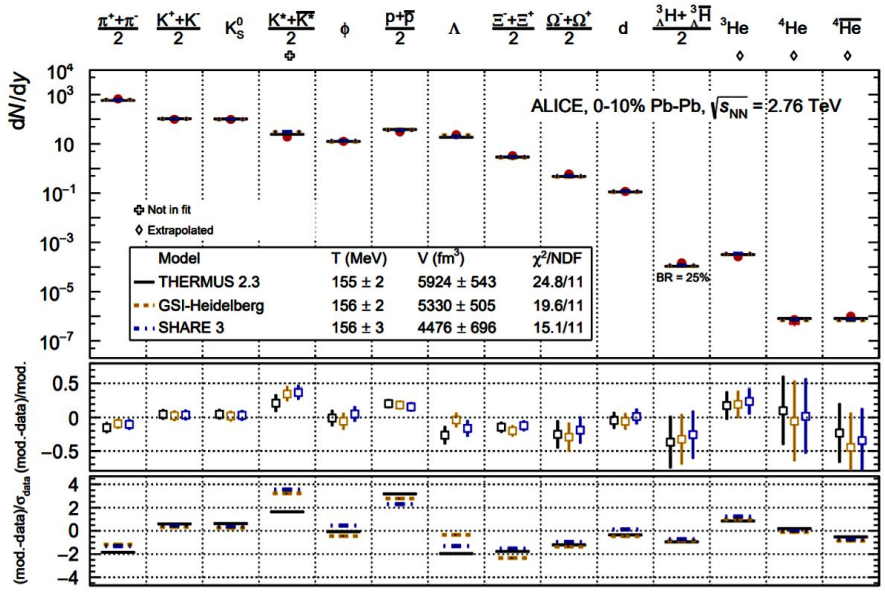

FIGURE 2.1: Grand canonical statistical hadronization model fits to all light-flavored hadrons measured in central Pb–Pb collisions at $\sqrt{s_{\rm NN}} = 2.76$ TeV. Taken from [5]

authors of Ref. [5] predicted the energy dependence of the yields of (anti)(hyper)nuclei, even

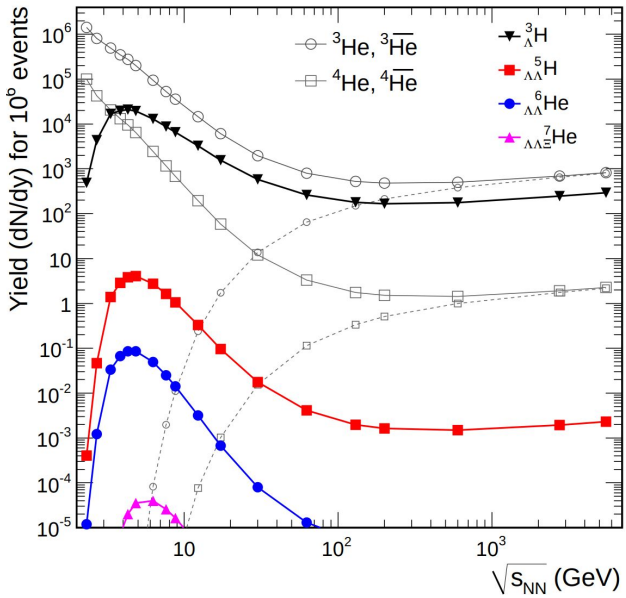

FIGURE 2.2: Prediction by the grand canonical SHM for Particle yields per 10^6 central Pb–Pb collisions as a function of the collision energy. Solid lines indicate particles, dotted lines antiparticles. Taken from [5].

multi-strange ones and ones including Ξ-baryons, which can be seen in Fig. 2.2. It shows an enhancement of nuclear production at lower energies $\sqrt{s} < 10$ GeV. This is because of an increased baryochemical potential $\mu_B \gg 0$. Similarly, antinuclei are strongly suppressed at such low energies. At LHC energies $\sqrt{s} > 1$ TeV, nuclei and antinuclei are produced in equal amounts as μ_B approaches 0.

Canonical statistical hadronization model

In systems characterized by a small reaction volume, such as peripheral heavy-ion, p–A, or pp collisions, the aforementioned reservoir becomes comparable in size to the probed region. As such, the grand-canonical ensemble is no longer applicable. Instead, the canonical ensemble has to be utilized, which not only conserves all quantum numbers on average but exactly [44], from one microscopic state to another. This results in a *canonical suppression* of particles carrying conserved charges. In the canonical ensemble, the abelian charges baryon number B, electric charge Q, and strangeness S are fixed to particular values and conserved exactly across a correlation volume V_c.

Canonical statistical hadronization model yields

In this section, the particle yield in the canonical statistical hadronization model is calculated

$$\langle N_j^{th} \rangle^{CE} = \mathcal{C}(B_j, Q_j, S_j) \langle N_j^{th} \rangle^{GCE}, \tag{2.8}$$

$$\mathcal{C}(B_j, Q_j, S_j) = \frac{\mathcal{Z}(B - B_j, Q - Q_j, S - S_j)}{\mathcal{Z}(B, Q, S)}, \tag{2.9}$$

The partition function can be written as follows:

$$\mathcal{Z}(B,Q,S) = \int_{-\pi}^{\pi}\frac{d\phi_B}{2\pi}\int_{-\pi}^{\pi}\frac{d\phi_Q}{2\pi}\int_{-\pi}^{\pi}\frac{d\phi_S}{2\pi}e^{-i(B\phi_B+Q\phi_Q+S\phi_S)}\times\exp\left[\sum_j\sum_n z_j^n e^{i(B_j\phi_B+Q_j\phi_Q+S_j\phi_S)}\right] \tag{2.10}$$

where the sum j runs of all hadron species, the sum n takes into account quantum statistics and the one-particle partition function z_j^n is defined as

$$z_j^n = (\mp 1)^{n-1}V_c\int dm\rho_j(m)d_j\frac{m^2T}{2\pi^2n^2}K_2(nm/T). \tag{2.11}$$

d_j is the degeneracy factor of the particle species j and the mass distribution ρ_j takes into account the finite width of resonances, which can be described by a Breit-Wigner function. The correlation volume V_c is usually given in multiples of the total volume per rapidity unit $V_c = kdV/dy$. Values of k usually range from $1 < k < 3$. Following the method in Ref. [45], the yield $\langle N_j^{th}\rangle^{CE}$ of particle species j in the canonical ensemble can be expressed as

$$\langle N_j^{th}\rangle^{CE} = \mathcal{C}(B_j,Q_j,S_j)\langle N_j^{th}\rangle^{GCE}, \tag{2.12}$$

where $\langle N_j^{th}\rangle^{GCE}$ is the yield in the grand canonical ensemble Eq. 2.1 and $\mathcal{C}(B_j,Q_j,S_j)$ is the canonical suppression factor

$$\mathcal{C}(B_j,Q_j,S_j) = \frac{\mathcal{Z}(B-B_j,Q-Q_j,S-S_j)}{\mathcal{Z}(B,Q,S)}, \tag{2.13}$$

where $\mathcal{Z}$ is the canonical partition function Eq. 2.10. Similarly to Eq. 2.7, the total yield can again be expressed by

$$\langle N_j\rangle^{CE} = \langle N_j^{th}\rangle^{CE} + \sum_i \Gamma_{i\to j}\langle N_i^{th}\rangle^{CE}. \tag{2.14}$$

In Ref. [6], the CSM calculations are implemented within the Thermal-FIST package. One of the main features of this package is that the conserved charges are fixed to the initial values $Q = S = B = 0$. This is well motivated as matter and antimatter are produced in equal amounts at LHC energies. All particles in this implementation are considered to be point-like. However, extensions include a finite volume exclusion, which has a minimal effect on integrated yields [46]. In Fig. 2.3, the $p/\pi, K/\pi, \phi/\pi, \Lambda/\pi, \Xi/\pi$ and Ω/π ratios are shown as a function of the charged pion yield, normalized by the predicted yield of the grand canonical thermal model. The data for different collision systems and energies is taken from ALICE, and it is compared to predictions by the CSM for various values of the correlation volume $V_c = \mathrm{d}V/\mathrm{d}y$, $3\mathrm{d}V/\mathrm{d}y$ and $6\mathrm{d}V/\mathrm{d}y$. The figure shows the struggle of the CSM to explain all yield ratios with a unified explanation. Indeed, the model performs decently for p/π with $V_c = 6\mathrm{d}V/\mathrm{d}y$. For the Λ-Baryon with strangeness $S = 1$, $V_c = 6\mathrm{d}V/\mathrm{d}y$ reproduces the data within 2 standard deviations, for the Ξ-baryon with $S = 2$, $V_c = 3dV/dy$ is preferred, and for the Ω-Baryon with $S = 3$, $V_c = \mathrm{d}V/\mathrm{d}y$ is the best fitting option. All tested options fail for the K/π ratio and for ϕ/π even the trend as a function of multiplicity is inverted. This is because canonical suppression has no effect on ϕ production since it is neutral. These issues can at least partially be remedied by introducing the strangeness saturation factor γ_S. This factor modifies Eq. 2.11: $z_j^n \to \gamma_S^{|s_j|}z_j^n$, $|s_j|$ being the total number of strange and antistrange quarks in particle species j. Since the deviations for ϕ/π are only at small multiplicities the factor γ_S is a function of multiplicity and $\gamma_S \leq 1$. Further, one can introduce a freeze-out temperature, which varies as a function of multiplicity. When fitting particle spectra with a Blast-Wave parameterization (Eq. 4.19) larger T_{kin} values are

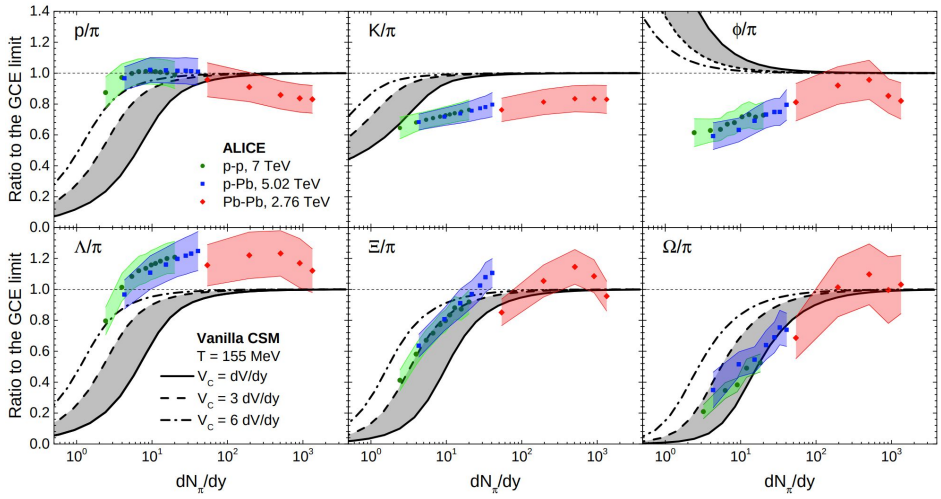

FIGURE 2.3: the ratios of various hadron-to-pion yields versus the charged pion yield. Comparison to predictions by the Vanilla CSM. Taken from [6]

observed in pp collisions ($T_{\text{kin}} \simeq 170$ MeV) compared to Pb–Pb collisions ($T_{\text{kin}} \simeq 100$ MeV). This indicates an earlier decoupling in smaller systems. The results of this modified CSM can be seen in Fig. 2.4. A much better agreement with the measured ratios can be achieved using $V_c = 3\mathrm{d}V/\mathrm{d}y$.

2.1.2 Coalescence model

A contrary approach to nuclei formation is the coalescence model. It states that only (anti)nucleons are produced in the collision. These nucleons can then bind together to form a cluster if they are close in phase space. Butler and Pearson first proposed this idea in 1963 [47] in order to explain the observations in p+A collisions at $p_{\text{beam}} = 25 - 30$ GeV/c. Their calculation is based on 3-to-2 scattering, differentiating 3 different processes: $p + n \rightarrow d^* \rightarrow X + d$, $X + p + n \rightarrow p^* + n \rightarrow d$ and $p + X + n \rightarrow p + n^* \rightarrow d$, where X denotes an interaction with the optical potential of the target nucleus A. The calculation is based on the idea that a proton-neutron pair with small relative momenta traverses the target nucleus A and, within this nucleus, feels an optical potential. The deuteron can be formed by interacting and exchanging momentum with this potential, i.e., the surrounding nucleons absorb the recoil momentum. Indeed, the problem of momentum and energy conservation is intricate in the coalescence approach. In principle, a $2 \rightarrow 1$ process, such as $p + n \rightarrow d$, can never be possible if the binding energy of the nucleus is non-zero. This is because there is no possible combination of initial momenta for the p-n pair that would allow the conservation of Energy and momentum at the same time. Usually, this can be resolved by assuming a 3rd body, which can be another nucleon or, e.g., a pion. Another ansatz to resolve this issue is by one of the nucleons being off their mass shell. This can either be in the early stages of the collision, where the surroundings are hot and dense or after scattering with yet another third particle. Similarly, also nucleons from the strong and electromagnetic decays of resonances, such as Δ^+ or N^*, resolve the issue in reactions such as $\Delta^0 + n \rightarrow d + \pi^-$. A signature of such a process could be observed in momentum correlation functions between $d + \pi$, where the Δ resonance mass peak should be clearly visible. In the model developed by Butler and Pearson the deuteron momentum distribution $\frac{d^3N_d}{dP^3}$

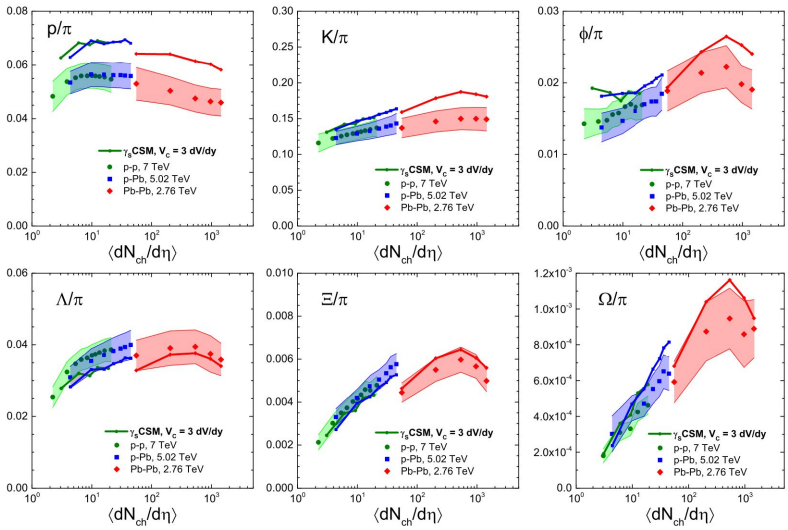

FIGURE 2.4: the ratios of various hadron-to-pion yields versus the charged pion yield. Comparison to predictions by a modified CSM, including the strangeness saturation factor γ_S and a freeze-out temperature depending on the multiplicity. Taken from [6]

can be expressed in terms of the nucleon momentum distributions $\frac{d^3N_p}{dP^3}$ as

$$\frac{d^3N_d}{dp^3} = \mathcal{B}\frac{1}{p^2}\left(\frac{d^3N_p}{dp^3}\right)^2, \tag{2.15}$$

With a momentum-independent prefactor $\mathcal{B}$. This approach neglects relativistic effects and isospin asymmetry and assumes a static optical potential. However, the latter cannot be assumed in relativistic heavy ion collisions since the projectile and the target interact so strongly and quickly. Similarly, in the same year as Butler and Pearson, Schwarzschild and Zupančič [48] pointed out that, regardless of the production mechanism, the deuteron momentum distributions should depend only on the nucleon momentum distributions and a momentum-dependent coefficient $\mathcal{B}(p)$.

$$\frac{d^3N_d}{dp^3} = \mathcal{B}(p)\left(\frac{d^3N_p}{dp^3}\right)^2 \tag{2.16}$$

This coefficient and particularly its momentum dependence will depend on the exact production mechanism. Kapusta [49] suggested a way to determine this coefficient. The main assumption of their model is that if two nucleons are close in phase space with the correct spin and isospin they are a deuteron. Thus, their argument is based on the probability of finding two nucleons within a small sphere in phase space with radius p_0. The probability for a single nucleon can be expressed as

$$P = \frac{1}{M}\frac{4\pi}{3}p_0\gamma\frac{d^3n_N}{dp^3}, \tag{2.17}$$

where M is the mean nucleon multiplicity. The probability for exactly two nucleons is

$$P_M(2) = \binom{M}{2}P^2(1-P)^{M-2}. \tag{2.18}$$

Assuming that $M \gg 1$ and P is small, the deuteron momentum density can be expressed as

$$\gamma \frac{d^3 n_d}{dp^3} = \frac{3}{4} \frac{4\pi}{3} p_0^3 \left(\gamma \frac{d^3 n_p}{dp^3} \right) \left(\gamma \frac{d^3 n_n}{dp^3} \right). \tag{2.19}$$

The free parameter p_0 has to be taken from fits to experimental data and can, in principle, also be momentum, system, and beam energy dependent. While its value is not predicted by the model, it is assumed to be of the order of the Fermi momentum inside the deuteron ($p_F \approx 450\,\mathrm{MeV}/c$). Indeed, later applications of this model give a p_0 of $\sim 100 - 300$ MeV/c [50, 51] depending on the collision energy, but also the underlying nucleon momentum distribution. One important observation is that the factor p_0 used in this way has to be inversely proportional to the volume of the system emitting the nucleons. This can be shown when assuming statistical production. The momentum density for a species emitted from a system with volume V, temperature T, chemical potential μ_i and spin S_i is

$$\frac{d^3 n_i}{dp_i^3} = \frac{S_i + 1}{(2\pi)^3} V \left[\exp\left(\frac{\sqrt{p^2 + m_i^2} - \mu_i}{T} \right) \pm 1 \right]^{-1}. \tag{2.20}$$

Following the assumption in Eq. 2.16 the deuteron and nucleon densities have to be equal times some prefactor:

$$\frac{3}{(2\pi)^3} V \left[\exp\left(\frac{\sqrt{(2p)^2 + (2m_N)^2} - \mu_d}{T} \right) - 1 \right]^{-1} = \mathcal{B} \frac{4}{(2\pi)^6} V^2 \left[\exp\left(\frac{\sqrt{p^2 + m_p^2} - \mu_N}{T} \right) + 1 \right]^{-2}. \tag{2.21}$$

From dimensional analysis already $B \propto 1/V$. Assuming $T \ll m_p$ one obtains

$$\gamma \frac{d^3 n_d}{dp^3} = \frac{3}{4} \frac{(2\pi)^3}{V} \frac{8}{\gamma} \left(\gamma \frac{d^3 n_p}{dp^3} \right) \left(\gamma \frac{d^3 n_n}{dp^3} \right), \tag{2.22}$$

or comparing with Eq. 2.19

$$\frac{4\pi}{3} p_0^3 = \frac{8}{\gamma} \frac{(2\pi)^3}{V}. \tag{2.23}$$

This dependence poses a problem when comparing measurements for different energies and systems and even impact parameters of the same energy and system. One way to resolve this issue is to introduce a hard cutoff in the distance of the nucleons coalescing into a deuteron. So far, the finite size of the deuteron has not been taken into account. However, it seems reasonable to assume that two nucleons that are 10 fm removed from each other should have a smaller probability of binding when compared to a pair that is only 1 fm apart. Using this method, a reasonable description of measurements can be achieved for small (pp) and big (Au–Au) collision systems for energies between $\sqrt{s} \sim \mathcal{O}(1)$ GeV to $\sqrt{s} \sim \mathcal{O}(10)$ TeV. The results for the d/p (and $\overline{\mathrm{d}}/\overline{\mathrm{p}}$) ratio of such a model, built on top of the UrQMD event generator can be seen in Fig. 2.5 [7]. In this study, the UrQMD model was used to obtain a two-particle phase space of protons and neutrons. Any given p-n pair is bound into a deuteron if its relative momentum Δp is less than $p_0 = 0.285$ MeV/c and its distance Δr is less than $r_0 = 3.575$ fm. These parameters are extracted in the rest frame of the pair (PRF). The cutoff parameters were obtained from a fit to AGS and SPS energies [52].
The coefficient $\mathcal{B}(p)$ from Eq. 2.16 is often referred to as the coalescence parameter B_2 in the

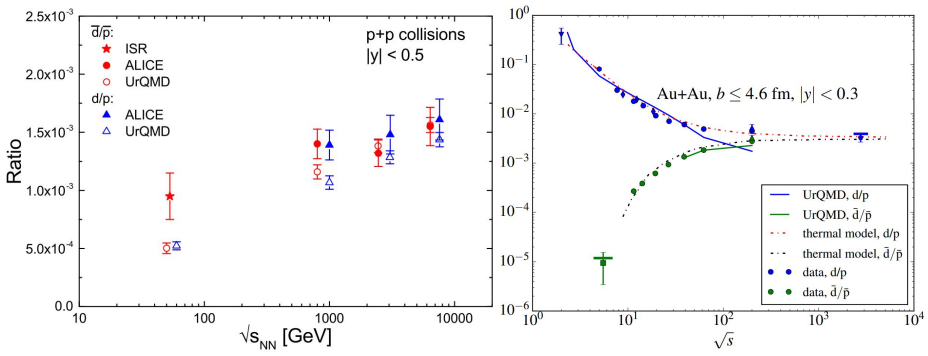

FIGURE 2.5: d/p (and $\overline{d}/\overline{p}$) ratio for p+p (left) and Au–Au collisions (right) from measurements and predictions by the UrQMD model. Adapted from [7].

case of deuterons, and more generally as B_A for A-cluster. It can be experimentally determined using measurements of the nucleon and nuclei p_{T} spectra as

$$B_A = \left(\frac{1}{2\pi p_{\mathrm{T}}^d}\frac{\mathrm{d}^2N_d}{\mathrm{d}y\mathrm{d}p_{\mathrm{T}}^d}\right) \Big/ \left(\frac{1}{2\pi p_{\mathrm{T}}^p}\frac{\mathrm{d}^2N_p}{\mathrm{d}y\mathrm{d}p_{\mathrm{T}}^p}\right)^A. \tag{2.24}$$

In the past, multiple efforts have been made to predict the coalescence parameter theoretically. Ref. [11], which builds on Ref. [53], models the momentum distribution of nucleons using an expanding fireball. For this, the Cooper-Frye formula

$$E\frac{d^3N_i}{d^3P} = \frac{2J+1}{(2\pi)^3}\int_{\Sigma_f} P\cdot d^3\sigma(R) f_i(R,P) \tag{2.25}$$

is utilized. It describes the invariant yield of particle i, which decouples from a thermalized fireball along a freeze-out surface $\Sigma_f(R)$ with momentum P and a normal four-vector $d^3\sigma_\mu(R)$. $f_i(R,P)$ is a local equilibrium distribution

$$f_i(R,P)) = \left[\exp\left(\frac{P\cdot u(R)-\mu_i(R)}{T(R)}\right)\pm 1\right]^{-1}, \tag{2.26}$$

with local temperature $T(R)$, local chemical potential $\mu_i(R)$ and local flow velocity $u^\mu(R)$. For a cluster of mass $A = Z + N$ one can assume that its yield is the overlap of A nucleons at the same position R and momenta P/A

$$E\frac{d^3N_A}{d^3P} = \frac{2J_A+1}{(2\pi)^3}\int_{\Sigma_f} P\cdot d^3\sigma(R) f_p^Z(R,P/A) f_n^N(R,P/A). \tag{2.27}$$

This equation only holds in a perfectly homogeneous, classical phase space. To combat this a quantum mechanical correction factor $\langle C_d(P)\rangle$ is introduced

$$\langle C_d(P)\rangle = \int \mathrm{d}^3r \frac{f_p^Z(R,P_d/A) f_n^N(R,P_d/A)}{f^A(R_A,P_A/A)}|\varphi(r)|^2, \tag{2.28}$$

where $\varphi(r)$ is the wave function of the target A-cluster. Under the assumption of a Gaussian wave function, e.g. for the deuteron

$$\varphi(r) = (\pi d^2)^{-3/4} \exp\left(-\frac{r^2}{2r_A^2}\right), \tag{2.29}$$

for ^{3}H and ^{3}He

$$\varphi(r_1, r_2, r_3) = (3\pi^2 d^4)^{-3/4} \exp\left(-\frac{\rho^2 + \lambda^2}{2r_A^2}\right), \tag{2.30}$$

$\langle C_A \rangle$ can be generalized as

$$\langle C_A \rangle = \prod_{i=1,2,3} \left(1 + \frac{r_A^2}{4R_i^2}\right)^{-\frac{1}{2}(A-1)}. \tag{2.31}$$

Here r_A is the size parameter of the nucleus, R_i is the i-th component of the size of the emission source. The size parameter r_A is related to the measured charge RMS radius of the nucleus λ_A^{meas} via

$$(\lambda_A^{\text{meas}})^2 - \lambda_p^2 = \frac{3}{2}\frac{A-1}{A}\frac{r_A^2}{2}, \tag{2.32}$$

where $\lambda_p = 0.879$ fm is the charge radius of the proton. Using this definition of $\langle C_A \rangle$ in Eqs. 2.24, 2.25 and 2.27 one obtains

$$B_A = \frac{2J_A + 1}{2^A \sqrt{A} m_{\text{T}}^{A-1}} \left(\frac{2\pi}{R^2 + \frac{r_A^2}{4}}\right)^{\frac{3}{2}(A-1)}, \tag{2.33}$$

where a homogeneous emission source ($R_1 = R_2 = R_3 = R$) was assumed. Eq. 2.33 relates the coalescence parameter to the size of the emission source. Experimentally determining the size of the emission source can be challenging. For this reason, the source size is usually related to charged particle multiplicity $\langle \mathrm{d}N_{\text{ch}}/\mathrm{d}\eta \rangle$ via

$$R = a\langle \mathrm{d}N_{\text{ch}}/\mathrm{d}\eta \rangle^{1/3} + b. \tag{2.34}$$

The rationale is that the particle multiplicity should depend on the overall emission volume. Thus, the radius should depend on the cube root of the multiplicity. Ref. [11] determined the parameters a=0.473 fm and b=0 fm constrained to central 0-10% Pb–Pb collisions. However, a fit to experimental pion and kaon HBT data [54–56] yields parameters a=0.339 fm, b=0.128 fm. With this translation Eq. 2.33 can be compared to experimental data as a function of $\langle \mathrm{d}N_{\text{ch}}/\mathrm{d}\eta \rangle$, as shown in Fig. 2.6. The shaded band indicates the two different source parameterizations. The previous formulation of coalescence included quantum mechanical processes as a correction factor on top of a classical calculation. Ref. [53] and already much earlier in similar form Ref. [49] proposed to do a fully quantum mechanical approach using density matrices. In this formulation, the yield of a cluster with a given momentum P_A is given by the projection of the deuteron density matrix onto the A-nucleon density matrix at freeze-out t_f

$$\frac{dN_A}{d^3P_A} \propto \frac{1}{2!} \int d^3x_1 \ldots d^3x_A d^3x'_1 \ldots d^3x'_A \phi^*(x_1, \ldots, x_A)\phi(x'_1, \ldots, x'_A) \times \langle \psi^\dagger(x'_A, t_f) \ldots \psi^\dagger(x'_1, tf)\psi(x_1, t_f) \ldots \psi(x_A, t_f)\rangle. \tag{2.35}$$

The cluster wave function ϕ is represented by a free momentum eigenstate $\phi(x_1, \ldots, x_A) =$

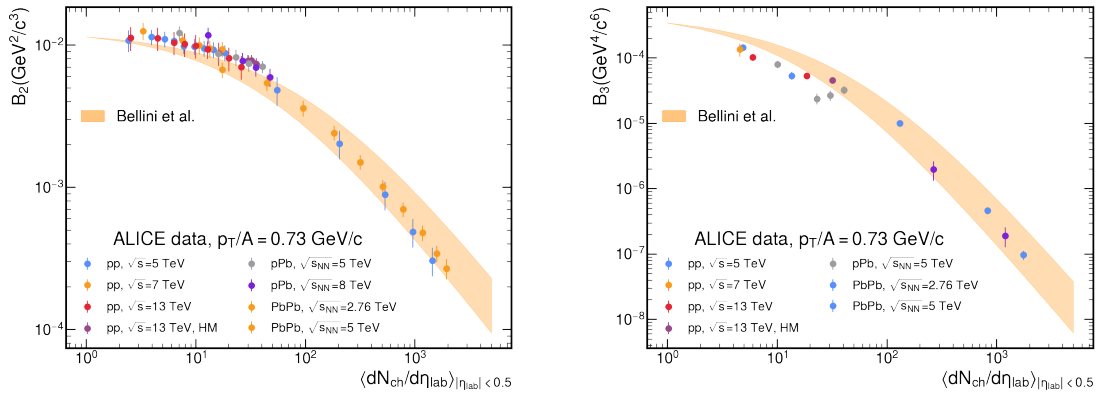

FIGURE 2.6: The coalescence parameter B_2(left) and B_3(right) measured by ALICE[8–10] compared to the prediction Eq. 2.33. The bands indicate the two different source parameterizations.

$\exp(iP_A \cdot (x_1 + \dots x_{A-1})/A)\varphi_A(\xi_1, \dots, \xi_{A-1})$ where φ is the internal wave function using relative coordinates ξ_N. For the A-nucleon density matrix, we can assume a factorization into each nucleon

$$\langle \psi^\dagger(x'_A, t_f) \dots \psi^\dagger(x'_1, tf)\psi(x_1, t_f) \dots \psi(x_A, t_f)\rangle = \langle \psi^\dagger(x'_A, t_f)\psi(x_A, t_f)\rangle \dots \psi^\dagger(x'_1, t_f)\psi(x_1, t_f)\rangle. \tag{2.36}$$

These single-particle densities can be expressed by the single-particle Wigner functions f_1^W

$$\psi^\dagger(x'_N, t_f)\psi(x_N, t_f)\rangle = \int \frac{d^3k}{(2\pi)^3} e^{ik\cdot(x_N - x'_N)} f_1^W\left(k, \frac{x_N + x'_N}{2}; t_f\right). \tag{2.37}$$

A different prescription of factorization will be discussed in Ch. 3. Further, the A-cluster density matrix can be replaced with the cluster Wigner function $\mathcal{D}$ [57]

$$\mathcal{D}(r_1, \dots, r_{A-1}; q_1, \dots, q_{A-1}) = (\pi\hbar)^{-A} \int_{-\infty}^{\infty} d^3\zeta_1 \dots d^3\zeta_{A-1} \varphi^*(r_1 + \zeta_1, \dots, r_{A-1} + \zeta_{A-1}) \varphi(r_1 - \zeta_1, \dots, r_{A-1} - \zeta_{A-1})\, e^{2i(q_1\cdot\zeta_1 + \dots + q_{A-1}\cdot\zeta_{A-1})/\hbar}. \tag{2.38}$$

With these replacements Eq. 2.35 reads for an A=2 cluster

$$\frac{dN_d}{d^3P_d} = \frac{G_d}{(2\pi)^3} \int d^3R \frac{d^3q}{(2\pi)^3} d^3r \mathcal{D}(r, q) f_1^W\left(\frac{P_d}{2} + q, R + \frac{r}{2}; t_f\right) f_1^W\left(\frac{P_d}{2} - q, R - \frac{r}{2}; t_f\right). \tag{2.39}$$

Here, the coordinates $\frac{x_N + x'_N}{2}$ have been replaced by central coordinates $R \pm \frac{r}{2}$. Finally, Ref. [12] argues that the $\pm q$ inside the f_1^W functions can be neglected to $\sim$ 10% accuracy in Pb–Pb collisions. With this approximation, the q integration can be performed

$$\int d^3q \mathcal{D}(r, q) = (2\pi)^3 |\varphi_d(r)|^2, \tag{2.40}$$

where we can define

$$|\varphi_d(r)|^2 = \int \frac{d^3q}{(2\pi)^3} e^{ik\cdot r} \mathcal{D}(q), \tag{2.41}$$

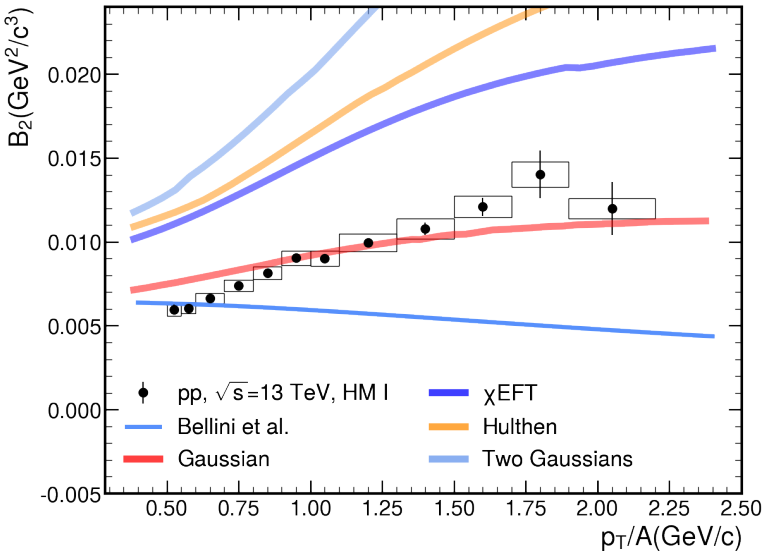

FIGURE 2.7: Comparison between the measurements by the ALICE collaboration in pp collisions at $\sqrt{s}$=13 TeV, in the multiplicity class HM I ($\langle dN_{ch}/d\eta \rangle = 35.8$ and theoretical predictions using Eq. 2.33(Bellini et al.)[11] and Eq.2.43[12] for various different wave functions of the deuteron. The latter is taken from Ref. [9].

and finally

$$\frac{dN_d}{d^3P_d} = \frac{G_d}{(2\pi)^3} \int \frac{d^3q}{(2\pi)^3} \mathcal{D}(q) \int d^3R\, d^3r\, f_1^W\left(\frac{P_d}{2}, R + \frac{r}{2}; t_f\right) f_1^W\left(\frac{P_d}{2}, R - \frac{r}{2}; t_f\right). \quad (2.42)$$

Using this formulation, a description of the coalescence parameter B_2 can be found [12]

$$B_2(p) \approx \frac{3}{2m} \int d^3q \mathcal{D}(q) \mathcal{C}_2^{\mathrm{PRF}}(p,q). \quad (2.43)$$

$\mathcal{C}_2^{\mathrm{PRF}}(p,q)$ is the two-nucleon momentum correlation function. The idea behind Eq. 2.43 is that the two-nucleon momentum distribution is projected on the deuteron final state in momentum space, similarly to Eq. 2.42, but the spatial part is integrated out. Under the assumption that the source distribution has a Gaussian shape and is homogeneous, i.e. $R = R_{\parallel} = R_{\perp}$, $\mathcal{C}_2^{\mathrm{PRF}}(p,q)$ takes the form [9]

$$\mathcal{C}_2^{\mathrm{PRF}}(p,q) = e^{-R^2q^2}, \quad (2.44)$$

where R is the source radius, p is the total momentum of the nucleon pair, and q is the relative momentum, defined in the pair rest frame. Ref. [14] has measured the source radius as a function of the pair transverse mass $m_T = \sqrt{\left(\frac{\vec{p}_{T,1}+\vec{p}_{T,2}}{2}\right)^2 + \left(\frac{m_1+m_2}{2}\right)^2}$. Using these measured radii, predictions of B_2 can be made using Eq. 2.33 and Eq. 2.43. They can be found in Fig. 2.7, compared to measurements by the ALICE collaboration [9]. The predictions using Eq. 2.43 and a Gaussian wave function show a very good agreement with the data. This is surprising, as the Gaussian is assumed to be a worse representation of the deuteron than other wave functions used, especially the one obtained from χEFT. Further, the prediction from Eq. 2.33 shows an inverted trend with transverse momentum. Eq. 2.43 can be obtained

from Eq. 2.33 with the replacement $m \to m_T$ and Ref. [53] has argued that this replacement should hold in general and should be used at finite p_T. This means Eq. 2.43 should only be used at $p_T = 0$. Further, neglecting the $\pm q$ terms in eq. 2.39 has an unquantified effect when applied to small systems. All of these factors contribute to an inaccurate prediction of B_2.

Kinetic approach

The kinetic approach is similar in spirit to the coalescence model. Nuclei are formed after hadronization. However, the main difference lies in the microscopic implementation. In the kinetic approach, nuclei are formed from multi-body scattering between nucleons and mesons in the hadronic phase. These scatterings include the reactions $Npn \leftrightarrow Nd$, $\pi pn \leftrightarrow \pi d$, ${}^3He\pi \leftrightarrow \pi npp$. One recent implementation was done in SMASH 2.0 for deuterons [13]. They implemented the process $\pi d \leftrightarrow \pi pn$ in two different ways: with only $2 \leftrightarrow 2$ reactions and $3 \leftrightarrow 2$ reactions. The former requires the process to happen in multiple steps. First, the nucleons form a non-existent excited state of the deuteron $pn \leftrightarrow d'$. Then, the excited deuteron would decay by interacting with a pion $\pi d' \leftrightarrow \pi d$. Since now the 3-body process is expressed in two 2-body processes, a geometric interaction criterion can be utilized, where a reaction occurs when the transverse distance d_T is smaller than the interaction distance d_{int} given by the cross-section σ:

$$d_T < d_{int} = \sqrt{\frac{\sigma}{\pi}}. \tag{2.45}$$

Reaction probability in the kinetic approach

In this section, the $2 \to 3$ and $3 \to 2$ reaction probabilities, which correspond to deuteron formation and breakup, respectively, in the kinetic approach, are calculated.

$$P_{2\to3} = \frac{\Delta t}{\Delta^3 x} v_{rel} \frac{1}{S'_{23}!} \int d\Phi_3 \frac{\frac{1}{\prod_{j=1}^{n} 2E_j} \int d\Phi_m \frac{1}{\prod_{j=1}^{n} g_j} \sum_{\text{i,f}} |T_{2\to3}|^2}{2\lambda^{1/2}(s, m_1^2, m_2^2)} \tag{2.46}$$

$$P_{3\to2} = \frac{g_{1'} g_{2'}}{g_1 g_2 g_3} \frac{S_{32}!}{S'_{32}!} \frac{\Delta t}{(\Delta^3 x)^2} \frac{E_{1'} E_{2'}}{2E_1 E_2 E_3} \frac{\Phi_2(s)}{\Phi_3(s)} v_{rel} \frac{1}{S'_{23}!} \int d\Phi_3 \frac{\frac{1}{\prod_{j=1}^{n} 2E_j} \int d\Phi_m \frac{1}{\prod_{j=1}^{n} g_j} \sum_{\text{i,f}} |T_{2\to3}|^2}{2\lambda^{1/2}(s, m_1^2, m_2^2)}, \tag{2.47}$$

This approach, however, has no general extension to 3-body interaction since there is no straightforward generalization of d_T to a 3-particle system. In order to alleviate the problem of introducing the non-existent d', a stochastic criterion was introduced. In the framework of this criterion, a probability $P_{n\to m}$ can be calculated for a $n \to m$ reaction as the number of reactions $\Delta N_{recations}$ over the number of all possible particle combinations inside a sub-volume $\Delta^3 x$ and time interval Δt

$$P_{n\to m} = \frac{\Delta N_{reactions}}{\prod_{j=1}^{n} \Delta N_j}. \tag{2.48}$$

Using the Boltzmann equation to quantify the number of reactions in a phase space element one obtains

$$P_{n\to m} = \frac{1}{S'!} \frac{\Delta t}{(\Delta^3 x)^{n-1}} \frac{1}{\prod_{j=1}^{n} 2E_j} \int d\Phi_m \frac{1}{\prod_{j=1}^{n} g_j} \sum_{\text{initial,final}} |T_{n\to m}|^2 \tag{2.49}$$

where S′ is the number of identical particles in the final state, g_j is the spin degeneracy factor $g_j = 2s_j + 1$ and $T_{n\to m}$ is the scattering matrix element summed over initial and final states.

$d\Phi_m$ is the m-particle phase space element

$$d\Phi_m = (2\pi)^4 \delta^{(4)} \left(P - \sum_{k=1}^{m} p_k \right) \prod_{k=1}^{m} d\Gamma_k, \tag{2.50}$$

where P is the total 4-momentum of the reaction and p_k the four momenta of the final state particles. For the phase space element $d\Gamma_k$ they use

$$d\Gamma = \frac{d^3p}{(2\pi)^3 2E} \tag{2.51}$$

for stable particles and for resonances

$$d\Gamma = \frac{d^4p}{(2\pi)^4} \frac{\pi}{\sqrt{s}} \mathcal{A}(\sqrt{s}) = \frac{dM}{2} \frac{1}{E_M} \frac{d^3p}{(2\pi)^3} \mathcal{A}(M), \tag{2.52}$$

where $M = \sqrt{s} = \sqrt{(p^0)^2 - p^2}$, $E_M^2 = p^2 + M^2$ and $\mathcal{A}(M)$ is the spectra function of the state, normalized to one

$$\int_0^\infty dM \mathcal{A}(M) = 1. \tag{2.53}$$

The limiting case of a stable particle would be an infinitely narrow resonance with $\mathcal{A}(M) = 2M\delta(M^2 - m^2)$. To simplify, one can assume that the scattering matrix element depends only on the initial center-of-mass energy $\sqrt{s}$ and not the available phase space. This allows us to pull it out of the integral in Eq. 2.49, and we can obtain the integrated m-body phase space

$$m = 1 : \Phi_1(M^2) = \frac{\pi}{M} \mathcal{A}(M) \tag{2.54}$$

$$m = 2 : \Phi_2(M^2; m_1^2, m_2^2) = \frac{\lambda^{1/2}(M^2, m_1^2, m_2^2)}{8\pi M^2} \tag{2.55}$$

$$m = 3 : \Phi_3(M^2; m_1^2, m_2^2, m_3^2) = \frac{1}{2\pi} \int_{(m_1+m_2)^2}^{(M-m_3)^2} ds_1 \Phi_2(M^2; s_1, m_3^2) \Phi_2(s_1; m_1^2, m_2^2), \tag{2.56}$$

where $\lambda(M^2; m_1^2, m_2^2) = (M^2 - m_1^2 - m_2^2)^2 - 4m_1^2 m_2^2$ is the Källén function. Finally, we can express the probabilities of deuteron formation and breakup $P_{3\to2}$ and $P_{2\to3}$

$$P_{2\to3} = \frac{\Delta t}{\Delta^3 x} v_{rel} \frac{1}{S'_{23}!} \int d\Phi_3 \frac{\frac{1}{\prod_{j=1}^n 2E_j} \int d\Phi_m \frac{1}{\prod_{j=1}^n g_j} \sum_{\text{initial,final}} |T_{2\to3}|^2}{2\lambda^{1/2}(s, m_1^2, m_2^2)} \tag{2.57}$$

$$P_{3\to2} = \frac{g_{1'} g_{2'}}{g_1 g_2 g_3} \frac{S_{32}!}{S'_{32}!} \frac{\Delta t}{(\Delta^3 x)^2} \frac{E_{1'} E_{2'}}{2E_1 E_2 E_3} \frac{\Phi_2(s)}{\Phi_3(s)} v_{rel} \frac{1}{S'_{23}!} \int d\Phi_3 \frac{\frac{1}{\prod_{j=1}^n 2E_j} \int d\Phi_m \frac{1}{\prod_{j=1}^n g_j} \sum_{\text{initial,final}} |T_{2\to3}|^2}{2\lambda^{1/2}(s, m_1^2, m_2^2)}, \tag{2.58}$$

where $v_{rel} = \frac{\lambda^{1/2}(s, m_1^2, m_2^2)}{2E_1 E_2}$ is the relative velocity. It is important to mention that the factor S'_{23} is the number of identical particles in the $2 \to 3$ reaction, and generally different than S'_{32} in the $3 \to 2$ reaction. $\Phi_2(s)$ and $\Phi_3(s)$ correspond to the 2- and 3-body phase spaces corresponding to the final and initial states, respectively.

Figure 2.8 shows the results for this model for simulations of Au–Au collisions at $\sqrt{s} = 7.7$ GeV. It shows the time evolution of the number of deuterons for four different scenarios: The full lines represent the scenario, wherein an initial hydrodynamic evolution of the system, deuterons will freeze out with other hadrons, akin to the thermal model. The

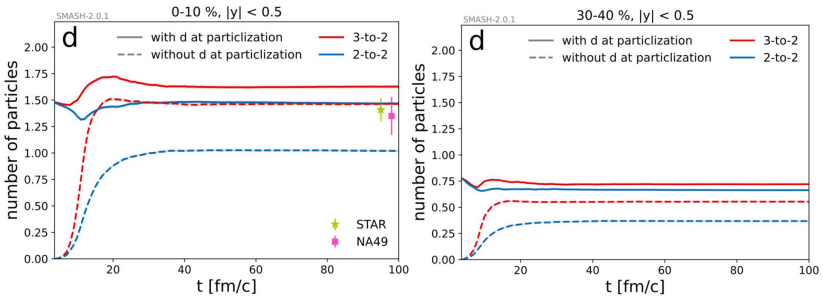

FIGURE 2.8: Time evolution of the deuteron numbers for Au+Au collisions at $\sqrt{s} = 7.7$ GeV using SMASH for 0-10%(left) and 30-40%(right) centrality. The results are given for an initial state with and without deuterons from thermal production ("with(out) d at particularization") and for deuterons produced in $2 \leftrightarrow 2$ and $3 \leftrightarrow 2$ reactions. Taken from [13].

dashed lines indicate the scenario where no deuterons, only nucleons, are produced at the freeze-out. Further, the blue lines indicate the prediction using only $2 \leftrightarrow 2$ reactions and a geometric collision criterion, while the red lines indicate production via $3 \leftrightarrow 2$ reactions and the stochastic criterion. Interestingly, two scenarios are compatible with data for 0-10% centrality, namely the thermal production and $2 \leftrightarrow 2$ reactions as well as no thermal production and $3 \leftrightarrow 2$ reactions. Moving toward more peripheral collisions, all four predictions show unique results, which indicates that high-precision data for peripheral collisions could help differentiate the four scenarios. Generally, the kinetic approach seems to resolve the aforementioned problem of "snowballs in hell", very lightly bound objects surviving the high temperatures of the fireball. It resolves it by showing that the nuclei don't necessarily survive the fireball, but they get reformed from multi-body reactions.

2.2 Femtoscopy

In the context of coalescence, nuclei are produced by final state interactions. Traditionally, the interactions between particles have been measured using scattering experiments. This means that the target and the beam have to be made up of the particles one wants to study. While this works well for (reasonably) long-lived and stable particles, it is technically challenging to produce a beam of very short-lived particles. Indeed, most particles that can be produced in hadronic collisions are so short-lived that even when flying close to the speed of light, they would only traverse several cm in their rest frame. Femtoscopy is an experimental technique to access the interactions between particles without the need for a beam made of exotic particles. It utilizes two-particle correlations in momentum space to access the Final State Interaction (FSI).

2.2.1 The correlation function

A theoretical prediction of the resulting correlation function as a function of the relative momentum in the pair's rest frame (PRF) can be expressed via the Koonin-Pratt equation [58, 59]

$$C(k^*) = \int \mathrm{d}^3 r^* \; S(r^*) |\psi(r^*, k^*)|^2. \tag{2.59}$$

Eq. 2.59 shows that the measured correlation function is the result of folding the two-particle wave function $\psi(r^*, k^*)$[1] with the source function $S(r^*)$, which corresponds to the distribution of relative distances of the particles after freeze-out. The source function can be determined using particles with known interaction, such as $\pi^{\pm}$, and constraining the source distribution with the measured correlation function. This approach works well in heavy ion collisions, where source sizes are large. However, in small systems, such as pp collisions, the lifetime of potential resonances feeding into pions is comparable to the size of the system. This leads to different source sizes for different hadron pairs. The ALICE collaboration has shown [14] that all hadron-hadron pairs are emitted with the same source size if strongly decaying resonances are removed. This allows one to construct the expected source size for any pair by adding all resonances decaying into them on top of the so-called core source size. Experimentally, the correlation function is defined as the probability of finding a pair with momenta p_1 and p_2, normalized to the uncorrelated sample

$$\mathcal{C}(p_1, p_2) = \frac{\mathcal{P}(p_1, p_2)}{\mathcal{P}(p_1)\mathcal{P}(p_2)}. \tag{2.60}$$

In practice, these probabilities are determined using the same and mixed event distributions $N_{\mathrm{s}}(k^*)$ and $N_{\mathrm{m}}(k^*)$, normalized with a constant such that the function for large k^* approaches unity

$$\mathcal{C}(p_1, p_2) = C(k^*) = \mathcal{N}\frac{N_{\mathrm{s}}(k^*)}{N_{\mathrm{m}}(k^*)} \overset{k^*\to\infty}{\longrightarrow} 1. \tag{2.61}$$

The same event distribution is defined as the distribution of pairs in k^* space, where the pair was constructed from two particles in the same event. The mixed event is similarly constructed, but the pair is from particles in different events. The latter removes trivial phase space correlations from the former, and one is left with only genuine two-particle correlations. These correlations can contain a large variety of contributions. Next to the genuine FSI, effects of the Bose-Einstein or Fermi-Dirac statistics can be seen. Fig. 2.9 shows the influence of these interactions on the correlation function, with the example of p–p pairs. The strong interaction between protons is attractive. As such, the correlation function rises towards lower values of k^*, here modeled using the Argonne v_{18} potential [35]. Since both particles are positively charged, their coulomb interaction is repulsive, and the correlation function is below unity, falling towards low k^*. Protons are fermions and, as such, adhere to the Fermi-Dirac statistics. This means that their correlation function approaches 0.5 at $k^* = 0$. When added up, the solid line is obtained as the theoretical p–p correlation function. In reality, more contributions have to be taken into account. For one, the protons could stem from a decay of a Λ Baryon, which is denoted p_Λ–p. This Λ would also interact with the other proton before it decays. Such a contribution would be added by adding the p–Λ correlation function weighted by the contribution of p_Λ–p pairs to the genuine p–p pairs. This weight is called the $\lambda_{p-\Lambda}$-parameter. Generally, these λ parameters can be obtained for all kinds of feed-down contributions into protons using

$$\lambda_{\mathrm{ik}} = P_{\mathrm{i}} f_{\mathrm{i}} \cdot P_{\mathrm{k}} f_{\mathrm{k}}, \tag{2.62}$$

where P_{j} is the experimental purity of particle species j and f_{j} the fraction of proton from species j. Lastly, particles can be wrongly identified or be the result of material knock-out of the detector. The latter is particularly important for p–p correlations. Also, for these, a λ parameter can be obtained from Monte Carlo studies. Finally, once all contributions are determined, a total correlation function can be calculated from the genuine correlation

[1] in this chapter the superscript * denotes the quantity evaluated in the PRF.

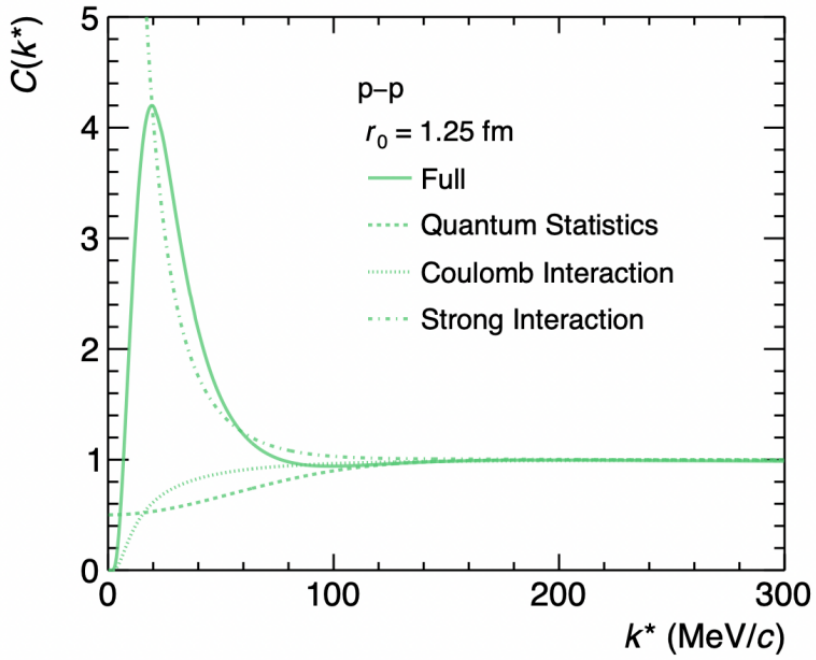

FIGURE 2.9: Theoretical correlation function for p–p pairs with a source size of 1.25 fm. The effect of Strong and Coulomb interaction, as well as Quantum statistics, is separated.

function and residual correlations

$$C(k^*) = \lambda_{\text{gen}} C_{\text{gen}}(k^*) + \sum \lambda_{\text{ij}} C_{\text{ij}}(k^*). \tag{2.63}$$

A special contribution to the residual correlations are unstable particles that decay into the two particles whose correlation function is under investigation. For example, a Δ resonance decays into a proton and a pion. In the correlation function of proton-pion, a signature of this decay will be visible, similarly to an invariant mass plot. Indeed, a direct connection between the relative momentum k^* and the invariant mass M can be made for a particle pair A and B

$$M = \sqrt{m_A^2 + k^{*2}} + \sqrt{m_B^2 + k^{*2}}. \tag{2.64}$$

2.2.2 The particle emission source

With the correlation function modeling under control, we can extract the genuine correlation function $C_{gen}(k^*)$ and compare it with Eq. 2.59. The required theoretical ingredients are the source size $S(r^*)$ and the two-body wave function $\Psi(r^*, k^*)$, which can be calculated by solving the Schrödinger equation with the interaction potential[60]. Traditionally, femtoscopy was performed in Heavy Ion collisions with pions to determine the source size. However, this paradigm has shifted over the years, and femtoscopy is used to access the final state interactions between hadrons. In order to perform these investigations, the source needs to be determined first. Investigations in Heavy Ion collisions have shown[61] that the size of the source depends on the particle species investigated. This would induce a huge uncertainty when studying exotic species as the source term would be unknown. ALICE[14] has studied the source size in pp collisions for p–p and p–Λ pairs. These pairs are used since the interaction is well-known from decades of scattering experiments. Thus, the wave function

in Eq. 2.59 can be determined using tools like CATS[60], which solve the Schrödinger equation for a known interaction potential. Furthermore, the analysis was done as a function of the transverse mass $\langle m_T \rangle$. In Heavy Ion collisions, it has been shown that the source size depends on $\langle m_T \rangle$, where it was attributed to collective behavior due to hadronic flow. As can be seen in Fig. 2.10 (left) the source size for p–p and p–Λ pairs is different. However, around 65% of protons and Λ are produced by feed-down from resonances. Interestingly, the resonances feeding into Λ are, on average, longer lived ($c\tau$ ~4.69 fm) than the ones feeding into protons ($c\tau$ ~1.65 fm). Utilizing the Resonance Source Model (RSM)[14], the source distribution is split up into a Gaussian core part of primordially produced hadrons and an exponential tail produced by various resonances decaying. Subtracting the resonances leads to the core source size in Fig. 2.10(right). As can be seen, it is equal for p–p and p–Λ pairs. In fact, this measurement has been repeated for π–π and K^+–p pairs, and the same scaling of the source with m_T can be observed[62]. Using this common hadron emission source, the

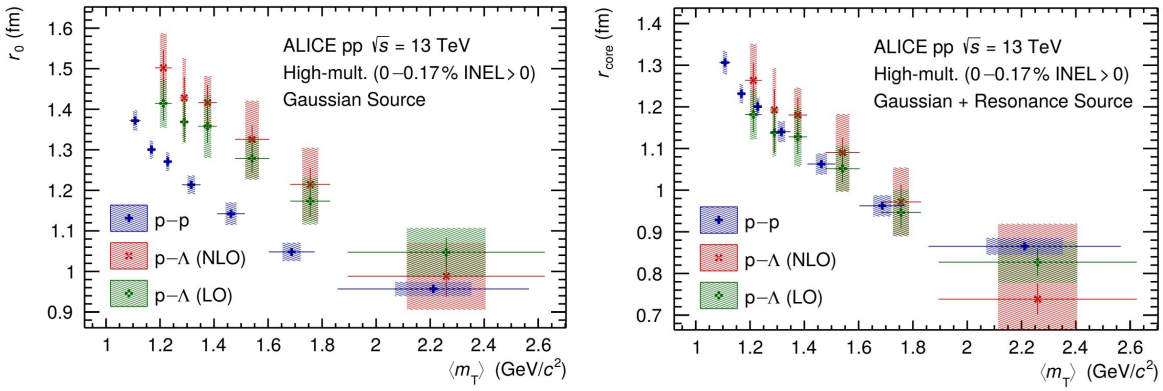

FIGURE 2.10: (left) Source radius r_0 for p–p and p–Λ pairs as a function of $\langle m_T \rangle$ assuming a purely Gaussian source. For p–Λ, the results for two different interaction potentials are shown. (right) Core source radius r_{core} as a function of $\langle m_T \rangle$ assuming a Gaussian core with an exponential tail produced by decaying resonances. The size of the Gaussian core is shown only. Taken from [14]

source for exotic pairs can be determined by adding the decays to these specific hadrons onto the core source. The source size including resonances can also be used in coalescence models, like Eq. 2.33 or Eq. 2.43.

Chapter 3

Wigner function coalescence

As explained in Ch. 2.1.2 the formation of light nuclei can be explained by the coalescence model, which states that nucleons can bind together if they are close in phase space after freeze-out. What it means to be close in phase space depends on the exact implementation of the model, of which several were given. Generally, it means that the particles are in the correct spin and isospin configuration and are close in momentum and coordinate space. The implementation used throughout this work, the so-called Wigner Function Formalism, will be explained in this chapter in detail.

3.1 Wigner function formalism

Wigner function formalism probability

In this section, the coalescence probability in the Wigner function formalism is derived

$$\mathcal{P}(r_0, q) \int \mathrm{d}^3 r \mathrm{d}^3 r_d \, H_{\mathrm{pn}}(\mathbf{r}, r_{\mathrm{d}}; r_0) \mathcal{D}(r, q), \tag{3.1}$$

Its starting point is very close to Eq. 2.35 from Ref. [53], but the derivation will very closely follow Ref. [63]. The Deuteron (or generally nuclei yield) can be found by projecting the deuteron density matrix ρ_{d} onto the two nucleon density matrix

$$\frac{d^3N}{dP_d^3} = \mathrm{tr}(\rho_{\mathrm{d}} \rho_{\mathrm{pn}}). \tag{3.2}$$

The nucleon density matrix can then be written as

$$\rho_{\mathrm{pn}} = |\psi_{\mathrm{n}} \psi_{\mathrm{p}}\rangle\langle\psi_{\mathrm{p}} \psi_{\mathrm{n}}|, \tag{3.3}$$

with normalization

$$\langle\psi_{\mathrm{n}} \psi_{\mathrm{p}}|\psi_{\mathrm{p}} \psi_{\mathrm{n}}\rangle = N_{\mathrm{n}} N_{\mathrm{p}}, \tag{3.4}$$

where N_{n} and N_{p} are the average multiplicities of neutrons and protons respectively. This neglects double counting, where one nucleon could, in principle, show up in multiple deuterons. This effect, however, should be of the order of the ^{3}He yield and thus less than a 1% effect. When evaluating the trace $\mathrm{tr}(\rho_{\mathrm{d}} \rho_{\mathrm{pn}})$ in its coordinate representation, one finds

$$\frac{d^3N}{dP_{\mathrm{d}}^3} = S \int \mathrm{d}^3 x_1 \mathrm{d}^3 x_2 \mathrm{d}^3 x_1' \mathrm{d}^3 x_2' \phi_{\mathrm{d}}^*(\mathbf{x}_1, \mathbf{x}_2) \phi_{\mathrm{d}}(\mathbf{x}_1', \mathbf{x}_2') \left\langle \psi_{\mathrm{n}}^\dagger(\mathbf{x}_2') \psi_{\mathrm{p}}^\dagger(\mathbf{x}_1') \psi_{\mathrm{p}}(x_1) \psi_{\mathrm{n}}(x_2) \right\rangle, \tag{3.5}$$

where $\psi_{\mathrm{i}}(\mathbf{x})$ is the wave function of nucleon i. S is a statistical factor denoting the probability that the constituent nucleons are in the correct spin and isospin state. S =3/8 for the

deuteron and S =1/12 for ^{3}He, ^{3}H and $^3_\Lambda$H [64]. The deuteron wave function $\phi_\mathrm{d}(\mathbf{x}_1, \mathbf{x}_2)$ can be factorized into a plane wave describing the CoM motion and an internal wave function $\varphi_\mathrm{d}(\mathbf{r})$

$$\phi_\mathrm{d}(\mathbf{x}_1, \mathbf{x}_2) = (2\pi)^{-3/2} \exp(i\mathbf{P}_\mathrm{d} \cdot (\mathbf{x}_1 + \mathbf{x}_2)/2)\varphi_\mathrm{d}(\mathbf{x}_1 - \mathbf{x}_2). \tag{3.6}$$

Similarly to Ref. [53], the density matrices can be replaced by their respective Wigner functions

$$\left\langle \psi^\dagger_\mathrm{n}(\mathbf{x}'_2)\psi^\dagger_\mathrm{p}(\mathbf{x}'_1)\psi_\mathrm{p}(\mathbf{x}_1)\psi_\mathrm{n}(\mathbf{x}_2) \right\rangle = \int \frac{\mathrm{d}^3p_\mathrm{n}\mathrm{d}^3p_\mathrm{p}}{(2\pi)^6} W_\mathrm{pn}\left(\mathbf{p}_\mathrm{n}, \mathbf{p}_\mathrm{p}, (\mathbf{x}_2 + \mathbf{x}'_2)/2, (\mathbf{x}_1 + \mathbf{x}'_1)/2\right) \exp(i\mathbf{p}_\mathrm{n} \cdot (\mathbf{x}_2 - \mathbf{x}'_2)) \exp(i\mathbf{p}_\mathrm{p} \cdot (\mathbf{x}_1 - \mathbf{x}'_1)) \tag{3.7}$$

and for the deuteron

$$\mathcal{D}(r, q) = \int \mathrm{d}^3\boldsymbol{\zeta} \exp(-i\mathbf{q} \cdot \boldsymbol{\zeta})\varphi_\mathrm{d}(\mathbf{r} + \boldsymbol{\zeta}/2)\varphi^*_\mathrm{d}(\mathbf{r} - \boldsymbol{\zeta}/2). \tag{3.8}$$

Finally, the deuteron yield can be written as

$$\frac{d^3N}{dP^3_\mathrm{d}} = \frac{S}{(2\pi)^6} \int \mathrm{d}^3q\, \mathrm{d}^3r\, \mathrm{d}^3r_\mathrm{d} \mathcal{D}(r, q) W_\mathrm{pn}(\mathbf{P}_\mathrm{d}/2 + \mathbf{q}, \mathbf{P}_\mathrm{d}/2 - \mathbf{q}, \mathbf{r}, \mathbf{r}_\mathrm{d}), \tag{3.9}$$

where $\mathbf{r} = \mathbf{r}_\mathrm{n} - \mathbf{r}_\mathrm{p} = (\mathbf{x}_2 + \mathbf{x}'_2)/2 - (\mathbf{x}_1 + \mathbf{x}'_1)/2$ and $\mathbf{r}_\mathrm{d} = \mathbf{r}_\mathrm{n} + \mathbf{r}_\mathrm{p} = (\mathbf{x}_2 + \mathbf{x}'_2)/2 + (\mathbf{x}_1 + \mathbf{x}'_1)/2$. The starting point for this derivation are single free nucleon momentum distributions. It is important to note that, strictly speaking, there is no overlap between the density matrix of two free nucleons and the one of two bound nucleons. This is because of energy and momentum conservation. The deuteron is bound by 2.2 MeV per nucleon, so either the formation happens via photon emission $p + n \to d + \gamma$, or a third particle (usually a pion) is required to take away excess momentum. One possibility would be that one of the nucleons comes from the decay of a resonance such as Δ or N^*, and during the decay, the pion catalyzes the fusion reaction. This process will be studied further in Ch. 4. However, in the work summarized in this chapter, the approximation that the binding energy is negligible is made since it is much smaller than the typical mass scales involved of $m_\mathrm{N} \sim 938$ MeV/c^2. Further, we will be utilizing event generators such as EPOS (Ch. 6) and ToMCCA (Ch. 7), which do not provide quantum mechanical nucleon density matrices but a classical approximation of one. In this approximation, the nucleon states are no longer orthogonal, and the overlap no longer vanishes[1]. The two-nucleon Wigner function can further be disassembled into a spatial and a momentum density

$$W_\mathrm{pn}(\mathbf{P}_\mathrm{d}/2 + \mathbf{q}, \mathbf{P}_\mathrm{d}/2 - \mathbf{q}, \mathbf{r}, \mathbf{r}_\mathrm{d}) = H_\mathrm{pn}(\mathbf{r}, \mathbf{r}_\mathrm{d})G_\mathrm{pn}(\mathbf{P}_\mathrm{d}/2 + \mathbf{q}, \mathbf{P}_\mathrm{d}/2 - \mathbf{q}). \tag{3.10}$$

For the spatial part $H_\mathrm{pn}(\mathbf{r}, \mathbf{r}_\mathrm{d})$ we can assume a Gaussian profile [14]

$$H_\mathrm{pn}(\mathbf{r}, \mathbf{r}_\mathrm{d}) = \frac{1}{(2\pi r_0^2)^3} \exp\left(-\frac{\mathbf{r}^2 + \mathbf{r}_d^2}{4r_0^2}\right). \tag{3.11}$$

[1]The resulting phase space is a Gaussian smeared Wigner distribution, a so-called Husimi distribution [65]. A deeper discussion about various phase space distributions and their validity goes far beyond the scope of this work.

Finally, the spatial distribution can be folded with the deuteron Wigner density to obtain a coalescence probability

$$\mathcal{P}(r_0, q) \int \mathrm{d}^3 r \mathrm{d}^3 r_d \, H_{\mathrm{pn}}(\mathbf{r}, r_{\mathrm{d}}; r_0) \mathcal{D}(r, q), \tag{3.12}$$

and subsequently, Eq. 3.9 assumes the final form

$$\frac{d^3N}{dP_{\mathrm{d}}^3} = S \int \mathrm{d}^3 q \mathcal{P}(r_0, q) \frac{G_{\mathrm{pn}}(\mathbf{P}_{\mathrm{d}}/2 + \mathbf{q}, \mathbf{P}_{\mathrm{d}}/2 - \mathbf{q})}{(2\pi)^6}. \tag{3.13}$$

3.2 Extension to A>2 nuclei

The calculation of the spectra within the coalescence model can be trivially extended to A=3 (hyper)nuclei

$$\frac{\mathrm{d}N}{\mathrm{d}^3P} = S \int \mathrm{d}^3\mathbf{x}_1 \int \mathrm{d}^3\mathbf{x}_2 \int \mathrm{d}^3\mathbf{x}_3 \int \mathrm{d}^3\mathbf{x}_1' \int \mathrm{d}^3\mathbf{x}_2' \int \mathrm{d}^3\mathbf{x}_3' \, \Psi^* \left(\mathbf{x}_1', \mathbf{x}_2', \mathbf{x}_3'\right) \Psi \left(\mathbf{x}_1, \mathbf{x}_2, \mathbf{x}_3\right) \times \left\langle \Psi_3^\dagger(\mathbf{x}_1{}') \Psi_2^\dagger(\mathbf{x}_2') \Psi_1^\dagger(\mathbf{x}_1') \Psi_1(\mathbf{x}_1) \Psi_2(\mathbf{x}_2) \Psi_3(\mathbf{x}_3) \right\rangle, \tag{3.14}$$

Where S accounts for spins and isospin configurations, $\Psi\left(\mathbf{x}_1, \mathbf{x}_2, \mathbf{x}_3\right)$ is the bound state wave function for $A = 3$ (hyper)nuclei with $\mathbf{x}_1$, $\mathbf{x}_2$, $\mathbf{x}_3$, $\mathbf{p}_1$, $\mathbf{p}_2$, and $\mathbf{p}_3$ being space-momentum coordinates for three hadrons coalescing into the a cluster. The three-particle density matrix is given as

$$\left\langle \Psi_3^\dagger(\mathbf{x}_3') \Psi_2^\dagger(\mathbf{x}_2') \Psi_1^\dagger(\mathbf{x}_1') \Psi_1(\mathbf{x}_1) \Psi_2(\mathbf{x}_2) \Psi_3(\mathbf{x}_3) \right\rangle = \frac{1}{(2\pi)^9} \int \mathrm{d}^3\mathbf{p}_1 \int \mathrm{d}^3\mathbf{p}_2 \int \mathrm{d}^3\mathbf{p}_3 \times e^{i\mathbf{p}_1 \cdot (\mathbf{x}_1 - \mathbf{x}_1') + i\mathbf{p}_2 \cdot (\mathbf{x}_2 - \mathbf{x}_2') + i\mathbf{p}_3 \cdot (\mathbf{x}_3 - \mathbf{x}_3')} W_{npp} \left(\mathbf{p}_1, \mathbf{p}_2, \mathbf{p}_3, \frac{\mathbf{x}_1 + \mathbf{x}_1'}{2}, \frac{\mathbf{x}_2 + \mathbf{x}_2'}{2}, \frac{\mathbf{x}_3 + \mathbf{x}_3'}{2} \right) \tag{3.15}$$

The exact form of the calculation depends on the choice of Jacobi coordinates and will be given for each wave function below separately.

3.3 Wave functions

In Eq. 3.8, one can see that the internal wave function of the nucleus is an important ingredient for the Wigner Function Formalism, similarly to Eq. 2.43. Fig. 3.1 shows four different wave functions of the deuteron, which will be tested in this work and introduced in Sec. 3.3.1. Further, for ^{3}He, ^{3}H and $^3_\Lambda$H wave functions will also be introduced in Sec. 3.3.2.

3.3.1 Deuteron wave functions

Four wave functions will be tested for the deuteron. Namely, the single Gaussian, the Hulthén, the Argonne v_{18}, and χEFT. All wave functions are normalized to $\int \mathrm{d}^3 r |\varphi(r)|^2 = 1$, so any difference in the final deuteron yield is attributed to the difference in shape. For the Argonne v_{18} and χEFT wave functions, contributions from s and d-waves are considered. As such, they are normalized to $\int \mathrm{d}^3 r (|u(r)/r|^2 + |w(r)/r|^2) = 1$, where u(r)/r and w(r)/r are the s and d-wave functions respectively.

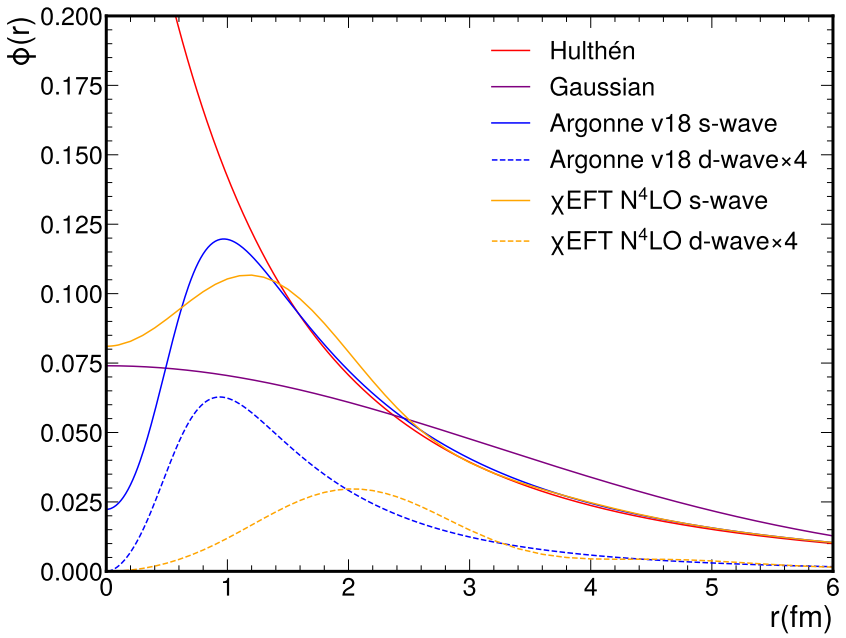

FIGURE 3.1: Deuteron wave functions using different potential hypotheses, namely Gaussian (purple), Hulthén (red), Argonne v_{18} s-wave and d-wave (blue, solid and dashed) and χEFT N^{4}LO s-wave and d-wave (orange, solid and dashed).

Single Gaussian wave function

The single Gaussian is the simplest assumption for the shape of the deuteron wave function

$$\varphi_{\mathrm{d}}(r) = \frac{e^{-\frac{r^2}{2d^2}}}{(\pi d^2)^{3/4}}, \tag{3.16}$$

where d is the size parameter of the harmonic oscillator potential. $d = 3.2$ fm, such that $r^2_{\mathrm{rms}} = \int \mathrm{d}^3 r (r/2)^2 |\varphi(r)|^2 = 1.96$ fm. The main purpose of this wave function is to simplify calculations. Indeed, for the single Gaussian, one can directly write the Wigner function

$$\mathcal{D}(r,q) = 8e^{-\frac{d^4q^2+r^2}{d^2}} \tag{3.17}$$

using the definition in Eq. 3.8, and the probability

$$\mathcal{P}(r_0,q) = 8\left(\frac{d^2}{d^2+4r_0^2}\right)^{3/2} e^{-q^2d^2} \tag{3.18}$$

using Eq. 3.1.

Hulthén wave function

The Hulthén wave function can be derived from the Hulthén potential, a Yukawa-type potential [66]

$$\text{Yukawa: } V(r) = -V_0 \frac{e^{-\mu r}}{\mu r} \tag{3.19}$$

$$\text{Hulthén: } V(r) = -V_0 \frac{e^{-\mu r}}{1 - e^{-\mu r}}, \tag{3.20}$$

with the potential depth V_0 and the effective range $r_0 = 1/\mu$. Their functional forms can be seen in Fig. 3.2, The Hulthén potential has functionally the same properties as the Yukawa potential, but the Schrödinger equation with a potential of this form is analytically solvable. The solution is a wave function of the Hulthén type

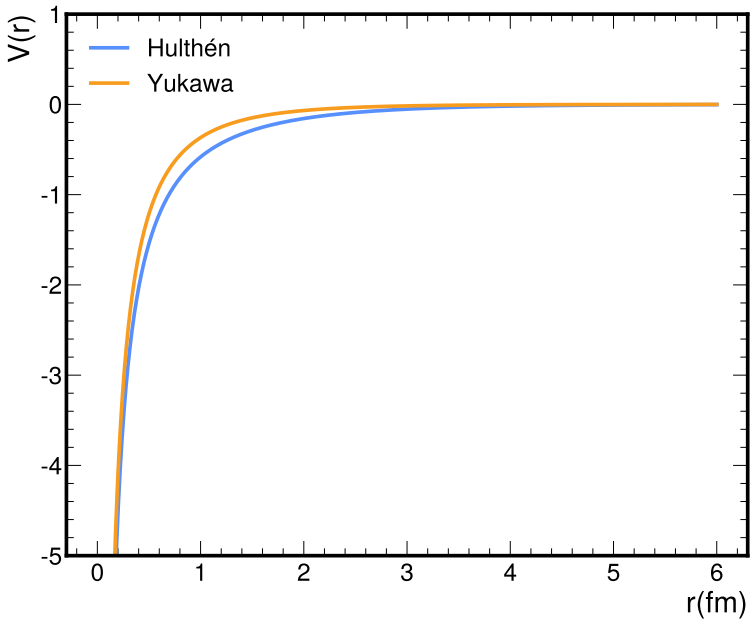

FIGURE 3.2: Functional form of the Hulthén and Yukawa potentials. Both potentials are equal for large and small r, only deviating slightly at intermediate distances. While the Schrödinger equation for a Yukawa potential can not be solved exactly, the Hulthén form allows for such a solution, providing a wave function practically equivalent to a Yukawa one. Such wave functions are often used in low energy pion exchange models of nuclear interaction.

$$\varphi(r) = \sqrt{\frac{\alpha\beta(\alpha+\beta)}{2\pi(\alpha-\beta)^2}} \frac{e^{-\alpha r} - e^{-\beta r}}{r}. \tag{3.21}$$

This is a modern description of the Hulthén wave function introduced in Ref. [67]. The parameter α is defined as $\alpha = \sqrt{m_p E_B} = 0.23\ \text{fm}^{-1}$ and $\beta = 1.61\ \text{fm}^{-1}$. β is chosen such that the deuteron radius $r_d = 1.98$ fm is reproduced[2]. The Fourier transform $\psi(k)$ of the wave

[2] In Tab. 3.3 one can see that this actually quite poorly reproduces the size of the deuteron with a value of $r_d = 1.86$ fm with a D-wave and 1.89 fm without. A better fit would be $\beta = 1.3 fm^{-1}$ for only the S-wave and

function is

$$\psi(k) = \frac{\sqrt{\alpha+\beta}}{\pi(\alpha-\beta)}\left(\frac{1}{k^2+\alpha^2} - \frac{1}{k^2+\beta^2}\right). \tag{3.22}$$

For convenience, the Fourier transform will be used to calculate the Wigner function, which in Fourier space is defined as

$$\mathcal{D}(r,q) = \int \mathrm{d}^3\zeta \mathrm{d}^3k_1 \mathrm{d}^3k_2 \psi^*(k_2)\psi(k_1) e^{-i(q\cdot\zeta + k_2\cdot(r-\zeta/2) + k_2\cdot(r-\zeta/2))}. \tag{3.23}$$

Using the substitutions $k_2 = 2q + k_1$ and $k_1 = k + q$, and performing the integration over ζ and k_2, one obtains the following expression for the Wigner function in Fourier space

$$\mathcal{D}(r,q) = \int \mathrm{d}^3k e^{ir\cdot k} \psi^*(q - k/2)\psi(q + k/2). \tag{3.24}$$

This integral depends on the angle between r and k. To eliminate this dependence, the average over this angle is performed using $\sin(\theta)$ as a weight. The final Wigner function for the Hulthén wave function is then

$$\begin{aligned}\mathcal{D}(q,r) = \frac{4(\alpha+\beta)^2}{\alpha\beta(\alpha-\beta)\pi qr}\int_0^\infty \mathrm{d}k \frac{\alpha^2\beta^2\sin(2kr)}{\alpha^2+\beta^2+2(k^2+q^2)}\times \\ \times\left\{\frac{1}{k^2+q^2+\alpha^2}\ln\left(\frac{(k+q)^2+\alpha^2}{(k-q)^2+\alpha^2}\right) - \frac{1}{k^2+q^2+\beta^2}\ln\left(\frac{(k+q)^2+\beta^2}{(k-q)^2+\beta^2}\right)\right\},\end{aligned} \tag{3.25}$$

which leaves one integral unsolved. The final probability is thus calculated numerically on a grid of r_0 and q. For a Hulthén type wave function, a d-state wave has been constructed in Ref. [27]

$$\varphi_D(r) = \eta N \frac{(1-e^{-\tau r})^5}{r}\left(e^{-\alpha r} + \frac{e^{-\alpha r}}{\alpha r} + \frac{e^{-\alpha r}}{\alpha^2 r^2}\right), \tag{3.26}$$

where $\eta = 0.026$ is the asymptotic D/S ratio, which is determined from the Reid68 potential [68]. Further, $\alpha = 0.23$ fm^{-1} is equivalent to the s-wave case, and $\tau = 1.09$ fm^{-1} is determined from the quadrupole moment of the deuteron. In this work, for historical reasons and comparability with previous works, the Hulthén wave function is assumed to be s-wave only, except for the calculation of the quadrupole moment in Tab. 3.3.

Argonne v_{18} wave function

The Argonne v_{18} wave function is based on the phenomenological Argonne v_{18} potential, which is constrained to Nucleon–Nucleon phase shift measurement [35]. The Argonne v_{18} potential is a highly accurate nucleon-nucleon interaction model. It includes a complete treatment of both the strong and electromagnetic forces, with a focus on charge independence breaking and charge asymmetry. The potential is constructed using the sum of an electromagnetic (EM) part, a one-pion exchange (OPE) part, and an intermediate to short-range phenomenological (R) part

$$V(NN) = V^{\mathrm{EM}}(NN) + V^{\mathrm{OPE}}(NN) + V^{\mathrm{R}}(NN). \tag{3.27}$$

It is fitted to the Nijmegen [69] NN scattering dataset as well as low energy nn scattering and deuteron properties and is able to reproduce it with a reduced $\chi^2_{\mathrm{n.d.f.}} = 1.09$ [35]. The Nijmegen NN scattering dataset contains 1787 pp and 2514 pn data points, in a range of

$\beta = 1.20 fm^{-1}$ for s- and d-wave, both giving a $r_d \sim 1.975$ fm. However, this small difference of ~ 5 % in size is negligible for the deuteron yields.

$T_{\text{lab}} = 0 - 350$ MeV. It incorporates 18 operators, 14 of which are charge-independent (CI), three of which are charge-dependent (CD), and one which is explicitly charge-asymmetric (CA). The CI part is an updated version of the Argonne v_{14} [70] potential. It is specifically constructed in a way that makes it easy to incorporate it into 3-body interaction models.
The deuteron wave function calculated from the Argonne v_{18} potential has the general form of a $^3S_1$ and $^3D_1$ mixed state

$$\varphi(r) = \frac{1}{\sqrt{4\pi}r}\left[u(r) + \frac{1}{\sqrt{8}}w(r)S_{12}(\hat{r})\right]\chi_{1m}, \tag{3.28}$$

where $S_{12}(\hat{r}) = 3\sigma_1 \cdot \mathbf{r}\,\sigma_2 \cdot \mathbf{r} - \sigma_1 \cdot \sigma_2$ is the spin tensor, σ_i are the Pauli matrices. χ_{1m} is a spinor, and u(r)/r and w(r)/r are the radial s and d-state wave functions, respectively. One can define $\mathbf{r}_1$ to be the coordinate of the proton and $\mathbf{r}_2$ the coordinate of the neutron, $\mathbf{r} = \frac{\mathbf{r}_1 - \mathbf{r}_2}{2}$ is the relative coordinate and $\mathbf{R} = \frac{\mathbf{r}_1 + \mathbf{r}_2}{2}$ is the absolute coordinate. The spin-averaged probability density of the deuteron is

$$|\varphi(\mathbf{r})|^2 = \frac{1}{3}\sum_{m=0,\pm1}\varphi(r_1)^\dagger\varphi(r_2) = \frac{1}{4\pi r_1 r_2}\left(u(r_1)u(r_2) + w(r_1)w(r_2)\frac{1}{2}\left(3(\hat{r}_1 \cdot \hat{r}_2)^2 - 1\right)\right). \tag{3.29}$$

In the case of Argonne v_{18} the s-state wave function is normalized to $\int d^3\mathbf{r}\frac{u(r)^2}{4\pi r^2} = 0.9424$ and the d-state wave function to $P_D = \int d^3\mathbf{r}\frac{w(r)^2}{4\pi r^2} = 0.0576$. These factors are the weight of the s and d-waves in the deuteron wave function, and they are mainly constrained from measurements of the nuclear radius and the quadrupole moment. The wave function is only available numerically and has no analytic form. In order to calculate the Wigner function, an analytical approximation has been performed using the sum of two Cauchy functions and one Gaussian

$$F(r) = \frac{N_1 a}{\pi(a^2 + r^2)} + \frac{N_2 b}{\pi(b^2 + (r-c)^2)} + N_3 e^{-r^2/f}. \tag{3.30}$$

The parameter values for N_1, N_2, N_3, a, b, c and f can be found in Tab. 3.1, for the s and d-wave, respectively. This form has been chosen as the tail of the double Cauchy function reproduces well the long-range tail of the wave function, and the Gaussian reproduces the suppression at low r. The fit quality is determined using a reduced $\chi^2 = \frac{1}{N}\sum_{k=1}^{N}\frac{(F_j - \varphi_j)^2}{\varphi_j}$, where φ_j is the value of the wave function at position r_j and F_j is the functional value at the same position, evaluated for all N points available up to $r = 15$ fm. The reduced χ^2 for the s-wave is $\chi^2 \sim 6.83 \cdot 10^{-8}$ and for the d-wave $\chi^2 \sim 1.3 \cdot 10^{-10}$.

Parameter	$u(r)/r$	$w(r)/r$
N_1	0.81370516	-0.34242388
N_2	4.49712863	1.0973295
N_3	-0.68798139	-0.25201684
a	-10.82747628	4.33930564
b	1.68243617	1.28156015
c	-0.400957858	0.22952727
f	0.39633979	0.42620769

TABLE 3.1: Fit parameters for F(r) obtained for $u(r)/r$ and $w(r)/r$ in the range $0 < r < 15$ fm.

The resulting Wigner function has the form

$$\mathcal{D}(r,q) = \frac{1}{8\pi}\sum_{i=1}^{6} T_i, \tag{3.31}$$

where the terms T_i are defined as follows

$$T_1 = (2\pi f)^{3/2} N_3^2 e^{-\frac{f^2q^2+4r^2}{2f}}, \tag{3.32}$$

$$T_2 = \frac{16a^2N_1^2}{\pi qr}\int_0^\infty \mathrm{d}\xi \frac{\sin(q\xi)}{4a^2+4r^2+\xi^2}\ln\left[\frac{4a^2+(\xi+2r)^2}{4a^2+(\xi-2r)^2}\right], \tag{3.33}$$

$$T_3 = \frac{8aN_1N_3}{qr}\int_0^\infty \mathrm{d}\xi \sin(q\xi) e^{-\frac{2a^2+4r^2+\xi^2}{2f}}\left[\mathrm{Ei}\left(\frac{4a^2+(\xi+2r)^2}{4f}\right) - \mathrm{Ei}\left(\frac{4a^2+(\xi-2r)^2}{4f}\right)\right] \tag{3.34}$$

$$T_4 = \frac{4bN_2N_3}{q}\int_0^\infty \mathrm{d}\xi \int_{-1}^{1} \mathrm{d}\gamma \sin(q\xi)\xi \times \\ \times\left(\frac{e^{-\frac{4r^2+4\gamma r\xi+\xi^2}{4r}}}{b^2+c^2-c\sqrt{4r^2-4\gamma r\xi+\xi^2}+r^2-\gamma r\xi+\xi^2/4} + \right. \\ \left. + \frac{e^{-\frac{4r^2-4\gamma r\xi+\xi^2}{4r}}}{b^2+c^2-c\sqrt{4r^2+4\gamma r\xi+\xi^2}+r^2+\gamma r\xi+\xi^2/4}\right) \tag{3.35}$$

$$T_5 = \frac{4abN_1N_2}{\pi q}\int_0^\infty \mathrm{d}\xi \int_{-1}^{1} \mathrm{d}\gamma \sin(q\xi)\xi\left[\frac{(a^2+r^2+\gamma r\xi+\xi^2/4)^{-1}}{b^2+(c-\frac{1}{2}\sqrt{4r(r-\gamma\xi)+\xi^2})^2} + \right. \\ \left. + \frac{(a^2+r^2-\gamma r\xi+\xi^2/4)^{-1}}{b^2+(c-\frac{1}{2}\sqrt{4r(r+\gamma\xi)+\xi^2})^2}\right] \tag{3.36}$$

$$T_6 = \frac{4N_2^2b^2}{\pi q}\int_0^\infty \mathrm{d}\xi \int_{-1}^{1} \mathrm{d}\gamma \sin(q\xi)\xi\left[\frac{1}{b^2+(c-\frac{1}{2}\sqrt{4r(r+\gamma\xi)+\xi^2})^2}\times \right. \\ \left. \times \frac{1}{b^2+(c-\frac{1}{2}\sqrt{4r(r-\gamma\xi)+\xi^2})^2}\right] \tag{3.37}$$

Here, Ei(x) is an exponential integral defined as $\mathrm{Ei}(x) = \int_x^\infty \mathrm{d}te^{-t}/t$.

χEFT wave function

Lastly, a wave function from Chiral Effective Field Theory (χEFT) was tested. The χEFT framework is used to study low-energy QCD phenomena, such as atomic nuclei or hadrons. In the low-energy regime, QCD becomes non-perturbative, i.e. the strong coupling constant α_s becomes large. This means that higher-order contributions no longer decrease in magnitude fast enough for perturbative power counting. In χEFT, pions and nucleons are the degrees of freedom. Importantly, pions, since they are a Goldstone Boson, are assumed in the chiral limit to be massless ($m_\pi \to 0$). In this framework, the effective Lagrangian can be subdivided into

$$\mathcal{L}_{\text{eff}} = \mathcal{L}_{\pi\pi} + \mathcal{L}_{\pi N} + \mathcal{L}_{NN}, \tag{3.38}$$

where $\mathcal{L}_{\pi\pi}$ deals with dynamics among pions, $\mathcal{L}_{\pi N}$ describes the interaction between pions and nucleons, and $\mathcal{L}_{NN}$ describes the two-nucleon contact interaction. For higher orders, also, 3,4,...body interactions come into play. In Ref. [71], the chiral expansion was performed up to 5th order (N^4LO) [71] and dependent on the charge, i.e. pp, pn and nn interactions use different potentials. Here, the construction is done consistently throughout all orders in the sense that the same power counting scheme, as well as the same cutoff procedure, was applied in all orders. By construction, the χEFT approach is applicable only for low momenta. Therefore, a cutoff momentum is required, ensuring the maximum momentum transfer q does not exceed the chiral symmetry-breaking scale $\Lambda_\chi \sim 1$ GeV. The physical observables should not depend strongly on this cutoff momentum, and typical variations range from 500-900 MeV. Ref. [71] uses a cutoff of Λ_c=500 MeV. The deuteron wave function can be determined from the resulting pn interaction potential[3]. As in the case of Argonne v_{18}, the wave function is composed of two components, $u(r)$ and $w(r)$, which correspond to the radial s and d-state wave functions. Also here, only numerical values of the radial wave functions are available, and an analytic expression was found using the function

$$F_\chi(r) = \frac{N_0}{(a^2r^2 - r_0^2)^2 b^{-1} + c^2 r_0^2} + \sum_{i=1}^{3} \frac{N_i \alpha_i}{\pi((r-\beta_i)^2 + \alpha_i^2)}. \tag{3.39}$$

This function, similarly to the Argonne v_{18} wave function, uses Cauchy functions to describe the large r tail, but this time also uses a Cauchy function to describe the depletion of the wave function at low r (see Fig. 3.1) caused by the hard core of the interaction potential. Only the second term is used for the d-wave function since it is sufficient to describe the numerical values. The fit parameters can be found in Tab. 3.2. The fit quality is again determined using a reduced χ^2 minimization in the range $0 < r < 15$ fm. For the s-wave $\chi^2 = 3.31 \cdot 10^{-8}$ and for the d-wave $\chi^2 = 3.23 \cdot 10^{-3}$. The fit for the d-wave is of inferior quality compared to Argonne v_{18} or the s-wave, however, due to the low d-state contribution (see Tab. 3.3) this only introduces a negligible contribution. The resulting Wigner density for $F_\chi(r)$ has the form

$$\mathcal{D}(r,q) = \frac{1}{2\pi^2 q} \int_0^\infty \mathrm{d}\xi \int_{-1}^{1} \mathrm{d}\gamma \sin(q\xi)\xi \sum_{\nu=0}^{3} \kappa_\nu(\gamma) \tag{3.40}$$

[3]The final wave function was provided by Ruprecht Machleidt and was not determined as part of this work.

where the κ_ν are defined as

$$\kappa_0 = \frac{4bN_0^2}{\left(4r_0^2 - a^2\left(\xi^2+4r^2+4\gamma\xi r\right)\right)^2 + 4bc^2r_0^2} \frac{1}{\left(4r_0^2 - a^2\left(\xi^2+4r^2-4\gamma\xi r\right)\right)^2 + 4bc^2r_0^2}, \tag{3.41}$$

$$\kappa_1 = \sum_{i=1}^{3} \frac{4N_i^2\alpha_i^2}{\left(2\beta_i - \sqrt{\xi^2+4r^2-4\gamma\xi r}\right)^2 + 4\alpha_i^2} \frac{1}{\left(2\beta_i - \sqrt{\xi^2+4r^2+4\gamma\xi r}\right)^2 + 4\alpha_i^2}, \tag{3.42}$$

$$\begin{aligned}\kappa_2 = &\sum_{\substack{i=1\\ i\neq j}}^{3}\sum_{j=1}^{3} 8N_iN_j\alpha_i\alpha_j \times \\ &\times \left\{ \left[\frac{1}{\left(2\beta_i - \sqrt{\xi^2+4r^2-4\gamma\xi r}\right)^2 + 4\alpha_i^2} \frac{1}{\left(2\beta_j - \sqrt{\xi^2+4r^2+4\gamma\xi r}\right)^2 + 4\alpha_j^2} \right] + \right. \\ &\left. + \left[\frac{1}{\left(2\beta_i - \sqrt{\xi^2+4r^2+4\gamma\xi r}\right)^2 + 4\alpha_i^2} \frac{1}{\left(2\beta_j - \sqrt{\xi^2+4r^2-4\gamma\xi r}\right)^2 + 4\alpha_j^2} \right] \right\},\end{aligned} \tag{3.43}$$

$$\begin{aligned}\kappa_3 = &\sum_{i=1}^{3} 4\,\pi N_0\, N_i\alpha_i \times \\ &\times \left\{ \left[\frac{1}{\left(2\beta_i - \sqrt{\xi^2+4r^2-4\gamma\xi r}\right)^2 + 4\alpha_i^2} \frac{4b}{\left(4r_0^2 - a^2\left(\xi^2+4r^2+4\gamma\xi r\right)\right)^2 + 4bc^2r_0^2} \right] + \right. \\ &\left. + \left[\frac{1}{\left(2\beta_i - \sqrt{\xi^2+4r^2+4\gamma\xi r}\right)^2 + 4\alpha_i^2} \frac{4b}{\left(4r_0^2 - a^2\left(\xi^2+4r^2-4\gamma\xi r\right)\right)^2 + 4bc^2r_0^2} \right] \right\}.\end{aligned} \tag{3.44}$$

Fit parameters	for $u(r)/r$	for $w(r)/r$
N_0	14.83063014	-
N_1	0.3644193	90.06036202
N_2	0.01876164	0.22901687
N_3	0.58780443	90.167747
a	2.95678555	-
b	7.03082423	-
c	2.85271022	-
r_0	2.65962623	-
α_1	0.86804832	1.75803721
α_2	-2.99220936	2.55621569
α_3	2.51249685	-1.7664106
β_1	1.81024872	2.07489033
β_2	12.77230151	4.11299107
β_3	2.95031591	2.0759802

TABLE 3.2: Fit parameters for $\mathcal{F}(r)$ obtained from the numeric values of $u(r)/r$ (2^{nd} column) and $w(r)/r$ (3^{rd} column) in the range $0 < r < 15$ fm.

Deuteron properties

With these different wave functions, it might be interesting to see how well they reproduce the basic properties of the deuteron. For this, one can calculate the charge radius r_d, quadrupole moment Q_d, magnetic moment μ_d, and the d-state probability P_d. Their values can be found in Tab. 3.3. For the quadrupole moment and the d-state probability, a d-state wave function is required to get a reasonable result, while for the magnetic moment, one only obtains a trivial result without a d-state. For this reason, the Hulthén wave function properties are calculated using the d-state wave function even though it was not used in the coalescence predictions. The Gaussian wave function does not have a d-State, and as such, these values are either in parentheses (μ_d) if they are trivial or not given. The deuteron charge radius can be calculated as

$$r_\mathrm{d} = \frac{1}{2}\left(\int_0^\infty \mathrm{d}r\, r^2[u^2(r) + w^2(r)]\right)^{1/2}. \tag{3.45}$$

The Quadrupole moment Q_d

$$Q_\mathrm{d} = \frac{1}{20}\int_0^\infty \mathrm{d}r\, r^2 w(r)[\sqrt{8}u(r) - w(r)], \tag{3.46}$$

the D-state probability P_d

$$P_\mathrm{d} = \int_0^\infty w^2(r)\mathrm{d}r \tag{3.47}$$

and the magnetic moment μ_d

$$\mu_\mathrm{d} = \mu_\mathrm{s} - \frac{3}{2}(\mu_\mathrm{s} - \frac{1}{2})P_\mathrm{d}, \tag{3.48}$$

with $\mu_\mathrm{s} = \mu_\mathrm{n} + \mu_\mathrm{p} = (-1.913 + 2.792)\mu_\mathrm{N}$. The constant $\mu_\mathrm{N} = \frac{e\hbar}{2m_\mathrm{p}} = 3.1525 \cdot 10^{-8}\mathrm{eV\ T^{-1}}$ is the nuclear magneton. If no d-wave is given, $P_\mathrm{d} = 0$ and $\mu_\mathrm{d} = \mu_\mathrm{s}$ equals the sum of the magnetic moments of its constituents. All tested wave functions reasonably reproduce the

Wave function	r_d (fm)	Q_d (fm^2)	$\mu_d(\mu_N)$	P_D(%)
Experiment	1.97537(85) [72]	0.2859(3) [72]	0.85744 [73]	7.6±4.6 [74]
Gaussian	1.9596	-	(0.879)	-
Hulthén	1.8578	0.3216	0.8392	7.00
Argonne v_{18}	1.9362	0.2664	0.8463	5.76
χEFT	1.9286	0.2680	0.8556	4.11
Fit Argonne v_{18}	1.9431	0.2676	0.8466	5.70
Fit χEFT	1.9436	0.2341	0.8556	4.12

TABLE 3.3: Calculated and experimental values for the matter radius r_d, Quadrupole Moment Q_d, Magnetic Moment μ_d, d-State probability P_D of the deuteron. For the Hulthén wave function, P_D was fixed to 7% according to Ref. [27], and the s-Wave was normalized to 93%. The magnetic moment of the Gaussian wave function is $\mu_p + \mu_n = 0.879$, because there is no d-wave. Experimental uncertainties are negligible if not given explicitly.

deuteron radius, even though for the Hulthén wave function, a slightly better description could be found using the parameters $\beta = 1.20\ \mathrm{fm^{-1}}$ giving a radius of $r_\mathrm{d} = 1.975$ fm. The Hulthén wave function also struggles to reproduce the quadrupole moment, while all others are almost equivalently 7% too low. While for Argonne v_{18} both the numerical and the approximated wave function perform equivalent for all other observables, the fitted χEFT

wave function performs worse for the quadrupole moment. This can be traced back to the comparatively poor fit of the d-state.

3.3.2 A=3 wave functions

The wave functions for A=3 nuclei are constructed in two different manners. ^{3}He and ^{3}H are constructed using the Argonne v_{18} two-body potential and the Urbana IX (UIX) [75] 3-body potential and utilizing the hyperspherical harmonics (HH) approach. The $^3_\Lambda$H wave function is constructed using a Λ–d potential and a free, undisturbed deuteron wave function.

The hyperspherical harmonics method for A=3

Three-body coalescence probability in hyperspherical harmonics

In this section, the coalescence probability for $A = 3$ is determined using hyperspherical harmonics

$$\mathcal{P}(q_1, q_2, \sigma, \cos(\theta_{12})) = \frac{3\sqrt{3}}{64(2\pi)^3\sigma^6} \int \rho^5 \rho'^5 \mathrm{d}\rho \mathrm{d}\rho' \mathrm{d}\Omega_2 \mathrm{d}\Omega_2 \phi_{^3\mathrm{He}}(\rho, \Omega_2) \phi^*_{^3\mathrm{He}}(\rho' \Omega'_2)$$
$$\exp\left(i\mathbf{Q} \cdot (\boldsymbol{\rho} - \boldsymbol{\rho}')\right) \exp\left(-\frac{\rho^2 + \rho'^2 + 2\mathbf{x}_1 \cdot \mathbf{x}'_1 + 2\mathbf{x}_2 \cdot \mathbf{x}'_2}{16\sigma^2}\right). \quad (3.49)$$

The derivation given here is a specific implementation of the one given in Ref [76]: Considering a system of A=3 particles with equal masses $m_1 = m_2 = m_3 = m_N$ and spatial absolute coordinates r_1, r_2, r_3, one can separate the center of mass (CM) motion and the relative motion of the particles. For this, a set of N=A-1=2 Jacobi-coordinates $\mathbf{x}_1, \mathbf{x}_2$ can be introduced as well as a CM coordinate $\mathbf{X}$

$$\mathbf{X} = \sum_{i=1}^{3} \mathbf{r}_i \quad (3.50)$$

$$\mathbf{x}_{2-j+1} = \sqrt{\frac{2j}{j+1}} \left(\mathbf{r}_{j+1} - \frac{1}{j} \sum_{i=1}^{j} \mathbf{r}_j\right), \quad (3.51)$$

where j=1,2, or specifically

$$J = \begin{pmatrix} -1 & 1 & 0 \\ -\frac{1}{\sqrt{3}} & -\frac{1}{\sqrt{3}} & \frac{2}{\sqrt{3}} \\ \frac{1}{3} & \frac{1}{3} & \frac{1}{3} \end{pmatrix}, \quad (3.52)$$

$$\begin{pmatrix} \mathbf{x}_1 \\ \mathbf{x}_2 \\ \mathbf{R} \end{pmatrix} = J \cdot \begin{pmatrix} \mathbf{r}_1 \\ \mathbf{r}_2 \\ \mathbf{r}_3 \end{pmatrix}, \quad (3.53)$$

with the Jacobi determinant $|J| = 2/\sqrt{3}$. For momenta, one can use the conjugates

$$\begin{pmatrix} \mathbf{q}_1 \\ \mathbf{q}_2 \\ \mathbf{P} \end{pmatrix} = J^{-1} \cdot \begin{pmatrix} \mathbf{p}_1 \\ \mathbf{p}_2 \\ \mathbf{p}_3 \end{pmatrix}. \quad (3.54)$$

This choice has the benefit that the condition

$$\mathbf{p}_1 \cdot \mathbf{r}_1 + \mathbf{p}_2 \cdot \mathbf{r}_2 + \mathbf{p}_3 \cdot \mathbf{r}_3 = \mathbf{q}_1 \cdot \mathbf{x}_1 + \mathbf{q}_2 \cdot \mathbf{x}_2 + \mathbf{P} \cdot \mathbf{R}, \quad (3.55)$$

is fulfilled. From these Jacobi-coordinates, one can define the hyperspherical coordinate system (ρ, Ω_2) by

$$\rho = \sqrt{\sum_{i=1}^{2} \mathbf{x}_i^2} = \sqrt{\frac{2}{3} \sum_{j>i=1}^{3} (\mathbf{r}_i - \mathbf{r}_j)^2} = \sqrt{2 \sum_{i=1}^{3} (\mathbf{r}_i - \mathbf{X})^2}, \tag{3.56}$$

$$\Omega_2 = \{\hat{x}_1, \hat{x}_2, \varphi_2\}. \tag{3.57}$$

$\hat{x}_i = (\theta_i, \phi_i)$ are the angular part of the Jacobi-vectors, and the hyper angle φ_2 is defined as

$$\cos(\varphi_2) = \frac{x_2}{\sqrt{x_1^2 + x_2^2}}, \tag{3.58}$$

ranging between $0 \leq \varphi_2 \leq \pi/2$. For the hypermomentum Q, we can define it similarly

$$Q = \sqrt{\sum_{i=1}^{2} \mathbf{q}_i^2}. \tag{3.59}$$

This has again the nice property

$$\mathbf{Q} \cdot \boldsymbol{\rho} = \mathbf{q}_1 \cdot \mathbf{x}_1 + \mathbf{q}_2 \cdot \mathbf{x}_2. \tag{3.60}$$

Within the now-constructed framework of hyperspherical harmonics, the kinetic energy operator can be written as

$$T = -\frac{\hbar^2}{m} \sum_{i=1}^{2} \Delta_{x_i} = \frac{\hbar^2}{m} \left(\frac{\partial}{\partial \rho^2} + \frac{3N-1}{\rho} \frac{\partial}{\partial \rho} - \frac{\Lambda_2^2(\Omega_2}{\rho^2} \right). \tag{3.61}$$

$\Lambda_2^2(\Omega_2)$ is the grand-angular momentum operator

$$\Lambda_2^2(\Omega_2) = \frac{\partial^2}{\partial \varphi_2^2} + [2(\cot \varphi_2 - \tan \varphi_2)] \frac{\partial}{\partial \varphi_2} + \frac{L_2^2}{\cos^2 \varphi_2} + \frac{L_1^2}{\sin^2 \varphi_2}, \tag{3.62}$$

defined via the angular momentum operator $-L_i^2$ associated with the i-th Jacobi-Vector. A very important property of the grand-angular momentum operator are its eigenfunctions, the so-called hyperspherical harmonics

$$\mathcal{Y}_{[K]}^{\mathrm{KLM}_L}(\Omega_2) = [[Y_{l_1}(\hat{x}_1) Y_{l_2}(\hat{x}_2)]_{L_2} Y_{l_2}(\hat{x}_2)]_{LM_L} \, {}^{(2)}\mathcal{P}_{n_2}^{K_1, l_2}(\varphi_2). \tag{3.63}$$

where L is the total orbital angular momentum and M_L is its projection on the z-axis. The Notation $[K]$ stands for a collection of quantum numbers $[K] = [l_1, l_2, L_2, n_2]$ and

$$K_1 = (l_1 + 2n_1), \tag{3.64}$$

is the grand-angular momentum. The function ${}^{(2)}\mathcal{P}_{n_2}^{K_1, J_2}$ is defined as

$${}^{(2)}\mathcal{P}_{n_2}^{K_1, J_2}(\varphi_2) = \mathcal{N}_{n_2}^{l_2, \nu_2} (cos\varphi_2)^{l_2} (\sin \varphi_2)^{K_1} \, P_{n_2}^{\nu_1, l_2 + 1/2}(\cos 2\varphi_2), \tag{3.65}$$

where $P_{n_2}^{\nu_1, l_2+1/2}(\cos 2\varphi_2)$ is a Jacobi polynomial

$$P_n^{\alpha,\beta}(x) = (n+\alpha)!(n+\beta)! \sum_{s=0}^{n} \frac{1}{s!(n+\alpha-s)!(\beta+s)!(n-s)!} \left(\frac{x-1}{2} \right)^{n-s} \left(\frac{x+1}{2} \right)^{s}. \tag{3.66}$$

If one considers the wave function in the isospin formalism, it must contain not only spatial parts but also spin and isospin contributions. The spin function $\chi_{[S]}^{SM_S}$ for total spin S and projection M_S and the isospin function $\xi_{[T]}^{TM_T}$ for total isospin T and projection M_T can be defined by coupling the individual spin functions $\chi_{1/2,\pm1/2}$ and isospin functions $\xi_{1/2,\pm1/2}$ as

$$\chi_{[S]}^{SM_S} = \left[[\chi_{1/2}(1)\chi_{1/2}(2)]_{S_1}\chi_{1/2}(3)\right]_{SM_S} \tag{3.67}$$

$$\xi_{[T]}^{TM_T} = \left[[\xi 1/2(1)\xi 1/2(2)]_{T_1}\xi 1/2(3)\right]_{TM_T}. \tag{3.68}$$

Including these into the HH basis functions, one obtains

$$\mathcal{Y}_{[KST]}^{KLSJJ_zTM_T}(\Omega_N) = [\mathcal{Y}_{[K]}^{KL}(\Omega_N)\chi_{[S]}^{S}]_{JJ_z}\xi_{[T]}^{TM_T}, \tag{3.69}$$

or specifically for an A=3 bound state

$$\mathcal{Y}_{[\alpha]n_2}^{K}(\Omega_2) = \left[[Y_{l_{1\alpha}}(\hat{x}_1)Y_{l_{2\alpha}}(\hat{x}_2)]_{L_\alpha}\left[[\chi_{1/2}(1)\chi_{1/2}(2)]_{S_{a\alpha}}\chi_{1/2}(3)\right]_{S_\alpha}\right]_{JJ_z} \left[[\xi_{1/2}(1)\xi_{1/2}(2)]_{T_{a\alpha}}\xi_{1/2}(3)\right]_{T_\alpha M_T} {}^{(2)}\mathcal{P}_{n_2}^{l_{1\alpha},l_{2\alpha}}(\varphi_2). \tag{3.70}$$

The so-called channels α are defined by

$$[\alpha] = [l_{1\alpha}, l_{2\alpha}, L_\alpha, S_{a\alpha}, S_\alpha, T_{a\alpha}, T_\alpha]. \tag{3.71}$$

With these definitions, one can finally write the 3-body wave function as

$$\phi_{^3\mathrm{He}}(\rho,\Omega_2) = \sum_{\alpha,n_2} u_{\alpha n_2}(\rho)\sum_{p=1}^{3}\mathcal{Y}_{[\alpha]n_2}^{K}(\Omega_2^{(p)}). \tag{3.72}$$

The hyperradial wave functions $u_{\alpha n_2}(\rho)$ can be obtained numerically for a given system by solving the Schrödinger equation for a potential $V = V_{2\mathrm{N}} + V_{3\mathrm{N}}$. In the study presented here Argonne v_{18} (2N) and Urbana IX (3N) are used and the resulting ^{3}He and ^{3}H properties can be found in Tab. 3.4 and 3.5 respectively. They can then be expanded in terms of known functions, such as Laguerre polynomials multiplied by an exponential term to ensure fast convergence

$$u_{\alpha n_2}(\rho) = \sum_{m=0}^{N_L} c_{\alpha n_2;m}\gamma^5\sqrt{\frac{m!}{(m+4)!}}L_m^{(4)}(\gamma\rho)\exp(-\gamma\rho/2), \tag{3.73}$$

where $L_m^{(4)}(\gamma\rho)$ is the associated Laguerre polynomial. The non-linear parameter γ needs to be variationally optimized and is usually between $2.5 - 4.5$ fm^{-1} for local potential models such as Argonne v_{18}. The truncation limit N_L can be set around 20-30 to achieve convergence of the binding energy at the 1 keV level. In this study, $\gamma = 3$ and $N_L = 20$ were chosen. Under the transformation into hyperspherical harmonics Eq. 3.14 transforms into

$$\frac{\mathrm{d}N_{^3\mathrm{He}}}{\mathrm{d}^3P} = \frac{S_{^3\mathrm{He}}}{(2\pi)^9 64\pi^3\sigma^6}\int \rho^5\rho'^5\mathrm{d}\rho\ \mathrm{d}\rho'\mathrm{d}\Omega_2\,\mathrm{d}\Omega_2'\ q^5\mathrm{d}q\,\mathrm{d}\Omega_q\,\phi_{^3\mathrm{He}}(\rho,\Omega_2)\,\phi_{^3\mathrm{He}}^*(\rho',\Omega_2')\ e^{i\mathbf{Q}\cdot(\rho-\rho')} \times e^{-\frac{\rho^2+\rho'^2+2\mathbf{x}_1\cdot\mathbf{x}_1'+2\mathbf{x}_2\cdot\mathbf{x}_2'}{16\sigma^2}}\times G_{npp}\left(\frac{\boldsymbol{P}_{^3\mathrm{He}}}{3}-\frac{1}{3}\left(3\boldsymbol{q}_1+\sqrt{3}\boldsymbol{q}_2\right),\frac{\boldsymbol{P}_{^3\mathrm{He}}}{3}+\frac{1}{3}\left(3\boldsymbol{q}_1-\sqrt{3}\boldsymbol{q}_2\right),\frac{\boldsymbol{P}_{^3\mathrm{He}}}{3}+\frac{2\boldsymbol{q}_2}{\sqrt{3}}\right). \tag{3.74}$$

An important observation is that the function G_{npp} is necessarily normalized. This means

that, while the transformation of the momenta introduces a factor $|J|^3 = (2/\sqrt{3})^3$, this factor needs to be absorbed so that

$$\frac{1}{(2\pi)^9}\int \mathrm{d}^3p_1\mathrm{d}^3p_2\mathrm{d}^3p_3 G_{npp}(\mathbf{p}_1,\mathbf{p}_2,\mathbf{p}_3) = 1, \tag{3.75}$$

$$\frac{1}{(2\pi)^9}|J|^3\int \mathrm{d}^3q_1\mathrm{d}^3q_2\mathrm{d}^3P G_{npp}(\mathbf{q}_1,\mathbf{q}_2,\mathbf{P}) = 1. \tag{3.76}$$

Finally, the coalescence probability is expressed as

$$\mathcal{P}(q_1,q_2,\sigma,\cos(\theta_{12})) = \frac{3\sqrt{3}}{64(2\pi)^3\sigma^6}\int \rho^5\rho'^5\mathrm{d}\rho\mathrm{d}\rho'\mathrm{d}\Omega_2\mathrm{d}\Omega_2\phi_{^3\mathrm{He}}(\rho,\Omega_2)\phi^*_{^3\mathrm{He}}(\rho'\Omega_2')e^{i\mathbf{Q}\cdot(\rho-\rho')}$$
$$\exp\left(-\frac{\rho^2+\rho'^2+2\mathbf{x}_1\cdot\mathbf{x}_1'+2\mathbf{x}_2\cdot\mathbf{x}_2'}{16\sigma^2}\right). \tag{3.77}$$

The dependence on $\cos(\theta_{12})$ arises in the scalar products of $\mathbf{x}_i\cdot\mathbf{x}_i'$. The factor $\phi_{^3\mathrm{He}}(\rho,\Omega_2)\phi^*_{^3\mathrm{He}}(\rho'\Omega_2')e^{i\mathbf{Q}\cdot(\rho-\rho')}$ represents the Wigner function under the transformation $\rho\to\xi+\zeta/2$, $\rho'\to\xi-\zeta/2$.

Potential ^{3}He	E_B (MeV)	$\langle r_C^2\rangle$ (fm)	$\langle \delta r_C^2\rangle$ (fm)
AV18	6.925	2.054	1.872
AV18+UIX	7.750	1.962	1.771
Experiment	7.718	1.96	1.77

TABLE 3.4: The total ^{3}He binding energy E_B, the charge radius $\langle r_C^2\rangle$, and its point charge radius $\langle \delta r_C^2\rangle$ for 2-body (AV18) and 2+3-body (AV18+UIX) interaction potentials, compared to experimental values. The charge radius and the point charge radius are related via $\langle \delta r_C^2\rangle = \langle r_C^2\rangle - \langle r_p^2\rangle - N/Z\langle r_n^2\rangle$, with $r_p = 0.8783$ fm, $r_n^2 = -0.1149$ fm^2, N=1, Z=2. Taken from [28].

Potential ^{3}H	E_B (MeV)	$\langle r_C^2\rangle$ (fm)	$\langle \delta r_C^2\rangle$ (fm)
AV18	7.624	1.809	1.653
AV18+UIX	8.479	1.745	1.582
Experiment	8.482	1.76	1.60

TABLE 3.5: The total ^{3}H binding energy E_B, the charge radius $\langle r_C^2\rangle$, and its point charge radius $\langle \delta r_C^2\rangle$ for 2-body (AV18) and 2+3-body (AV18+UIX) interaction potentials, compared to experimental values. The charge radius and the point charge radius are related via $\langle \delta r_C^2\rangle = \langle r_C^2\rangle - \langle r_p^2\rangle - N/Z\langle r_n^2\rangle$, with $r_p = 0.8783$ fm, $r_n^2 = -0.1149$ fm^2, N=2, Z=1. Taken from [28].

Wave function for $^3_\Lambda$H

The wave function used in this work for $^3_\Lambda$H was developed in Ref. [29], and it is a simplified version of a full 3-body wave function. The simplification arises from the fact that the $^3_\Lambda$H is treated as an undisturbed deuteron surrounded by a halo Λ. This approach, while simple, is well motivated by the fact that the Λ–d binding energy is only ~ 100 keV. This means that not only is the interaction very small, but also the distance is very large. This leaves the deuteron core undisturbed. The basic idea of the Λ–d potential construction is as follows:

1. perform a separable fit to the Λ–N hard-core s-wave potential by the Nijmegen group [69]

2. average this potential over all spin configurations found in ${}^{3}_{\Lambda}\mathrm{H}$
3. Sum the Λ–N potential for the constituents of the deuteron and average over the deuteron wave function.

For the internal deuteron wave function, the Argonne v_{18} wave function was used, including both s- and d-wave, while the Λ–d interaction is only in the s-wave channel.

In this section, the coalescence probability for ${}^{3}_{\Lambda}\mathrm{H}$ is calculated under the assumption that it is a halo nucleus with an undisturbed deuteron at its center and a Λ in orbit around it.

$$\mathcal{P}(q_1,q_2,\sigma)=\frac{S}{(2\pi)^3\sigma^6}\frac{(2\beta^2+1)^{3/2}}{(2\beta+1)^3}\int \mathrm{d}^3r_1\mathrm{d}^3r_2\mathcal{D}_\Lambda(q_1,r_1)\mathcal{D}_\mathrm{d}(q_2,r_2)e^{-\frac{r_1^2(2\beta+1)^2+4r_2^2(2\beta^2+1)}{4\sigma^2(2\beta+1)^2}}. \tag{3.78}$$

The coordinates used for this derivation are Jacobi coordinates in momentum space

$$\mathbf{K}=\mathbf{k}_a+\mathbf{k}_b+\mathbf{k}_c, \tag{3.79}$$
$$\mathbf{p}=(m_c\mathbf{k}_b-m_b\mathbf{k}_c)/(m_b+m_c), \tag{3.80}$$
$$\mathbf{q}=[(m_b+m_c)\mathbf{k}_a-m_a(\mathbf{k}_b+\mathbf{k}_c)]/(m_a+m_b+m_c). \tag{3.81}$$

If the Λ is called particle a, then in the center of mass frame, one obtains

$$\mathbf{p}=\frac{1}{2}(\mathbf{k}_2-\mathbf{k}_3), \tag{3.82}$$
$$\mathbf{q}=\mathbf{k}_\Lambda. \tag{3.83}$$

Note that the center of mass motion given here is not a proper Jacobi coordinate. In principle, it should be

$$\mathbf{K}=\frac{m_a\mathbf{k}_a+m_b\mathbf{k}_b+m_c\mathbf{k}_c}{m_a+m_b+m_c}. \tag{3.84}$$

In general, the used Jacobi coordinates can be expressed by the transformation matrices

$$J=\frac{1}{\frac{1}{2}+\beta^2}\begin{pmatrix}0 & \frac{1}{2}\beta+\beta^2 & \frac{1}{2}+\beta\\ \frac{1}{2}+\beta^2 & -\frac{1}{4}\beta-\frac{1}{2}\beta & \frac{1}{2}\beta+\beta^2\\ -\frac{1}{2}-\beta^2 & -\frac{1}{4}\beta-\frac{1}{2}\beta & \frac{1}{2}\beta+\beta^2\end{pmatrix}, \tag{3.85}$$

$$J^{-1}=\begin{pmatrix}0 & \frac{1}{2} & -\frac{1}{2}\\ \frac{2\beta}{2\beta+1} & -\frac{1}{2\beta+1} & -\frac{1}{2\beta+1}\\ \frac{1}{2\beta+1} & \frac{\beta}{2\beta+1} & \frac{\beta}{2\beta+1},\end{pmatrix} \tag{3.86}$$

where $\beta=m_N/m_\Lambda=0.842$. The coordinate transformation is achieved via

$$\begin{pmatrix}\mathbf{p}\\ \mathbf{q}\\ \mathbf{K}\end{pmatrix}=J^{-1}\cdot\begin{pmatrix}\mathbf{k}_a\\ \mathbf{k}_b\\ \mathbf{k}_c\end{pmatrix}, \tag{3.87}$$

$$\begin{pmatrix}\mathbf{x}_1\\ \mathbf{x}_2\\ \mathbf{R}\end{pmatrix}=J\cdot\begin{pmatrix}\mathbf{r}_a\\ \mathbf{r}_b\\ \mathbf{r}_c\end{pmatrix}. \tag{3.88}$$

While the derivation of the potential is performed in the center-of-mass frame, and thus the CoM motion is set to 0, the Wigner function formalism for 3-body coalescence is defined in

terms of lab frame coordinates. Thus, this change in coordinates is made, which does not affect the wave function derived here but is critical for the coalescence formulation. The fit to the Λ–N potential in momentum space is performed using a Gaussian potential form

$$V_{\Lambda N}(k',k) = -\lambda^{\Lambda N} g(k') g(k) \tag{3.89}$$

$$g(k) = \exp[-(k/\Lambda_{\Lambda N})^2]. \tag{3.90}$$

The parameters $\lambda^{\Lambda N}$ and $\Lambda_{\Lambda N}$ can be found in Tab. 3.6. Only the parameters obtained using the Nijmegen hard-core potential are shown. While the parameter values for the soft-core potential differ significantly after spin- and momentum averaging, the results become equivalent. The majority of ${}^{3}_{\Lambda}\mathrm{H}$ is in a $S = 1/2$ state, with a small admixture of $S = 3/2$. The

Wave	$\lambda^{\Lambda N}$	$\Lambda_{\Lambda N}$
ΛN–${}^1S_0$	0.1238	0.1400
ΛN–${}^3S_1$	0.1129	0.1402

Table 3.6: Potential parameters for the ΛN interaction for the singlet and triplet states. Both potentials assume the hard-core Nijmegen potential. Adapted from Ref. [29].

deuteron is in a spin triplet state with $S = 1$. This means the deuteron is 2/3 in$\cdot|m_s| = 1$ and 1/3 in $|m_s| = 0$. If the deuteron is in an $|m_s| = 1$ state, the Λ–N interaction is always a singlet state ($p^{\uparrow}n^{\uparrow}\Lambda^{\downarrow}$), if the deuteron is in a $|m_s| = 0$ state the Λ–N interaction is part singlet part triplet ($p^{\uparrow}n^{\downarrow}\Lambda^{\uparrow}$). This results in a total chance of 75% for the Λ–N interaction to be in a single state with $J = 0$ and 25% chance to be in a triplet state with J=1. The small $S = 3/2$ part of ${}^{3}_{\Lambda}\mathrm{H}$ always results in a triplet state for the Λ–N interaction. For different total angular momentum L, one can evaluate the spin-averaged $\lambda^{\mathrm{eff}}_{\mathrm{L}}$

$$\lambda^{\mathrm{eff}}_0 = 3/4\,\lambda^{\Lambda N}_{\mathrm{J}=0} + 1/4\,\lambda^{\Lambda N}_{\mathrm{J}=1} = 0.1211\ \mathrm{fm}^2 \tag{3.91}$$

$$\lambda^{\mathrm{eff}}_1 = \lambda^{\Lambda N}_{\mathrm{J}=1} = 0.1129\ \mathrm{fm}^2. \tag{3.92}$$

For the Soft-Core potential $\lambda^{\mathrm{eff}}_0 = 0.1213\ \mathrm{fm}^2$, so both the soft and the hard-core potentials yield the same result for ${}^{3}_{\Lambda}\mathrm{H}$. Since the range $\Lambda_{\Lambda N}$ is practically equivalent between both spin configuration a value of $\Lambda_{\Lambda N} = 1.401\ \mathrm{fm}^{-1}$ is adopted. In order to obtain the Λ–d potential from the hyperon–nucleon potential, a momentum average over the deuteron wave function is performed

$$\langle \mathbf{q}'|V_{\Lambda \mathrm{d}}|\mathbf{q}\rangle = \int \mathrm{d}^3p'\mathrm{d}^3p \Psi^{\dagger}_{\mathrm{d}}(\mathbf{p}')\langle \mathbf{p}'\mathbf{q}'|V_2 + V_3|\mathbf{p}\mathbf{q}\rangle \Psi_{\mathrm{d}}(\mathbf{p}). \tag{3.93}$$

V_i describes the potential between Λ and N_i. The resulting potential can be expressed similarly to the hyperon–nucleon case

$$V_{\Lambda \mathrm{d}}(q',q) = -\lambda^{\Lambda \mathrm{d}} F(q') F(q), \tag{3.94}$$

$$F(q) = \exp[-(q/\Lambda_{\Lambda \mathrm{d}})^2]. \tag{3.95}$$

The parameter $\lambda^{\Lambda \mathrm{d}}$ can be found to be approximately $\lambda^{\Lambda \mathrm{d}} \approx 0.22$ regardless of the deuteron wave function used and $\Lambda_{\Lambda \mathrm{d}} = 1.17\ \mathrm{fm}^{-1}$. Finally, from this potential, a wave function can be obtained by solving the time-independent Schrödinger equation

$$\left(\frac{q^2}{2\mu} + V_{\Lambda \mathrm{d}}\right)|\Psi_{\Lambda}\rangle = -B_{\Lambda}|\Psi_{\Lambda}\rangle \tag{3.96}$$

where $\mu = 3.547\ \mathrm{fm}^{-1}$ is the reduced mass of the Λ–d system, $q = k_\Lambda$ and $B_\Lambda = 0.13$ MeV is the Λ separation energy. The solution using $\alpha = \sqrt{2\mu B_\Lambda} = 0.068\ \mathrm{fm}^{-1}$ is

$$\Psi_\Lambda(q) = N(\Lambda_{\Lambda\mathrm{d}})\frac{\exp[-(q/\Lambda_{\Lambda\mathrm{d}})^2]}{q^2+\alpha^2}. \tag{3.97}$$

The normalization constant is

$$N(\Lambda_{\Lambda\mathrm{d}}) = \left\{\frac{\pi}{4\alpha}\left[\mathrm{cerfe}\left(\frac{\sqrt{2}\alpha}{\Lambda_{\Lambda\mathrm{d}}}\right)\left(1+\frac{4\alpha^2}{\Lambda_{\Lambda\mathrm{d}}^2}\right) - \frac{2\alpha}{\Lambda_{\Lambda\mathrm{d}}}\sqrt{2/\pi}\right]\right\}^{-1/2}, \tag{3.98}$$

with $\mathrm{cerfe}(x) = \exp(x^2)(1-\mathrm{erf}(x))$, $N(\Lambda_{\Lambda\mathrm{d}} = 1.17)^2 = 0.103911$.

Using this wave function for Λ, the total wave function can be expressed as

$$\Psi_{^3_\Lambda H}(q) = \Psi_\Lambda(q) \sum_{(l,S)=(0,\frac{1}{2})(2,\frac{3}{2})} \Psi_\mathrm{d}^{(l)}(p)[\mathcal{Y}_{10}^l(\hat{p},\hat{q}) \otimes \chi_{1\frac{1}{2}}^S]_{\frac{1}{2}m_j}[\Lambda(\uparrow\downarrow - \downarrow\uparrow)/\sqrt{2}]. \tag{3.99}$$

This shows the coupling of the spin-1 deuteron to a spin-$\frac{1}{2}$ Λ with a total spin of either $\frac{1}{2}$ or $\frac{3}{2}$. The deuteron s-wave requires S=$\frac{1}{2}$, the d-wave $S = \frac{3}{2}$. The spinor is defined as

$$\chi_{1\frac{1}{2}}^{SM_S} = \sum_{m_d,m_\Lambda} \langle SM_S|1m_\mathrm{d};\frac{1}{2}m_\Lambda\rangle \chi_1^{m_\mathrm{d}}\chi_{\frac{1}{2}}^{m_\Lambda}, \tag{3.100}$$

and it is coupled to a spherical harmonic with angular momentum l for the deuteron and 0 for the Λ

$$\mathcal{Y}_{l_1l_2}^{lm}(\hat{p},\hat{q}) = \sum_{m_1,m_2} \langle lm|l_1m_1;l_2m_2\rangle Y_{l_1}^{m_1}(\hat{p})Y_{l_2}^{m_2}(\hat{q}). \tag{3.101}$$

With this total wave function, one can calculate the Wigner function as the product of the deuteron and the Λ Wigner function

$$\begin{aligned}\mathcal{D}(q_1,q_2,r_1,r_2) &= \int \mathrm{d}^3\zeta_1\mathrm{d}^3\zeta_2 \Psi_\Lambda(\mathbf{q}_1+\frac{\zeta_1}{2})\Psi_\Lambda^*(\mathbf{q}_1-\frac{\zeta_1}{2})\Psi_\mathrm{d}(\mathbf{q}_2+\frac{\zeta_2}{2})\Psi_\mathrm{d}^*(\mathbf{q}_2-\frac{\zeta_2}{2})e^{i(\mathbf{r}_1\cdot\zeta_1+\mathbf{r}_2\cdot\zeta_2)} \\ &= \mathcal{D}_\Lambda(q_1,r_2)\mathcal{D}_\mathrm{d}(q_2,r_2). \end{aligned} \tag{3.102}$$

The deuteron Wigner function is taken from Eq. 3.31 because the Wigner functions are equivalent, whether they are calculated from the coordinate space or Fourier space wave functions. The Λ Wigner function $\mathcal{D}_\Lambda$ can be calculated as

$$\mathcal{D}_\Lambda(q_1,r_1) = \frac{N(\Lambda_{\Lambda\mathrm{d}})}{4\pi}\int_0^\infty \mathrm{d}k \frac{4i\pi(e^{2ikr_1}-1)}{q_1r_1(k^2+4(\alpha^2+q_1^2))}\log\left(\frac{4\alpha^2+(k-2q_1)^2}{4\alpha^2+(k+2q_1)^2}\right)e^{-\frac{k^2+2ik\Lambda_{\Lambda\mathrm{d}}^2r_1+4q_1^2}{2\Lambda_{\Lambda\mathrm{d}}^2}}. \tag{3.103}$$

As a cross-check, one can verify that $\mathcal{D}_\Lambda(0,0) = 8$ as expected. Eventually, the coalescence probability can be calculated using $\beta = m_\mathrm{N}/m_\Lambda$ as

$$\mathcal{P}(q_1,q_2,\sigma) = \frac{S}{(2\pi)^3\sigma^6}\frac{(2\beta^2+1)^{3/2}}{(2\beta+1)^3}\int \mathrm{d}^3r_1\mathrm{d}^3r_2\mathcal{D}_\Lambda(q_1,r_1)\mathcal{D}_\mathrm{d}(q_2,r_2)e^{-\frac{r_1^2(2\beta+1)^2+4r_2^2(2\beta^2+1)}{4\sigma^2(2\beta+1)^2}}. \tag{3.104}$$

An important note to be given here is that the source size σ is assumed to be equal for nucleons and Λ-Baryons. This has been shown to be not true [14]. In the three-body coalescence approach described in Sec. 7.4, the source size for all three particles is assumed to be independent of each other, and only one "effective" source size parameter takes its place.

Chapter 4

π-d Femtoscopy

As mentioned above, one big problem of the coalescence model is the conservation of energy and momentum. Indeed, processes such as $p + n \rightarrow d$, or generally any $2 \rightarrow 1$ processes, are kinematically forbidden due to the lower mass of the bound state compared to the single nucleon states. As such, coalescence, as modeled in the Wigner function formalism, can only be seen as an approximation. The induced error is small (only ≈ 2.2 MeV in the case of the deuteron), but a physical explanation needs to be given of how exactly this problem is resolved in nature. One solution is the addition of a third particle, usually a pion, which can carry away the excess energy, and the process becomes a $3 \rightarrow 2$ process. In light of this search, the scenario where one nucleon inside the deuteron comes from a resonance decay becomes exceedingly interesting, as the pion from the decay would automatically be close in phase space and could catalyze the fusion reaction this way. One way to study this process is to search for residual correlations between the pion and the nucleon inside the deuteron. This can be done by employing the femtoscopy technique, which can be used to study the momentum correlation between the pion and the deuteron. Indeed, a resonance decay will induce a visible correlation between the daughter particles at the value of k^*, which is related to the invariant mass of the resonance as

$$m_{\mathrm{R}} = \sqrt{(k^*)^2 + m_{\mathrm{p}}^2} + \sqrt{(k^*)^2 + m_{\pi}^2} \Leftrightarrow k^* = \sqrt{\left(\frac{m_{\mathrm{R}}^2 + m_{\pi}^2 - m_{\mathrm{p}}^2}{2m_{\mathrm{R}}}\right)^2 - m_{\pi}^2}. \tag{4.1}$$

By analyzing pion-deuteron momentum correlations in proton-proton collisions at $\sqrt{s} = 13$ TeV at the LHC with the ALICE detector, direct evidence will be provided that (anti)deuterons are predominantly formed following the decay of short-lived resonances, such as the $\Delta^{++,+,0,-}(1232)$. This means that their production cannot happen at the same time as all other hadrons, as assumed in statistical hadronization models, but has to happen later via final state interactions. A valid interpretation of the data is that the pion that emerges from the resonance decay helps catalyze the reaction, which resolves the issues with coalescence models hinted at earlier, where a $2 \rightarrow 1$ process would violate energy and momentum conservation.

In this chapter, the measured pion-deuteron correlation data are briefly presented, serving as the foundation for the subsequent focus on model interpretations. These interpretations provide a comprehensive framework for understanding the data and converge on a single, robust conclusion: (anti)deuterons are primarily produced following resonance decays and maintain the residual nucleon–pion correlation induced by the Δ decay throughout the coalescence process.

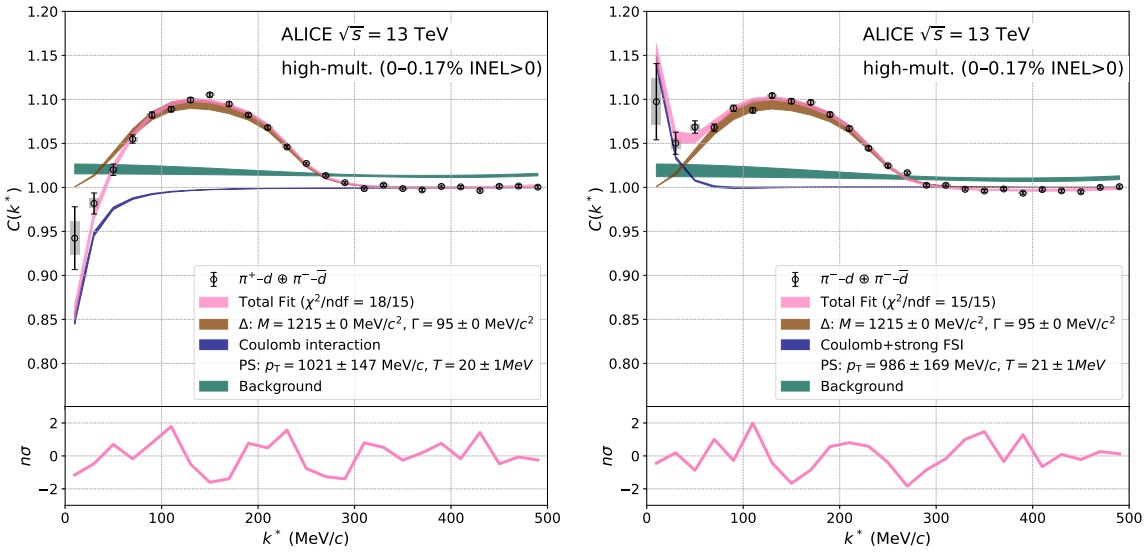

FIGURE 4.1: Measured π^+–d (left) and π^-–d (right) correlation functions fitted with model calculations and the number of standard deviations in the bottom panel. The model calculations include the Coulomb interaction (blue), the residual correlation from a Δ–decay (brown) as well as trivial background correlations (green). The product of all contributions constitutes the overall fit (magenta)

4.1 Experimental data

The data presented here was collected for pp collisions at $\sqrt{s} = 13$ TeV with the ALICE detector [77, 78] during the LHC Run2 (2015-2018). Only events that pass a software high-multiplicity (HM) trigger were selected. The HM trigger requires the total signal amplitude measured by the V0 detector to exceed a predefined threshold, which results in an average charged particle multiplicity at mid rapidity of $\langle \mathrm{d}N_{\mathrm{ch}}/\mathrm{d}\eta \rangle_{|\eta|<0.5} \approx 30$. The V0 detector consists of two plastic scintillator arrays placed on both sides of the interaction point at pseudorapidities $2.8 < \eta < 5.1$ and $-3.7 < \eta < -1.7$. Pseudorapidity is defined in terms of the polar angle θ between the track and the beam axis or the absolute momentum p and longitudinal momentum p_z as

$$\eta = -\ln\left[\tan\left(\frac{\theta}{2}\right)\right] = 0.5\ln\left(\frac{p+p_z}{p-p_z}\right). \tag{4.2}$$

The events remaining after triggering account for 0.17% of all pp collisions with at least one particle in the range $|\eta| < 1.0$ (INEL>0). 10^9 events pass this selection. This triggering is done, as deuteron production in each event is increased 5-fold compared to the untriggered minimum bias data sample. For the particle identification and tracking, the Inner Tracking System (ITS), Time Projection Chamber (TPC), and Time of Flight (ToF) detectors of the ALICE were used. They cover the full azimuth as well as the pseudorapidity interval $|\eta| < 0.9$. The detectors are surrounded by a 0.5T solenoid magnet, which causes the tracks of charged particles to bend. The curvature of these bent tracks is used to measure the particle momenta. The excellent tracking capabilities of the ALICE detector allow for a transverse momentum (p_{T}) resolution from 2% down to less than 1% for tracks with p_{T} < 1 GeV/c. Particle identification was performed using the particles' specific energy loss

(dE/dx) in the TPC detector as well as their velocity, measured by the ToF detector. The selection criteria can be found in Tab. 4.1 and 4.2. Deuterons with p < 1.4 GeV/c are identified using only the TPC, while TPC and ToF information are required for candidates with p > 1.4 GeV/c and a combined $n_{\sigma,\text{combined}} = \sqrt{n^2_{\sigma,\text{TPC}} + n^2_{\sigma,\text{ToF}}}$ limit is required. This way, the resulting samples of $\pi^{\pm}$ and d/$\overline{\text{d}}$ have a purity of 99% and 100%, respectively. Figure 4.1 shows the measured π^+–d $\oplus$ π^-–$\overline{\text{d}}$ (left) and π^-–d $\oplus$ π^+–$\overline{\text{d}}$ correlation function (right). The black markers indicate the measured correlation function, the black lines the statistical uncertainties, and the gray boxes the systematic uncertainties. The latter were obtained by repeating the analysis 44 times, using slight random variations of the selection criteria, also found in Tab. 4.1 and 4.2. The data is fitted using a phenomenological model that can be described via the relation

$$C_{\text{fit}}(k^*) = \epsilon(k^*) \otimes B(k^*)[\lambda_{\text{gen}} C_{\text{gen}}(k^*) + (1 - \lambda_{\text{gen}})]. \tag{4.3}$$

The λ-parameters have already been introduced in Ch. 2.2 and λ_{gen} = 0.816 for all charge combinations of $\pi^{\pm}$–d . The parameter $\epsilon(k^*)$ incorporates momentum resolution effects. Details on this procedure can be found in [14]. The baseline $B(k^*) = a + bk^{*2} + ck^{*3}$ accounts for the remaining correlations from the particle production process. Finally, $C_{\text{gen}}(k^*)$ is the genuine correlation function. It incorporates the genuine interaction as well as contributions from the Δ resonance, and it is modeled via

$$C_{\text{gen}}(k^*) = C_{\text{int}}(k^*)[F_\Delta C_\Delta(k^*) + (1 - F_\Delta)]. \tag{4.4}$$

The interaction correlation function $C_{\text{int}}(k^*)$ contains the strong interaction and Coulomb. Since the strong interaction between $\pi^{\pm}$–d is very small [79], no strong interaction is included in π^+–d , and only the real part ($\Re(f_0) = -0.037$ fm) of the potential in π^-–d . The imaginary contribution is even smaller with $\Im(f_0) = -0.008$ fm [79]. F_Δ is an effective parameter that describes the fraction of $\pi^{\pm}$–d pairs that come from the decay of a Δ. $C_\Delta(k^*)$ is modeled using a Sill-distribution [80] for the vacuum spectral shape of the delta, which is further modified by a Boltzmann-like phase space factor

$$C_\Delta(k^*) = PS(p_{\text{T},\Delta}, T)\text{Sill}(E; M_\Delta, \Gamma_\Delta). \tag{4.5}$$

The Sill distribution is a Breit-Wigner type distribution with low mass threshold effects

$$\text{Sill}(M_\Delta, \Gamma_\Delta; s) = \frac{1}{\pi} \frac{\sqrt{s - s_{\text{thr}}}\,\Gamma}{(s - M^2)^2 + (\sqrt{s - s_{\text{thr}}}\,\Gamma)^2} \Theta(s - s_{\text{thr}}). \tag{4.6}$$

The threshold is set to $s_{\text{thr}} = m_{\text{d}}^2 + m_\pi^2 = 3.535$ GeV^2 and with the conversion Eq. 4.1 this distribution in s can be transformed into a k^* distribution, with $k^*_{\text{thr}} = 0$. The function $\Theta(x - x_0)$ is a Heaviside step function, which forces the distribution to 0 below the threshold. The mass is set to the sum of the nucleon and a modified Δ mass of 1.215 GeV/c^2, $M = m_{\text{N}} + m_{\Delta,mod} = 2.15$ GeV/c^2, and the width is a modified width of $\Gamma = 95$ MeV/c^2. The modifications of the mass and width of the Δ come from the rescattering of its decay products. Such a behavior has been observed previously by the STAR [81] collaboration in the spectral shape of reconstructed mesons and, most recently, in ALICE measurements of the $p + \pi^{\pm}$ correlation functions[1], where the parameters for $m_{\Delta,mod}$ and Γ have been taken

[1] obtained from private communication

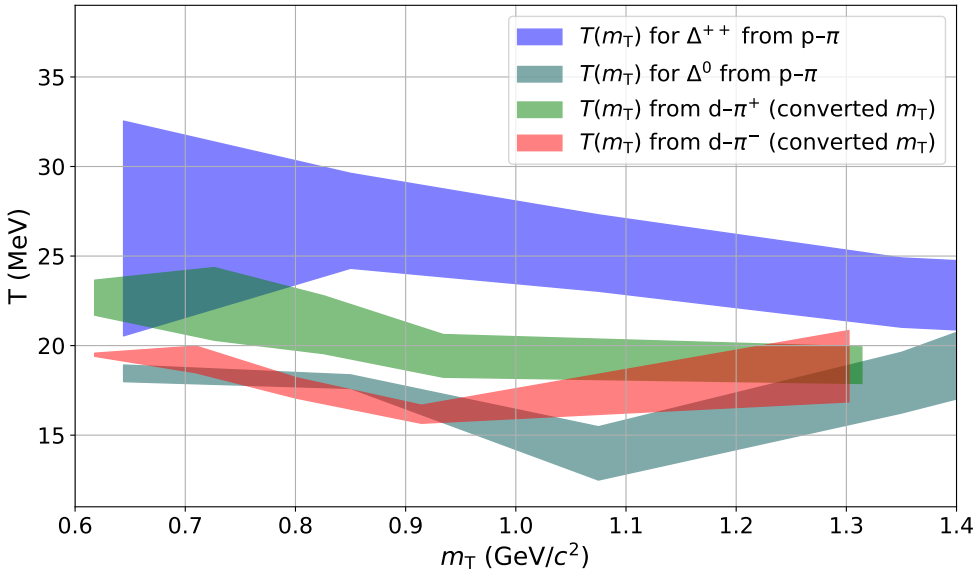

FIGURE 4.2: The kinetic decoupling temperature extracted from $\pi^{\pm}$–p and $\pi^{\pm}$–d as a function of the average pair transverse mass. The shift in the protonic systems stems from the Coulomb interaction between the proton and the charged pion. In the deuteronic systems the presence of the neutron weakens these effects.

from. This modification of the spectral shape can be modeled by introducing the aforementioned phase space factor

$$PS(p_{T,\Delta}, T; s) \propto \frac{\sqrt{s}}{\sqrt{s + p_{T,\Delta}^2}} \exp\left(-\frac{\sqrt{s + p_{T,\Delta}^2}}{T}\right). \tag{4.7}$$

This phase space factor depends on the p_T of the Δ, which can be calculated from the $\pi^{\pm}$–d pair as

$$p_{T,\Delta} = \vec{p}_{T,d}/2 + \vec{p}_{T,\pi} \tag{4.8}$$

In principle, this momentum should be smeared by the coalescence momentum, i.e. the momentum change of the constituent when it coalesces with another nucleon, but it was seen that the effect was negligible. Lastly, the phase space factor also depends on the parameter T, which is called the kinetic decoupling temperature. The interpretation is that at the surface of the last scattering, this is the average temperature of the system. From the fits, one obtains values of $\approx$ 20 MeV, which is very small in comparison to the typical freeze-out temperature of $\approx$ 155 MeV obtained from the thermal model. While the parameters for the modified mass and the modified width have been taken from the $\pi^{\pm}$–p correlation function, the temperature T has been left as a free parameter. Interestingly, the resulting temperature lies between the values obtained from π^+–p and π^-–p correlations. They can be seen in Fig. 4.2. In π–p, this can be understood as an earlier decoupling of the π^+–p system compared to the π^-–p system due to their repulsive Coulomb interaction. The primary interaction candidate for each π–p pair is the decay partner to re-form the initial Δ, and the repulsive nature of their Coulomb interaction makes the regeneration and decay process less likely. On the contrary, π^-–p has an attractive interaction and thus interacts for longer. In the case of the deuteron, the difference is less extreme. The π^+–d system decouples from the hadronic rescattering phase earlier than the π^-–d system for the same reason as the π^+–p

due to the proton inside the deuteron. However, if the π^+ comes from a $\Delta^+ \rightarrow \pi^+ + n$ decay, there is no enhanced or diminished re-interaction probability due to the Coulomb interaction. Thus, the overall effect of rescattering on the π^+–d system is less than that of only the proton. For the π^-–d system, the same logic holds, and the rescattering effect is not as strongly enhanced as in the π^-–p system. The factor F_Δ in Eq. 4.4 represents the fraction of $\pi^\pm$–d pairs which are associated to a Δ decay and it is estimated via the fit to the measured correlation function to be of the order of 2%. Assuming that at most one deuteron is present in each event, one can directly convert this into a fraction of the deuterons associated with a resonance decay. This is done by counting the number of pairs and dividing it by the total number of deuterons in the sample, and the number comes out to be $\sim (36 \pm 4)\%$. When accounting for the unseen decay into π^0, this number rises to $(54.4 \pm 6)\%$, and extrapolating for all resonances gives $(80.5 \pm 8.9)\%$. The calculation is performed by defining the ratios

$$f'_{\text{peak}} = \frac{\text{Number of extracted d}\pi \text{ pairs from the } \Delta \text{ peak}}{\text{number of measured deuterons}} = (54.4 \pm 6)\% \tag{4.9}$$

$$f'_{\Delta} = \frac{\text{Number of d with at least one } \Delta}{\text{number of measured deuterons}} \tag{4.10}$$

The prime means that the value is not corrected for detection efficiency. Indeed, the detection efficiency for pions and deuterons is of the order of only 70%. In the end, we want f_Δ including efficiency corrections in order to compare to the simulation. f'_{peak} is what we obtain uncorrected from the measurement. We use the following values obtained from the statistical hadronization model: $P_\Delta = (43.05 \pm 0.65)\%$, $P_{\text{R}} = (64.5 \pm 0.3)\%$, which are the probabilities for any given proton to stem from a Δ or from any resonance respectively. Assuming Y_{d} is the corrected yield of deuterons, ϵ_{d} is its detection efficiency and ϵ_π the pion detection efficiency we can write

$$f'_{\text{peak}} = \frac{\epsilon_{\text{d}}\epsilon_\pi 2P_\Delta(1-P_\Delta)Y_{\text{d}} + \mathbf{2}\epsilon_{\text{d}}\epsilon_\pi^2 P_\Delta^2 Y_{\text{d}} + 2\epsilon_{\text{d}}\epsilon_\pi(1-\epsilon_\pi)P_\Delta^2 Y_{\text{d}}}{\epsilon_{\text{d}} Y_{\text{d}}} = 2\epsilon_\pi P_\Delta \tag{4.11}$$

$$f'_{\Delta} = \frac{\epsilon_{\text{d}}\epsilon_\pi 2P_\Delta(1-P_\Delta)Y_{\text{d}} + \epsilon_{\text{d}}\epsilon_\pi^2 P_\Delta^2 Y_{\text{d}} + 2\epsilon_{\text{d}}\epsilon_\pi(1-\epsilon_\pi)P_\Delta^2 Y_{\text{d}}}{\epsilon_{\text{d}} Y_{\text{d}}} = 2\epsilon_\pi P_\Delta \left(1 - \frac{\epsilon_\pi P_\Delta}{2}\right) \tag{4.12}$$

$$f'_{\Delta} = f'_{\text{peak}} \left(1 - \frac{\epsilon_\pi P_\Delta}{2}\right) \tag{4.13}$$

The second summand in f'_{peak} considers the case where both nucleons come from a Δ and one actually detects both. Thus, this counts 2 d-π pairs, and we need to introduce a factor 2. If $\epsilon_\pi = 1$:

$$f_{\text{peak}} = 2P_\Delta \tag{4.14}$$

$$f_\Delta = 2P_\Delta \left(1 - \frac{P_\Delta}{2}\right) = \frac{f'_{\text{peak}}}{\epsilon_\pi}\left(1 - \frac{f'_{\text{peak}}}{4\epsilon_\pi}\right) \tag{4.15}$$

Now we have a relation between the measured pair yields f'_{peak} and the desired fraction f_Δ depending on the efficiency of π and the probability P_Δ. Substituting $\epsilon_\pi = 0.7$ and $f'_{\text{peak}} = (54 \pm 6)\%$ we get $f_\Delta = (62.3 \pm 6.9)\%$. With the help of the thermal model, we can extrapolate to all resonances using simple combinatorics. Using $f_\Delta^{\text{SHM}} = 1 - (1 - P_\Delta)^2 = (67.6 \pm 1)\%$, $f_{\text{R}}^{\text{SHM}} = 1 - (1 - P_{\text{R}})^2 = (87.4 \pm 0.4)\%$ and the relation

$$\frac{f_\Delta^{\text{SHM}}}{f_{\text{R}}^{\text{SHM}}} = \frac{f_\Delta}{f_{\text{R}}}, \tag{4.16}$$

we get $f_R = (80.5 \pm 8.9)\%$.

The uncertainties indicated are only of a statistical nature, and the predictions of ThermalFIST for the expected fractions are taken to be without uncertainty. Realistically, these predictions probably have an uncertainty of the order of 10% since the SHM, even in its canonical form used here, is not perfectly applicable to pp collisions, and many tensions are still present, specifically in proton and π predictions [6]. This shows that not only is resonance-assisted fusion most likely a contributor to nuclear formation, but it is, in fact, the main contribution. This leaves us with two scenarios: either all nuclei are produced via some fusion process and the remaining $(19 \pm 9)\%$ of nuclei are formed from other fusion processes such as $pp \to d + \pi$ or pion catalysis from non-associated pions, or thermal production of nuclei happens, but the vast majority are destroyed in the hot environment. Considering that SHMs currently predict exactly the measured yield, over 80% would have to be destroyed within a few fm/c.

Property	Selection Criterion	Variations
Filterbit	128 (TPC only)	–
Pseudorapdity	$\lvert\eta\rvert < 0.8$	0.76–0.84
Transverse momentum	$0.8 < p_T < 2.4$ GeV/c	(0.75–0.85) GeV/c
Number of TPC Clusters	n_{TPC} >80	70–90
Crossed TPC Pad Rows	$n_{crossed}$ >70 (out of 159)	–
Findable TPC Clusters	$n_{crossed}/n_{findable}$ >0.83	–
Tracks with shared TPC Clusters	rejected	–
Distance of closest approach xy plane	$\lvert DCA_{xy}\rvert < 0.1$ cm	–
Distance of closest approach z direction	$\lvert DCA_z\rvert < 0.2$ cm	0.15–0.25
Particle identification (TPC)	$n_{\sigma,d} < 3$ for p <1.4 GeV/c	$n_{\sigma,d} < 2.5$–3.5
	$n_{\sigma,e} > 6$ for p <1.4 GeV/c	–
Particle identification (TOF+TPC)	$n_{\sigma,TPC,\,d} < 3$ and $n_{\sigma,TPC,\,\pi} > 3$	$n_{\sigma,d} < 2.5$–3.5
	$-3 < n_{\sigma,TOF,\,d} < 5$	

TABLE 4.1: Summary of the default d ($\bar{d}$) selection criteria.

Property	Selection Criterion	Variations
Filterbit	96	–
Pseudorapdity	$\lvert\eta\rvert < 0.8$	0.7–0.9
Transverse momentum	$0.14 < p_T < 4.0$ GeV/c	(0.12–0.15) < p_T
Number of TPC Clusters	n_{TPC} >80	70–90
Crossed TPC Pad Rows	$n_{crossed}$ >70 (out of 159)	–
Distance of closest approach xy plane	$\lvert DCA_{xy}\rvert < 0.3$ cm	–
Distance of closest approach z direction	$\lvert DCA_z\rvert < 0.3$ cm	–
Particle identification	$n_{\sigma,TPC} < 3$, (p <0.5 GeV/c)	$n_{\sigma,d} < 2.7$–3.3
	$n_{\sigma,combined} < 3$, ($p \geq$0.5 GeV/c)	–

TABLE 4.2: Summary of the default $\pi^{\pm}$ selection criteria.

4.2 Predictions using coalescence

Figure 4.3 shows the predictions of the π^+–d correlation function obtained from several models. The red model denoted 'EPOS' shows the resulting correlation function when nuclei are formed from coalescence. For this, the EPOS 3.117 [82, 83] event generator is run

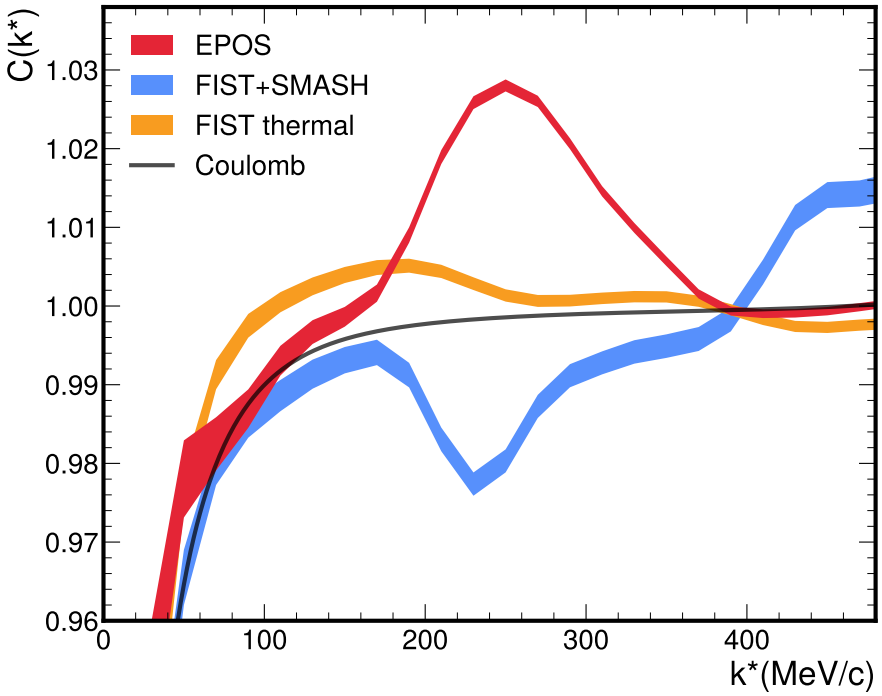

FIGURE 4.3: Simulated π^+–d correlation function using three different methods. The red line is a simulation using EPOS 3.117 with a coalescence afterburner presented in Ch. 6. The peak is generated by decaying $\Delta^{++/+} \rightarrow \pi^+$+N and the nucleon subsequently coalescing with another nucleon. The orange line shows the result obtained using the statistical hadronization model ThermalFIST. Here, pions and deuterons are created simultaneously. Thus, no feed-down from resonances is possible. The blue line shows the correlation function from ThermalFIST after an additional hadronic afterburner SMASH. a depletion around k^*=230 MeV/c can be seen from the deuteron breaking up. All correlation functions are multiplied with the Coulomb correlation function (black)

for pp collisions at $\sqrt{s} = 13$ TeV, and the output is analyzed by a coalescence afterburner. Importantly, the resonance yields produced by EPOS are reweighted to correspond to the yields predicted by the SHM. The afterburner uses the Wigner function formalism described in Ch. 3 with the Argonne v_{18} wave function. In order to boost the precision of the result, the coalescence probability was boosted by omitting the spin-isospin factor. Furthermore, since no Coulomb interaction is present in EPOS and thus the result is charge-independent, the π^+–d and π^-–d correlation functions were added. Both of these modifications do not change the result within the uncertainty, but they improve the statistical significance of the result. The correlation function is constructed in an equal manner to the measurement. All deuterons and pions in the same event are recorded for the same event distribution, and a buffer of the last 50 pions from previous events is kept. Every deuteron is then also compared to this buffer to form the mixed event. The buffer size is very large compared to measurements, where sizes usually range from 10-20 because the statistics of the simulation are very limited, and this reduces the uncertainty for the final correlation function.

A counting exercise similar to the measured data can be performed in EPOS. After tuning the resonance yields to the ones from ThermalFIST (see Ch. 6 and App. A for details), the charged pion final states contain $(46 \pm 5)\%$ contribution from Δ decays, extrapolating

to all Δ final states gives $(69 \pm 7)\%$. Further extrapolating to all resonances, one obtains $(89.2 \pm 1.6)\%$. This is compatible with the measurement within 2 standard deviations. However, similar to the estimation using the data, the resonance fractions were taken from ThermalFIST, which leaves a large uncertainty related to the actual yields unknown.

4.3 Predictions using thermal production

The other two predictions in Fig. 4.3 are obtained using the event generator for ThermalFIST [84]. It uses the yields from the canonical implementation of the SHM in ThermalFIST to generate particle yields on an event-by-event basis. A Blast-Wave parameterization [85] is used to randomly sample the momenta of the particles. Its parameters were obtained in Ref. [86] by fitting p_{T} spectra of π, K and protons with a Blast-Wave parameterization

$$\left.\frac{\mathrm{d}^2N}{\mathrm{d}y\mathrm{d}p_{\mathrm{T}}}\right|_{y=0} = \mathcal{N}\int_0^{R_0} r\,\mathrm{d}r\, I_0\left(p_{\mathrm{T}}\frac{\sinh[\tanh^{-1}(\langle\beta\rangle r^n)]}{T_{\mathrm{kin}}}\right) K_1\left(m_{\mathrm{T}}\frac{\cosh[\tanh^{-1}(\langle\beta\rangle r^n)]}{T_{\mathrm{kin}}}\right) \tag{4.17}$$

$$I_0(x) = \frac{1}{2\pi}\int_0^{2\pi} \exp\left(x\cos\phi\right)\mathrm{d}\phi \tag{4.18}$$

$$K_1(x) = \int_0^{\infty} \cosh y \exp(-x\cosh y)\mathrm{d}y. \tag{4.19}$$

I_0 and K_1 are modified Bessel functions. In the Blast-Bave model, a thermalized medium expands radially with a subsequent instantaneous freeze-out. Its main parameters are the average expansion velocity $\langle\beta\rangle$, its kinetic freeze-out temperature T_{kin}, and the velocity profile exponent n. The parameter R_0 is the radial extension of the fireball, and it is constrained by the thermal yields of the particles rather than their shape. Indeed, an important parameter for the SHM yield predictions is the volume $\mathrm{d}V/\mathrm{d}y$ of the system. From this, a radius can be calculated. For further information on the canonical SHM, see Ch. 2.1.1. The parameters used in this study can be found in Tab. 4.3. The Blast-wave model has been shown to work well in reproducing the measured yields and p_{T} spectra of pions, kaons, and protons in pp collisions [86].

Parameter	Value	Unit		Parameter	Value	Unit
$\langle\beta\rangle$	0.51	–		T_{c}	0.165	GeV
T_{kin}	0.16	GeV		μ_B	0	–
n	1.4	–		γ_S	0.85	–
η_{max}	1.5	–		$\mathrm{d}V/\mathrm{d}y$	75	fm^3
R_0	1.8	fm		V_c	3	–
Ref.	[86]	–	Ref.	[6]	–	

TABLE 4.3: Parameters used in the π^+–d correlation function predictions for thermal production. Parameters on the left side are used for the Blast-Wave parameterization, and parameters on the right are used for the ThermalFIST yields.

4.3.1 Direct production

For the orange line in Fig. 4.3, the output, after strong and electromagnetic decays, of the ThermalFIST event generator is taken and directly analyzed. Equivalently to the experimental method and the study with EPOS mentioned above, deuterons, which in this case are

directly produced, are combined with all π in the same event. A buffer of the last 50 pions of previous events is taken for the mixed event. Only pairs within the experimental acceptance are taken for a fair comparison. The resulting correlation function shows no correlated pairs beyond a trivial baseline. The baseline is an enhancement towards low k^*, but critically, it is a smooth evolution and not a peak-like structure. The origin of this baseline is not entirely clear, but the event generator uses a freeze-out hypersurface obtained from hydrodynamic simulations with MUSIC [87–89]. These hydrodynamic models, as well as the Blast-Wave model, include radial flow, which could cause enhancement towards lower values of k^*. A

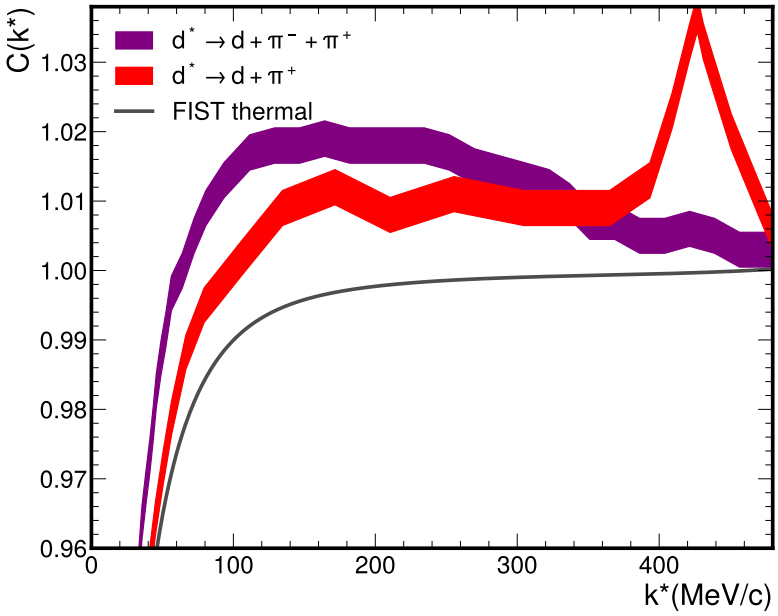

FIGURE 4.4: π^+–d correlation function obtained from ThermalFIST including the dibaryon state $d^*(2380)$. Two decay chains are tested, a 2-body decay $d^*(2380) \rightarrow d + \pi^+$(red) and a 3-body decay $d^*(2380) \rightarrow d + \pi^+ + \pi^-$(purple). All branching ratios are set to 100% to see an extremal effect. The Coulomb correlation function is shown in black. All shown correlation functions are multiplied by the Coulomb one. The 3-body decay does not show a peak-like structure. The 2-body decay shows a peak at a much larger k^* than observed. The feed-down effect at this level is not compatible with current deuteron yield measurements.

further study is the influence of the tentative observation of a $d^*(2380)$ dibaryon resonance by the WASA-at-COSY collaboration [90]. This state has a mass of m = 2380 MeV/c^2 and a width of $\Gamma = 70$ MeV and is currently understood as a Δ–Δ bound state with $J^P = 3^+$. This state can be implemented into ThermalFIST with these exact quantum numbers. Since its decay channels and their branching ratios are not known, two extreme scenarios have been tested: 100% decay into $d^*(2380) \rightarrow d + \pi^+ + \pi^-$ and $d^*(2380) \rightarrow d + \pi^+$. The latter would indicate two states, one double positively charged and one neutrally charged since the signal appears in π^-–d and π^+–d correlations. Notably, due to the similar mass and high degeneracy of the state (J=3 means 7-fold degeneracy), its production yield is approximately 15% of the deuteron yield. A 100% branching ratio into deuterons would cause the predicted deuteron yield to be $\approx$ 15% higher than the measured ones. Nonetheless, the resulting correlation functions can be seen in Fig. 4.4. The green line shows the 3-body decay,

and the purple line shows the 2-body decay. Also shown in black is the Coulomb baseline. All correlation functions shown are multiplied by the Coulomb one. The 3-body decay shows a slight enhancement of around 2% at low k^* but no peak-like structure. This is to be expected from 3-body decay channels since they do not present a sharp line but a wide distribution in their 2-body spectral shapes. The 2-body decay, on the other hand, shows a peak-like structure. However, its peak position is at much larger k^* of $\sim$ 450 MeV/c compared to the 250 MeV/c expected and observed from Δ decay. Furthermore, as previously eluded to, if this decay channel would show any significant enhancement of the $\pi^{\pm}$–d correlation function, its contribution to the deuteron production would also be significant, which would not be compatible with current measurements.

4.3.2 π–d interactions

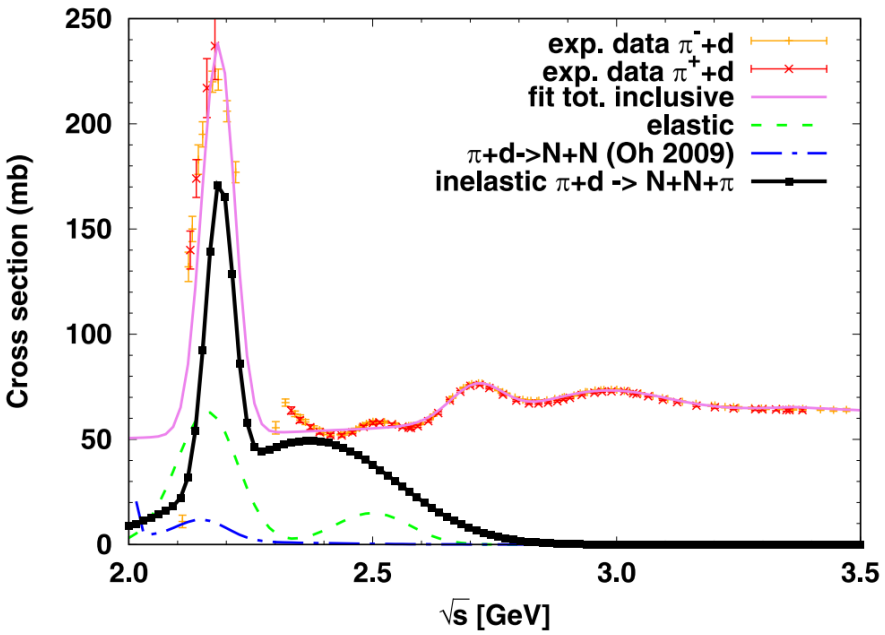

FIGURE 4.5: Elastic and inelastic $\pi^{\pm}$–d cross section. The cross sections are charge-independent and show a strong enhancement around the Δ mass for elastic and inelastic processes. Taken from [15].

In order to exclude final state interactions as the cause of the bump structure observed in the measurement, hadronic rescattering is also tested. For this, the output of ThermalFIST is fed into the hadronic afterburner SMASH [91]. In this hadronic rescattering model, not only elastic processes such as $\pi + d \leftrightarrow \pi + d$ but also inelastic channels $\pi + d \leftrightarrow \pi + p + n$ are included. The stochastic criterion is used in this study in order to enable $3 \leftrightarrow 2$ processes. Importantly, in SMASH, all processes are reversible. This means that final state deuterons could either be produced thermally or due to rescattering. However, the inclusion of such processes is critical in order to study the effect of deuteron destruction on the correlation function. Indeed, the π–d cross-section shown in Fig. 4.5 shows a very strong enhancement around the Δ mass for both, elastic and inelastic processes. However, the inelastic channel is a factor $\sim$ 3 larger than the elastic one. This cross-section can be interpreted as the reaction $\pi^{\pm} + d \rightarrow (\Delta - N) \rightarrow \pi^{\pm} + p + n$ or $\rightarrow \pi^{\pm} + d$. This dynamic resonance excitation is what could cause an enhancement. However, as can be seen from the blue line in Fig. 4.3, quite the opposite is true. A depletion around the Δ mass arises. The reason for this is twofold: on the one hand, pairs that undergo dynamic resonance excitation without destruction of

the deuteron are already at a k^* value corresponding to the Δ mass. This means when they decay back to a $\pi^{\pm}$–d , their k^* might get reshuffled slightly, but no pairs from outside the resonance region will be added to this region. This means such a process cannot enhance the correlation function. On the other hand, pairs that undergo dynamic resonance excitation and actually do destroy the deuteron will do so, preferably at the resonance mass. Also, the destructive process is the dominant one of the two. This shows that final state interaction will never cause an enhancement of the correlation function.

4.4 Conclusive remarks

In this chapter, the measured $\pi^{\pm}$–d correlation function measured in pp collisions at $\sqrt{s} =$ 13 TeV with the ALICE detector was presented. They show an enhancement of the correlation function, which is compatible with the decay of a $\Delta^{++,+,0,-}$-baryon into an N+$\pi^{\pm}$ pair and a subsequent fusion of the nucleon with a second nucleon into a deuteron. This reaction is furthermore catalyzed by the pion in order to conserve energy and momentum, solving a longstanding issue with the coalescence model. It was found that 80.9 ± 8.9 of deuterons are associated with the decay of a Δ. In order to further understand the measurement, model calculations were performed. The first is a coalescence-based simulation using the EPOS event generator. The EPOS resonance yields were reweighted in order to reproduce the predictions by the thermal model. Then, the resulting proton and neutron yields were analyzed using a coalescence afterburner (details in Ch. 6), which decides on a pair-by-pair basis which pairs form a deuteron and which do not. The deuterons resulting from this afterburner were used to determine the $\pi^{\pm}$–d correlation function. This correlation function shows an enhancement around the k^* value attributed to the mass of the Δ baryon (see Eq. 4.1). This enhancement is the result of the residual correlation of one nucleon and the pion being conserved in the nuclear formation process. The contribution of resonances to the deuteron yield was estimated to be $89.2 \pm 1.6\%$ after the resonance yields were tuned to the thermal model predictions, which is in agreement with the measured fraction. Further simulations were performed using the SHM thermalFIST. Here, nuclei are not formed via coalescence but alongside all other hadrons. No correlation between the pion and the deuteron is observed since no Δ decays contribute to the deuteron formation. In a second step, the interaction between the pion and the deuteron was tested. Indeed, one could expect that pseudoelastic scatterings of the form $\pi + (pn) \rightarrow (\Delta n) \rightarrow \pi + (pn)$ could lead to a correlation between the pion and the deuteron. This hypothesis was tested by using the SMASH hadronic afterburner, which simulates the rescattering of particles. Interestingly, a depletion around the Δ mass is observed. This is caused by deuteron destruction in the rescattering phase. Indeed, the π–d cross-section measurements in Fig. 4.5 show that the inelastic channel is approximately 4 times higher than the (pseudo)elastic one. This shows that the measurement can only be explained by deuteron formation via meson-catalyzed fusion.

Chapter 5

Existing antinuclei measurements

In this chapter, an overview of antinuclei measurements in small systems will be given. While ample measurements are available in heavy-ion collisions (primarily Au–Au and Pb–Pb), measurements in small systems (pp and e^+e^-) are sparse, especially at low energies. These measurements are interesting for comparisons with model predictions (See, e.g., Fig. 7.9) and in order to gauge how the yields behave for different collision energies.

5.1 e^+e^- collisions

The measurement of antideuterons in e^+e^- is particularly interesting for the study of antinuclei from Dark Matter annihilations. Indeed, the expectation is that DM particles are point-like, and their annihilation is qualitatively similar to annihilations of other fundamental particles, such as electrons. While this data is not directly used in this work, it is still an important pillar in the understanding required for cosmic ray antinuclei research and is thus given for completeness.

5.1.1 ARGUS 10 GeV

The ARGUS collaboration at DESY [92] reported the first observation of antideuteron production in e^+e^- collisions at $\sqrt{s} \approx 10$ GeV in 1985. The measurements were performed for beam energies at the $\Upsilon(1S)$ (m = 9.46 GeV/c^2), $\Upsilon(2S)$ (m = 10.02 GeV/c^2), $\Upsilon(4S)$ (m = 10.58 GeV/c^2) resonance energy as well as in the continuum from 9.4-10.6 GeV. Overall, six antideuterons were found in $\approx 7 \cdot 10^5$ events, and factoring in the detection efficiency of 55% one arrives at a total production rate of $(1.6^{+1.2}_{-0.7}) \cdot 10^{-5}$ antideuterons per hadronic event. No measurement of the matter counterpart was performed due to a high background from the spallation of gas molecules, creating deuteron in the detector. The measurement was performed for two regions of kinetic Energy $1.97 \leq E_{\overline{\mathrm{d}}} \leq 2.29$ GeV and $2.29 \leq E_{\overline{\mathrm{d}}} \leq 2.6$ GeV, with a yield $\frac{\mathrm{d}^2N}{\mathrm{d}y\mathrm{d}p_\mathrm{T}} = (2.45^{+2.37}_{-1.35}) \cdot 10^{-5}$ and $(1.85^{+1.85}_{-0.925}) \cdot 10^{-5}$ respectively. The measured antideuteron and antiproton spectra are shown in Fig. 5.1. The data was converted into the form $\mathrm{d}^2N/\mathrm{d}y\mathrm{d}p$. A conversion to p_T was not possible because only the total energy was published. For this, the total energy E_h was converted into p using the mass. The rapidity was obtained for each bin using the angular acceptance of $\theta \in (\pi/2 \pm \pi/4)$ [93].

5.1.2 ALEPH 91.2 GeV

The ALEPH experiment at LEP [94] observed deuteron and antideuteron production in hadronic Z decays, providing the first measurement of antideuteron production for e^+e^- collisions at the Z-boson resonance ($m_Z = 91$ GeV/c^2). The measured anti-deuteron yield per hadronic Z decay in the momentum range $0.62 < p < 1.03$ GeV/c is $(5.9 \pm 1.8 \pm 0.5) \cdot 10^{-6}$. The coalescence parameter B_2, was determined to be $(3.3 \pm 1.0 \pm 0.8) \cdot 10^{-3}$ GeV^2 in this momentum range. These results confirm a suppression of antideuteron production in

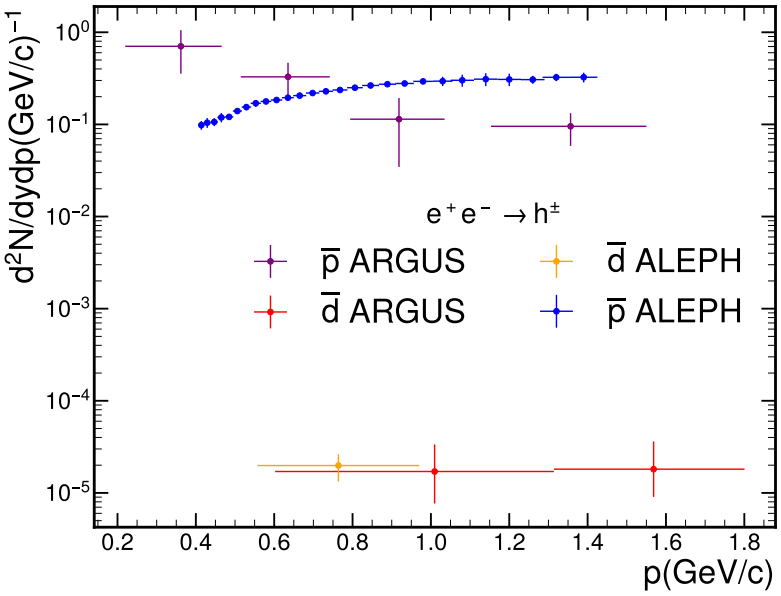

FIGURE 5.1: Measured antideuteron and antiproton spectra $\mathrm{d}^2N/\mathrm{d}y\mathrm{d}p$ as a function of momentum p, measured in e^+e^- collisions at $\sqrt{s} \approx 10$ GeV in the case of ARGUS and $\sqrt{s} = m_Z c^2 = 91$ GeV in the case of ALEPH.

e^+e^- collisions compared to proton-proton collisions, in which B_2 is of the order of 10^{-2}. The measured deuteron and proton yield, converted to $\mathrm{d}^2N/\mathrm{d}y\mathrm{d}p$, is shown in Fig. 5.1. The antideuteron yield is well in line with the one obtained from ARGUS, while the antiproton spectra show a very different spectral shape, and the overall yield is comparable to the ARGUS result. The ARGUS spectra show a very similar shape to the ones obtained in minimum bias pp collisions, while the ALEPH results seem to resemble the spectra obtained in jets more closely [51]. This is expected since hadronic production in e^+e^- collisions is driven by $\mathrm{q\bar{q}}$ jets. On the other hand, this makes the suppression of deuteron production surprising since the nuclear production in jets for hadronic collisions increases the coalescence probability 10-fold [51].

5.2 pp collisions

The measurements of antideuterons in pp collisions, especially the huge catalog of measurements provided by ALICE, are used as a benchmark for model predictions. While the models described in Ch. 6 and Ch. 7 are tuned to the ALICE measurements, it is also important to see a comparison to the other measurements, specifically by IHEP in Serpukhov and by the ISR at CERN. Indeed, these measurements provide anchor points at low collision energies, which are much more interesting for antinuclear measurements in cosmic rays [4].

5.2.1 Serpukhov 11.5 GeV pp

In the 1980s, the Russian Institute for High Energy Physics (IHEP) at Serpukhov performed multiple measurements on the production of (anti)protons[17], (anti)deuterons[16], and even triton[16], using a proton beam with a momentum of 70 GeV/c, colliding with either a hydrogen target (pp) or a heavy target (Be, Cu, Pb). (Anti)protons were measured in the p_T region from 0.48 to 2.21 GeV/c and (anti)deuterons from p_T =0.46 to 3.89 GeV/c. The

measurement results, as well as Levy-Tsallis fits using Eq. 6.2 are shown in Fig. 5.2. The fit parameters are shown in Tab. 5.1. The data is converted from $E\frac{d^3\sigma}{dp^3} = \sigma_{inel}\frac{1}{\Delta\phi p_T}\frac{d^2N}{dydp_T}$ to the more commonly used $\frac{d^2N}{dydp_T}$. An inelastic pp cross-section of $\sigma_{inel} = 30.766$ mb was used, taken from the PDG. The measurement was performed using two spectrometers placed at 160mrad at approximately 90° in the collision center-of-mass frame. The actual acceptance of these spectrometers depends on the particle momentum and reaches its peak at p_T =2.21 GeV/c with an acceptance of 126 μsr. A conservative value of 63μsr was adopted for the conversion since most particles fall below p_T =2.21 GeV/c. Indeed, the mean $\langle p_T \rangle$ of (anti)protons is 0.518 GeV/c and 0.639 GeV/c for (anti)deuterons. The rapidity acceptance depends not only on the p_T but also on the particle mass and their (mean) p_T. For protons, the rapidity range is $y = -0.686 \pm 0.053$, and for deuterons, $y = -1.060 \pm 0.050$. The pion acceptance is $y = -0.013 \pm 0.055$, which is what one would consider mid-rapidity. The published (anti)protons are not corrected for the feed-down from weakly decaying resonances, such as Λ-Baryons. Using the parameterization developed in [95]

$$\Lambda/p = c_1 + \frac{c_2}{1 + (c_3/s)^{c_4}}, \tag{5.1}$$

with the parameters $c_1 = 0.31$, $c_2 = 0.30$, $c_3 = (146\ GeV)^2$, $c_4 = 0.9$, one obtains a prompt Λ/p ratio of 0.313. Using branching ratio arguments and production symmetries between Σ and Λ Baryons[95], we can conclude that about 25.4% of (anti)protons come from weak feed-down. This will be taken into account when calculating the B_2 parameter (shown in Fig. 7.9) since protons from weak decays are too far removed from other nucleons to undergo coalescence.

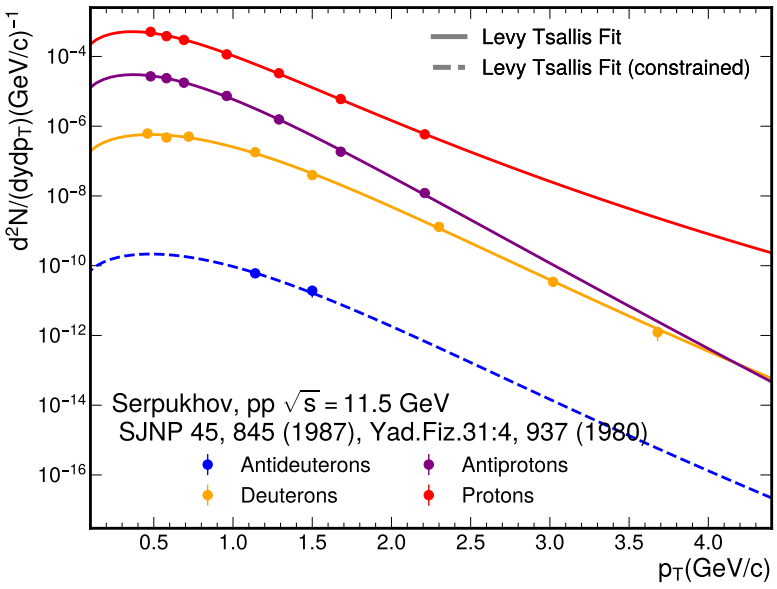

FIGURE 5.2: (Anti)deuteron measurement results by Serpukhov[16, 17] at $\sqrt{s} = 11.5$ GeV. The fits shown are Levy-Tsallis fits (Eq. 6.2). The fit to the antideuteron yields is constrained in shape to the deuteron spectrum. Only the total yield is left as a free parameter.

Species	dN/dy	n	T	m (GeV/c^2,fixed)
Proton	$(3.48 \pm 0.09) \cdot 10^{-4}$	20.8 ± 2.2	0.128 ± 0.003	0.938272
Antiproton	$(2.013 \pm 0.108) \cdot 10^{-5}$	98.55 ± 98.14	0.136 ± 0.007	0.938272
Deuteron	$(4.842 \pm 0.317) \cdot 10^{-7}$	35.81 ± 9.77	0.117 ± 0.006	1.875
Antideuteron	$(1.811 \pm 0.287) \cdot 10^{-10}$	35.81(fixed)	0.117(fixed)	1.875

TABLE 5.1: Parameters obtained from Levy-Tsallis (Eq. 6.2) fits to the measured data by Serpukhov[16, 17]. For Antideuterons, the shape parameters (T, n) are fixed to the Deuterons because only 2 data points are available, but Eq. 6.2 has 3 free parameters. Since the shape parameters of (anti)protons are in agreement with each other within their fit uncertainties, this is a reasonable assumption.

5.2.2 CERN ISR 53 GeV pp

The CERN Intersecting Storage Rings (ISR), operational from 1971 to 1984, were the world's first hadron collider. Located at CERN, the ISR consisted of two counter-rotating proton beams stored in intersecting rings, achieving center-of-mass energies up to 62 GeV. However, (anti)deuteron spectra were only measured for 53 GeV. In Fig. 5.3, the measured spectra of (anti)deuterons and (anti)protons are shown. The (anti)deuteron spectra were measured by the British-Scandinavian-MIT (antideuteron) and CHLM (deuteron) collaborations [22, 96], while the (anti)proton spectra were measured by the British-Scandinavian collaboration [21]. All spectra are fitted using a Levy-Tsallis function. Due to the low statistics and limited p_T-range, the (anti)deuteron spectra were fitted simultaneously by fixing the shape parameters for both and allowing the normalization to vary. The deuterons were measured under a lab-frame angle of 25°-55°, corresponding to a rapidity range of 0.22<y<0.65. The (anti)proton spectra are shown for different rapidity slices. Red and purple represent (anti)protons at mid-rapidity (0<y<0.1), brown corresponds to protons at 0.3<y<0.5, and orange to antiprotons at 0.5<y<0.7. The latter rapidity range was selected to allow comparison with Serpukov data taken at y$\sim$0.6; however, a slightly lower rapidity range was chosen due to the scarcity of protons in this region. For a given rapidity range, antiprotons and protons show consistent shape parameters, justifying the approach of fixing the shape parameters for deuterons and antideuterons. For mid-rapidity protons, contamination at low p_T —possibly from detector material being ejected—was observed, leading to the exclusion of the lowest four data points. Tab. 5.2 summarizes the extracted Levy-Tsallis parameters.

Species	Rapidity	dN/dy	n	T	m (fixed)
Proton	0-0.2	$(6.42 \pm 0.20) \cdot 10^{-2}$	15.03 ± 0.99	0.156 ± 0.005	0.938272
Antiproton	0-0.2	$(4.54 \pm 0.11) \cdot 10^{-2}$	16.75 ± 1.40	0.156 ± 0.005	0.938272
Proton	0.3-0.5	$(7.31 \pm 0.32) \cdot 10^{-2}$	10.85 ± 1.86	0.137 ± 0.010	0.938272
Antiproton	0.5-0.7	$(3.80 \pm 0.11) \cdot 10^{-2}$	11.26 ± 1.80	0.131 ± 0.001	0.938272
Deuteron	0.22<0.65	$(8.64 \pm 2.30) \cdot 10^{-5}$	11.36 ± 83.21	0.103 ± 0.080	1.875
Antideuteron	0.22<0.65	$(2.55 \pm 0.80) \cdot 10^{-5}$	11.36 ± 83.21	0.103 ± 0.080	1.875

TABLE 5.2: Levy-Tsallis parameters obtained from fitting the spectra measured at the ISR. Due to the low number of available data points, deuterons and antideuterons were fitted simultaneously, only leaving the normalization dN/dy free.

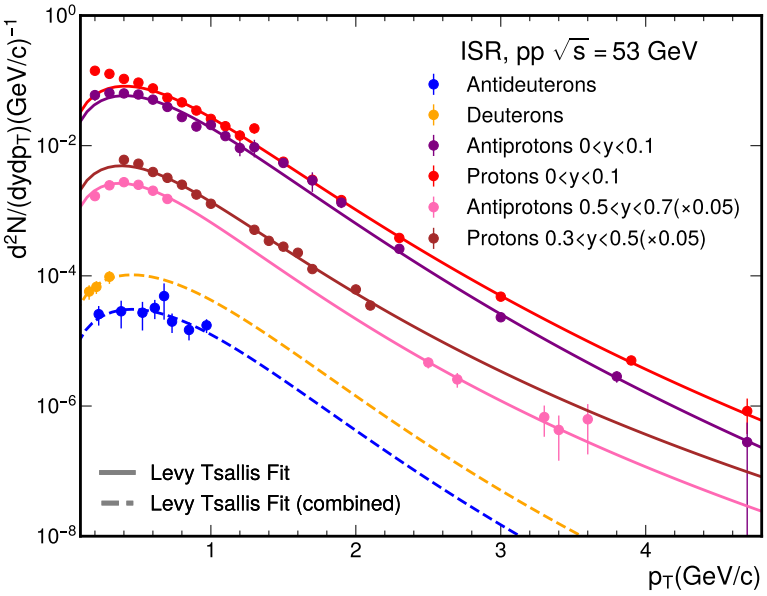

FIGURE 5.3: Measurements of (anti)protons and (anti)deuterons by the British-Scandinavian-MIT, CHLM and British-Scandinavian collaborations. While the (anti)deuterons were measured at a rapidity of $0.22 < y < 0.65$, the (anti)protons were measured in multiple rapidity windows ranging from $|y| = 0$ to $|y| = 0.9$. A small selection of those is shown here alongside Levy-Tsallis fits. Because of the low number of datapoints, the (anti)deuterons were fitted simultaneously, only leaving the overall normalization independent between the two species.

5.2.3 ALICE 5-13 TeV

The ALICE collaboration provides the most comprehensive catalog of (anti)nuclei measurements in small collision systems. Measurements of (anti)deuterons have been conducted at center-of-mass energies ranging from 5.02 to 13 TeV, with results categorized into up to nine multiplicity classes for each collision energy. Additionally, for 13 TeV collisions, a high-multiplicity triggered data set (0–0.1%) has been further subdivided into three separate classes. Multiplicity classes are determined using the summed signal of charged particles, referred to as the V0M amplitude, which is measured in the V0A ($-3.7 < \eta < -1.7$) and V0C ($2.8 < \eta < 5.1$) plastic scintillator detectors. The V0M amplitude distribution is divided into percentile bins of 10%, with events classified accordingly. Crucially, multiplicity classification is performed using signals from outside the mid-rapidity region ($|\eta| < 0.8$) to avoid biasing the data sample. This approach mitigates significant biases observed in particle yield measurements; for example, studies of charged and neutral kaons[97] have demonstrated that such biases can lead to a reduction of up to 20% in neutral kaon yields for high-multiplicity events. The underlying cause is that charged kaons not only contribute to the particle yield but also artificially increase the charged particle count when multiplicity is determined at mid-rapidity. ALICE measures particles at mid-rapidity (| y | <0.5) using multiple detectors to perform PID and momentum determination. For nuclei the most important ones are the Time Projection Chamber (TPC) and the Time of Flight (ToF). Both can be used to perform PID and momentum determination, and they are used in combination at high p_T. However, at low p_T, the efficiency of the ToF is extremely low, and only the TPC is used. The ToF detector is the outermost detector system in the ALICE experiment,

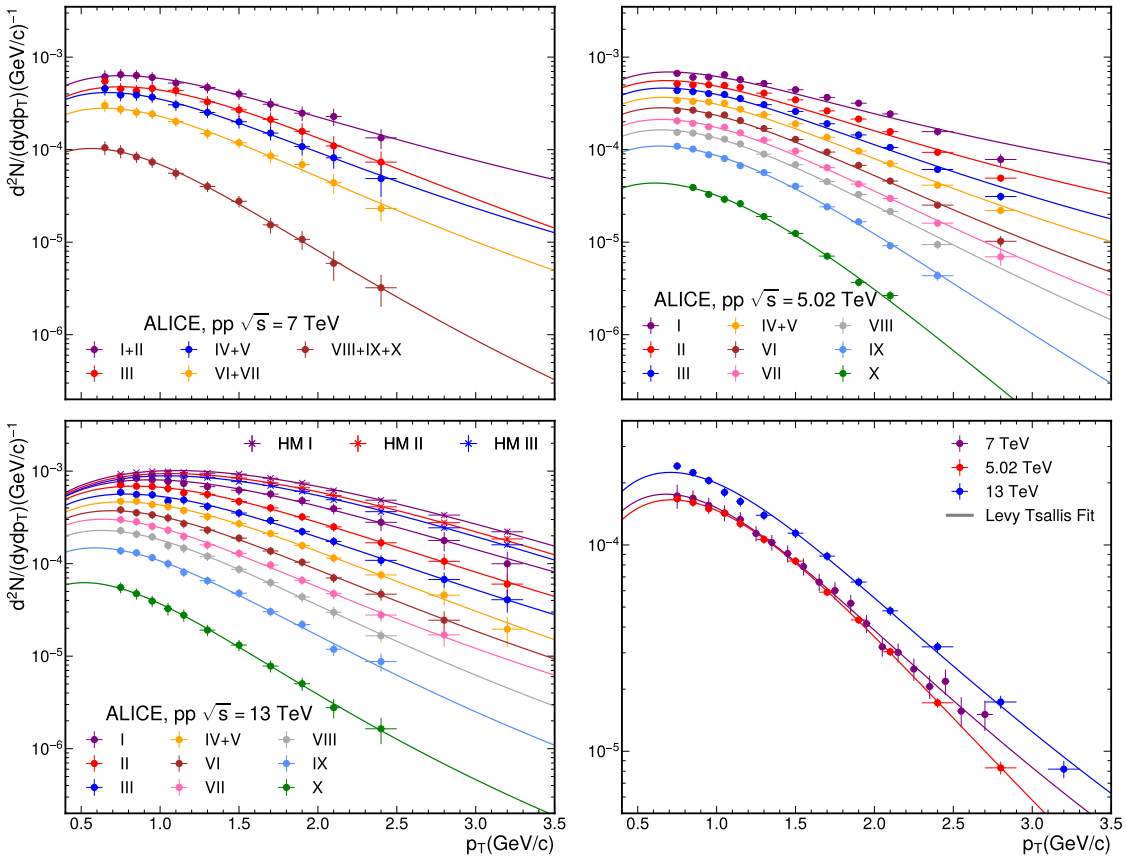

FIGURE 5.4: Averaged (anti)deuteron p_{T} spectra (d+$\overline{\mathrm{d}}$)/2 measured by ALICE at three different energies, 5 TeV (top right), 7 TeV (top left) and 13 TeV (bottom left) at mid-rapidity ($|y|<0.5$). The spectra are measured differentially in up to nine multiplicity classes as well as multiplicity integrated (minimum bias, bottom right).

and low-momentum particles are often stopped before they reach it, especially large particles such as nuclei. This can cause large variations at low p_{T}, which are especially visible when compared to model predictions (See Fig. 7.10 for example). The resulting transverse momentum (p_{T}) spectra are shown in Fig. 5.4. The top-left panel presents the spectra for 7 TeV, measured across five multiplicity classes. The mean charged-particle multiplicities corresponding to these classes are listed in Tab. 5.3. The top right shows the results for 5.02 TeV in nine classes. The bottom left panel shows 13 TeV in nine classes, and the 13 TeV with an included high multiplicity (HM) trigger, further separated into 3 classes. The bottom right panel shows the multiplicity integrated, so-called minimum bias (MB) spectra. All spectra shown are the average of matter and antimatter (d+$\overline{\mathrm{d}}$)/2.

Energy	I	II	III	IV+V	VI	VII	VIII	IX	X
5.02 TeV	18.5	14.5	11.9	9.7	7.8	6.3	5.2	3.9	2.4
7 TeV	17.47	(to I)	13.50	10.76	7.54	(to VI)	3.30	(to VIII)	(to VIII)
13 TeV	26.02	20.02	16.17	12.91	10.02	7.95	6.32	4.50	2.55
13 TeV HM	35.8	32.2	30.1	–	–	–	–	–	–

TABLE 5.3: Multiplicity classes used by ALICE for 5-13 TeV pp collisions. The classes IV and V are always merged. For 7 TeV the classes I and II are merged, as well as VI+VII and VIII+IX+X. 13 TeV with high multiplicity (HM) trigger only has three classes. [8–10, 20]

Chapter 6

Coalescence in EPOS

6.1 The EPOS event generator

In order to test the Coalescence model one needs an assumption on the momentum distribution G_{np} and the spatial distribution H_{np} in Eq. 3.9. These can either be obtained analytically or from simulations. In this study, we employ the EPOS 3 event generator [82, 83]. EPOS stands for **E**nergy conserving quantum mechanical approach, based on **P**artons, parton ladders, strings, **O**ff-shell remnants and **S**plitting of parton ladders. EPOS operates with a Core-Corona approach to particle collisions. Immediately after the collisions, particles are created using strings, which themselves are created from parton-parton pomeron exchanges. These strings have a non-zero momentum, and when splitting, they transfer a fraction of that momentum onto the created fragments. Fragments that have low momentum stay inside the core, while high-momentum fragments escape to the corona. Fragments in the core get dissolved into a QGP which is evolved using hydrodynamics. During the evolution, the temperature of the medium drops until it becomes cool enough to freeze out ($T \simeq 170$ MeV) and hadronize using a Cooper-Frye[98] description. The hadrons are further fed into the UrQMD [99, 100] model to handle decays of resonances and the hadronic cascade, i.e. rescattering. Particles in the Corona are directly fed into UrQMD. Interestingly, this prescription, using hydrodynamic evolution of the core is used regardless of the collision system and energy, even on pp collisions. Unlike many other event generators, EPOS also assigns positions to particles. These positions can be accessed for each particle after each stage of the collision, e.g. Core particles' positions can be accessed before being fed into UrQMD.

6.2 Tuning the event generator

Despite the use of QCD-inspired models, the production of particles in event generators is not perfect. Indeed, they need to be tuned to one's specific needs if one wants to investigate coalescence despite the shortcomings of the event generator. The main parameters that influence coalescence are the nucleon momentum distributions, the source size, and the charged particle multiplicity.

6.2.1 Charged particle multiplicity

The starting point of the correction of the event generator is the charged particle multiplicity. Since the source has only been measured in high multiplicity (HM) (0-0.17%) pp collisions at $\sqrt{s} = 13$ TeV, one has to also compare the coalescence predictions to high multiplicity deuteron data measured in the same collision system and energy[9]. This way, a benchmark can be set free of any biases by the event generator. In order to compare to HM measurements, an HM trigger that mimics the experimental one needs to be implemented into the event generator. This is done in two steps: First, in the settings of the simulation the impact

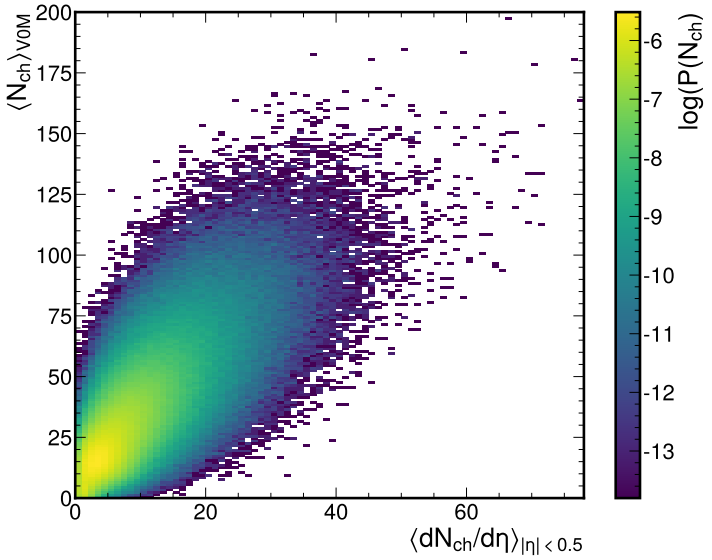

FIGURE 6.1: $\mathrm{d}N_{\mathrm{ch}}/\mathrm{d}\eta$ vs V0M amplitude distribution in EPOS.

parameter b is set to 0. This ensures only head-on collisions, which reduces the number of low multiplicity events and, thus, the loss factor when triggering for high multiplicity. The effect on the mean multiplicity can be seen in Fig. 6.2. The second step is an HM trigger, which mimics the ALICE V0 trigger system [9]. In this trigger events are selected based on the number of charged particles ($\pi^{+/-}, K^{+/-}, p, \overline{p}, e^{+/-}$) at backward and forward rapidity ($-3.7 < \eta < -1.7$ and $2.8 < \eta < 5.1$, where η is the pseudorapidity relative to the beam axis of the particle) which from now on will be referred to as the V0M region, after the V0M detectors in ALICE. This method reduces auto-correlation biases when measuring charged particles since a particle of interest would automatically also have a higher chance to be in an HM event since it itself increases the multiplicity by one [101]. The distribution of $\langle \mathrm{d}N_{\mathrm{ch}}/\mathrm{d}\eta \rangle_{|\eta|<0.5}$ vs V0M amplitude obtained from EPOS can be found in Fig. 6.1. Different minimal thresholds in V0M amplitude can be chosen with this distribution, and the resulting mid-rapidity distribution can be obtained. The 0-0.01% multiplicity class in ALICE has a mean multiplicity of $\langle \mathrm{d}N_{\mathrm{ch}}/\mathrm{d}\eta \rangle_{|\eta|<0.5} = 35.8$, so a V0M threshold has been chosen to give a mean mid-rapidity multiplicity as close to the experimental value as possible. When triggering for at least 127 charged particles in the V0M region a mean multiplicity of $\langle \mathrm{d}N_{\mathrm{ch}}/\mathrm{d}\eta \rangle_{|\eta|<0.5} = 35.4$ can be achieved. The resulting distribution compared to the mean value can be found in Fig. 6.2.

6.2.2 The source size

To account for realistic particle emission and correlation, in our implementation of the coalescence afterburner, we rely on the ALICE measurement of the nucleon emission source [14], which has been performed in pp collisions at $\sqrt{s} = 13$ TeV with a high multiplicity trigger in the 0-0.17% multiplicity class. As mentioned above, this is the only existing measurement differential in $\langle m_{\mathrm{T}} \rangle$ of the emission source in pp collisions available. While the measurement utilizes the femtoscopy technique [14] in the event generator, we can directly use the space-time coordinates stored by the event generator. The extraction of the distance has to be done at equal times. This is achieved by boosting into the rest frame of

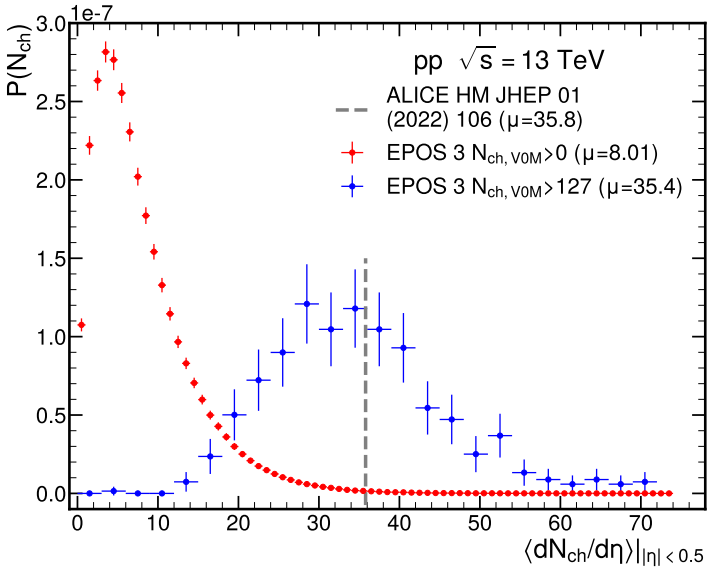

FIGURE 6.2

the pair (PRF) under investigation and propagating the particle with the smaller time coordinate. Since in the Femtoscopy technique only pairs with a small relative momentum $k^* \lesssim 300$ MeV/c contribute to the signal a similar cut has been applied to the pairs in the event generator. Thus the propagation can be done non-relativistically because the particles are moving slowly in their respective pair rest frame (PRF). Note that this equalization of time is especially important for nucleons that come from strongly decaying resonances such as Δ and N^*, where the time differences can be multiple fm/c. Such a scenario is shown in Fig. 6.3 where the distance between a proton and a neutron $d_{\mathrm{pn}}^{\mathrm{native}}$ is determined. The proton stems from a Δ^+ resonance, while the neutron is a primordial one. The neutron needs to be propagated forward in time by the lifetime Δt_Δ of the Δ^+. Otherwise, a very different distance will be extracted. The strong effect of resonances motivates an investigation of the resonance cocktail inside EPOS.

The resonance cocktail

In App. A an overview of all resonances which feed into protons and neutrons with a mass of less than 2 GeV/c^2 can be found. Alongside their ISAJET PID, PDG PID, their contribution fraction to protons in EPOS and extracted from thermal FIST [84]. Based on the relative contribution fractions, a correction factor for each resonance is obtained. The resulting nucleon is reweighted by this correction factor when obtaining the source size, as well as momentum distributions (Sec. 6.2.3). The product of the weights of the proton and the neutron is used to reweight (anti)deuterons. Note that in the ISAJET convention, multiple states with similar masses but very different quantum numbers and lifetimes have been merged, such as the $\Delta^-(1620)$ with the ISAJET ID 2222 is a combination of the $\Delta^-(1600)$ and the $\Delta^-(1620)$ states with lifetimes of $c\tau = 0.79$ fm/c and $c\tau = 1.52$ fm/c respectively. The lifetime of the EPOS states is randomly picked from any merged states.

Scaling the Source

After the resonances are retuned the native source size can be determined. For each nucleon their mother is determined by keeping track of all resonances created in the event and later

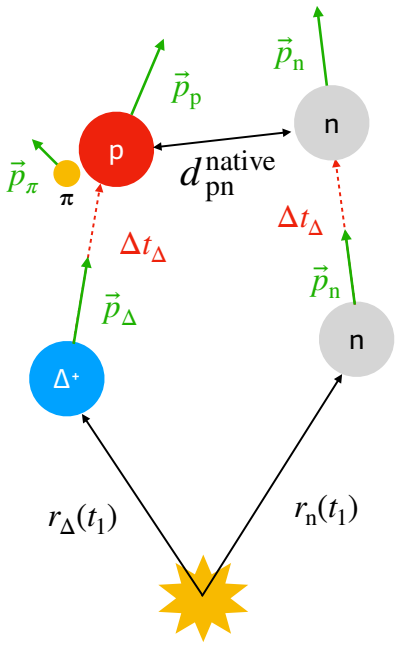

FIGURE 6.3: Scheme of the determination of the proton-neutron distance in MC simulations $d_{pn}^{nateive}$ in the case of a proton coming from the decay of a Δ^+ resonance.

matched to the final state nucleon. This can be easily done since EPOS keeps track of the ID of the mother particle. Then one determines each proton-neutron pair, as well as their antimatter counterparts, find their distance as described above, and stores it along the pair average transverse mass $\langle m_T \rangle = \sqrt{(\frac{p_{T,p}+p_{T,n}}{2})^2 + m_N^2}$, assuming $m_p = m_n = m_N$. Then, for each value of $\langle m_T \rangle$, the distance distribution, where each entry is weighed by the product of the previously determined resonance weights, is fitted using an effective Gaussian source estimate

$$S(r; r_0) = \frac{4\pi r^2}{(4\pi r_0^2)^{3/2}} \exp\left(-\frac{r^2}{4r_0^2}\right). \tag{6.1}$$

Here r_0 is the source size. It is important to note that the mean of this function is $r_\mu = 4/\sqrt{\pi} r_0$. This means the source size can easily be determined using the mean of the function. In Fig. 6.4, the native source size r_0^{native} is shown as a function of $\langle m_T \rangle$ for EPOS. From the comparison with the ALICE measurement r_0^{ALICE} [14] (black points), it is clear that the native source size predicted by EPOS (blue band) does not reproduce the observed $\langle m_T \rangle$ dependence. Hence, an additional $\langle m_T \rangle$-scaling $\mathcal{S}(\langle m_T \rangle) = r_0^{ALICE}/r_0^{native}$ is introduced and the corrected proton-neutron distance is obtained as $d_{pn}^{scaled} = S(\langle m_T \rangle) d_{pn}^{native}$. When applying the correction and re-determining the source size, the orange band in Fig. 6.4 is obtained, which shows that the rescaling scheme is able to successfully correct the $\langle m_T \rangle$ scaling behavior of the source in EPOS. Previous works [63, 102] have either fixed the source size to one value or used the measured size and sampled from it. The approach of this work has the advantage that space-momentum correlations, which are created by the event generator, are conserved. This means that pairs with a relatively small distance will still have a comparatively small distance and vice versa. The effect can be seen in Fig. 6.5. On the left figure, the correlation between the relative momentum q and the distance r of nucleons after the source scaling is shown. On the right side, the same is shown, but with a random sampling of the distance according to the measurement. The region of interest for coalescence is marked

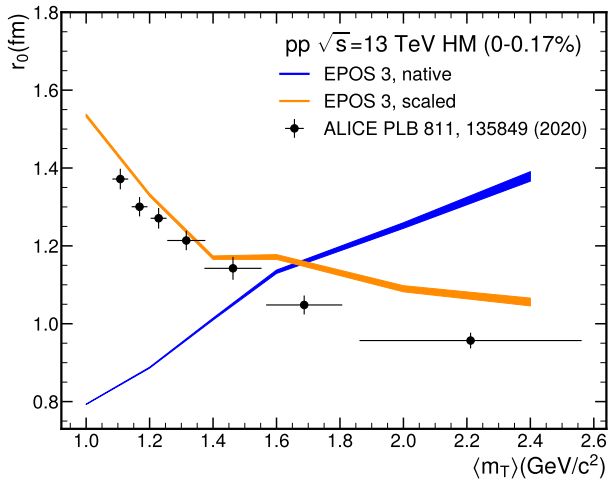

FIGURE 6.4: Comparison between the source size r_0 measured by ALICE[14], the native EPOS source and the source obtained after the source modeling, as a function of the transverse mass $\langle m_T \rangle$. For the ALICE data, statistical and systematic uncertainties are summed in quadrature and shown as vertical bars, while for EPOS, uncertainties are shown as a colored band.

with a red box covering $q \in [0, 0.285]$ GeV/c and $r \in [0, 3.5]$ fm, as motivated in Ref. [103]. It is clear that conserving the $q - r$ correlations leads to more p-n pairs in the region of interest. The influence on the deuteron yields can be seen in Fig. 6.9.

6.2.3 Momentum distribution

Experimentally, the full 3D momentum distribution can be reconstructed by combining three different measurements: the transverse momentum p_T-distribution, the rapidity distribution, and the azimuthal angular distribution. The azimuthal distribution is assumed to be flat and properly reproduced in event generators. The same holds for the rapidity distribution. The transverse momentum (p_T) distribution can be obtained from measurements. In this study, $p + \overline{p}$ data measured by the ALICE collaboration was chosen. They measure nucleon spectra in pp collisions at $\sqrt{s} = 13$ TeV with a high multiplicity (HM) trigger [9]. In Fig. 6.6 the measured spectra for the 0-0.01% multiplicity class are compared to the native output of EPOS, triggered to the same mean multiplicity. It is obvious that EPOS cannot natively reproduce the measured spectra. Thus, a correction scheme is employed to re-weight each nucleon to reproduce the measured spectra. For this, the ALICE and EPOS spectra were fitted using a Lévy-Tsallis function [104]

$$\frac{\mathrm{d}^2N}{\mathrm{d}y\mathrm{d}p_T} = \frac{\mathrm{d}N}{\mathrm{d}y}\frac{p_T}{nT}\frac{(n-1)(n-2)}{nT + m(n-2)}\left(1 + \frac{\sqrt{p_T^2 + m^2} - m}{nT}\right)^{-n}, \tag{6.2}$$

where m is the mass of the particle of interest, p_T its transverse momentum, dN/dy its yield per unit of rapidity, and n, T are fit parameters. The resulting fit parameters can be found in Tab. 6.1. Note that the mass m was left as a free parameter in the case of EPOS to ensure a better fit quality. Also, the proton and neutron spectra from EPOS were fitted separately since EPOS does not provide perfect isospin symmetry, which is, however, assumed in the coalescence model due to a lack of neutron measurements. Indeed the assumption of isospin symmetry is consistently employed and assumed throughout the entirety of this

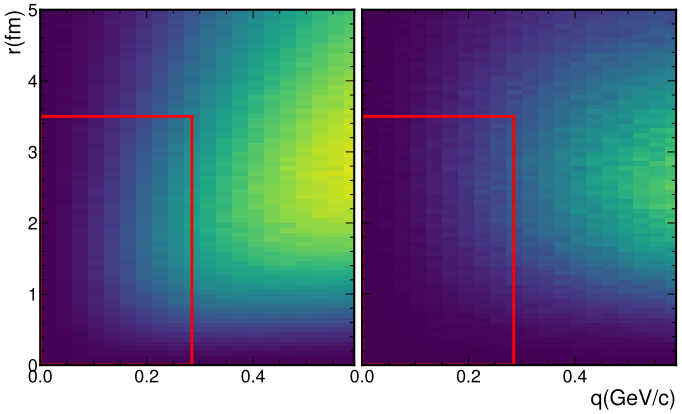

FIGURE 6.5: Distribution of relative momenta q against distance r of nucleons produced by EPOS. (left) Distribution after applying the source model, conserving the correlation. (right) Distribution after destroying correlations.

Parameter	ALICE	EPOS Proton	EPOS Neutron
dN/dy	2.1535	3.5104	3.6515
n	4.1477	3.9814	5.1614
T	0.3515	0.3248	0.3059
m	0.938272	-9.16·10^{-5}	-0.0302

TABLE 6.1: Fit parameters for nucleon spectra used in the correction of EPOS. While technically a physical parameter the mass was left free in the case of EPOS to ensure a better fit.

work. The correction then works as follows: For each nucleon in the EPOS simulation the p_T is determined. Then a correction factor is calculated as the ratio between Eq. 6.2 with the parameters for ALICE from Tab. 6.1 and Eq. 6.2 with the parameters for EPOS. The nucleon is then weighted whenever it is counted with this correction factor. Deuterons are weighted with the product of the weights of their constituents. After applying this correction scheme, the reweighted nucleon spectra coincide with the measured ones, as shown in Fig. 6.6.

6.3 Angular correlations

As mentioned in the previous section, the relative momentum of two particles is driven by the absolute momenta and the angle between them. The relative angle is usually expressed in 2D $\Delta\eta - \Delta\varphi$ correlations. Often only the 1D $\Delta\varphi$ correlation is studied since it is more sensitive than the $\Delta\eta$ one. The correlation function $C(\Delta\varphi)$ is defined as

$$C(\Delta\varphi) = \frac{SE(\Delta\varphi)}{ME(\Delta\varphi)}, \tag{6.3}$$

where $SE(\Delta\varphi)$ and $ME(\Delta\varphi)$ are the normalized same and mixed event $\Delta\varphi$ distributions respectively. The same event distribution is the distribution of relative angles $\Delta\varphi$ between pp pairs in the same event, while the mixed event distribution pairs up protons from different events. The mixed event distribution contains the trivial phase space contribution, while the same event distribution additionally contains the particle interaction. In Fig. 6.7 the measurement of the $\Delta\varphi$ correlation function $C(\Delta\varphi)$ by the ALICE collaboration in pp collisions at $\sqrt{s} = 7$ TeV is shown and compared to the same correlation obtained from EPOS

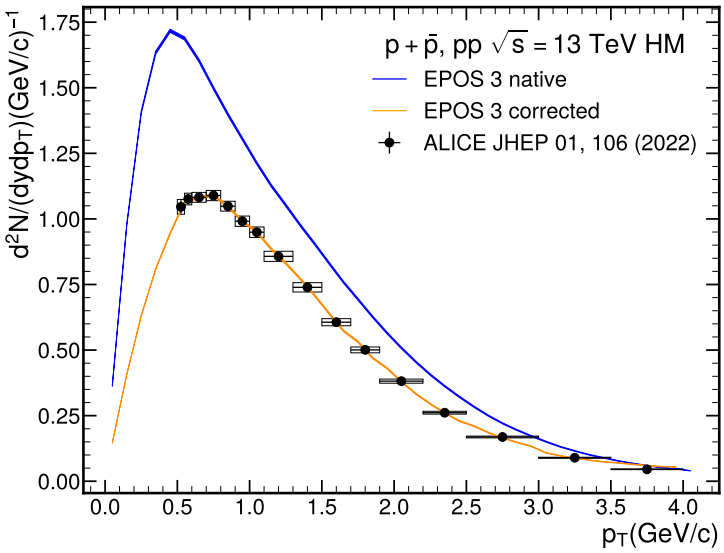

FIGURE 6.6: Proton spectra generated by EPOS 3, compared with the ALICE measurement [9]. Shown are the native p_{T} distribution (blue) and the corrected one (orange).

3 in $\sqrt{s} = 13$ TeV pp collisions. However, no qualitative difference between 7 and 13 TeV predictions is expected. It is clear that EPOS 3 cannot reproduce the measured angular correlation. While there is a significant depletion in the measured correlation function around $\varphi = 0$, the EPOS predictions show an increase in the correlation function in the same region. Furthermore, the region around $\Delta\varphi = \pi$ shows a significant increase in the correlation, while any correlation is absent in EPOS. This could be a sign of recoil jet quenching due to the hydrodynamic phase in EPOS. In Ref. [18], this data is compared to even more models, such as Pythia 6, Pythia 8, and PHOJET. All of these models fail to reproduce the depletion at low $\Delta\varphi$ but qualitatively reproduce the peak at $\Delta\varphi = \pi$. This hints at a fundamental issue in the hadronization procedure in EPOS. Correcting such a fundamental issue is beyond the scope of this work, and the angular correlations will not be corrected. A resolution to the problem will be given in Ch. 7.

6.4 The coalescence afterburner in EPOS

Following the successful calibration of all components of the event generator influencing nuclear formation via coalescence to experimental data, the coalescence afterburner is now introduced. The first step involves determining whether each event qualifies as a high-multiplicity event by counting the number of charged pions, kaons, and protons within the V0M region. Subsequently, a list of all potential proton-neutron pairs at mid rapidity ($|y| < 0.8$) is compiled, along with their corresponding mother particles, positions, and four-momenta. The looser rapidity cut is to remove edge effects where a deuteron could be created inside the acceptance from one nucleon slightly out of the $|y| < 0.5$ acceptance. Indeed, the rapidity of the deuteron is the average of the nucleon rapidities $y_d = (y_p + y_n)/2$. For each pair, the spatial separation is calculated and rescaled, and the relative momentum in the pair's rest frame is determined. These rescaled distances and relative momenta are then used to compute the coalescence probability, $\mathcal{P}(q, \sigma)$ (Eq. 3.1). Here, in order to preserve space-momentum correlations and also, importantly, the correlations between q and

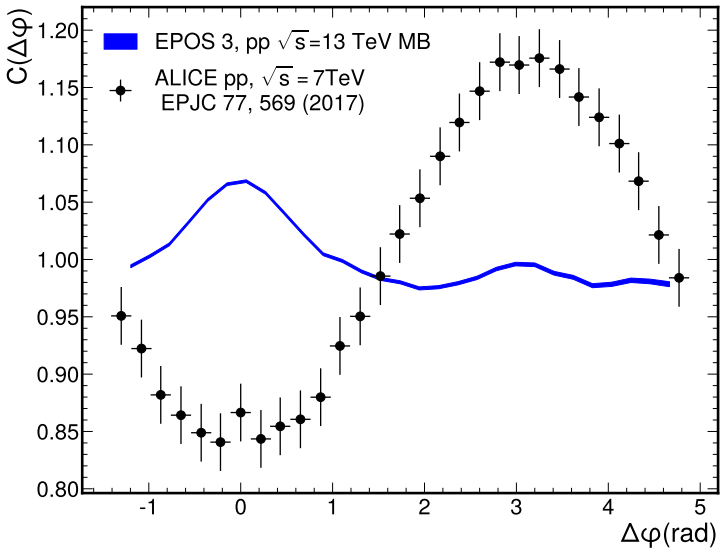

FIGURE 6.7: $\Delta\eta$-integrated $\Delta\varphi$ $pp \oplus \overline{pp}$ correlation function $C(\Delta\varphi)$ of (anti)proton pairs measured by ALICE (black points) [18] and predictions by EPOS 3 (blue band).

r, not the actual source size is used but $\sigma = r/(4/\sqrt{\pi})$ as previously motivated. A random number $r \in [0,1]$ is then drawn according to a uniform distribution, and if $r < \mathcal{P}$, the pair is accepted as a deuteron. Finally, the deuteron is added to a histogram, with the weights of its constituents and the weights of the mother resonances.

6.5 Results and implication for future studies

The results of the coalescence afterburner are obtained using four different wave functions: a single Gaussian, the Hulthén, Argonne v_{18} and N^{4}LO χEFT. Details of the wave functions can be found in Ch. 3.3. The expectation is that Argonne v_{18} and N^{4}LO χEFT perform the best since they are the most realistic description of the deuteron, reproducing modern scattering data with $\chi^2_{NDF} \sim 1$. The Gaussian is a very simplified ansatz, but its simplicity allows for a fully analytic calculation of the Wigner function and its formation probability. The Hulthén has been used in previous publications as an improved wave function and is included for comparability. Figure 6.8 shows the p_{T} spectra of deuterons obtained with this model and is compared to measurements by ALICE [9]. The global χ^2 per degree of freedom for each wave function is shown in Tab. 6.2. It is clear that both Argonne v_{18} and χEFT are able to reproduce the data within the uncertainties. On the other hand, both the Hulthén and the Gaussian wave functions fail by 30% and 50%, respectively. All wave functions show a similar trend with p_{T}; only the overall yield varies. Not shown in the plot, but included in the global χ^2 calculation is a p_{T}-independent systematic uncertainty of 6%. This systematic has two major sources. The first part was obtained by varying the target source size from the ALICE measurement by $\pm$7%, based on the uncertainties reported in [14]. The resulting systematic uncertainty was obtained from the relative deviation in the final spectra between the default source size and the varied one. The second source of systematic uncertainty is related to the fraction of primordial nucleons. Indeed, not all nucleons stem from resonance decays, but $\sim$ 35.4% of nucleons are directly produced in the collision. This value is obtained using ThermalFIST [84]. In order to estimate the systematic uncertainty,

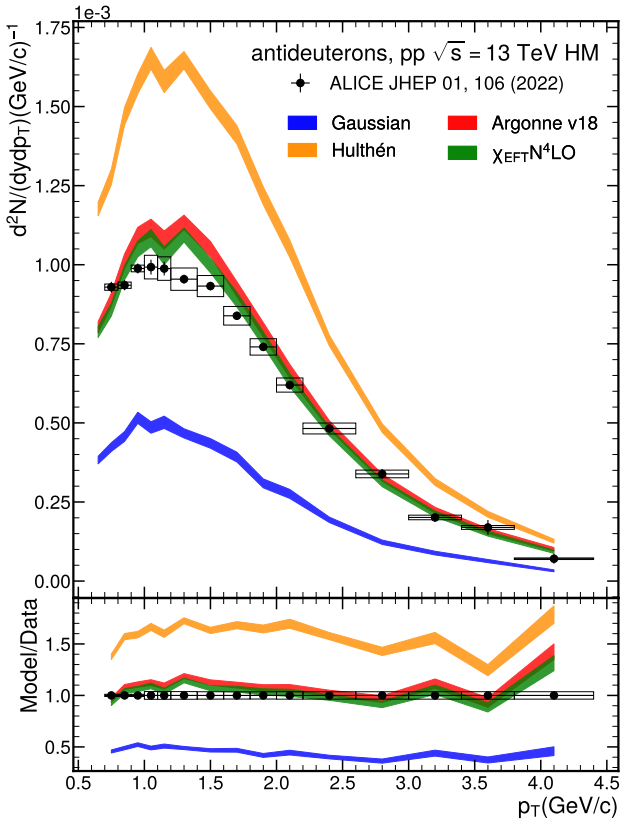

FIGURE 6.8: Deuteron transverse momentum spectra obtained from EPOS 3, applying the coalescence model with different hypotheses for the deuteron wave function, compared with the ALICE measurement [9]. The width of the bands represents the statistical uncertainty of the predictions. A global systematic uncertainty of 6% is not shown. In the bottom panel, the model to data ratio is shown.

the primordial fraction was varied by ±10%, and the amount stemming from resonances changed accordingly. The final systematic uncertainty is the quadratic sum of both relative deviations from the source and the primordial fraction.

In order to show the effect of the source modeling Fig. 6.9 shows the predictions for three different scenarios. The default prediction with the source modeling is shown in blue, as described above. In orange the prediction using the native source is shown. The scaled and the native source size are comparable around $\langle m_T \rangle$ =1.8 GeV/c^2, which corresponds to a deuteron-$p_T \sim$ 3.1 GeV/c. This explains why the native and the scaled prediction almost coincide for large p_T. However, at low p_T, where the discrepancy of the source is large, the predictions deviate by ∼50%. Shown in red is the prediction using a distance sampled from the measurement. This procedure destroys the correlations between q and r, as shown in Fig. 6.5. As a result, the overall yield of deuterons is reduced by ∼ 8%, but the yield for $p_T < 2$ GeV/c is even reduced by 13%. This outcome directly results from the reduced population in the phase space region relevant for coalescence caused by the breakdown of the correlation between q and r. Using the spectra of protons and deuterons shown in

Wave function	Argonne v_{18}	N^{4}LO χEFT	Hulthén	Gaussian
$\chi^2_{\text{n.d.f}}$	1.063	0.613	21.351	57.900

TABLE 6.2: Global $\chi^2_{\text{n.d.f}}$ of the deuteron predictions obtained with EPOS and compared to ALICE measurements [9] for four different wave functions. The calculation includes a global systematic uncertainty of 6%. All uncertainties are assumed to be fully correlated.

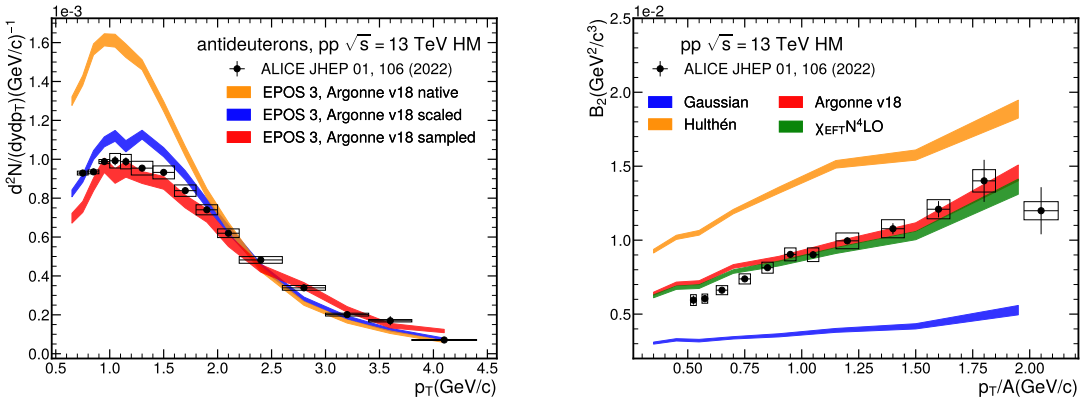

FIGURE 6.9: (left) Deuteron p_{T} spectra obtained with EPOS 3, with the source modeling (scaled), without (native) and sampled from the measurement, breaking the q-r correlations (sampled) for the same wave function hypothesis, i.e., Argonne v_{18}. Predictions are compared with the corresponding ALICE measurement [9]. (right) B_2 parameter obtained from EPOS 3 using four different wave functions, Gaussian, Hulthén, Argonne v_{18} and χEFT. Results are compared to the corresponding measurement by ALICE [9].

Figs. 6.6 and 6.8 it is possible to calculate the coalescence parameter B_2 (See Ch. 3)

$$B_2 = \left(\frac{1}{2\pi p_{\text{T}}^d}\frac{\mathrm{d}^2N_d}{\mathrm{d}y\mathrm{d}p_{\text{T}}^d}\right) \Big/ \left(\frac{1}{2\pi p_{\text{T}}^p}\frac{\mathrm{d}^2N_p}{\mathrm{d}y\mathrm{d}p_{\text{T}}^p}\right)^2. \tag{6.4}$$

Here, the superscripts d and p indicate deuterons and protons, respectively. Importantly, it is assumed that the transverse momentum of protons is half that of deuterons ($p_{\text{T}}^p = p_{\text{T}}^d/2$). The comparison between the B_2 obtained by ALICE [9] and by EPOS 3 are shown in Fig. 6.9. The Argonne v_{18} and χEFT wave function achieve the best compatibility with the measurement, while the Hulthén and Gaussian again fail to describe the data. The Gaussian underestimates the data by 50-70% while the Hulthén overestimates B_2 by 20-50%. This is a significant improvement to previous studies [9] where the Gaussian showed the best agreement with data (See Sec. 2.1.2, Fig. 2.7). The main difference between the work in Ref. [9] and this work is that the difference in momentum between nucleons ($\vec{q} = (\vec{p}_{\text{p}} - \vec{p}_{\text{n}})/2$) is neglected in the Wigner function of the p-n state ($f_1^W(\frac{\vec{p}_{\text{d}}}{2} \pm \vec{q}, \vec{R} \pm \frac{\vec{r}}{2}; t_f) \rightarrow f_1^W(\frac{\vec{p}_{\text{d}}}{2}, \vec{R} \pm \frac{\vec{r}}{2}; t_f)$. The authors of [12] state that such approximation, motivated by ease of computation, is valid to an accuracy of around 10% in Pb–Pb collisions while the accuracy in pp collisions is not estimated and could potentially be much larger.

Utilizing a general-purpose event generator, this study demonstrates that the coalescence model can successfully reproduce experimental data when appropriate parameters, such as the source size and wave function, are applied. The use of an event generator proves advantageous for such exploratory research, as it provides many of the essential

components needed to describe nuclear formation. These include the generation of nucleons on an event-by-event basis and the incorporation of their correlations. Furthermore, the event generator framework helps identify the critical elements required to accurately describe deuteron formation. However, this approach is not without its limitations. Not all relevant observables have been experimentally measured across different energies, multiplicities, and system sizes. In particular, the source size in small systems has only been measured m_{T}-differentially in high-multiplicity proton-proton (HM pp) collisions at $\sqrt{s} = 13$ TeV. As illustrated in Fig. 6.9, the shape of the m_{T}-scaling of r_0 exerts a significant influence on the resulting deuteron spectra. This emphasizes the necessity for further refinement of tools to study nuclear formation across a broader range of energies and multiplicities. To address these challenges, the ToMCCA model has been developed (see Ch.7).

6.6 Rapidity dependent coalescence

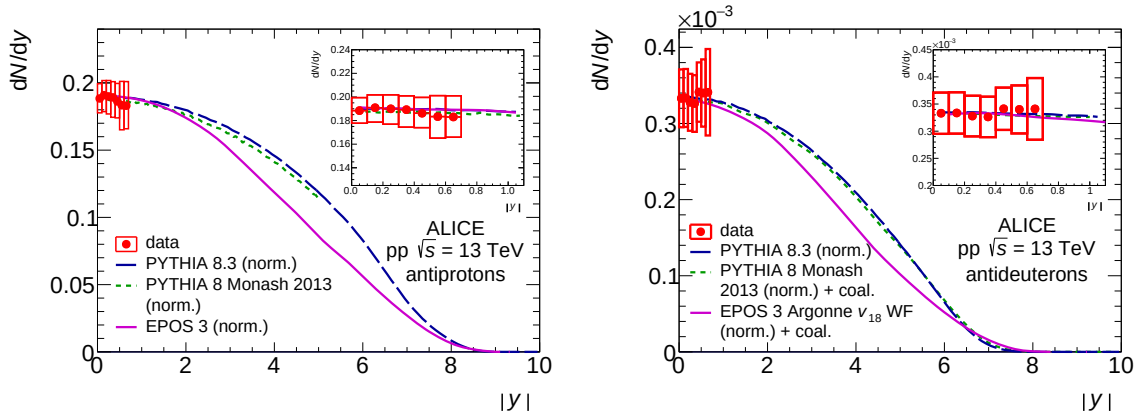

FIGURE 6.10: Integrated yields of antiprotons (left) and antideuterons (right) as a function of rapidity, compared with the corresponding predictions of three models (see text for details). Statistical and systematic uncertainties are represented by vertical bars and boxes, respectively. The statistical uncertainties are smaller than the size of the markers in the reported scale and, hence, not visible. In the insets of the figures, a zoom in the low-rapidity region is displayed. The integrated yields estimated by models are normalized to the measured ones.

While the previous results were obtained integrated over the mid-rapidity interval, studying the rapidity differential yields is also of interest for astroparticle physics. Indeed, since collisions between cosmic rays and the interstellar medium happen with a stationary target, the forward rapidity region could have a potentially strong influence on deuteron production. Previous measurements by the BRAHMS and STAR collaborations [105] have already shown that the expected rapidity dependence of the coalescence parameter B_2 should be small. Testing the coalescence model for this observation is thus critical if one wants to apply it to astrophysics. In this study, the ALICE detector was taken to the limits of its acceptance. Indeed, while typically, particle yields are determined in the rapidity range $|y| < 0.5$, in which the p_{T} acceptance is almost constant, the detector can, in principle, detect (anti)deuterons up to $|y| = 0.7$, with a limited acceptance in p_{T}. The measured antiproton and antideuteron yields are shown in Fig. 6.10 as the red circles. The measurement was performed for minimum bias pp collisions at $\sqrt{s} = 13$ TeV. The squares denote the systematic uncertainties, the statistical uncertainties are smaller than the symbols and thus not shown. Also shown are the predictions of the yields for Pythia 8.3 with default

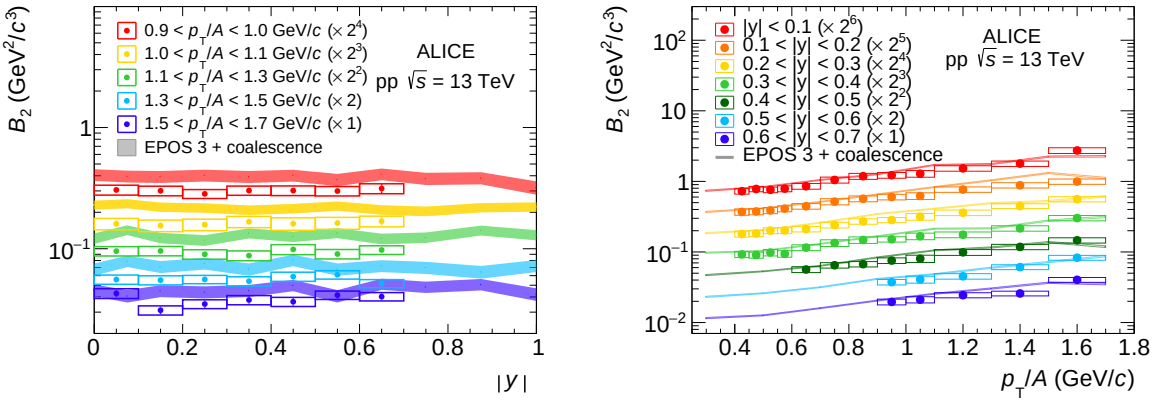

FIGURE 6.11: Coalescence parameter B_2 as a function of the transverse momentum per nucleon for different rapidity intervals (right) and as a function of rapidity for different p_T intervals (left). Data are compared to model predictions from a Wigner function formalism coalescence model used as an afterburner of EPOS 3 shown as colored lines. Statistical and systematic uncertainties on the data points are represented by vertical bars and boxes, respectively. The statistical uncertainties of the data points are smaller than the size of the markers in the reported scale and, hence, not shown.

tune and Monash 2023 tune[1] and for EPOS 3.117. All model predictions are normalized to |y|<0.1. The deuteron yield predictions are obtained using a coalescence model in the case of Pythia+Monash and EPOS 3, and using the Dal-Raklev [106] nuclear reaction model akin to the kinetic approach discussed in Sec. 2.1.2. The Coalescence model used in Pythia 8.3 Monash is a simple spherical approximation model with $\Delta p < 142.5$ MeV/c. In EPOS 3, the Wigner Function formalism was used, and for the source, a size of $r_0 = 1.18$ fm was used [107], with the same m_T scaling as observed in HM collisions. The source size was also taken to be independent of rapidity. Note that the absolute magnitude of the source is of limited importance since the yields are scaled to the measurement. A very interesting trend that can be observed in Fig. 6.10 is that EPOS consistently underproduces particles towards large rapidities. This is very likely due to the initial condition setting in EPOS, where for this production, the impact parameter was set to $b = 0$ fm, i.e., every pp collision simulated is a direct head-on collision. This could cause a large shadowing in the forward region. Figure 6.11 Coalescence parameter B_2 from the measurement compared to model predictions by EPOS. The left panel shows B_2 as a function of rapidity for different p_T-intervals. The right panel shows B_2 as a function of p_T per nucleon for different rapidity intervals. The data is shown as colored markers, the boxes indicate the systematic uncertainties. The statistical uncertainties are smaller than the marker and are thus not shown. The EPOS predictions are shown as bands, and the colors indicate the p_T- or $|y|$-interval. The different slices are scaled for visibility. As can be clearly seen, the trend of B_2 is flat as a function of rapidity in the data and in the EPOS predictions. EPOS seems to overestimate B_2, but since the results are all scaled to the data, this is likely a slight inaccuracy in the applied scaling. The behavior of B_2 as a function of p_T shows the enhancement towards larger p_T, already seen in the HM results in Fig. 6.9. EPOS captures this trend due to the m_T-scaling behavior of the source size. Overall, the coalescence model shows an excellent agreement with the data presented here.

[1]The Pythia predictions were obtained by Ramona Lea.

Chapter 7

The ToMCCA Event Generator

7.1 Goals of ToMCCA

The study described in Chapter 6 utilized the EPOS event generator to achieve a precision of approximately 5%. This required the simulation of about 300 million events, consuming on the order of 10^5–10^6 CPU hours. Extending such high-precision studies to cosmic ray physics, which would necessitate computations across tens to hundreds of collision energies, could demand thousands of CPU years. While high-performance computing clusters with up to 10^5 CPUs could potentially handle this workload, the resource requirements would be immense. To address this computational challenge and enable such studies on smaller infrastructures, such as local computer farms with 10^2–10^3 CPUs, the ToMCCA model was developed. Its target is to produce upwards of 1 million events per CPU minute, representing a speedup of approximately 10^5 compared to the EPOS study. ToMCCA, short for **To**y **M**onte **C**arlo **C**oalescence **A**fterburner, is a lightweight, high-performance tool designed specifically for coalescence predictions. One promising application of ToMCCA is in predicting antideuteron yields over the entire energy range of interest for cosmic rays (< TeV). These predictions can then be integrated into cosmic ray propagation software such as GALPROP [108], enabling estimates of antideuteron fluxes in cosmic rays [4]. This capability opens new possibilities for exploring cosmic ray physics with unprecedented precision. A key limitation of ToMCCA, however, lies in its dependence on experimental measurements for input. In regions lacking data, extrapolation or interpolation is required, potentially introducing biases. In contrast, models like EPOS are rooted in pQCD-based calculations, offering greater robustness when extrapolating into unmeasured regions. That said, ToMCCA provides tremendous speed advantages and offers flexibility—its parameterized inputs can be easily adjusted as new data becomes available or improved extrapolation methods are developed. The power and utility of ToMCCA are demonstrated throughout this chapter. This combination of speed, flexibility, and applicability to cosmic ray studies highlights its potential as a transformative tool for advancing our understanding of coalescence phenomena. In a previous study [50], the authors used the event generator EPOS-LHC, a lightweight version of EPOS, to generate 25 trillion proton-proton collisions utilizing 5000 CPU hours. Here, statistical accuracies of a few percent were reached for the whole energy range. However, this study was limited by the use of the spherical approximation as a coalescence model, which introduced uncertainties upwards of 30% because of the uncertainty of the free parameter p_0. In the case of ToMCCA, the Wigner Function formalism introduced in Ch. 3, is used which has been shown to reproduce deuteron spectra without any free parameter (see Ch. 6). In this chapter, first, the exact procedure with which ToMCCA generates nuclei spectra predictions will be discussed (Sec. 7.2), including then the necessary parameterizations, which are obtained in a data-driven method. In Sec. 7.3, the resulting deuteron spectra and in Sec. 7.4, the extension and results for A=3 nuclei will be discussed.

7.2 ToMCCA event loop

The event loop is the most characteristic difference between ToMCCA and a full-fledged Monte-Carlo event generator. It relies purely on parameterizations and only generates components that are strictly necessary for coalescence predictions. These components are the yields of nucleons, their full 3-dimensional momentum distributions, also relative to each other, the charged particle multiplicity, and the source size. First, the number of protons and neutrons in the event is determined. Then, for the first proton, its three-dimensional momentum is sampled and subsequently for all neutrons *relative* to this proton. Lastly, the source size for each pair is determined and the coalescence condition (Eq. 3.1) is evaluated. If any pair gets accepted, both nucleons are removed from the candidates, and a deuteron is counted with its 4-momentum, the sum of both nucleons' 4-momenta. Then, for the next proton, its full kinematics is determined, and subsequently, for all remaining neutrons, a new three-dimensional momentum is assigned, again relative to the now-checked proton.

Importantly, two different approaches to ToMCCA will be discussed: a very simple tune called *Default*, which only contains the bare minimum parameterizations, and the *Advanced* one, which contains more intricate mechanisms, more advanced parameterizations and more input from general-purpose event generators.

7.2.1 Charged particle multiplicity

The starting point of every ToMCCA event is the charged particle multiplicity of the event. This number is usually given as the pseudorapidity density $\langle \mathrm{d}N_{\mathrm{ch}}/\mathrm{d}\eta \rangle$, in collider experiments, usually at mid-rapidity $|\eta| < 0.5$. However, in ALICE, particle spectra are usually measured as rapidity densities $\mathrm{d}N/\mathrm{d}p_{\mathrm{T}}\mathrm{d}y$ with $|y| < 0.5$. In order to transform between the two, a scaling constant α is introduced such that $\alpha \langle \mathrm{d}N_{\mathrm{ch}}/\mathrm{d}\eta \rangle_{|\eta|<0.5} = \langle \mathrm{d}N_{\mathrm{ch}}/\mathrm{d}y \rangle_{|y|<0.5}$. Using the EPOS event generator, a value of $\alpha = 1.192$ is found.
For a given $\langle \mathrm{d}N_{\mathrm{ch}}/\mathrm{d}\eta \rangle$, the distribution can be shaped in several different ways. The simplest approach would be to let all events have $N_{\mathrm{ch}} = \langle \mathrm{d}N_{\mathrm{ch}}/\mathrm{d}\eta \rangle$. However, coalescence is a non-linear process, which means it is sensitive to higher orders of the multiplicity distribution. Indeed, an event with $N_{\mathrm{ch}} = 20$ would contribute 4 times as many deuteron candidates as an event with $N_{\mathrm{ch}} = 10$ charged particles. A simple solution would be to use a Poissonian

$$P(N;\lambda) = \frac{\lambda^N \exp(-\lambda)}{N!}, \tag{7.1}$$

which has a mean and a variance of λ. However, this produces rather narrow distributions, especially for higher multiplicities. A better description can be found using an Erlang distribution [109]

$$f(N;k,\lambda) = \frac{\lambda^k N^{k-1} \exp(-\lambda N)}{(k-1)!}, \tag{7.2}$$

which has a mean of k/λ and variance k/λ^2. While this function is technically only defined for $k \in \mathbb{N}^+$, it can be extended to $k \in \mathbb{R}_{\geq 1}$ without introducing any poles by generalizing the factorial to the Γ function using $\Gamma(x) = (x-1)!$. The rate parameter λ is well defined for $\lambda > 0$. This function can be interpreted as the sum of k independent, exponential emitters with rate λ and mean $1/\lambda$. In our case, k is not an integer, so this direct physical interpretation no longer holds, but k is rising as a function of N_{ch}, so the general trend is still valid. The two parameters k and λ were obtained depending on N_{ch} from EPOS 3. Similarly to Sec. 6.2.1, multiplicities were obtained by triggering in the far forward and backward rapidity regions ($-3.7 < \eta < -1.7$ and $2.8 < \eta < 5.1$) and obtaining the resulting multiplicity

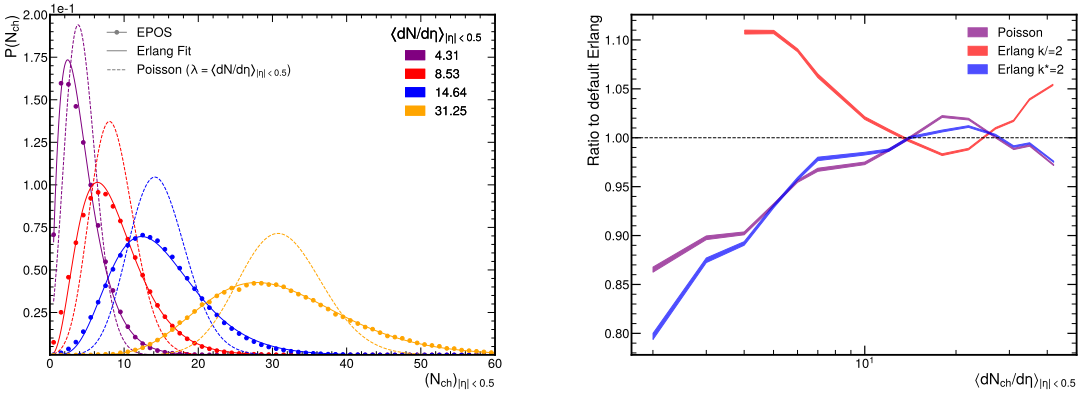

FIGURE 7.1: (left) Selected EPOS mid-rapidity ($|\eta| < 0.5$) charged particle multiplicity distributions (colored markers) obtained by triggering in the forward/backward region ($-3.7 < \eta < 1-7$ and $2.8\eta < 5.1$). The solid lines represent the results of the Erlang function parameterization included in ToMCCA. The dashed lines represent a Poissoninan distribution with a mean $\lambda = \langle \mathrm{d}N_{\mathrm{ch}}/\mathrm{d}\eta \rangle_{|\eta|<0.5}$. The $\langle \mathrm{d}N_{\mathrm{ch}}/\mathrm{d}\eta \rangle_{|\eta|<0.5}$ for all cases is indicated by the color. (right) Ratio of the deuteron yield obtained from using different multiplicity distributions compared to the Default Erlang function parameterization. The purple line shows the ratio using a Poissonian, as indicated on the left. The blue (red) curve shows the effect of doubling (halving) the k parameter in the parameterization. To counteract the change in the resulting $\langle \mathrm{d}N_{\mathrm{ch}}/\mathrm{d}\eta \rangle_{|\eta|<0.5}$, the λ parameter was halved (doubled) accordingly. The red curve is only defined for $\langle \mathrm{d}N_{\mathrm{ch}}/\mathrm{d}\eta \rangle_{|\eta|<0.5} > 4$, since for smaller values of multiplicity the k parameter would be < 1, and would thus lead to undefined behavior.

distribution at mid-rapidity. This was done in slices of 10% as well as for 0-1%. The resulting distributions are insensitive to the width of the triggering percentile. These distributions were then fitted using Erlang distributions. Figure 7.1 (left) shows selected EPOS distributions with their respective Erlang fits alongside the corresponding Poissonian distribution.

The Erlang distributions show an excellent agreement with the simulations, while the Poissonian description becomes worse for larger multiplicities, underestimating the width of the distribution. The behavior of the parameters k and λ as a function can be described by power laws of the form $a\, N_{\mathrm{ch}}^{b}$. Since $\langle \mathrm{d}N_{\mathrm{ch}}/\mathrm{d}\eta \rangle_{|\eta|<0.5} = k/\lambda$, only one needs to be parameterized, and the parameters can be found in Tab. 7.1. Both are shown for completeness and as a cross-check $k/\lambda = 1.067\langle \mathrm{d}N_{\mathrm{ch}}/\mathrm{d}\eta \rangle^{0.98}_{|\eta|<0.5}$, which is very close to the desired $k/\lambda = \langle \mathrm{d}N_{\mathrm{ch}}/\mathrm{d}\eta \rangle_{|\eta|<0.5}$. The functional shapes of the parameterization as well as the values obtained from EPOS are shown in Fig. 7.2. Clearly visible is the boundary condition $k > 1$ as long as $\langle \mathrm{d}N_{\mathrm{ch}}/\mathrm{d}\eta \rangle_{|\eta|<0.5} \geq 1$. For the subsequent results $\lambda = k/\langle \mathrm{d}N_{\mathrm{ch}}/\mathrm{d}\eta \rangle_{|\eta|<0.5}$ is chosen.

parameter	a	b
k	0.77544	0.74669
λ	0.72653	-0.23343

TABLE 7.1: Parameters used in the power law description of the k and λ parameter as a function of $\langle \mathrm{d}N_{\mathrm{ch}}/\mathrm{d}\eta \rangle_{|\eta|<0.5}$.

Figure 7.1(right) shows the effect of different multiplicity distribution shapes on the

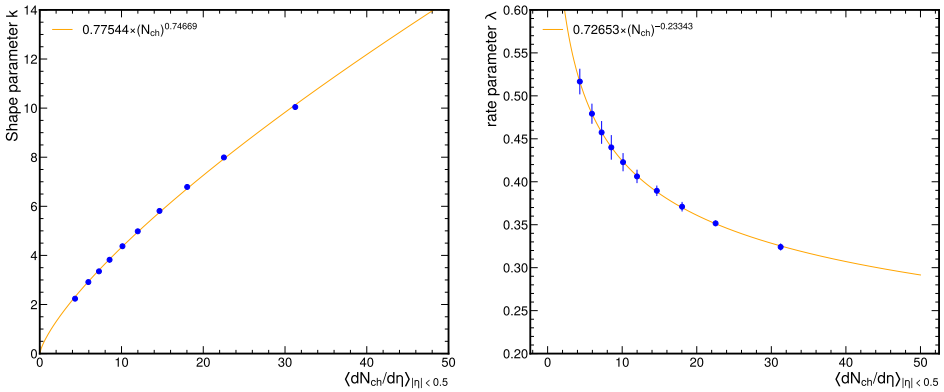

FIGURE 7.2: Change of the obtained shape parameter k (left) and rate parameter λ (right) as a function of $\langle \mathrm{d}N_{\mathrm{ch}}/\mathrm{d}\eta \rangle_{|\eta|<0.5}$. Both are fitted using a power law function, with the parameters shown in the legend. Since $\langle \mathrm{d}N_{\mathrm{ch}}/\mathrm{d}\eta \rangle_{|\eta|<0.5} = k/\lambda$, only the parameterization of k is used in ToMCCA, and λ is derived from the value of k.

deuteron yield as a function of $\langle \mathrm{d}N_{\mathrm{ch}}/\mathrm{d}\eta \rangle_{|\eta|<0.5}$ compared to the default description using an Erlang distribution. The purple line shows the yield ratio when using a Poisson distribution. For small multiplicities ($\langle \mathrm{d}N_{\mathrm{ch}}/\mathrm{d}\eta \rangle_{|\eta|<0.5}$ <10), the limited width of the Poissonian reduces the yield by up to 15%. In intermediate multiplicity events, the effect is minimal. The blue and the red lines show the effect of doubling or halving the k parameter, respectively. In order to conserve the correct multiplicity, λ is changed accordingly. Increasing(reducing) λ(and thus reducing(increasing) k) has the effect of widening(narrowing) the distribution. The effect is very pronounced at lower multiplicities, while for larger multiplicities, they roughly reproduce the same yield as the default configuration. The red line starts only at $\langle \mathrm{d}N_{\mathrm{ch}}/\mathrm{d}\eta \rangle_{|\eta|<0.5}$ =4 instead of 2, since for smaller multiplicities, the value for k<1 and thus the Erlang distribution is no longer well defined. Overall, the effect is that wider distributions lead to larger yields, and the effect is much more pronounced at low multiplicities. The most extreme effect is observed when compared to minimum bias (MB) data.

7.2.2 Particle production mechanism

Once the number of charged particles N_{ch} in an event is determined, the chemical composition of the event needs to be found. While the exact composition, including particles such as pions and Kaons, is not important, the number of (anti)protons and (anti)neutrons and their relation to each other is. Note that, as of now, antimatter is not implemented in ToMCCA since, at the LHC, one measures an equal amount of matter and antimatter. Currently, there are four different methods implemented in order to determine the number of nucleons in each event from N_{ch}, Uncorrelated Emission (UE), String Fragmentation (SF), Quark Recombination (QR), and Tuned Emission (TE). All predictions in Sec. 7.3 and beyond are obtained using TE unless denoted otherwise.

Uncorrelated emission

UE is the most simplistic approach to particle production. In this method, for every charged particle created, there is a probability for it to be a proton given by

$$p_{\text{prot}} = (\mathrm{d}N_p/\mathrm{d}y)/\langle \mathrm{d}N_{\text{ch}}/\mathrm{d}y\rangle_{|y|<0.5}, \tag{7.3}$$

where $\mathrm{d}N_p/\mathrm{d}y$ is the production *yield* of protons and $\langle \mathrm{d}N_{\text{ch}}/\mathrm{d}y\rangle_{|y|<0.5}$ is the average number of charged particles created at mid-rapidity ($|y| < 0.5$). The yield of protons is anchored to measured spectra and will be discussed in Sec. 7.2.3. Thus, a simple loop over all charged particles in the event is performed, and for each, this probability is evaluated, and the number of successful protons is counted. A mirroring technique is utilized for neutrons, where N_{ch} neutral particles are created, and with an equal probability, the number of neutrons is determined. As of now, ToMCCA assumes perfect isospin symmetry, as no evidence of its breaking has been observed at the LHC. Adding in an isospin-breaking term would be trivial in this production method

$$p_{\text{neut}} = p_{\text{prot}}(1 + \Delta_{\text{IS}}) \tag{7.4}$$

where Δ_{IS} is the isospin enhancement factor defined in ref. [95] as

$$\Delta_{\text{IS}} = \frac{N_{\text{neut}}}{N_{\text{prot}}} - 1. \tag{7.5}$$

At lower energies than then LHC, evidence of isospin breaking has been found by NA49 [110] by comparing pp with pn scattering data with a value of $\Delta_{\text{IS}} = 0.13 \pm 0.10$ when assuming fully correlated systematic uncertainties and $\Delta_{\text{IS}} = 0.37 \pm 0.06$ when fully uncorrelated [95]. At the LHC, the best measurements of the $p/\overline{p}$ ratio performed by ALICE gave a value of $\Delta_{\text{IS}} < 0.06$ [95]. The Uncorrelated Emission method produces no correlation between the number of protons and neutrons in the event, i.e., they fluctuate fully independently. This can be quantified by measuring the Pearson correlation coefficient ρ_{pn} discussed in Sec. 7.2.2,

String fragmentation

The second method implemented in ToMCCA is called String Fragmentation. It mimics the much more complex hadronization methods used in general-purpose event generators such as Pythia or EPOS. While in those models, multiple strings are created, which have their own intrinsic momenta, which get inherited by the particles created from the string, in ToMCCA, only one string is created, and it is used for the sole purpose of providing a number of nucleons. This string starts out with either a u or d quark on one end and its antimatter counterpart at the other end. The number of fragmentation points equals the number of charged particles N_{ch} in the event. At each fragmentation point, a quark-antiquark (q–$\overline{\text{q}}$) or diquark-antidiquark (uu–$\overline{\text{uu}}$,ud–$\overline{\text{ud}}$,dd–$\overline{\text{dd}}$) is placed, and ordered such that each fragment is a color neutral particle, either in q$\overline{\text{q}}$ or qqq($\overline{\text{qqq}}$) configuration. In order to avoid tetraquark configurations at the fragmentation point directly after a diquark, no other diquark pair can be created. After each fragment has been created, all Baryonic fragmentation points are assigned their respective nucleon. The combination uuu(ddd) corresponding to the $\Delta^{++}(\Delta^0)$ resonance is assigned to be a proton(neutron) since it decays exclusively into the assigned nucleon. Mesons that would be created at the other fragmentation points are ignored for simplicity. Figure 7.3 shows an example of a string with an initial d–$\overline{\text{d}}$ configuration fragmenting into 6 particles. In this method, the total nucleon yields are driven by the probability of creating a diquark at a fragmentation point. For a very long string with many

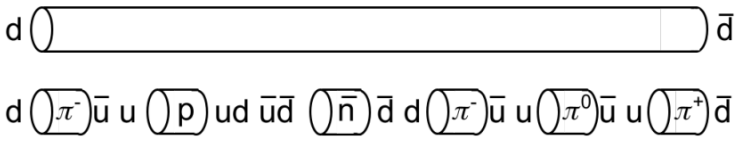

FIGURE 7.3: An example of a string with an initial d–$\bar{\text{d}}$ configuration fragmenting into 6 particles. Pions are indicated for clarity but are ignored in ToMCCA.

fragmentation points, the diquark probability p_{diquark} approaches $\approx 2 \cdot p_{\text{prot}}$ as introduced above. The factor 2 arises from the fact that protons and neutrons are being created alongside each other and not only charged particles. Due to the fact that edges cannot be diquarks and blocking of neighboring fragmentation points, this probability needs to be modified as a function of the charged particle multiplicity

$$p_{\text{diquark}}(\mathrm{d}N_p/\mathrm{d}y = p_{\text{prot,modified}}(\mathrm{d}N_p/\mathrm{d}y) = p_{\text{prot}}(\mathrm{d}N_p/\mathrm{d}y) \cdot (A + B(\langle \mathrm{d}N_{\text{ch}}/\mathrm{d}\eta \rangle_{|\eta|<0.5})^C). \tag{7.6}$$

The parameters A, B, and C can be found in Tab. 7.2 and as expected, $A = 2.13957998 \approx 2$. With this model, a potential isospin asymmetry can be introduced by giving dd-$\bar{\text{d}}\bar{\text{d}}$ diquark pairs an increased probability. However, such an inclusion is not straightforward and would have to be again parameterized as a function of multiplicity. This model also quite naturally includes antimatter, but Δ_{IS} has no effect on the $p/\overline{p}$ ratio even though $\Delta_{IS} > 0$ should lead to $p/\overline{p}$>1.

Quark recombination

The Quark Recombination model is loosely based on a Quark-Gluon-Plasma (QGP), and it is modeled by a sea of u and d quarks, which get recombined at random into Mesons and Baryons. The total number of each species is $N_{\text{d}} = N_{\text{u}} = \mathrm{d}N_{\text{ch}}/\mathrm{d}y$. First, a u and a d quark are combined randomly, and then, with probability $p_{\text{prot,modified}}$ given by Eq. 7.6, a third quark is added from the pool to create a Baryon. The parameters can be found in Tab. 7.2 under Quark Recombination. This is repeated until no quarks are left. This model does not include antiquarks, but adding them could trivially add antimatter to the model. Also, by modifying the initial u/d ratio an isospin asymmetry can be introduced, which can also be extended to antimatter via u/d=$\bar{\text{d}}/\bar{\text{u}}$.

Parameter	String Fragmentation	Quark Recombination
A	2.13957998	0.87627309
B	-3.8557517	1.01566945
C	-2.0928103	-0.54537776

TABLE 7.2: Fit parameters of Eq. 7.6 for the modification of the diquark probability (String Fragmentation) and quark adding probability (Quark Recombination) as a function of mean charged particle multiplicity $\langle \mathrm{d}N_{\text{ch}}/\mathrm{d}\eta \rangle_{|\eta|<0.5}$.

Tuned emission

While the Uncorrelated Emission provides no correlation between protons and neutrons, String Fragmentation and Quark Recombination lead to a strong but fixed anticorrelation that is also constant as a function of multiplicity. In order to provide more flexibility to

tune this anticorrelation, the Tuned Emission method is developed, which functions similarly to the Uncorrelated Emission but includes a suppression parameter a_S, which modifies the neutron probability depending on the number of protons in the event. It is defined as follows

$$p_{\text{neut,tuned}} = (a_S(\mathrm{d}N_\mathrm{p}/\mathrm{d}y - N_\mathrm{p}) + 1)p_{\text{prot}}. \tag{7.7}$$

It assigns a degree of suppression depending on the expected number of protons $\mathrm{d}N_\mathrm{p}/\mathrm{d}y$ compared to the number of existing protons N_p. The value of a_s is a free parameter and, as of now, is not constrainable to data. At this point, it is chosen such that ρ_{pn} is roughly in the middle of Uncorrelated Emission and String Fragmentation (see Tab. 7.3) that is also constant as a function of multiplicity. This is achieved by defining $a_S = 1.508(\mathrm{d}N_{\text{ch}}/\mathrm{d}y)^{-1}$ where $\mathrm{d}N_{\text{ch}}/\mathrm{d}y$ is the number of charged particles in a given event. A better parameterization can be found once the measurement of ρ_{pd} [39] is extended to pp collisions. The effect of this suppression is significant at low multiplicities where the difference in deuteron yields between Uncorrelated Emission and String Fragmentation for the same source size is about 200% for $\langle \mathrm{d}N_{\text{ch}}/\mathrm{d}\eta \rangle_{|\eta|<0.5} \sim 3$, but only $\sim 10\%$ for $\langle \mathrm{d}N_{\text{ch}}/\mathrm{d}\eta \rangle_{|\eta|<0.5} \sim 30$.

The ρ_{pn} coefficient

The main difference between all production mechanisms is that they give a different degree of anticorrelation between protons and neutrons. This can be quantified by measuring the Pearson correlation coefficient ρ_{pn} between the proton and neutron numbers

$$\rho_{\text{pn}} = \frac{\langle (n_p - \langle n_p \rangle)(n_n - \langle n_n \rangle) \rangle}{\sqrt{\kappa_{2p}\kappa_{2n}}}, \tag{7.8}$$

where $\kappa_{2a} = \langle (n_a - \langle n_a \rangle)^2 \rangle$ is the second-order cumulant and $\langle n_a \rangle$ is the mean of the multiplicity distribution of particle species a. The value of ρ_{pn} can be between 1 and -1. $\rho_{\text{pn}} = 1$ means, in our case, that for each proton added, also a neutron gets added, while $\rho_{\text{pn}} = -1$ means that each proton added removes one neutron. There are no measurements of this quantity at LHC energies due to the difficulty of measuring neutrons, but measurements of ρ_{pd} [19] in Pb–Pb collisions show a slightly negative value. This is expected due to Baryon number conservation since adding one Baryon requires the addition of an antibaryon, but also, the Coalescence mechanism indicates a negative correlation between protons and deuterons since forming a deuteron removes a proton. So, it is difficult to disentangle which process is the driving factor for the measured negative values. Ref. [39] showed that the canonical SHM can explain the data but not the coalescence models. However, the tested coalescence models did not include any anticorrelation between N_p and N_n. Instead, the two tested scenarios had $\rho_{\text{pn}} = 0$ and > 0. Figure 7.4 shows ρ_{pd} using the ToMCCA model with various degrees of anticorrelation and equal source size. The results are compared to mea-

	Unc. Em.	String Fragm.	Quark Rec.	Tuned Em.
ρ_{pn}	0	-0.052	-0.058	-0.024

TABLE 7.3: The Pearson correlation coefficient ρ_{pn} for protons and neutrons obtained from the four different particle production mechanisms. They range from no correlation (ρ_{pn}=0) for Uncorrelated Emission to slight anticorrelation ($\rho_{\text{pn}} = -0.058$) for Quark Recombination.

surements [39] performed in Pb–Pb collisions at $\sqrt{s_{\text{NN}}}$ = 5.02 TeV. From the tested scenarios, it seems that Tuned Emission is the best description of the data. However, a different tuning of the source could lead to comparable results from the other mechanisms. Further, the data is obtained in Pb–Pb collisions instead of pp collisions, which makes a direct comparison not

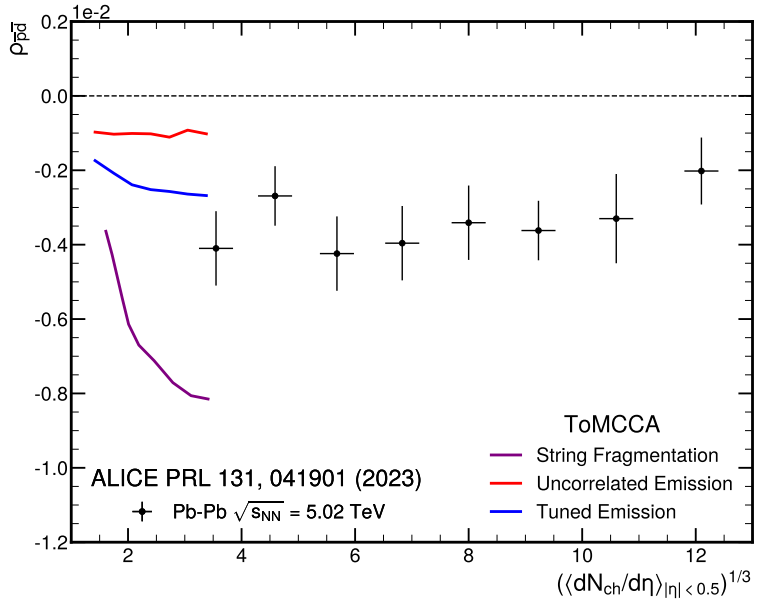

FIGURE 7.4: Pearson correlation coefficient ρ_{pd} for protons and deuterons as a function of the cubic root of the charged-particle multiplicity $\langle dN_{ch}/d\eta \rangle_{|\eta|<0.5}$, predicted by ToMCCA with the three different particle production mechanisms. The results are compared to the ALICE measurement in Pb–Pb collisions [19].

feasible. The values of ρ_{pn} obtained by utilizing the different methods are shown in Tab. 7.3. They range from $\rho_{pn} = 0$ for Uncorrelated Emission to slight anticorrelation $\rho_{pn} = -0.058$ in the case of Quark Recombination. It should be noted that for String Fragmentation and Quark Recombination, the deuteron spectra at low multiplicity cannot be reproduced since even when setting the source size to $\sigma = 0$ fm, the total yield is still underestimated. From this, one can conclude that these methods provide a too strong suppression and that the real value of ρ_{pn} should lie between 0 and -0.052.

7.2.3 Kinematics

Once the number of nucleons is calculated, their kinematics have to be determined. The three-dimensional momenta are calculated from p_T distributions and angular correlations.

Nucleon momentum distributions

In ToMCCA, the nucleon distributions are described using Levy-Tsallis functions (Eq.6.2), as they have been shown to reproduce measured spectra over a wide range of energies (see Ch. 5). However, even at a fixed energy, the shape of the spectra changes with the multiplicity of the event. For this reason, the spectral shape needs to be parameterized as a function of $\langle dN_{ch}/d\eta \rangle_{|\eta|<0.5}$. In ToMCCA, this was achieved by fitting the proton spectra measured by ALICE in pp collisions at $\sqrt{s}$ = 5 TeV and 13 TeV with a High Multiplicity trigger. This way, the multiplicity region from $\langle dN_{ch}/d\eta \rangle_{|\eta|<0.5}$ =2.4 – 35.8 is covered. The spectra have been fitted with a Levy-Tsallis function, and the evolution of the parameters dN/dy, n and C with the event multiplicity is shown in Fig. 7.5. Their evolution with the

multiplicity is parameterized using a power law function

$$f(\langle \mathrm{d}N_{\mathrm{ch}}/\mathrm{d}\eta \rangle_{|\eta|<0.5}) = A + B(\langle \mathrm{d}N_{\mathrm{ch}}/\mathrm{d}\eta \rangle_{|\eta|<0.5})^{C}. \tag{7.9}$$

The parameters are shown in Tab. 7.4. Due to the high correlation between the parameters n and C, the former was fixed to this functional form. As expected, the absolute yield

	$\mathrm{d}N/\mathrm{d}y$	n	C	C^{QR}_{mod}	C^{SF}_{mod}
A	–	7.323	–	0.9953433	0.9947258
B	0.05199	2.086	0.11693	-0.7380489	-4.341114
C	1.00246	-1	0.36305	-2.0069334	-4.555843

TABLE 7.4: Values of the parameterization of the Levy-Tsallis fits to the proton p_{T} spectra and the modification for Quark Recombination and String Fragmentation.

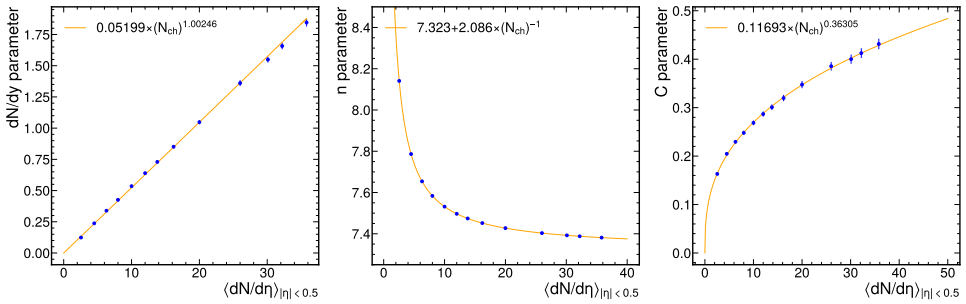

FIGURE 7.5: Levy-Tsallis fit parameters to ALICE proton p_{T} spectra at $\sqrt{s} = 5$ TeV and 13 TeV as a function of $\langle \mathrm{d}N_{\mathrm{ch}}/\mathrm{d}\eta \rangle_{|\eta|<0.5}$. Due to the high correlation between n and C, the former was fixed to the shown functional form.

parameter $\mathrm{d}N/\mathrm{d}y$ behaves linearly with $\langle \mathrm{d}N_{\mathrm{ch}}/\mathrm{d}\eta \rangle_{|\eta|<0.5}$, with an exponent of $1.00246 \approx 1$. Furthermore, depending on the particle production model, the C parameter needs to be modified to counteract edge effects, similar to the nucleon probability. For this, C gets modified as

$$C_{\mathrm{mod}}(\langle \mathrm{d}N_{\mathrm{ch}}/\mathrm{d}\eta \rangle_{|\eta|<0.5}) = C(\langle \mathrm{d}N_{\mathrm{ch}}/\mathrm{d}\eta \rangle_{|\eta|<0.5}) \cdot (A + B(\langle \mathrm{d}N_{\mathrm{ch}}/\mathrm{d}\eta \rangle_{|\eta|<0.5})^{C}). \tag{7.10}$$

The parameters can also be found in Tab. 7.4. Since in the modification term $A \approx 1$ and $C < 0$, this correction only applies to low multiplicity events, with the modification being less than 3% for $\langle \mathrm{d}N_{\mathrm{ch}}/\mathrm{d}\eta \rangle_{|\eta|<0.5} = 6$ for both production models. In addition to p_{T}, the rapidity y is drawn from a flat distribution $y \in [-0.5, 0.5]$. This is well motivated by the rapidity distributions of nucleons and nuclei at the LHC (Fig. 6.10). The resulting proton spectra are shown in Fig. 7.6.

Angular correlations

From the p_{T} and y, one can reconstruct a full three-dimensional momentum if one assumes a random azimuthal angle φ. While this works for single particles, in this work, we are interested in two-particle correlations. Thus, instead of drawing a random azimuthal angle, one needs to determine a relative angle between particles. This can be done by utilizing the

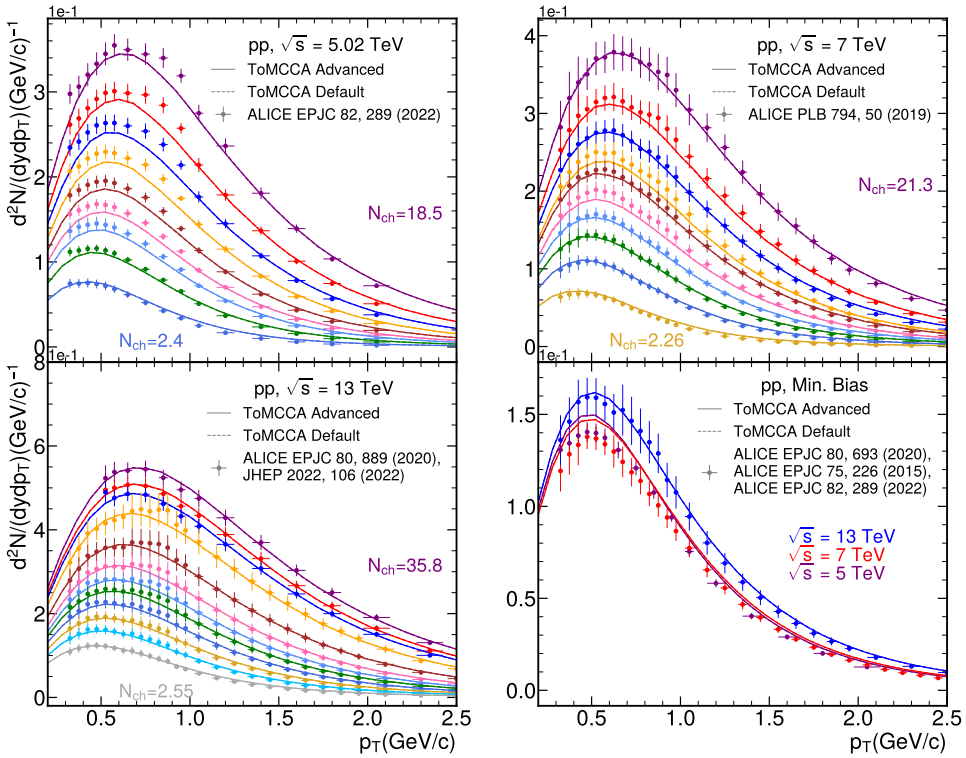

FIGURE 7.6: Proton spectra measured by ALICE in pp collisions at $\sqrt{s}$ = 5, 7, and 13 TeV together with the comparison to ToMCCA obtained after the parameterization. The fit was performed to 5 TeV and 13 TeV HM, while 7 TeV, 13 TeV, and the Minimum Bias spectra were used as a cross-check. The Default tune is mostly hidden since the two ToMCCA tunes produce almost exactly the same output.

angular correlation, which experimentally is defined as [111]

$$C(\Delta\varphi) = \frac{S(\Delta\varphi)}{B(\Delta\varphi)}, \tag{7.11}$$

where $S(\Delta\varphi)$ is the same event $\Delta\varphi$ distribution, i.e. the angular distribution of the azimuthal angle between two particles in the same event. Conversely, $B(\Delta\varphi)$ is the $\Delta\varphi$ distribution of pairs from different events. The latter removes trivial correlations from the same event distribution and reduces it to the genuine correlation. Since, in most cases, the correlation function is more interesting than the same or mixed event distribution, only $C(\Delta\varphi)$ is usually published. However, in ToMCCA, one needs the true $\Delta\varphi$ distribution between two particles in the same event, which means $S(\Delta\varphi)$ needs to be recovered. This is done by inverting Eq. 7.11 to $S(\Delta\varphi) = C(\Delta\varphi) \cdot B(\Delta\varphi)$, taking $C(\Delta\varphi)$ and obtaining $B(\Delta\varphi)$ from an event generator. While generally, event generators cannot reproduce the $\Delta\varphi$ distribution for two particles (See Fig. 6.7), the mixed event distribution only contains trivial correlations from kinematics, collision geometry, and energy conservation, which should be well reproduced by event generators. For ToMCCA, $B(\Delta\varphi)$ is obtained from EPOS 3 and is assumed to be independent of event multiplicity. $C(\Delta\varphi)$ has been measured by ALICE [111] as a function of event multiplicity for $pp \oplus \overline{pp}$ pairs. This is the first point where the Default and Advanced

Tune differ: Default uses only an average value of the angular correlations, taken from the 20-40% multiplicity, while the Advanced Tune has a full parameterization of the angular correlations as a function of multiplicity. The effect of this is small and only changes the final deuteron spectra within a few percent. The same event distribution can then be obtained from the following function

$$S(\Delta\varphi) = \underbrace{(N_0(\langle \mathrm{d}N_{\mathrm{ch}}/\mathrm{d}\eta\rangle_{|\eta|<0.5})\sin(\Delta\varphi - \pi/2) + c(\langle \mathrm{d}N_{\mathrm{ch}}/\mathrm{d}\eta\rangle_{|\eta|<0.5}))}_{C(\Delta\varphi,\langle \mathrm{d}N_{\mathrm{ch}}/\mathrm{d}\eta\rangle_{|\eta|<0.5})} \times \underbrace{(N_1|\Delta\varphi| + B)(N_2 e^{-\Delta\varphi^2/A^2})}_{B(\Delta\varphi)}. \tag{7.12}$$

In the Advanced tune, $N_0(\langle \mathrm{d}N_{\mathrm{ch}}/\mathrm{d}\eta\rangle_{|\eta|<0.5})$ and $c(\langle \mathrm{d}N_{\mathrm{ch}}/\mathrm{d}\eta\rangle_{|\eta|<0.5})$ are further parameterized as power laws (Eq. 7.9), and their parameters are shown in Tab. 7.5. In the Default tune $N_0 = 0.16633$ and $c = 1$.

Parameter	$B(\Delta\varphi)$	$N(\langle \mathrm{d}N_{\mathrm{ch}}/\mathrm{d}\eta\rangle_{\lvert\eta\rvert<0.5})$	$c(\langle \mathrm{d}N_{\mathrm{ch}}/\mathrm{d}\eta\rangle_{\lvert\eta\rvert<0.5})$
A	0.85747601	0	0.80951051
B	5.7197689	0.40613	0.12854252
C	–	-0.37254	0.11140016
N_1	-0.89304215	–	–
N_2	0.26041062	–	–

TABLE 7.5: Parameters used to obtain the angular correlations as a function of $\langle \mathrm{d}N_{\mathrm{ch}}/\mathrm{d}\eta\rangle_{|\eta|<0.5}$. The Default tune uses $N_0 = 0.16633$ and $c = 1$.

7.2.4 Source size

The last key ingredient for coalescence is the source size σ, which is a measure of the distance between particles and has been introduced in 2.2.2. In ToMCCA, the source is assumed to be a Gaussian function

$$S(r,\sigma) = \frac{4\pi r^2}{(4\pi\sigma^2)^{3/2}} e^{-\frac{r^2}{4\sigma^2}}. \tag{7.13}$$

In principle, the Wigner function coalescence formalism requires not the distance but the source size as an input. However, in order to mimic event-by-event fluctuations of the source size, in the Default tune an actual distance is drawn from this Gaussian distribution. It is then related back to the source size via the relation

$$r_\mu = \sigma \cdot \frac{4}{\sqrt{\pi}}. \tag{7.14}$$

r_μ is the mean of the Gaussian source distribution, and instead of σ, ToMCCA uses $\sigma' = \frac{r}{4/\sqrt{\pi}}$ in order to calculate its coalescence probability. In the advanced tune, the EPOS event generator is used to get a more realistic phase space distribution and have an actual correlation between the relative momenta and their distance (See Fig. 6.5). For this, the phase space of p–p pairs in EPOS was extracted as a function of q,r,$\langle m_{\mathrm{T}}\rangle$, and $\langle \mathrm{d}N_{\mathrm{ch}}/\mathrm{d}\eta\rangle_{|\eta|<0.5}$. This uses the same EPOS simulation as used in Ch. 6, i.e. pp collisions at $\sqrt{s}$ = 13 TeV and the impact parameter between the protons set to $b = 0$. From this distribution, ToMCCA can then draw a distance distribution, which depends on the multiplicity of the event, the average pair $\langle m_{\mathrm{T}}\rangle$, and their relative momentum q. From this distribution, the source size σ is then extracted using Eq. 7.14. This source size is then used to calculate the coalescence

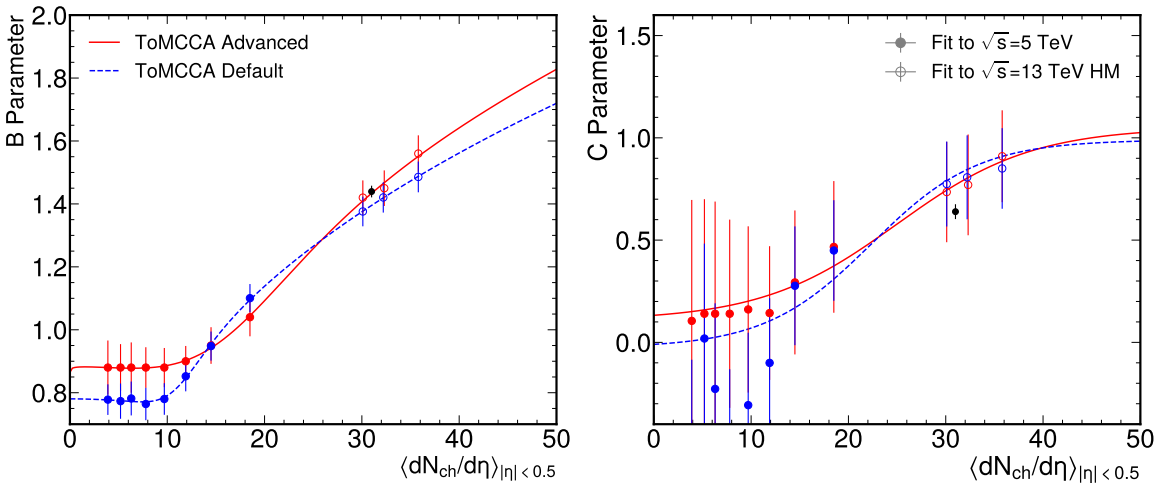

FIGURE 7.7: Fit results and parameterization of the parameters B and C for the m_{T} scaling of the source size σ. The fill points are the result of fitting to the pp $\sqrt{s}$ = 5 TeV data and the empty circles to the 13 TeV high multiplicity data. The red line shows the fit used by the advanced tune, including the EPOS phase space correlations, and the blue one shows the parameterization used in the Default tune, using the uncorrelated ToMCCA phase space. The B parameter is fitted using a `Root-3-Sigmoid` function (Eq. 7.15), the C parameter is fitted using a sigmoid function (Eq. 7.16). The best fit parameter for the ALICE measurement in high multiplicity collisions is shown in black [14].

probability (Eq. 3.1). Since the source size in pp collisions has only been measured at $\sqrt{s}$ = 13 TeV in High-Multiplicity collisions with $\langle \mathrm{d}N_{\mathrm{ch}}/\mathrm{d}\eta \rangle_{|\eta|<0.5} \sim 30$, and it is expected that the source size depends on the multiplicity of the event [11] and not the collision energy. The mean multiplicity of a minimum bias event at $\sqrt{s}$ = 13 TeV is $\langle \mathrm{d}N_{\mathrm{ch}}/\mathrm{d}\eta \rangle_{|\eta|<0.5} \sim 7$, so a description of the source for arbitrary multiplicities is required to accurately describe nuclei yields. For this purpose, the coalescence model is reverted, leaving the source size as a free parameter and fitting measured deuteron momentum distributions. For this, the deuteron spectra measured by ALICE in pp collisions at $\sqrt{s}$ = 5 TeV [8] and 13 TeV with a high multiplicity trigger [9] have been fitted using Levy-Tsallis functions. This is done to reduce statistical fluctuations as well as to allow for a finer-grained source size fit through interpolation. The other measurements at $\sqrt{s}$ = 13 TeV [10] as well as at 7 TeV [20] are left as a cross-check (see Sec. 7.3). The fit is performed by producing spectra for a fixed multiplicity class with varying source size, independently of $\langle m_{\mathrm{T}} \rangle$. Afterward, for each momentum bin extracted from the Levy-Tsallis fit, a $\chi^2_{\mathrm{n.d.f}}$ is calculated per source size and minimized. This then gives a σ–$\langle m_{\mathrm{T}} \rangle$ relation for each multiplicity, which further gets fitted using a power law (Eq. 7.9, with A=0). The behavior of the two parameters B and C as a function of $\langle \mathrm{d}N_{\mathrm{ch}}/\mathrm{d}\eta \rangle_{|\eta|<0.5}$ is shown in Fig. 7.7. The results for both tunes are quite similar, and they are parameterized using the same function. For the B parameter, a `Root-3-Sigmoid` function is used (Eq. 7.15). This function describes a smooth transition from a 0-degree polynomial to a function $\propto x^{1/3}$. The latter is a phenomenological observation that in heavy ion collisions, the source size as a function of the particle multiplicity scales $\sigma \propto (N_{\mathrm{ch}})^{1/3}$. This relation can be easily understood in the picture of statistical hadronization. Here, the overall yield of particles is directly proportional to the volume of the system, i.e. $V \propto N_{\mathrm{ch}} \Leftrightarrow r \propto N_{\mathrm{ch}}^{1/3}$, see Eq. 2.1. The 0-degree polynomial behavior is purely phenomenological as well, but it can be understood as a minimum size of the source, regardless of the multiplicity. Interestingly, this size is similar to the size of the proton $r_p \approx 0.85$ fm [112]. This could indicate that

this minimum size is driven by the geometric extension of the nucleon. The C parameter is described using a sigmoid function (Eq. 7.16). This functional shape is chosen because the slope of the m_{T} scaling appears to stay approximately constant for $\langle \mathrm{d}N_{\mathrm{ch}}/\mathrm{d}\eta \rangle_{|\eta|<0.5} < 15$ and seems to also stagnate in heavy-ion collisions [113].

$$F(x) = \frac{Ax^{1/3}}{1+e^{-B(x-M)}} - \frac{C}{1+e^{-B(x-M)}} + D. \tag{7.15}$$

$$F(x) = \frac{A}{B+e^{Dx-C}} + M. \tag{7.16}$$

The resulting σ–$\langle m_{\mathrm{T}} \rangle$ scaling behavior is shown in Fig. 7.8 for various $\langle \mathrm{d}N_{\mathrm{ch}}/\mathrm{d}\eta \rangle_{|\eta|<0.5}$,

Default	B(N_{ch})	C(N_{ch})	B(N_{ch})	C(N_{ch})	Advanced
A	0.5978	-0.8524	0.6930	0.6152	A
B	0.5898	0.8382	0.2134	0.4560	B
C	1.264	4.2530	1.6483	-2.7995	C
D	0.7814	4.4352	0.9234	-2.9428	D
M	10.8889	0.9902	15.4682	0.1525	M

TABLE 7.6: Parameters used in the description of the B and C parameter, which describe the overall size and slope of the source scaling, respectively. The parameter B is described using a `Root-3-Sigmoid` function (Eq. 7.15), which describes the transition from a minimal source size to the expected $N_{\mathrm{ch}}^{1/3}$ behavior at high multiplicities. C is parameterized using a sigmoid function (Eq. 7.16).

from 4.0 to 40.0. While the overall size is very similar between the two tunes, the Default tune is much steeper overall. The source size scaling obtained in this way should not be seen as a prediction. It compensates for all shortcomings that still exist in the model, and considering that ToMCCA is a simplified model, they have potentially significant influence. A very good cross-check is that the advanced tune reproduces the measured $\langle m_{\mathrm{T}} \rangle$-scaling. Further cross-checks will be to test the model with $A = 3$ nuclei (Sec. 7.4) because many effects will have a different impact on $A = 3$ nuclei compared to deuterons with only 2 nucleons. The main implication of the $\langle m_{\mathrm{T}} \rangle$ scaling of the source size is that the underlying phase space that is being used influences the obtained scaling, and the EPOS phase space does not reproduce this specific effect. The model uncertainties are estimated by repeating the fitting procedure using a parameterization of the lower and upper bounds of the $\mathrm{d}N/\mathrm{d}y$ parameter in the Levy-Tsallis fits obtained from the proton and deuteron spectra fits. The uncertainties of $\mathrm{d}N/\mathrm{d}y$ were obtained from the covariance matrix output of the fits.[1]. The obtained global uncertainties are 3.5% from the protons and 4.4% from the deuterons, which, added in quadrature, gives $\delta B(\langle \mathrm{d}N_{\mathrm{ch}}/\mathrm{d}\eta \rangle_{|\eta|<0.5}) = 5.7\%$. The C parameter is unaffected since it governs only the shape of the spectrum, not the yield. Varying the B parameter by 5.7% changes the deuteron yield on average by $\approx 4.6\%$. These uncertainties are not further propagated and are only estimated to evaluate the robustness of the model, and to verify that no unreasonably large uncertainties emerge from the method used to obtain the source sizes.

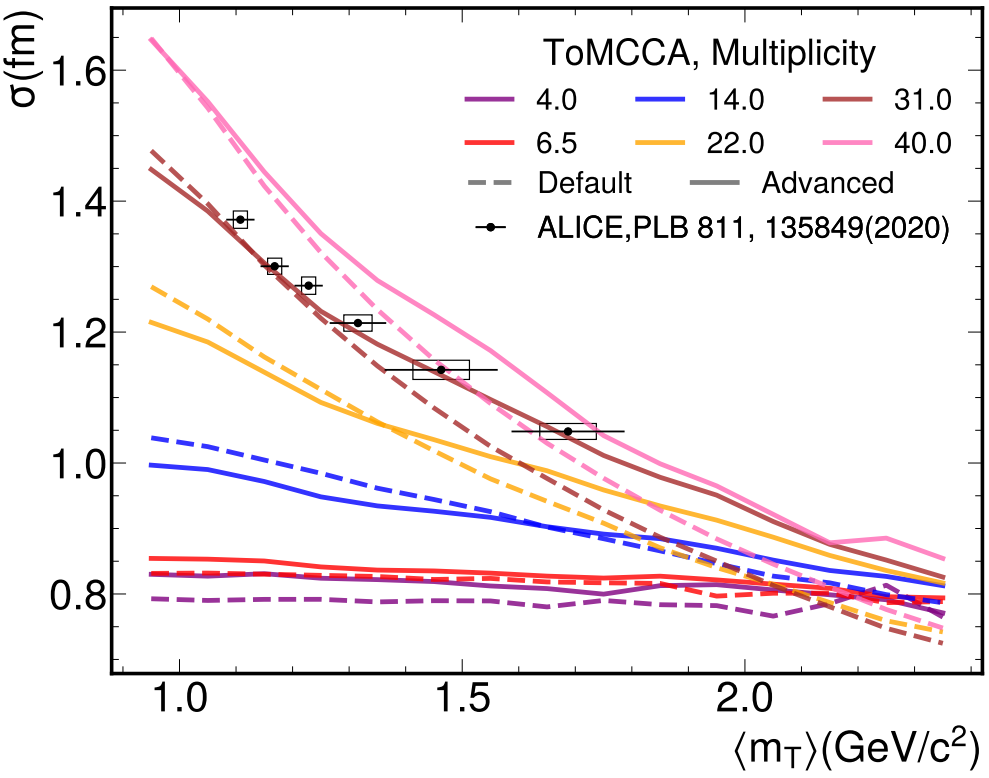

FIGURE 7.8: Scaling of the baryon-emitting source size as a function of $\langle m_{\mathrm{T}} \rangle$, for various $\langle \mathrm{d}N_{\mathrm{ch}}/\mathrm{d}\eta \rangle_{|\eta|<0.5}$, from 4.0 to 40.0. The predictions from ToMCCA for the Default tune and the Advanced tune are shown in dashed and solid lines, respectively. The ALICE measurement [14] is well reproduced by the Advanced tune.

7.3 Results for deuteron production

This section will present the deuteron results obtained from ToMCCA utilizing all the parameterizations introduced above. The deuteron coalescence is done via the Wigner function formalism introduced in Ch. 3 using the Argonne v_{18} wave function. Since all parameters are now available as a function of the event multiplicity, predictions of deuteron yields and p_{T} distributions can be made for arbitrary $\langle \mathrm{d}N_{\mathrm{ch}}/\mathrm{d}\eta \rangle_{|\eta|<0.5}$. In Fig. 7.9, the global trend of deuteron yields as a function of multiplicity is shown. Figure 7.9 (left) shows the d/p ratio as a function of $\langle \mathrm{d}N_{\mathrm{ch}}/\mathrm{d}\eta \rangle_{|\eta|<0.5}$ obtained from ALICE measurements [8–10, 20] as well as ISR [21, 22] and Serpukhov [16], which were obtained in Ch. 5. For the latter two, the results are split into $\bar{\mathrm{d}}/\bar{\mathrm{p}}$ and d/p. While the ISR measurements are at least compatible within their large uncertainties, the Serpukhov d/p results have very small uncertainties and are 9σ away from the model predictions. The antimatter ratio is even further removed. The ToMCCA predictions for the Default and Advanced tunes are shown as the red and purple curves, respectively. The width of the curves indicates the statistical uncertainty. Further, in the Advanced tune for large multiplicities $\langle \mathrm{d}N_{\mathrm{ch}}/\mathrm{d}\eta \rangle_{|\eta|<0.5} > 35$, the uncertainty increases drastically because the underlying EPOS phase space does not reach such high multiplicities. For some combinations of $\mathrm{d}N_{\mathrm{ch}}$m $\langle m_{\mathrm{T}} \rangle$ and k^*, there are no pairs found in the EPOS events analyzed, and as such, no source size could be estimated. The band is proportional to the fraction of p–n pairs for which no source size could be estimated. This fraction is $\sim 1\%$

[1]The fit results and the covariance matrix are obtained using the python package `scipy.optimize.curve_fit` (https://docs.scipy.org/doc/scipy/reference/generated/scipy.optimize.curve_fit.html)

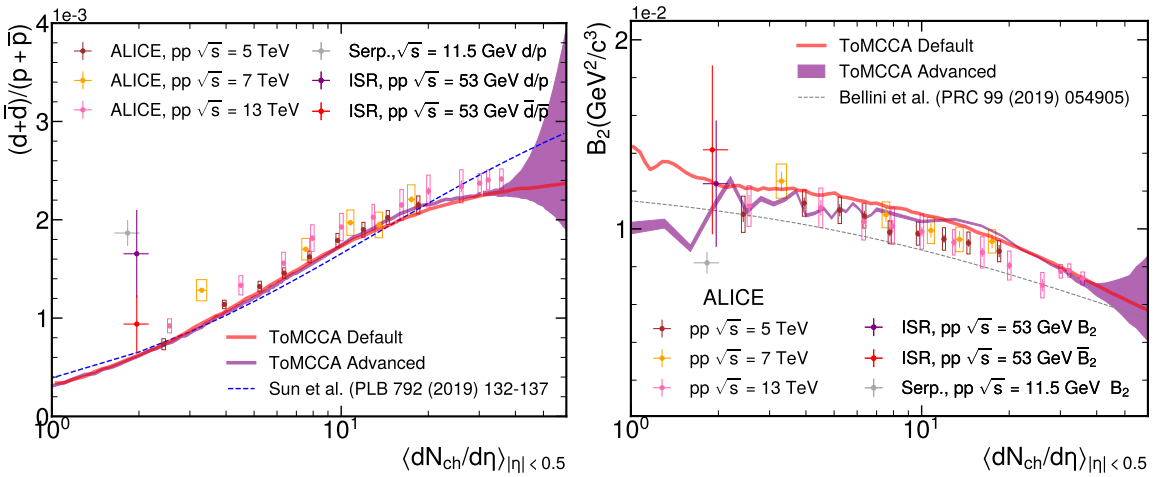

FIGURE 7.9: (left) d/p ratio as a function of $\langle dN_{ch}/d\eta \rangle_{|\eta|<0.5}$ measured by ALICE [8, 9, 20] in pp collisions with $\sqrt{s} = 5 - 13$ TeV shown in markers. The boxes indicate systematic uncertainties, and the bars are statistical ones. Matter and antimatter measurements are added. The measurements by Serpukhov [16] and ISR [21, 22] obtained from Ch. 5 are also shown, separated into d/p and $\overline{\text{d}}/\overline{\text{p}}$, because at these energies matter and antimatter are produced at different rates. The Serpukhov measurement for antimatter is not shown since it is out of scale $(1.206 \pm 0.201) \cdot 10^{-5}$). The red and purple lines show the predictions by ToMCCA with the Default and Advanced tunes, respectively. The width of the band indicates the statistical uncertainties. The increase in uncertainty of the Advanced tune for $\langle dN_{ch}/d\eta \rangle_{|\eta|<0.5} > 35$ comes from limited statistics in the EPOS phase space used as input. (right) B_2 parameter as a function of $\langle dN_{ch}/d\eta \rangle_{|\eta|<0.5}$ for $p_T/A \approx 0.75$ GeV/c measured by ALICE [8–10, 20] in pp collisions with $\sqrt{s} = 5 - 13$ TeV shown in markers. Boxes indicate systematic, bars statistical uncertainties. The measurement by ISR [21, 22] in pp collisions at $\sqrt{s} = 51$ GeV are shown, separated into matter B_2 and antimatter ($\overline{B}_2$). The Serpukhov points for $\overline{B}_2$ are out of the frame ($(8.72 \pm 1.38) \cdot 10^{-4}$) and are thus not shown. The measurement for the matter particles is in good agreement with the ISR and ALICE measurements. The red and purple lines show the predictions of ToMCCA, and the increase in uncertainty in the Advanced tune comes from uncertainty in the underlying phase space from EPOS.

at $\langle dN_{ch}/d\eta \rangle_{|\eta|<0.5} = 35$ and reaches 35% at $\langle dN_{ch}/d\eta \rangle_{|\eta|<0.5} = 60$. In the case of the Default tune, the phase space can be arbitrarily extended in $\langle dN_{ch}/d\eta \rangle_{|\eta|<0.5}$. Overall, both methods manage to reproduce the measured ratios equally well, with the Default tune reaching a $\chi^2_{\text{n.d.f.}} = 0.75$ and the Advanced tune a $\chi^2_{\text{n.d.f.}} = 0.53$. Interestingly, both follow an existing prediction [25], which uses Gaussian wave functions and an analytical coalescence model to predict the ratio from pp to Pb–Pb collisions. However, at high multiplicity pp collisions ($\langle dN_{ch}/d\eta \rangle_{|\eta|<0.5} \geq 30$), the data and ToMCCA seem to flatten out, while the analytical prediction seamlessly transitions to the results obtained from p–Pb and Pb–Pb collisions. Unfortunately, the uncertainties on the measurement in this region are large, and they are compatible with both predictions. Future measurements with higher statistics could allow for measurements beyond $\langle dN_{ch}/d\eta \rangle_{|\eta|<0.5} = 35$, which already make up only 0.01% of all collisions at $\sqrt{s} = 13$ TeV.

On the right side of Fig. 7.9, the measurements of the B_2 parameter (Eq. 2.24) as a function of $\langle dN_{ch}/d\eta \rangle_{|\eta|<0.5}$ by the ALICE collaboration in pp collisions at $\sqrt{s} = 5 - 13$ TeV are shown as the round markers. The boxes indicate the systematic, and the bars the statistical

uncertainties. The ISR results are also shown, separated into matter (B_2) and antimatter ($\overline{B}_2$). The Serpukhov results are out of the frame and thus not shown. All results are taken at p_T/A = 0.75 GeV/c. The ToMCCA results are shown as red and purple bands. The width of the band indicates the statistical uncertainty. The increase in uncertainty for the Advanced tune is due to the underlying phase space used, as described above. Overall, both predictions are in excellent agreement with the data with a $\chi^2_{\text{n.d.f.}} = 0.71(\chi^2_{\text{n.d.f.}} = 0.45)$ for the Default (Advanced) tune.

Figure 7.10 (left) shows the p_T spectra $\frac{d^2N}{dyd p_T}$ of (d+$\overline{\text{d}}$)/2 predicted by ToMCCA in comparison with the measurements by ALICE in several multiplicity classes ranging from $\langle dN_{ch}/d\eta\rangle_{|\eta|<0.5} = 2.4$ to $\langle dN_{ch}/d\eta\rangle_{|\eta|<0.5} = 35.8$ and for three different collision energies $\sqrt{s} = 5 - 13$ TeV. The ToMCCA predictions are shown as lines, dashed for the Default tune and full for the Advanced tune. The right side of Fig. 7.10 shows the $B_2(p_T/A)$ parameter measured for the same event classes. For most multiplicities and energies, the ToMCCA predictions are in good agreement with the data, reproducing it within 1σ for almost all data points. However, especially for $\sqrt{s} = 7$ TeV and 13 TeV at low p_T/A, there seems to be some tension. Looking at the B_2, one can see a rise, which is absent in the high multiplicity and $\sqrt{s} = 5$ TeV data. The shape of the B_2 parameter is mainly driven by the behavior of the source size with p_T (see e.g., Fig. 6.4. An increase of B_2 at low p_T/A would indicate that the source size decreases at low p_T, which is not observed in measurements of the source size. Figure 7.11 (left) shows the p_T spectra $\frac{d^2N}{dyd p_T}$ and (right) the $B_2(p_T/A)$ parameter for minimum bias collisions measured by ALICE in pp collisions at $\sqrt{s} = 5 - 13$ TeV. This means that there are no selection cuts implemented on the multiplicity of the events, except the requirement of one charged particle within $|\eta| < 1$, the so-called INEL>0 condition. Modeling minimum bias collisions in ToMCCA poses a challenge, as the underlying event multiplicity distribution is no longer narrow and can be described using Erlang distributions. For this, an option was added to ToMCCA to read a histogram that provides a predefined multiplicity distribution. These distributions can have any arbitrary form. For the predictions shown in Fig. 7.11 the published multiplicity distributions [23] from ALICE were used. Note that the published ones are not $\langle dN_{ch}/d\eta\rangle_{|\eta|<0.5}$ but $N_{ch,|\eta|<0.8}$, and thus, a conversion factor of 1.6 was needed to reproduce the proper mean multiplicities. With this mode, the event multiplicity is now drawn from the provided ROOT histogram, and all other processes inside ToMCCA work as previously explained. In a sense, the minimum bias results are the ultimate closure test that the parameterizations as a function of $\langle dN_{ch}/d\eta\rangle_{|\eta|<0.5}$ work as intended. The predictions by ToMCCA using both tunes are in agreement with the measurements, with the sole outlier again for 13 TeV at low p_T. All results presented in this section show an excellent agreement with the measured data for all multiplicities covered by pp collisions, up to $\langle dN_{ch}/d\eta\rangle_{|\eta|<0.5} \sim 36$. They demonstrate that the coalescence Model implemented in ToMCCA works for any tested collision energy and only depends on the event multiplicity.

7.4 Extension to $A = 3$ nuclei

7.4.1 Changes in ToMCCA

In order to allow for the coalescence of A=3 nuclei, some fundamental changes need to be made in ToMCCA. These modifications concern particle production and yields, angular correlations, and source size calculation, which will be discussed in the following sections. However, the first extension of the model is that a 3rd nucleon loop needs to be implemented. For ^{3}He, this third particle is a proton, for ^{3}H a neutron, and for $^3_\Lambda$H a Λ. The latter is more involved and will be discussed in the next section. This loop is implemented in

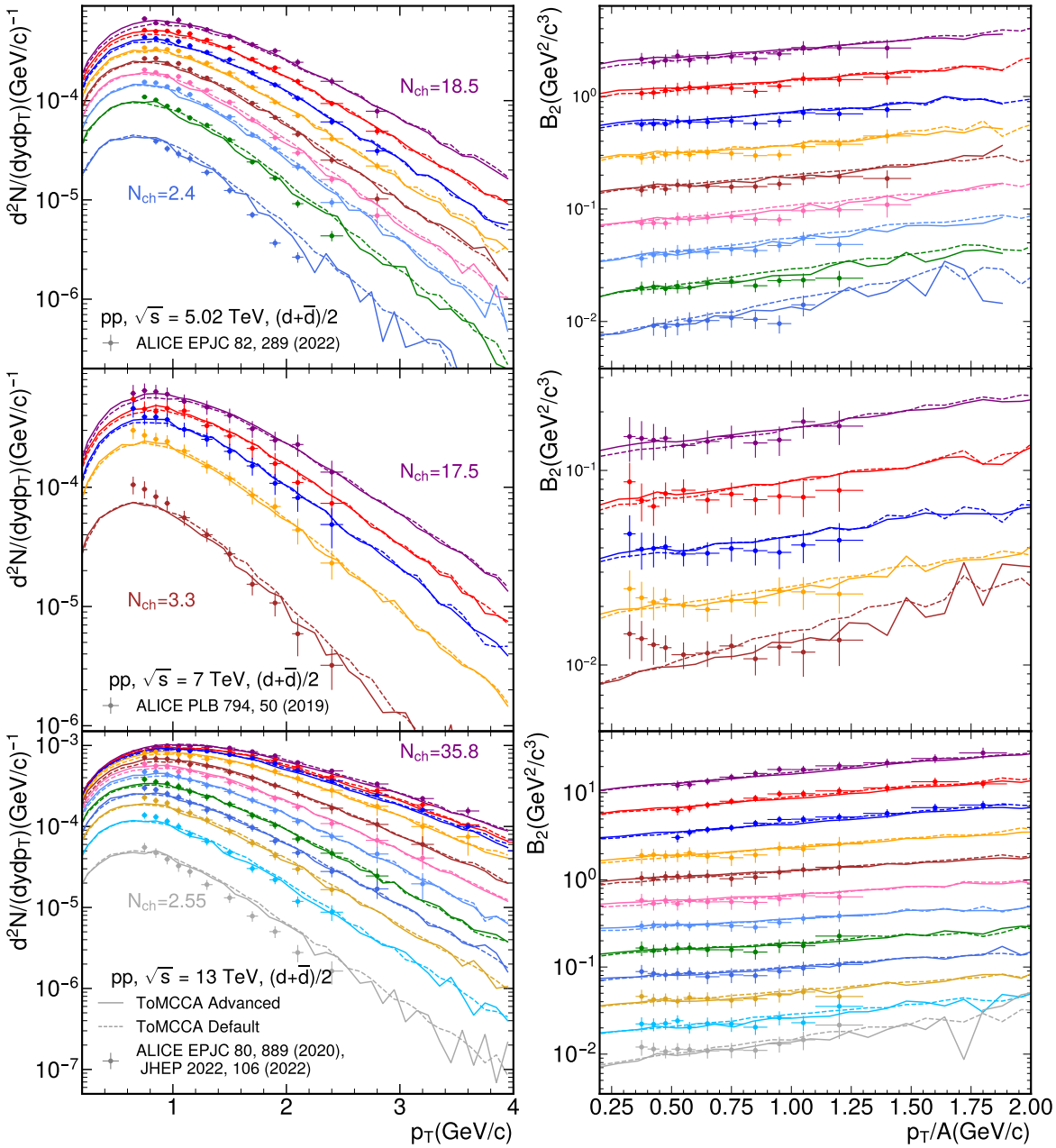

FIGURE 7.10: (left) p_{T} spectra measured by ALICE in pp collisions at $\sqrt{s} = 5 - 13$ TeV [8–10, 20] in various multiplicity classes. The multiplicities range from $\langle \mathrm{d}N_{\mathrm{ch}}/\mathrm{d}\eta \rangle_{|\eta|<0.5} = 2.4$ to $\langle \mathrm{d}N_{\mathrm{ch}}/\mathrm{d}\eta \rangle_{|\eta|<0.5} = 35.8$. The exact values for each multiplicity class can be found in Tab. 5.3. The bars indicate systematic and statistical uncertainties added in quadrature. The colored lines indicate the ToMCCA result in the corresponding multiplicity class. Dashed lines show the Default tune and full lines show the Advanced tune. Uncertainties on the Model predictions are not shown. (right) Same as left, but with the B_2 parameter as a function of $p_{\mathrm{T}}/\mathrm{A}$.

exactly the same way as the two before, but the sum now only runs over $N_{\mathrm{N}} - 1$ nucleons because the first one is used for the first proton loop.

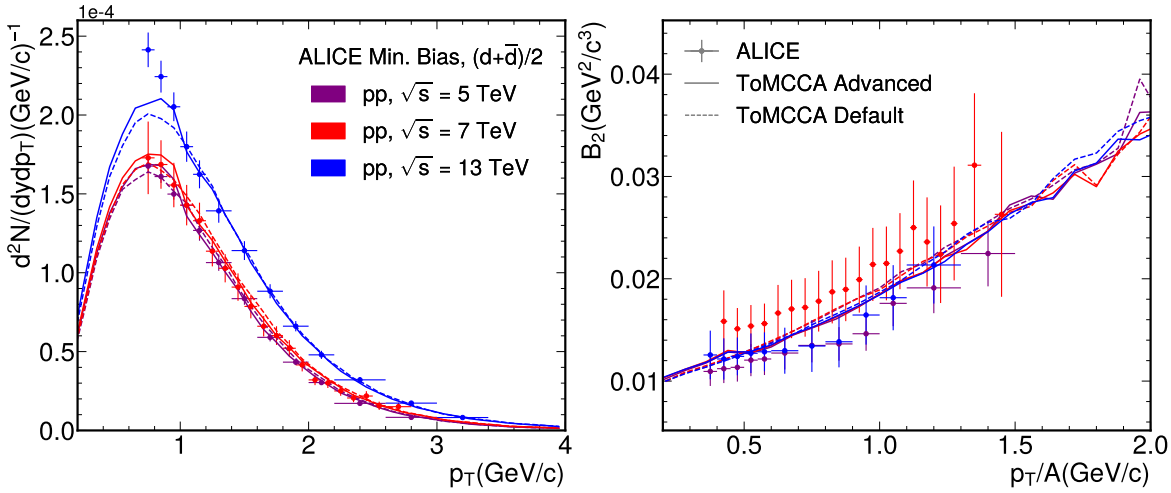

FIGURE 7.11: (left) deuteron p_T-spectra measured by ALICE in pp collisions at $\sqrt{s} = 5 - 13$ TeV. Matter and antimatter are averaged to improve statistical uncertainties. The measurements are compared to ToMCCA predictions using the published multiplicity distributions from ALICE [23]. Results for ToMCCA are shown for both tunes, the Default in dashed and advanced in solid lines, colors represent the different collision energies. (right) Same as left, but for the coalescence parameter B_2 as a function of p_T.

Particle production

While the number of neutrons and protons is calculated in precisely the same way as for the $A = 2$ coalescence, including $A = 3$ nuclei introduces the possibility of studying hypernuclei, i.e., nuclei where a nucleon has been replaced by a hyperon, such as the Λ. The lightest and only $A = 3$ hypernucleus is hypertriton ${}^3_\Lambda$H. Studying hypernuclei requires the production of hyperons in ToMCCA. Like with the nucleons, one first needs the absolute yield. This is done by using the previous parameterization of proton yields and modifying it using the measured p/Λ ratio. Figure 7.12 shows this ratio measured by ALICE in pp collisions at $\sqrt{s} = 7$ TeV (blue) and pPb collisions at $\sqrt{s} = 2.76$ TeV (orange) [24] as a function of the charged particle multiplicity. The purple line shows the ToMCCA output. In ToMCCA, this ratio is implemented via the function

$$\frac{\mathrm{p}}{\Lambda} = (N_{\mathrm{ch}})^A + B, \tag{7.17}$$

with $A = -0.6741$ and $B = 1.3112$. Currently, Λ production is only implemented in the Tuned Emission particle production model. It functions exactly the same way as for protons and neutrons, but the Λ production probability (see Eq. 7.3) is modified via $N_\Lambda = N_{\mathrm{nucleon}}/\mathrm{p}/\Lambda$. The Λ production probability is affected by the baryon number conservation in the same way as neutrons are, but the suppression factor in Eq. 7.7 is modified from $(\mathrm{d}N_\mathrm{p}/\mathrm{d}y - N_\mathrm{p})$ to $(2\mathrm{d}N_\mathrm{p}/\mathrm{d}y - (N_\mathrm{p} + N_\mathrm{n}))$ under the assumption that protons and neutrons are produced in the same amount. Looking at Fig. 7.12, this method seems to produce ~5% too many Λs, which is still well within the experimental uncertainty.

Angular correlations

The next modification concerns the Angular $\Delta\varphi$ correlations. Before, the same event $\Delta\varphi$ distribution was constructed from the measured angular correlation function and a mixed event distribution from EPOS. This approach, however, only works for two particles. For 3

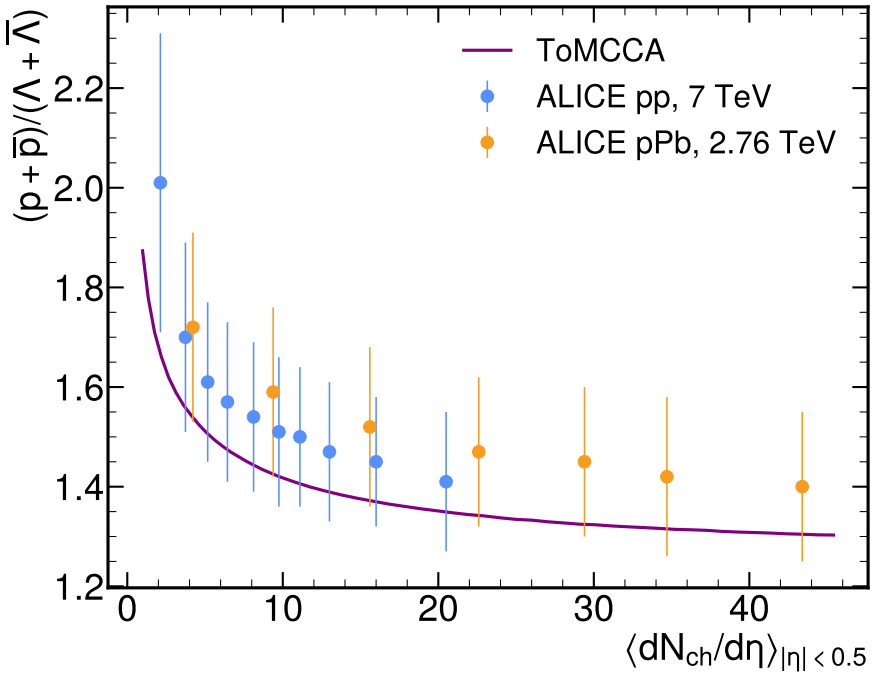

FIGURE 7.12: $(p+\bar{p})/(\Lambda+\bar{\Lambda})$ ratio measured by ALICE in pp collisions at $\sqrt{s} = 7$ TeV (blue) and pPb collisions at $\sqrt{s} = 2.76$ TeV (orange) [24] as a function of charged particle multiplicity $\langle dN_{ch}/d\eta \rangle_{|\eta|<0.5}$. The statistical and systematic uncertainties are added in quadrature, however statistical uncertainties are negligible. The purple line shows the p/Λ ratio output from ToMCCA.

particles, a different approach is used. The first particle gets assigned a random $\varphi_1 \in [0, 2\pi]$. For the second particle, a flat φ distribution is assumed, which gets modified according to

$$\mathcal{P}(\varphi_2) = 1 \times (N \sin(a\,\Delta\varphi_{12} - b) + c), \tag{7.18}$$

with the parameters from Tab. 7.5. $\Delta\varphi_{12} = \varphi_1 - \varphi_2$ is the relative angle between the first two particles. For two particles, this yields the exact same result as the approach used in A=2 coalescence. The third particle gets modified further, depending on $\Delta\varphi_{13}$ and $\Delta\varphi_{23}$, the relative angles to particles 1 and 2

$$\mathcal{P}(\varphi_3) = 1 \times (N \sin(a\,\Delta\varphi_{13} - b) + c) \times (N \sin(a\,\Delta\varphi_{23} - b) + c). \tag{7.19}$$

With this approach, the $\Delta\varphi_{12}$, $\Delta\varphi_{13}$ and $\Delta\varphi_{23}$ distributions all give the same result as the simple 2-body approach used before, but it is extendable to an arbitrary number of nucleons.

Source size

The last change is the determination of the source size. The coalescence probability requires one source size as an input. In the A=2 case, this is not a problem because the source size describes the distance between two particles, and thus, one only obtains one value. For 3 particles, various approaches are possible. In the Default tune the source size depends only on $\langle m_T \rangle$, which can be easily calculated for 3 particles

$$\langle m_T \rangle = \sqrt{\left(\frac{\mathbf{p}_{T,1} + \mathbf{p}_{T,2} + \mathbf{p}_{T,3}}{3}\right)^2 + \left(\frac{m_1 + m_2 + m_3}{3}\right)^2}. \tag{7.20}$$

In the Advanced tune, the source size depends not only on the $\langle m_T \rangle$ but also on the relative momentum k^* of the pair. One approach would be to determine the source size from EPOS as a function of $\langle m_T \rangle$ and the hypermomentum Q_3

$$Q_3 = \sqrt{-q_{12}^2 - q_{23}^2 - q_{31}^2}, \tag{7.21}$$

where q_{ij} are the relative 4-momenta of the nucleons. However, this approach is very limited by the statistics of the underlying EPOS simulation and this would cause issues, especially at low $\langle \mathrm{d}N_{\mathrm{ch}}/\mathrm{d}\eta \rangle_{|\eta|<0.5}$, where the triplet yield is very small. Another way, and the one used throughout this work, is to work with the two-body source size as in the case of A=2, obtaining three different source sizes and then averaging them.

Averaging three-particle source size

In the following, an equation is obtained to average the source size for three particles with independent single-particle source sizes R_i

$$R_{\mathrm{av}} = \sqrt{\frac{8(R_1^2+R_2^2+R_3^2)(R_2^2R_3^2+R_1^2(R_2^2+R_3^2))^3}{3R_1R_2R_3\sqrt{R_1^{-2}+R_2^{-2}+R_3^{-2}}((R_1^2+R_2^2)(R_1^2+R_2^2+4R_3^2))^{5/2}}}. \tag{7.22}$$

The formula for averaging is obtained by assuming a three-particle source with three independent single-particle source sizes R_i

$$S(\mathbf{r}_1,\mathbf{r}_2,\mathbf{r}_3) = \frac{1}{(2\pi)^{9/2}R_1^3R_2^3R_3^2}\exp\left(-\frac{1}{2}\left[\frac{r_1^2}{R_1^2}+\frac{r_2^2}{R_2^2}+\frac{r_3^2}{R_3^2}\right]\right). \tag{7.23}$$

Employing a coordinate transformation into Jacobi coordinates

$$\begin{pmatrix}\mathbf{r}_1\\ \mathbf{r}_2\\ \mathbf{r}_3\end{pmatrix} = \begin{pmatrix}1 & 1/2 & -1/3\\ 1 & -1/2 & -1/3\\ 1 & 0 & 2/3\end{pmatrix}\begin{pmatrix}\mathbf{R}\\ \mathbf{r}_{12}\\ \mathbf{r}_{312},\end{pmatrix} \tag{7.24}$$

and transforming into hyperspherical coordinates (Eq. 3.56 and Eq. 3.57) one obtains

$$\begin{aligned} S(\rho) = \int \mathrm{d}\Omega \frac{3\sqrt{3}}{8}\frac{\rho^5}{8\pi^3R_1^3R_2^3R_3^3(R_1^{-2}+R_2^{-2}+R_3^{-2})^{3/2}} \\ \exp\left(-\frac{1}{8}\left[\frac{R_1^2+R_2^2+4R_3^2}{R_2^2R_3^2+R_1^2(R_2^2+R_3^2)}\right]\rho^2\cos^2\varphi\right)\times \\ \times\exp\left(-\frac{3}{8}\left[\frac{R_1^2+R_2^2}{R_2^2R_3^2+R_1^2(R_2^2+R_3^2)}\right]\rho^2\sin^2\varphi\right) \\ \exp\left(-\frac{1}{2}\left[\frac{R_1^2-R_2^2}{R_2^2R_3^2+R_1^2(R_2^2+R_3^2)}\right]\mathbf{r}_{12}\cdot\mathbf{r}_{312}\right). \end{aligned} \tag{7.25}$$

With

$$\mathbf{r}_{12}\cdot\mathbf{r}_{312} = r_{12}r_{312}\cos\theta_{12} = \frac{3}{4}\rho^2\cos\varphi\sin\varphi\cos\theta_{12} \tag{7.26}$$

and

$$\mathrm{d}\Omega = \cos^2\varphi\,\sin^2\varphi\,\mathrm{d}\varphi\,\mathrm{d}\cos\theta_{12}\underbrace{\mathrm{d}\cos\theta_{312}}_{2}\underbrace{\mathrm{d}\phi_{12}}_{2\pi}\underbrace{\mathrm{d}\phi_{312}}_{2\pi} \tag{7.27}$$

and solving the φ and $\cos\theta_{12}$ integrals one obtains

$$S(\rho) = \frac{3\sqrt{3}\rho^3}{4(2R_3^2 - R_1^2 - R_2^2)R_1R_2R_3\sqrt{R_1^{-2} + R_2^{-2} + R_3^{-2}}} \exp\left(-\frac{1}{4}\left[\frac{R_1^2 + R_2^2 + R_3^2}{R_2^2R_3^2 + R_1^2(R_2^2 + R_3^2)}\right]\rho^2\right) \times \mathcal{I}_1\left(\frac{1}{8}\left[\frac{2R_3^2 - R_1^2 - R_2^2}{R_2^2R_3^2 + R_1^2(R_2^2 + R_3^2)}\right]\rho^2\right). \quad (7.28)$$

$\mathcal{I}_1$ is the modified Bessel function of the first kind

$$\mathcal{I}_\alpha(x) = \sum_{m=0}^{\infty} \frac{1}{m!\Gamma(m + \alpha + 1)}\left(\frac{x}{2}\right)^{2m+\alpha}. \quad (7.29)$$

This equation is only well defined as long as $2R_3^2 > R_1^2 + R_2^2$. Technically, if all sources are exactly equal, this would lead to an undefined source size, but due to machine precision, they can never be exactly equal. In ToMCCA, the source sizes obtained from the particle pairs are thus ordered according to $R_1 < R_2 < R_3$ to avoid any problems. Now, in order to calculate the average source size, one can compare the mean $\langle\rho^2\rangle = \int_0^\infty \mathrm{d}\rho S(\rho)\rho^2$ of a source with three equal R_i to the one with three different sizes. Setting $R_1 = R_2 = R_3$ in Eq 7.25, one obtains

$$\langle\rho_1^2\rangle = \int_0^\infty \mathrm{d}\rho\rho^5 \frac{1}{32R^6} \exp\left(-\frac{\rho^2}{4R^2}\right)\rho^2 = 24R^2. \quad (7.30)$$

Assuming three independent sources, one obtains

$$\langle\rho_3^2\rangle = \frac{128(R_1^2 + R_2^2 + R_3^2)(R_2^2R_3^2 + R_1^2(R_2^2 + R_3^2))^3}{R_1R_2R_3\sqrt{R_1^{-2} + R_2^{-2} + R_3^{-2}}((R_1^2 + R_2^2)(R_1^2 + R_2^2 + 4R_3^2))^{5/2}}. \quad (7.31)$$

Now, the averaged source is $R = \sqrt{\langle\rho_3^2\rangle/24}$. Note that R, R_1, R_2 and R_3 are all single particle source sizes. In experiments, we measure the two-particle source size. They are related via

$$R_{12}^2 = \frac{1}{2}(R_1^2 + R_2^2) \quad (7.32)$$

$$R_{13}^2 = \frac{1}{2}(R_1^2 + R_3^2) \quad (7.33)$$

$$R_{23}^2 = \frac{1}{2}(R_2^2 + R_3^2). \quad (7.34)$$

This system of equations can be solved for R_1, R_2, R_3:

$$R_1^2 = R_{12}^2 - R_{23}^2 + R_{13}^2 \quad (7.35)$$

$$R_2^2 = R_{23}^2 - R_{13}^2 + R_{12}^2 \quad (7.36)$$

$$R_3^2 = R_{13}^2 - R_{12}^2 + R_{23}^2. \quad (7.37)$$

Now, the R_{ij} can be obtained in the same way as in the $A = 2$ case and averaged to obtain one single source size for three particles. This method works for any particle mass or values of $\langle m_\mathrm{T}\rangle$, because it only assumes that the particles have different single-particle source radii, regardless of the origin of this difference.

7.4.2 Results for ^{3}He and ^{3}H

In this section, the results for ^{3}H and ^{3}He coalescence using ToMCCA are presented. Results are obtained using the Argonne v_{18} potential for 2-body interactions and the Urbana IX (UIX) potential for the genuine three-body interaction. For all predictions a momentum transfer cutoff of $\Lambda_c = 1$ GeV was used. For details, see Ch. 3.3. The impact of incorporating a three-body potential is illustrated in Fig. 7.13 (left). The figure shows the ratio between p_T-integrated ^{3}He yields as a function of $\langle dN_{ch}/d\eta \rangle_{|\eta|<0.5}$ using wave functions constructed with only two-body potentials (AV18) and with both two- and three-body potentials (AV18+UIX). The results reveal a significant sensitivity to three-body interactions, with differences of approximately 20% in high-multiplicity pp collisions. Figure 7.13 (right) shows the ^{3}H/^{3}He ratio as a function of $\langle dN_{ch}/d\eta \rangle_{|\eta|<0.5}$, both obtained using AV18+UIX. The previous predictions from an analytic coalescence calculation [25] using Gaussian wave functions tuned to the size of ^{3}He and ^{3}H are also shown. They model their wave functions

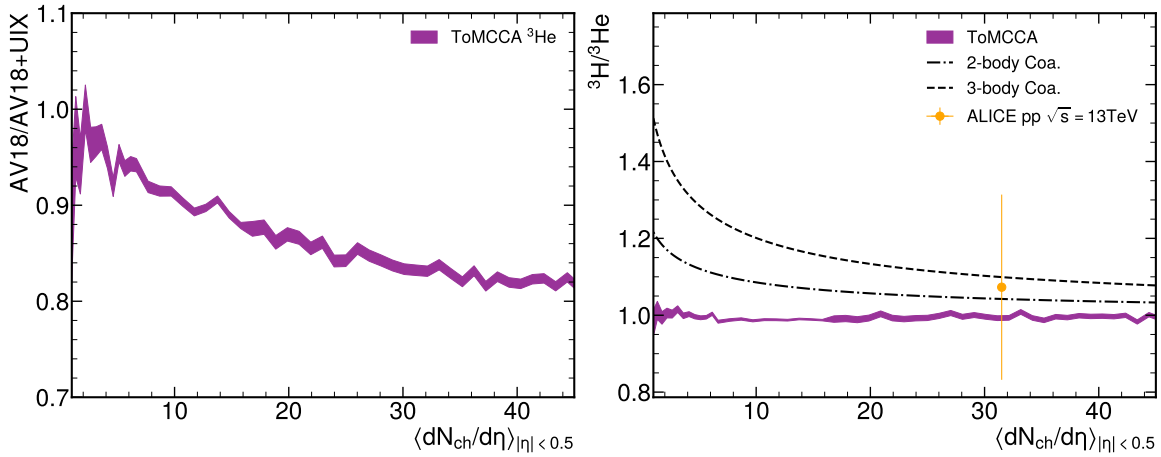

FIGURE 7.13: (left) Ratio of p_T-integrated ^{3}He yields as a function of $\langle dN_{ch}/d\eta \rangle_{|\eta|<0.5}$, comparing wave functions constructed with two-body potentials (AV18) and those including both two- and three-body potentials (AV18+UIX). The results highlight a ∼20% sensitivity to three-body interactions in high-multiplicity pp collisions. (right) The ratio between the p_T integrated yields of ^{3}H and ^{3}He as a function of $\langle dN_{ch}/d\eta \rangle_{|\eta|<0.5}$ obtained from ToMCCA. The measured data is from ALICE [9] in high multiplicity pp collisions at $\sqrt{s} = 13$ TeV. The statistical and systematic uncertainties are added in quadrature. The analytic coalescence model calculations from Ref. [25] using Gaussian wave functions for 2-body and 3-body coalescence assumptions are also shown.

either as a 3-nucleon bound state (3-body Coalescence) where all nucleons have the same average distance from each other or as an N–d bound state, with a tightly bound deuteron and a third nucleon slightly further removed. Also shown is the measured ratio obtained by ALICE in high-multiplicity pp collisions at $\sqrt{s} = 13$ TeV. The ToMCCA prediction shows no sensitivity to the multiplicity and, thus, the source size. On the contrary, the analytic calculation predicts an increase in the ratio toward lower multiplicities, which corresponds to a smaller source size. This arises in the formalism due to the different sizes of the ^{3}H and ^{3}He nuclei. Indeed, the ^{3}H has a radius of $r_C^{H3} = 1.76$ fm, while the ^{3}He nucleus has a radius of $r_C^{He3} = 1.96$ fm [114] and both values are also well reproduced by the AV18+UIX wave functions (See Tab. 3.4 and Tab. 3.5). Due to the Gaussian nature of the wave functions used in Ref. [25], the nuclei yields are proportional to $\propto \left[1 + \left(\frac{r_C}{\sigma}\right)^2\right]^{-1}$ which explains

the behavior for low source sizes. Experimentally, the two scenarios are not distinguishable since the experimental precision on the ^{3}H yields is poor due to it being equally charged to the proton and having an (almost) equal mass to ^{3}He. Interestingly, in SHM models, the expected yield ratio is also independent of multiplicity and approximately unity since the SHM is not sensitive to the size of the objects it produces but only to the mass and quantum numbers. Since both nuclei have approximately the same mass (up to $\sim$ 0.01%) and equal spin degeneracy, their production in the SHM is equal. Figure 7.14 shows the ratios

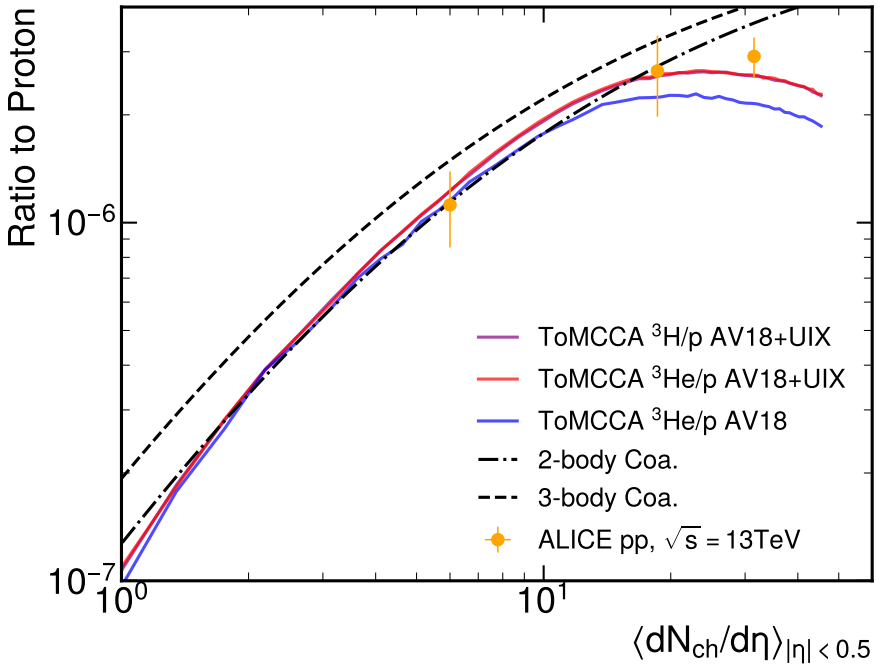

FIGURE 7.14: Ratio between ^{3}He and ^{3}H p_T integrated yields and proton integrated yields. The ^{3}He yields in ToMCCA are obtained using AV18 only and AV18+UIX potentials, and the ^{3}H yields are obtained using the AV18+UIX wave function. The model predictions are compared to measurements by ALICE in pp collisions at $\sqrt{s} = 13$ TeV in three different multiplicity classes from $\langle dN_{ch}/d\eta \rangle_{|\eta|<0.5}$ = 6.0 to 31.5. Also shown are predictions from Ref. [25], which use Gaussian wave functions with two different geometric assumptions to analytically calculate the ratio. The 2-body coalescence assumes a tightly bound deuteron with a third nucleon farther removed, while the 3-body coalescence assumes three equidistant nucleons.

of ^{3}He/p and ^{3}H/p between the nuclei and proton yields as a function of $\langle dN_{ch}/d\eta \rangle_{|\eta|<0.5}$. As before, the ^{3}He calculation is done using AV18 and AV18+UIX, and the ^{3}H calculation is done using AV18+UIX. As expected from Fig. 7.13 the ^{3}He/p (AV18+UIX) and ^{3}H/p ratios are indistinguishable from each other and the ^{3}He/p (AV18) shows strong deviations from ^{3}He/p (AV18+UIX) for large multiplicities. The predictions for ^{3}He/p from the analytic calculation [25] using Gaussian wave functions, again for 3 equidistant nuclei and for a d–N bound system, as well as experimental results from ALICE, measured in pp collisions at $\sqrt{s} = 13$ TeV for three different multiplicities [9], are also shown. The multiplicity classes were constructed by separating the minimum bias into two classes, MB-I with a mean multiplicity of $\langle dN_{ch}/d\eta \rangle_{|\eta|<0.5} = 18.7 \pm 0.3$ and MB-II with $\langle dN_{ch}/d\eta \rangle_{|\eta|<0.5} = 6.0 \pm 0.2$. The high multiplicity class corresponds to the 0.1% of events with the highest multiplicity and reaches $\langle dN_{ch}/d\eta \rangle_{|\eta|<0.5} = 31.5$. While the analytic calculation predicts a rising ^{3}He/p ratio throughout the full multiplicity range covered by pp collisions, ToMCCA predicts an inversion of the slope around $\langle dN_{ch}/d\eta \rangle_{|\eta|<0.5} \sim 25$ and then a gentle dropoff. The data

suggests at least a flattening of the slope going from $\langle \mathrm{d}N_{\mathrm{ch}}/\mathrm{d}\eta \rangle_{|\eta|<0.5}$ = 19 to 31, but due to the large experimental uncertainties, both predictions are covered within 2 standard deviations. More precise data or measurements at higher multiplicities could differentiate between the two scenarios. While a drop in the ratio has experimentally not been observed, a flattening, similar to the case of deuterons, would be expected. This could be achieved in ToMCCA by introducing a maximum source size. As of now, the B parameter in the source parameterization rises with $(N_{\mathrm{ch}})^{1/3}$ indefinitely, but due to the limited geometric size of the colliding protons, it would be expected that the source size saturates to a maximum value. This would then lead to a flattening in the ratio. However, no direct experimental evidence has been provided to motivate such a flattening. Figure 7.15 shows the B_3 parameter for $p_{\mathrm{T}}/A = 0.75$ GeV/c obtained from ToMCCA predictions as well as using the same analytic calculation shown in Fig. 7.9 (right). The results measured by ALICE in pp collisions at $\sqrt{s} = 13$ TeV in the same multiplicity ranges as in Fig. 7.14 are also depicted. The B_3 parameter is defined as

$$B_3 = \frac{4}{3}\pi^2 p_{\mathrm{T,p}}^2 \frac{\frac{d^2 N_{^3\mathrm{He},^3\mathrm{H}}}{\mathrm{d}y \mathrm{d}p_{\mathrm{T,p}}}}{\left(\frac{d^2 N_{\mathrm{p}}}{\mathrm{d}y \mathrm{d}p_{\mathrm{T,p}}}\right)^3} \tag{7.38}$$

At lower It shows similarly that ToMCCA is in good agreement, especially for the lower multiplicities, but at high multiplicity, the predicted values underestimate the B_3 parameter. This could also be caused by the source size growing indefinitely instead of leveling at a maximum value. Figure 7.16 shows the ^{3}He p_{T}-spectra measured in the same multiplicity

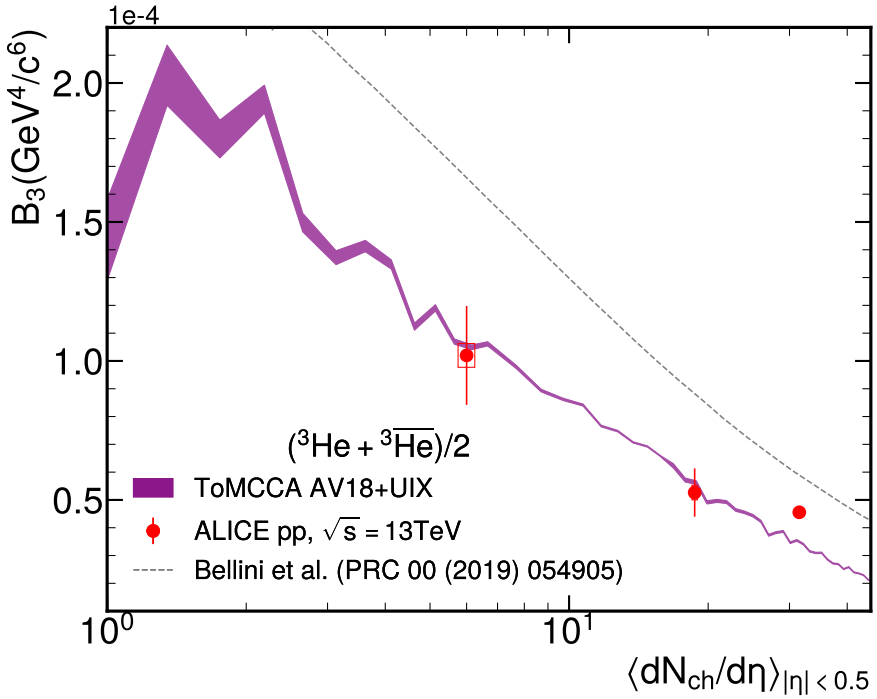

FIGURE 7.15: B_3 parameter as a function of $\langle \mathrm{d}N_{\mathrm{ch}}/\mathrm{d}\eta \rangle_{|\eta|<0.5}$ for p_{T}/A=0.75 GeV/c measured by ALICE in pp collisions at $\sqrt{s} = 13$ TeV in three multiplicity classes from $\langle \mathrm{d}N_{\mathrm{ch}}/\mathrm{d}\eta \rangle_{|\eta|<0.5}$ = 6 to 31.5. The measurement is compared to the ToMCCA predictions (purple band) and an analytic coalescence calculation from Ref. [11], which uses a Gaussian wave function.

classes as Fig. 7.15 by ALICE in pp collisions at $\sqrt{s} = 13$ TeV alongside the corresponding predictions by ToMCCA. Further, the high multiplicity data with $\langle \mathrm{d}N_{\mathrm{ch}}/\mathrm{d}\eta \rangle_{|\eta|<0.5} = 31.5 \pm 0.3$ and the minimum bias data with $\langle \mathrm{d}N_{\mathrm{ch}}/\mathrm{d}\eta \rangle_{|\eta|<0.5} = 6.9 \pm 0.1$ charged particles. The

experimental data is averaged between matter and antimatter to reduce uncertainties, while in ToMCCA there is no difference between matter and antimatter. The experimental data shown in Fig. 7.16 is in excellent agreement with the ToMCCA predictions. Some systematic

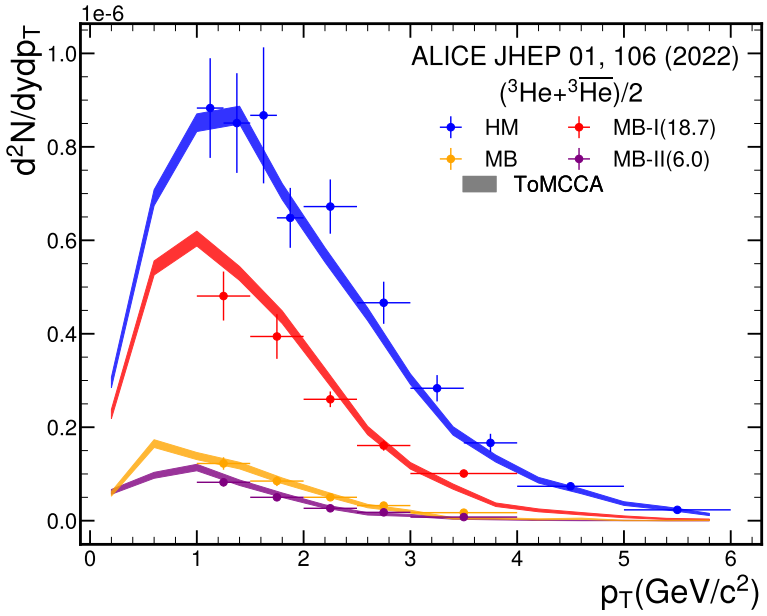

FIGURE 7.16: ^{3}He p_T spectra measured by ALICE in pp collisions at $\sqrt{s}$ = 13 TeV in three different multiplicity classes from $\langle dN_{ch}/d\eta \rangle_{|\eta|<0.5}$ = 6.0 to 31.5 as well as in minimum bias events. The measurements are compared to the ToMCCA predictions in the colored bands for the corresponding multiplicity classes. The ToMCCA predictions are shown only for the AV18+UIX wave function.

variations were performed in order to gauge the stability of the coalescence model. As for the $A = 2$ case, the source size was varied by ±5.7%. This resulted in a change of ±13% for $\langle dN_{ch}/d\eta \rangle_{|\eta|<0.5}$ = 2 up to ±18% for $\langle dN_{ch}/d\eta \rangle_{|\eta|<0.5}$ = 45. Additionally, the cutoff Λ_c was varied by ±50 MeV. This resulted in a global variation of ±7%. These two uncertainties are by far the largest on the predictions shown here, with a combined global uncertainty of ≈17%. These values are comparable with the uncertainties on the experimental data, which has uncertainties of approx. 15-25%. With these uncertainties included, using the AV18+UIX wave function the measured ^{3}He/p and ^{3}H/p ratio is reproduced with a global $\chi^2_{\text{n.d.f.}} = 0.16$ and $\chi^2_{\text{n.d.f.}} = 0.18$ respectively. Using only the AV18 wave function the global $\chi^2_{\text{n.d.f.}} = 0.68$. This shows that currently, there is not enough precision in the predictions to be sensitive to the effect of 3-body forces.

7.4.3 Results for $^3_\Lambda$H

In this section, the A=3 coalescence model is expanded to include hyperons, as explained in Sec. 7.4.1, which replace the third particle in the loop. Further, since the p–Λ source size is roughly 0.1 fm larger than the p–p source size, this flat offset is added onto R_{23} and R_{13} from Eq. 7.33 and Eq. 7.34. Whether this flat offset holds for the full multiplicity range is unknown and will have to be part of future femtoscopic measurements. All $^3_\Lambda$H predictions are obtained using the Congleton wave function (Sec. 3.3). Figure 7.17 (left) shows the $^3_\Lambda$H/Λ ratio predicted by ToMCCA as the purple band and the ALICE measurement as squares. The measurement shown in blue is the result of high multiplicity pp collisions at $\sqrt{s}$ = 13 TeV.

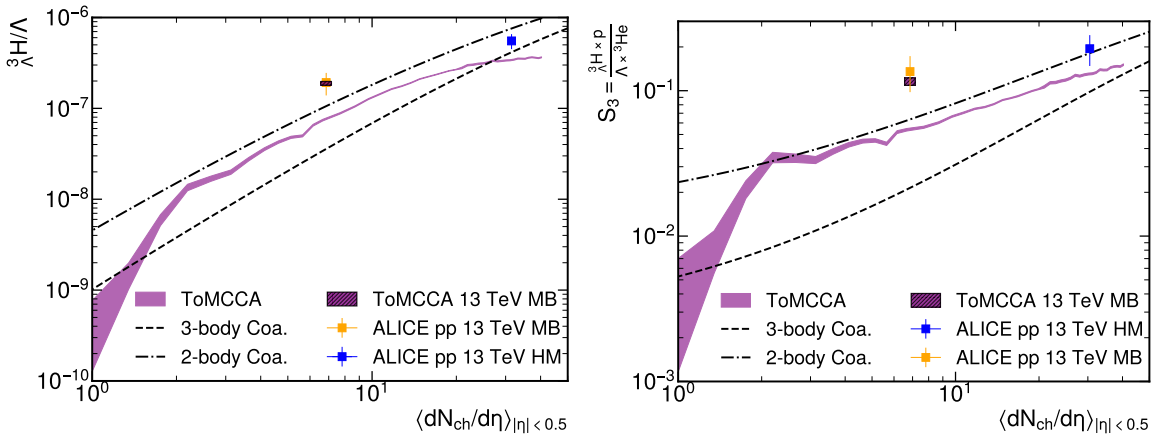

FIGURE 7.17: (left) $^3_\Lambda$H/Λ ratio predicted by ToMCCA (purple) and the measurement by ALICE in high multiplicity pp collisions at $\sqrt{s} = 13$ TeV. The orange square shows the ALICE minimum bias result, while the hatched purple box indicates the ToMCCA result using a minimum bias multiplicity distribution. The dashed and dot-dashed black lines are the predictions from Ref. [25] using Gaussian wave functions in a 3-body and 2-body coalescence approach. (right) Same as left, but for the S_3 double ratio. The ^{3}He yields were taken from the prediction using AV18+UIX.

The orange square shows the minimum bias result. Since the minimum bias results are not comparable with the measurements performed in narrow multiplicity classes, a ToMCCA prediction using a minimum bias multiplicity distribution is shown in the hatched purple box. Predictions from Ref. [25] using an analytical coalescence model and Gaussian wave functions are shown in dashed and dot-dashed black lines. The predictions are separated into 2-body and 3-body coalescence, which differ in the wave function used. Similarly to the ^{3}He predictions, the 2-body coalescence assumes a deuteron surrounded by a Λ, and the 3-body coalescence assumes three equidistant baryons. Unlike the ^{3}He case, in the case of the $^3_\Lambda$H, the 2-body coalescence closer represents the structure of the nucleus, which is often described as the ultimate halo nucleus, with a deuteron core and a halo Λ. This structure is also visible in the Congleton wave function, which assumes a fully undisturbed deuteron and a far removed Λ. While ToMCCA does an excellent job of predicting the minimum bias results, the high multiplicity results for $^3_\Lambda$H/Λ are underestimated by 3.3σ and for S_3 by 1.9σ. Similarly to the ^{3}He and ^{3}H cases, this can probably be traced back to the source size continuing to increase instead of leveling off. Another explanation could be the wave function used, which is only an approximation of an undisturbed deuteron and no genuine 3-body interaction potential is included. The right side of Fig. 7.17 shows the $S_3 = \frac{^3_\Lambda\mathrm{H} \times p}{\Lambda \times ^3\mathrm{He}}$ double ratio of integrated yields, also known as the strangeness population factor. The ^{3}He predictions used here are the ones obtained using AV18+UIX. The S_3 parameter shows the same trend as the $^3_\Lambda$H/Λ ratio. It reproduces the minimum bias value, but for higher multiplicities, it underestimates the yield of $^3_\Lambda$H. The predictions from Ref. [25] are also shown in Fig. 7.17. For ^{3}He only the 3-body coalescence is used as it makes more sense considering the structure of the Helium nucleus. Figure 7.18 (left) shows predictions by ToMCCA of the $^3_\Lambda$H p_T-spectra for the same multiplicity classes as used in the ^{3}He measurements by ALICE. The predictions for minimum bias collisions as $\sqrt{s} = 13$ TeV are also shown alongside the measurement by ALICE[2]. As can be seen the predictions are in excellent agreement with the

[2]At the time of writing this, the data is not yet published, but the analysis has been approved. The analysis is performed by Francesco Mazzaschi.

measurement.

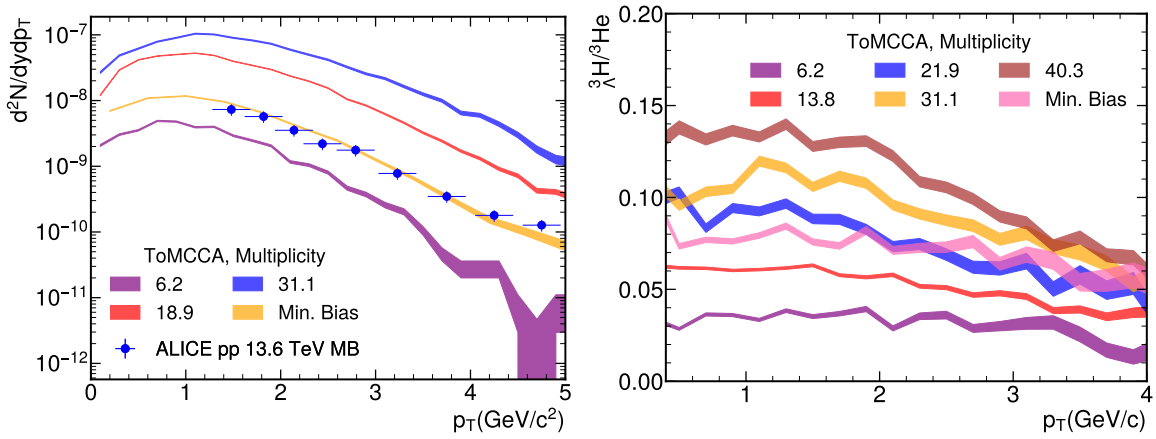

FIGURE 7.18: (left) Predictions of ${}^3_\Lambda\mathrm{H}$ p_T spectra obtained using ToMCCA for the same multiplicities as previously the ${}^3\mathrm{He}$ spectra were obtained. The only available measured spectra are for minimum bias collisions shown as the blue markers. (right) Ratio between the p_T spectra of ${}^3_\Lambda\mathrm{H}$ and ${}^3\mathrm{He}$ obtained with ToMCCA. Previous predictions in heavy ion collisions suggested that this ratio could help differentiate between coalescence and thermal production of clusters, with SHMs + Blast wave models predicting a rise of the ratio with p_T and coalescence models predicting a fall [26]. ToMCCA also predicts a falling ratio and the slope is dependent on the event multiplicity.

Figure 7.18(right) shows the ratio between the p_T spectra of ${}^3_\Lambda\mathrm{H}$ and ${}^3\mathrm{He}$ obtained with ToMCCA. Previous predictions [26] made for heavy ion collisions suggested that this ratio could help differentiate between coalescence and thermal production of clusters, with SHMs predicting a rise of the ratio with p_T and coalescence models predicting a fall. This is due to a suppression of ${}^3_\Lambda\mathrm{H}$ in smaller source sizes compared to ${}^3\mathrm{He}$ due to its larger size of $r_{{}^3_\Lambda\mathrm{H}} = 4.9$ fm [115]. It is known from measurements in heavy-ion and pp collisions [14] that the source size drops with increasing p_T. For SHM predictions, one needs, in addition, a Blast-Wave model to determine the momentum distributions (see Sec. 4.3 for details). These Blast-Wave models can be seen as an effective approximation of the hydrodynamic evolution of a quark-gluon plasma. Using Eq. 4.19 one can derive that the ${}^3_\Lambda\mathrm{H}/{}^3\mathrm{He}$ ratio behaves as [26]

$$\frac{\frac{\mathrm{d}^2 N_{{}^3_\Lambda\mathrm{H}}}{\mathrm{d}y\mathrm{d}p_\mathrm{T}}}{\frac{\mathrm{d}^2 N_{{}^3\mathrm{He}}}{\mathrm{d}y\mathrm{d}p_\mathrm{T}}} \propto \exp\left(-\frac{m^2_{{}^3_\Lambda\mathrm{H}} - m^2_{{}^3\mathrm{He}}}{(m_{\mathrm{T},{}^3_\Lambda\mathrm{H}} + m_{\mathrm{T},{}^3\mathrm{He}})T_\mathrm{eff}}\right), \tag{7.39}$$

which increases with p_T (m_T), because $m_{{}^3_\Lambda\mathrm{H}} > m_{{}^3\mathrm{He}}$. A phenomenological explanation is, that the flow velocity is independent of the mass of the particle, which leads to heavier particles flowing with higher momenta than lighter particles. ToMCCA also predicts a falling ratio and the slope is dependent on the event multiplicity, similar to the predictions obtained for different centrality intervals in Ref. [26], showing a flattening of the ratio for lower multiplicities.

Chapter 8

Final remarks and outlook

The goal of this thesis was to study the formation mechanism of (anti-)nuclei. Traditionally, nuclear formation is described using two phenomenological models: The statistical hadronization model (SHM, Sec. 2.1.1) and the coalescence model (Sec. 2.1.2). Only the coalescence model can explain all the evidence provided. The approach of statistical hadronization is fundamentally and model-independently incompatible with the findings presented in this work because the femtoscopic measurements of $\pi^{\pm}$–d pairs show that the deuteron must be produced after or during the decay of strongly decaying resonances, and not at the same time as all other hadrons as assumed in SHMs. The task was approached from two different angles: Femtoscopy and nuclear production via coalescence.
In Ch. 4 π–d, momentum correlation functions were studied using the femtoscopy technique. The obtained correlation functions showed a prominent enhancement at low k^*, which was attributed to the decay of Δ-baryons. In order to understand the origin of this enhancement, several Monte Carlo studies were performed. The predictions for the two competing production models, SHMs and coalescence, were obtained and qualitatively compared to the measurement (Fig. 8.1). The predictions for the SHMs were obtained

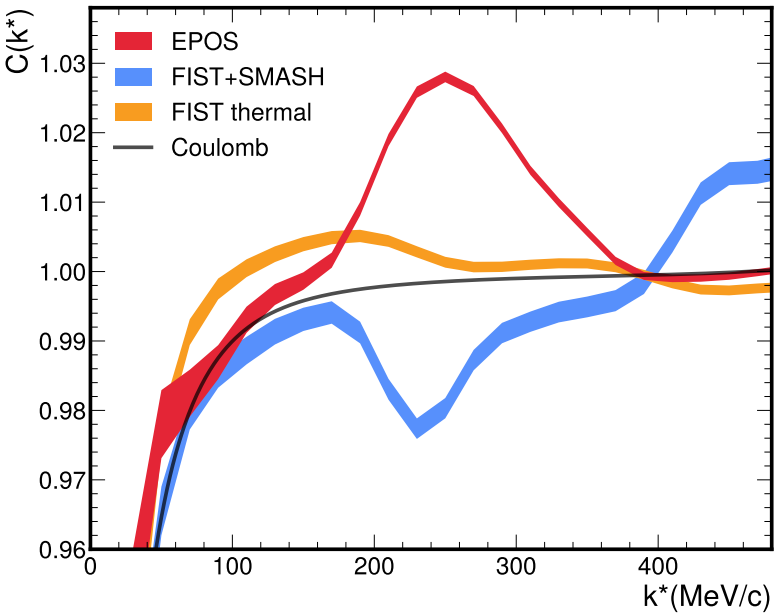

FIGURE 8.1: π–d correlation function obtained from thermal and coalescence models. Same as Fig. 4.3.

by employing the thermalFIST model and the FIST sampler. The latter is needed since, by default, SHMs only provide the absolute yields of particles but not their momentum

distributions. The FIST sampler provides an event-by-event momentum distribution of the particles according to the yields obtained from thermalFIST. The resulting π–d correlation function shows no features beyond a trivial baseline, which is dominated by momentum conservation and radial flow. However, no peaked structure akin to the enhancement observed in the measurements can be seen. To further rule out hadronic rescattering as the origin of the enhancement, the SMASH model was used as a hadronic afterburner. The FIST sampler only provides particles at the chemical freeze-out, which means their traversal of the hot and energetic environment is not described. Indeed, in such environments, deuterons could undergo so-called pseudoelastic reactions such as $\pi + (pn) \rightarrow (\Delta n) \rightarrow \pi + (pn)$ in which a pion reacts with a nucleon inside the deuteron in order to form a Δ-baryon. The subsequent decay of this baryon releases only a moderate amount of energy ($\approx$ 150 MeV), and the deuteron could remain intact afterward. The released π and the nucleon inside the deuteron would then be correlated due to the decay kinematics and would have a relative momentum of $k^* \approx 200$ MeV/c, which is exactly where the enhancement in the measured data is visible. The SMASH model includes such reactions via the measured elastic cross-sections, which include elastic and pseudoelastic contributions. However, the correlation function obtained from the FISTr+SMASH approach shows a completely opposite result: The correlation function presents with a depletion where the enhancement from the Δ would be expected. This depletion is caused by deuterons not surviving the pseudoelastic scattering. Indeed, the inelastic scattering π–d cross-section (Fig 4.5) is approximately four times larger than the elastic channel. Furthermore, even if the deuteron survives, it will not cause an enhancement in the correlation function. This counterintuitive result can be understood by, again, consulting the measured elastic cross-section. While the hadrons emerging from the pseudoelastic interaction are indeed correlated with a fixed relative momentum, this reaction only occurs for pairs that already have the required relative momentum to form the Δ-baryon. Consequently, the final distribution of relative momenta remains unchanged, as no additional pairs appear in the region of interest beyond those that were already present.

The last model tested was the coalescence model. For this purpose, the EPOS 3 event generator was used. EPOS does not produce (anti)nuclei natively, and their formation needs to be modeled by an afterburner. This afterburner was developed previously and is presented in detail in Ch. 6. The prediction from EPOS, including this afterburner, is also shown in Fig. 4.3. It shows a very prominent peak around $k^* \approx 200$ MeV/c. This peak is the result of a primordially produced Δ-baryon decaying into a nucleon and a pion, and the former subsequently coalesces with another nucleon and forms a deuteron. This process can be understood as resonance-assisted fusion, and it solves the longstanding problem of energy conservation during the coalescence process. Indeed, coalescence in its simplest form $p + n \rightarrow d$ would violate the conservation of 4-momentum since the mass of the deuteron is slightly lower than the one of the two nucleons combined. This is due to the binding energy of $E_\mathrm{d} \approx 2.3$ MeV/nucleon. The resonance-assisted fusion overcomes this problem by catalyzing the fusion reaction via the meson, which carries away any excess energy that is released by the binding of the nucleons. While this catalysis can in principle occur for any pion that is close to the nucleon pair, the pion is automatically close in phase space if at least one nucleon is the decay product of a resonance such as the Δ-baryon. Using the measured correlation function as well as the EPOS simulation, it is even possible to estimate the fraction of deuterons that originate from resonance-assisted fusion. The measurement extrapolates from the fraction of Δ-baryons observed in the π–d correlation to all resonances by employing the production yields from the canonical statistical hadronization model and the experimental detection efficiency of particles to arrive at a fraction of (80.5 ± 8.9)% of deuterons from resonance-assisted fusion. In the EPOS model, the yields of resonances were also tuned to the predictions from the canonical

statistical hadronization model. In the event generator, the origin of the nucleons that make up the deuteron can be determined, and $(89.3 \pm 1.6)\%$ of deuterons have at least one nucleon stemming from a resonance. These two results are in excellent agreement with each other and provide clear evidence that only the coalescence model can explain nuclear production. A final, model-independent argument in favor of coalescence as the origin of nuclei is given by simple causality. It has been shown that the enhancement must stem from the decay of a primordially produced Δ-baryon. This means the deuteron must be formed after (or during) the decay of the Δ-baryon and not alongside all other hadrons, as is assumed in statistical hadronization models. It has to be formed by final state interactions between the nucleons as described by the coalescence model.

Findings of the femtoscopic study

In the Femtoscopic study of $\pi^{\pm}$—d momentum correlations, an enhancement related to the decay of Δ-resonances is observed. Model studies showed that such a scenario is only compatible with the production of (anti)nuclei by final state interaction, such as the coalescence model, and incompatible with the thermal production of light clusters.

The next step to understanding nuclear formation is to directly develop a coalescence model and compare the resulting yields and yield ratios to existing nuclear measurements and models. For this, the Wigner function formalism was utilized and first tested with the EPOS event generator and later wrapped into a specialized toy Monte Carlo model called ToMCCA. The Wigner function formalism requires a nuclear wave function as an input. In this work, for the first time, realistic wave functions were used, one based on the Argonne v_{18} potential and one based on χEFT, compared to the previously used Gaussian and Hulthén wave functions. The studies using EPOS made it possible to further understand all the components that influence the nuclei spectra. These components were the charged particle multiplicity $\langle \mathrm{d}N_{\mathrm{ch}}/\mathrm{d}\eta \rangle_{|\eta|<0.5}$, the transverse momentum distribution of nucleons, the particle emission source size, and the angular correlations between nucleons. Once all these factors, except the last one, are under control and the Wigner function formalism with a realistic wave function is used, the deuteron spectra can be explained without the need for any free parameter. The effect of angular correlations was estimated to be around 10%, but a correction was not possible since these are caused by very deeply ingrained mechanisms inside EPOS. The resulting deuteron p_{T} spectra for different wave functions are shown again in Fig. 8.2.

Findings of the EPOS coalescence study

In the study applying the Wigner function formalism to the EPOS event generator, it was found that it is able to reproduce the measured deuteron spectra without any free parameter. This requires the fixing of certain parameters from measurements. These parameters are the charged particle multiplicity, the momentum distribution of nucleons, the particle emission source size, and the use of a realistic wave function, such as Argonne v_{18} or one obtained from χEFT.

On the basis of the EPOS study, a purpose-built event generator called ToMCCA was developed. ToMCCA's goal is to be a lightweight model that is purpose-built to study nuclear production. Indeed, the study using EPOS required $\approx 10^5$ CPU hours to achieve a precision of $\sim$ 5% for one energy and collision system only. An extrapolation into the

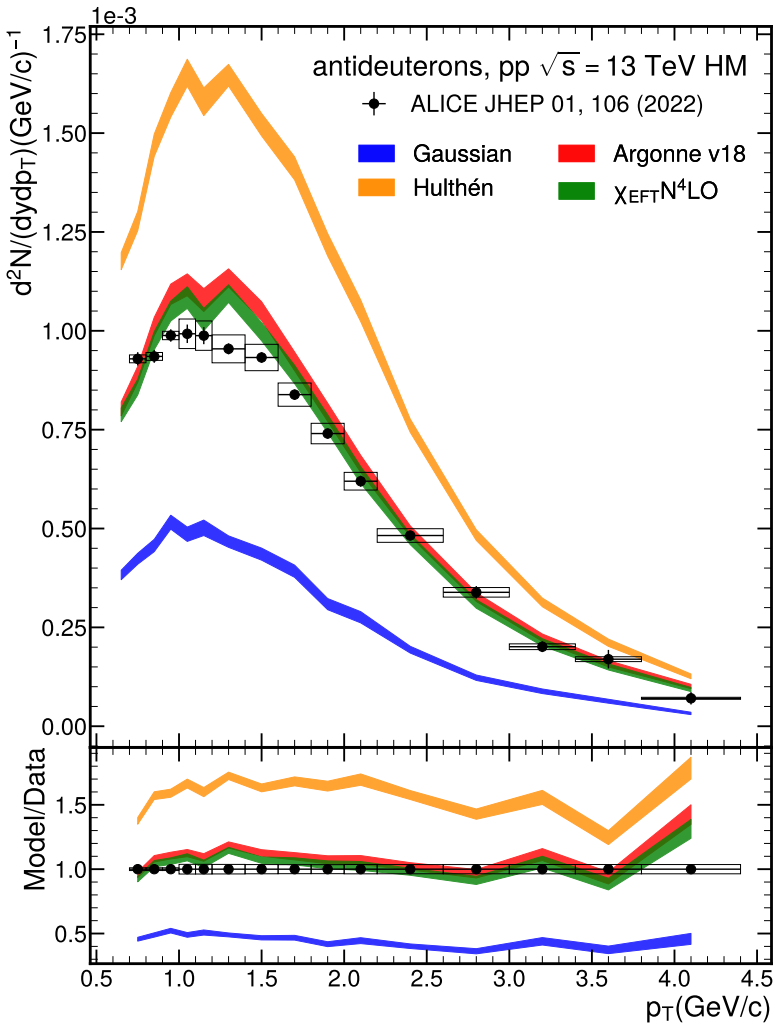

FIGURE 8.2: Deuteron spectra obtained using the EPOS 3 event generator and the Wigner function formalism. The results for different wave function assumptions of the deuteron are shown. Same as Fig. 6.8.

energies that are relevant for astrophysical searches would be unfeasible. ToMCCA is a toy Monte Carlo generator, which means it is not based on an underlying theory, such as perturbative QCD or Regge theory, to determine the particle yields and momenta, but it uses direct input from measurements. For this purpose, a large collection of ALICE measurements was utilized for pp collisions in the energy range of 5-13 TeV. These include the proton p_T spectra, the angular correlations between protons, and the measurement of the source size. While the first two have been measured over the whole range of multiplicities accessible with pp collisions, the source has only ever been measured in high multiplicity collisions with a $\langle dN_{ch}/d\eta \rangle_{|\eta|<0.5} \sim 30$. ToMCCA was used in a reversed configuration in order to fit the source size to match the deuteron spectra obtained in $\sqrt{s} = 5$ TeV collisions in the multiplicity range $\langle dN_{ch}/d\eta \rangle_{|\eta|<0.5}$ = 2.4 – 18.5 and in the high multiplicity regime up to $\langle dN_{ch}/d\eta \rangle_{|\eta|<0.5}$ = 35.8. The cross-check with the measurements at 7 TeV and 13

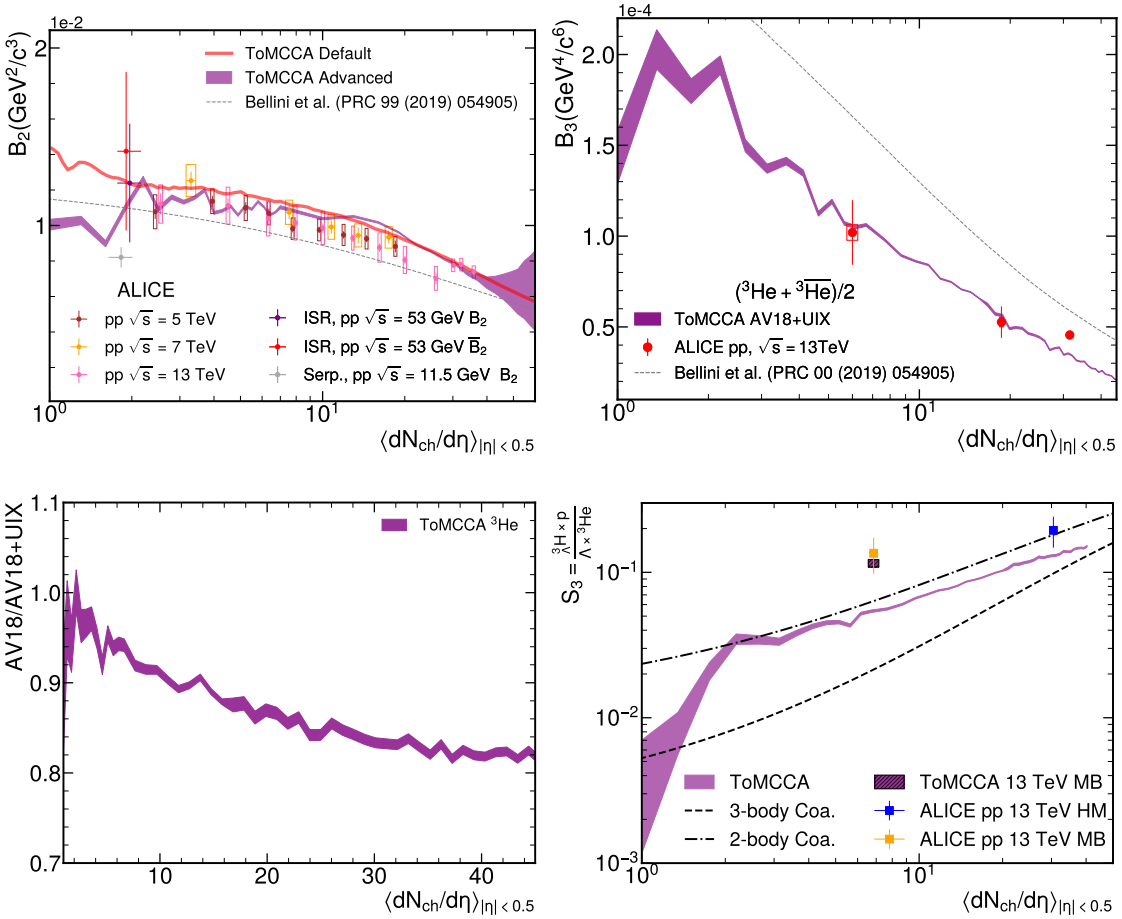

FIGURE 8.3: (top left) B_2 as a function of $\langle \mathrm{d}N_{\mathrm{ch}}/\mathrm{d}\eta \rangle_{|\eta|<0.5}$ predicted by ToMCCA using two different tunes. Shown alongside are the measurements by ALICE in pp collisions at $\sqrt{s} = 5 - 13$ TeV as well as the measurements at the ISR and in Serpukhov for pp collisions at $\sqrt{s} = 53$ and 11.5 GeV respectively. Same as Fig. 7.9. (top right) B_3 as a function of $\langle \mathrm{d}N_{\mathrm{ch}}/\mathrm{d}\eta \rangle_{|\eta|<0.5}$, predicted by ToMCCA and measured by ALICE in pp collisions at $\sqrt{s} = 13$ TeV. Same as Fig. 7.15. (bottom left) The ratio between the p_{T} integrated ^{3}He yields using a 2-body and 2+3-body potential for the wave function. Same as Fig. 7.13. (bottom right) The S_3 double ratio predicted by ToMCCA and measured by ALICE in high multiplicity pp collisions and Minimum bias. The hatched box indicates the ToMCCA result for minimum bias collisions. Same as Fig. 7.17.

TeV showed that the source size only depends on the charged particle multiplicity, not on the energy. This relation can be easily understood when considering that the particle multiplicity is related to the volume of the system, e.g., see Eq. 2.1, and this volume should be directly related to the distances between particles. Using the extracted source sizes, predictions for deuterons can be made across the whole range of $\langle \mathrm{d}N_{\mathrm{ch}}/\mathrm{d}\eta \rangle_{|\eta|<0.5}$, from 1 – 50 charged particles. The predicted values of the B_2 parameter, a parameter which is related to the coalescence probability, are shown again in Fig. 8.3 (top left). Lastly, the ToMCCA model was extended to also include nuclei with mass number A = 3. These nuclei include the regular nuclei ^{3}He, ^{3}H, and also the hypernucleus $^3_\Lambda$H, where one nucleon was replaced with a Λ-baryon. The B_3 parameter, which is similar to the B_2 parameter related to the coalescence probability of three nucleons, is shown in Fig. 8.3 (top right). The strangeness population factor S_3, which is a double ratio between the $^3_\Lambda$H/Λ ratio

and the ^{3}He/p ratio, is depicted in Fig. 8.3 (bottom right). All $A = 3$ results show a good agreement with the data from low to intermediate multiplicities, while yields are underestimated at high multiplicities. The $A = 3$ sector is an interesting one because it enables the study of 3-body forces. Indeed, using only 2-body potentials such as Argonne v_{18}, the binding energy of nuclei cannot be explained, but an additional genuine 3-body interaction potential such as Urbana IX has to be added to achieve the measured values. In ToMCCA, wave functions obtained from potential with and without 3-body interactions can be used and their differences studies. Fig. 8.3 (bottom left) shows the ratio of the ^{3}He yields obtained as a function of $\langle \mathrm{d}N_{\mathrm{ch}}/\mathrm{d}\eta \rangle_{|\eta|<0.5}$ between wave functions using only 2-body (Argonne v_{18}) and 2+3-body (Argonne v_{18} + UIX) interaction potentials. The expected difference obtained from the ToMCCA model is up to 20% for high multiplicity pp collisions.

Findings of the ToMCCA study

ToMCCA is a purpose-built toy Monte Carlo generator. It was used to extend the range of the Wigner function formalism into regions of the phase space where not all ingredients are measured. It is able to reproduce the measured deuteron spectra for the whole range of energies and multiplicities covered by pp collisions at LHC energies, and it shows excellent agreement with the measurements of $A = 3$ nuclei in the same system.

The goal of this thesis was to finally pin down the production mechanism of nuclei beyond a reasonable doubt. The excellent results of the coalescence model in Ch. 6 and Ch. 7, which reproduce the measured results without any fine-tuning - "out of the box" - and the femtoscopic results which can only be explained by a delayed emission of deuterons let me believe that this work has indeed succeeded in its quest. The results presented here show unequivocally that nuclear production in high-energy collisions can only be explained by the coalescence mechanism, which binds nucleons together in final-state interactions. The coalescence model developed in this thesis is able to reproduce measured spectra of not only deuterons but also $A = 3$ nuclei with excellent agreement. Considering the small uncertainties of $\approx 5\%$ in the case of deuterons, even in a conservative approach of doubling this uncertainty in the extrapolation process, antideuteron spectra in cosmic rays could be predicted with an uncertainty of no more than 10%, drastically improving on previous predictions.

Appendix A

Strongly decaying resonances in EPOS

In this appendix, a selection of the resonances feeding into nucleons and their fraction of final state protons stemming from this resonance is presented. The fractions are taken from EPOS pp events at $\sqrt{s} = 13$ TeV with the high multiplicity trigger described in Sec. 6.2.1. The FIST fractions are obtained from thermalFIST using the settings presented in Tab. 4.3. This is used in Ch. 6 and Ch. 4 to correct the cocktail of resonances in EPOS. An important note that must be made first is that EPOS uses a different nomenclature than the common PDG scheme. It uses the ISAJET/VENUS convention, which, due to limited numbering space, groups heavier resonances together. An additional caveat is the production in EPOS is split up into the core (hydro) and corona. The particles produced from hydro are sometimes denoted by their PDG PIDs and sometimes by their ISAJET/VENUS PIDs. In this table, they are grouped together. If the fraction is in parenthesis, the state does not decay into protons, and the neutron fraction is given.

EPOS State	EPOS PID	PDG State	PDG PID	Fraction EPOS (%)	Fraction FIST (%)
$N^+(1440)$	1122	$N^+(1440)$	12212	2.09	1.18
$N^0(1440)$	1222	$N^0(1440)$	12112	4.29	0.98
$N^+(1530)$	1123	$N^+(1520)$	2124	2.31	1.74
		$N^+(1535)$	22212		1.14
$N^0(1530)$	1223	$N^0(1520)$	1214	2.46	2.04
		$N^0(1535)$	22112		0.54
$N^+(1665)$	1125	$N^+(1650)$	32212	1.51	0.54
		$N^+(1675)$	2216		1.38
		$N^+(1680)$	12216		1.16
$N^0(1665)$	1225	$N^0(1650)$	32112	1.69	0.47
		$N^0(1675)$	2116		0.92
		$N^0(1680)$	12116		1.07
$N^+(1710)$	1127	$N^+(1700)$	22124	2.03	1.09
		$N^+(1710)$	42212		0.38
		$N^+(1720)$	32124		1.00
$N^0(1710)$	1227	$N^0(1700)$	21214	1.98	0.32
		$N^0(1710)$	42112		0.20
		$N^0(1720)$	31214		0.26
$\Lambda(1520)$	1234	$\Lambda(1520)$	3124	0.50	0.71
$\Sigma^+(1775)$	1133	$\Sigma^+(1775)$	3226	0.63	0.46

TABLE A.1: N^* and strange resonances feeding into protons.

EPOS State	EPOS PID	PDG State	PDG PID	Fraction EPOS (%)	Fraction FIST (%)
$\Delta^{++}(1232)$	1111	$\Delta^{++}(1232)$	2224	16.47	11.47
$\Delta^{+}(1232)$	1121	$\Delta^{+}(1232)$	2214	8.09	8.00
$\Delta^{0}(1232)$	1221	$\Delta^{0}(1232)$	2114	4.36	3.99
$\Delta^{-}(1232)$	2221	$\Delta^{-}(1232)$	1114	(14.34)	(11.47)
$\Delta^{++}(1620)$	1112	$\Delta^{++}(1600)$	32224	4.05	2.14
		$\Delta^{++}(1620)$	2222		0.92
$\Delta^{+}(1620)$	1124	$\Delta^{+}(1600)$	32214	1.83	1.61
		$\Delta^{+}(1620)$	2122		0.68
$\Delta^{0}(1620)$	1224	$\Delta^{0}(1600)$	32224	1.46	0.99
		$\Delta^{0}(1620)$	2222		0.41
$\Delta^{-}(1620)$	2222	$\Delta^{++}(1600)$	32224	0	0.36
		$\Delta^{++}(1620)$	2222		0.13
$\Delta^{++}(1700)$	1113	$\Delta^{++}(1700)$	12224	1.95	1.34
$\Delta^{+}(1700)$	1126	$\Delta^{+}(1700)$	12214	0.59	0.95
$\Delta^{0}(1700)$	1226	$\Delta^{0}(1700)$	12114	0.49	0.52
$\Delta^{-}(1700)$	2226	$\Delta^{-}(1700)$	11114	0	0.13
$\Delta^{++}(1925)$	1114	$\Delta^{++}(1900)$	12222	2.60	0.26
		$\Delta^{++}(1905)$	2226		0.75
		$\Delta^{++}(1910)$	22222		0.27
		$\Delta^{++}(1920)$	22224		0.56
		$\Delta^{++}(1930)$	12226		0.51
		$\Delta^{++}(1950)$	2228		0.71
$\Delta^{+}(1925)$	1128	$\Delta^{+}(1900)$	12122	2.70	0.21
		$\Delta^{+}(1905)$	2126		0.56
		$\Delta^{+}(1910)$	22122		0.20
		$\Delta^{+}(1920)$	22214		0.41
		$\Delta^{+}(1930)$	12126		0.36
		$\Delta^{+}(1950)$	2218		0.52
$\Delta^{0}(1925)$	1228	$\Delta^{0}(1900)$	11212	2.82	0.14
		$\Delta^{0}(1905)$	1216		0.33
		$\Delta^{0}(1910)$	21212		0.12
		$\Delta^{0}(1920)$	22114		0.23
		$\Delta^{0}(1930)$	11216		0.20
		$\Delta^{0}(1950)$	2118		0.30
$\Delta^{-}(1925)$	2228	$\Delta^{-}(1900)$	11112	0	0.06
		$\Delta^{-}(1905)$	1116		0.10
		$\Delta^{-}(1910)$	21112		0.03
		$\Delta^{-}(1920)$	21114		0.06
		$\Delta^{-}(1930)$	11116		0.04
		$\Delta^{-}(1950)$	1118		0.07

TABLE A.2: Δ resonances feeding into protons.

Bibliography

[1] Wit Busza, Krishna Rajagopal, and Wilke Van Der Schee. Heavy ion collisions: the big picture and the big questions. *Annual Review of Nuclear and Particle Science*, 68(1): 339–376, 2018.
Cited on pages xi and 4.

[2] Diego-Mauricio Gomez-Coral, Arturo Menchaca Rocha, et al. Deuteron and antideuteron production simulation in cosmic-ray interactions. *Phys. Rev. D*, 98(2): 023012, July 2018. doi: 10.1103/PhysRevD.98.023012.
Cited on pages xi and 8.

[3] M. M. Kachelrieß, S. Ostapchenko, et al. Revisiting cosmic ray antinuclei fluxes with a new coalescence model. *J. Cosmol. Astropart. Phys.*, 2020(08):048, August 2020. ISSN 1475-7516. doi: 10.1088/1475-7516/2020/08/048.
Cited on pages xi and 8.

[4] Laura Šerkšnytė et al. Reevaluation of the cosmic antideuteron flux from cosmic-ray interactions and from exotic sources. *Phys. Rev. D*, 105(8):083021, 2022. doi: 10.1103/PhysRevD.105.083021.
Cited on pages xi, 8, 60, and 79.

[5] A. Andronic et al. Production of light nuclei, hypernuclei and their antiparticles in relativistic nuclear collisions. *Phys. Lett. B*, 697(3):203–207, March 2011. ISSN 0370-2693. doi: 10.1016/j.physletb.2011.01.053.
Cited on pages xi, 13, and 14.

[6] Volodymyr Vovchenko et al. Canonical statistical model analysis of $p-p$, p-Pb, and Pb-Pb collisions at energies available at the CERN Large Hadron Collider. *Phys. Rev. C*, 100(5):054906, November 2019. ISSN 2469-9993. doi: 10.1103/PhysRevC.100.054906.
Cited on pages xi, 15, 16, 17, 52, and 54.

[7] Sukanya Sombun, Kristiya Tomuang, Ayut Limphirat, Paula Hillmann, Christoph Herold, Jan Steinheimer, Yupeng Yan, and Marcus Bleicher. Deuteron production from phase-space coalescence in the urqmd approach. *Phys. Rev. C*, 99:014901, Jan 2019. doi: 10.1103/PhysRevC.99.014901. URL https://link.aps.org/doi/10.1103/PhysRevC.99.014901.
Cited on pages xi, 18, and 19.

[8] Shreyasi Acharya et al. Production of light (anti)nuclei in pp collisions at $\sqrt{s} = 5.02$ TeV. *Eur. Phys. J. C*, 82(4):289, 2022. doi: 10.1140/epjc/s10052-022-10241-z.
Cited on pages xi, xv, xvi, xix, 21, 65, 90, 92, 93, and 95.

[9] Shreyasi Acharya et al. Production of light (anti)nuclei in pp collisions at $\sqrt{s} = 13$ TeV. *JHEP*, 01:106, 2022. doi: 10.1007/JHEP01(2022)106.
Cited on pages xi, xiii, xiv, xv, xvi, xx, 22, 67, 68, 71, 73, 74, 75, 76, 90, 93, 100, and 101.

[10] S. Acharya et al. (Anti-)deuteron production in pp collisions at $\sqrt{s} = 13$ TeV. *Eur. Phys. J. C*, 80(9):889, 2020. doi: 10.1140/epjc/s10052-020-8256-4.
Cited on pages xi, xv, xvi, xix, 21, 65, 90, 92, 93, and 95.

[11] Francesca Bellini et al. Testing production scenarios for (anti-)(hyper-)nuclei and exotica at energies available at the CERN Large Hadron Collider. *Phys. Rev. C*, 99(5): 054905, May 2019. ISSN 2469-9993. doi: 10.1103/PhysRevC.99.054905.
Cited on pages xi, xvi, 19, 20, 22, 90, and 102.

[12] Kfir Blum and Masahiro Takimoto. Nuclear coalescence from correlation functions. *Phys. Rev. C*, 99(4):044913, April 2019. ISSN 2469-9993. doi: 10.1103/PhysRevC.99.044913.
Cited on pages xi, 21, 22, and 76.

[13] J. Staudenmaier et al. Deuteron production in relativistic heavy ion collisions via stochastic multiparticle reactions. *Phys. Rev. C*, 104(3):034908, September 2021. ISSN 2469-9993. doi: 10.1103/PhysRevC.104.034908.
Cited on pages xii, 23, and 25.

[14] S. Acharya, D. Adamová, A. Adler, J. Adolfsson, M. M. Aggarwal, G. Aglieri Rinella, M. Agnello, N. Agrawal, Z. Ahammed, S. Ahmad, et al. Search for a common baryon source in high-multiplicity pp collisions at the LHC. *Phys. Lett. B*, 811:135849, December 2020. ISSN 0370-2693. doi: 10.1016/j.physletb.2020.135849.
Cited on pages xii, xiii, xv, 22, 26, 27, 28, 30, 46, 49, 68, 70, 71, 74, 90, 92, and 105.

[15] G. Coci et al. Dynamical mechanisms for deuteron production at mid-rapidity in relativistic heavy-ion collisions from energies available at the GSI Schwerionensynchrotron to those at the BNL Relativistic Heavy Ion Collider. *Phys. Rev. C*, 108(1): 014902, July 2023. doi: 10.1103/PhysRevC.108.014902.
Cited on pages xiii and 56.

[16] V. V. Abramov et al. High p_T Deuteron and Anti-deuteron Production in pp and p a Collisions at 70-GeV. *Sov. J. Nucl. Phys.*, 45:845, 1987.
Cited on pages xiii, xv, xix, 60, 61, 62, 92, and 93.

[17] V. V. Abramov et al. Hadron production at transverse momenta from 0.5 up to 2.2 GeV/c in proton-proton collisions at 70 GeV. *Nucl. Phys. B*, 173(2):348–364, October 1980. ISSN 0550-3213. doi: 10.1016/0550-3213(80)90223-0.
Cited on pages xiii, xix, 60, 61, and 62.

[18] J. Adam et al. Insight into particle production mechanisms via angular correlations of identified particles in pp collisions at TeV. *Eur. Phys. J. C*, 77(8):569–17, August 2017. ISSN 1434-6052. doi: 10.1140/epjc/s10052-017-5129-6.
Cited on pages xiii, 73, and 74.

[19] ALICE Collaboration et al. First Measurement of Antideuteron Number Fluctuations at Energies Available at the Large Hadron Collider. *Phys. Rev. Lett.*, 131(4):041901, July 2023. doi: 10.1103/PhysRevLett.131.041901.
Cited on pages xv, 85, and 86.

[20] S. Acharya et al. Multiplicity dependence of (anti-)deuteron production in pp collisions at s=7TeV. *Phys. Lett. B*, 794:50–63, July 2019. ISSN 0370-2693. doi: 10.1016/j.physletb.2019.05.028.
Cited on pages xv, xvi, xix, 65, 90, 92, 93, and 95.

[21] B. Alper et al. Production spectra of $\pi\pm$, K$\pm$, p$\pm$ at large angles in proton-proton collisions in the CERN intersecting storage rings. *Nucl. Phys. B*, 100(2):237–290, December 1975. ISSN 0550-3213. doi: 10.1016/0550-3213(75)90618-5.
Cited on pages xv, 62, 92, and 93.

[22] S. Henning et al. Production of Deuterons and anti-Deuterons in Proton Proton Collisions at the CERN ISR. *Lett. Nuovo Cim.*, 21:189, 1978. doi: 10.1007/BF02822248.
Cited on pages xv, 62, 92, and 93.

[23] ALICE Collaboration. Multiplicity dependence of charged-particle production in pp, p-Pb, Xe-Xe and Pb-Pb collisions at the LHC. *arXiv*, November 2022. doi: 10.48550/arXiv.2211.15326.
Cited on pages xvi, 94, and 96.

[24] Krzysztof Redlich et al. Exact strangeness conservation in heavy ion collisions. *EPJ Web Conf.*, 259:07002, 2022. ISSN 2100-014X. doi: 10.1051/epjconf/202225907002.
Cited on pages xvi, 96, and 97.

[25] Kai-Jia Sun et al. Suppression of light nuclei production in collisions of small systems at the Large Hadron Collider. *Phys. Lett. B*, 792:132–137, May 2019. ISSN 0370-2693. doi: 10.1016/j.physletb.2019.03.033.
Cited on pages xvi, xvii, 93, 100, 101, and 104.

[26] Dai-Neng Liu, Che Ming Ko, Yu-Gang Ma, Francesco Mazzaschi, Maximiliano Puccio, Qi-Ye Shou, Kai-Jia Sun, and Yuan-Zhe Wang. Softening of the hypertriton transverse momentum spectrum in heavy-ion collisions. *Phys. Lett. B*, 855:138855, 2024. doi: 10.1016/j.physletb.2024.138855.
Cited on pages xvii and 105.

[27] Ronald J. Adler, T. K. Das, et al. Analytic wave function for the deuteron D state. *Phys. Rev. C*, 16(3):1231, September 1977. doi: 10.1103/PhysRevC.16.1231.
Cited on pages xix, 34, and 39.

[28] A. Kievsky et al. A high-precision variational approach to three- and four-nucleon bound and zero-energy scattering states. *J. Phys. G: Nucl. Part. Phys.*, 35(6):063101, May 2008. ISSN 0954-3899. doi: 10.1088/0954-3899/35/6/063101.
Cited on pages xix and 43.

[29] J. G. Gongleton. A simple model of the hypertriton. *J. Phys. G: Nucl. Part. Phys.*, 18(2):339, February 1992. ISSN 0954-3899. doi: 10.1088/0954-3899/18/2/015.
Cited on pages xix, 43, and 45.

[30] Stefano Camarda, Giancarlo Ferrera, et al. Determination of the strong-coupling constant from the Z-boson transverse-momentum distribution. *Eur. Phys. J. C*, 84(1):39–11, January 2024. ISSN 1434-6052. doi: 10.1140/epjc/s10052-023-12373-2.
Cited on page 3.

[31] E. Andersen, F. Antinori, et al. Strangeness enhancement at mid-rapidity in Pb–Pb collisions at 158 A GeV/c. *Phys. Lett. B*, 449(3):401–406, March 1999. ISSN 0370-2693. doi: 10.1016/S0370-2693(99)00140-9.
Cited on page 4.

[32] F. Antinori et al. and The WA97 Collaboration. Transverse mass spectra of strange and multi–strange particles in Pb–Pb collisions at 158 A GeV/c. *Eur. Phys. J. C*, 14(4):633–641, June 2000. ISSN 1434-6052. doi: 10.1007/s100520000386.
Cited on page 4.

[33] T. Ludlam and S. Aronson. Hunting the quark gluon plasma. 4 2005. doi: 10.2172/15015225.
Cited on page 4.

[34] Mitja Rosina and Bogdan Povh. Contribution of the covalent and the Van der Waals force to the nuclear binding. *Nucl. Phys. A*, 572(1):48–56, May 1994. ISSN 0375-9474. doi: 10.1016/0375-9474(94)90420-0.
Cited on page 6.

[35] R. B. Wiringa et al. Accurate nucleon-nucleon potential with charge-independence breaking. *Phys. Rev. C*, 51(1):38–51, January 1995. doi: 10.1103/PhysRevC.51.38.
Cited on pages 6, 26, and 34.

[36] Hideki Yukawa. On the interaction of elementary particles. i. *Proceedings of the Physico-Mathematical Society of Japan. 3rd Series*, 17:48–57, 1935.
Cited on page 6.

[37] Peter Braun-Munzinger et al. PARTICLE PRODUCTION IN HEAVY ION COLLISIONS. In *Quark?Gluon Plasma 3*, pages 491–599. WORLD SCIENTIFIC, Singapore, January 2004. ISBN 978-981-238-077-7. doi: 10.1142/9789812795533_0008.
Cited on page 12.

[38] Volodymyr Vovchenko et al. Analysis of hadron yield data within hadron resonance gas model with multi-component eigenvolume corrections. *J. Phys. Conf. Ser.*, 779(1): 012078, January 2017. ISSN 1742-6596. doi: 10.1088/1742-6596/779/1/012078.
Cited on page 12.

[39] ALICE Collaboration. Measurements of chemical potentials in Pb-Pb collisions at $\sqrt{s_{\mathrm{NN}}} = 5.02$ TeV. *arXiv*, November 2023. doi: 10.48550/arXiv.2311.13332.
Cited on pages 13 and 85.

[40] S. Wheaton et al. THERMUS—A thermal model package for ROOT. *Comput. Phys. Commun.*, 180(1):84–106, January 2009. ISSN 0010-4655. doi: 10.1016/j.cpc.2008.08.001.
Cited on page 13.

[41] Anton Andronic et al. Decoding the phase structure of QCD via particle production at high energy. *Nature*, 561(7723):321–330, September 2018. ISSN 1476-4687. doi: 10.1038/s41586-018-0491-6.
Cited on page 13.

[42] G. Torrieri, S. Jeon, J. Letessier, and Johann Rafelski. SHAREv2: Fluctuations and a comprehensive treatment of decay feed-down. *Comput. Phys. Commun.*, 175:635–649, 2006. doi: 10.1016/j.cpc.2006.07.010.
Cited on page 13.

[43] HotQCD Collaboration et al. Equation of state in $(2+1)$-flavor QCD. *Phys. Rev. D*, 90 (9):094503, November 2014. ISSN 2470-0029. doi: 10.1103/PhysRevD.90.094503.
Cited on page 13.

[44] Volodymyr Vovchenko et al. Multiplicity dependence of light nuclei production at LHC energies in the canonical statistical model. *Phys. Lett. B*, 785:171–174, October 2018. ISSN 0370-2693. doi: 10.1016/j.physletb.2018.08.041.
Cited on page 14.

[45] Francesco Becattini. A Thermodynamical approach to hadron production in e+ e- collisions. *Z. Phys. C*, 69(3):485–492, 1996. doi: 10.1007/BF02907431.
Cited on page 15.

[46] Volodymyr Vovchenko. Cooper-Frye sampling with short-range repulsion. *Phys. Rev. C*, 106(6):064906, December 2022. ISSN 2469-9993. doi: 10.1103/PhysRevC.106.064906.
Cited on page 15.

[47] S. T. Butler et al. Deuterons from High-Energy Proton Bombardment of Matter. *Phys. Rev.*, 129(2):836–842, January 1963. ISSN 1536-6065. doi: 10.1103/PhysRev.129.836.
Cited on page 16.

[48] A. Schwarzschild and Č. Zupančič. Production of tritons, deuterons, nucleons, and mesons by 30-gev protons on a1, be, and fe targets. *Phys. Rev.*, 129:854–862, Jan 1963. doi: 10.1103/PhysRev.129.854. URL https://link.aps.org/doi/10.1103/PhysRev.129.854.
Cited on page 17.

[49] Joseph I. Kapusta. Mechanisms for deuteron production in relativistic nuclear collisions. *Phys. Rev. C*, 21(4):1301–1310, April 1980. ISSN 2469-9993. doi: 10.1103/PhysRevC.21.1301.
Cited on pages 17 and 20.

[50] Anirvan Shukla, Amaresh Datta, Philip von Doetinchem, Diego-Mauricio Gomez-Coral, and Carina Kanitz. Large-scale simulations of antihelium production in cosmic-ray interactions. *Phys. Rev. D*, 102(6):063004, September 2020. ISSN 2470-0029. doi: 10.1103/PhysRevD.102.063004.
Cited on pages 18 and 79.

[51] ALICE Collaboration, S. Acharya, et al. Enhanced Deuteron Coalescence Probability in Jets. *Phys. Rev. Lett.*, 131(4):042301, July 2023. ISSN 1079-7114. doi: 10.1103/PhysRevLett.131.042301.
Cited on pages 18 and 60.

[52] Qingfeng Li, Yongjia Wang, et al. Influence of clustering and hadron potentials on the rapidity distribution of protons from the UrQMD model. *arXiv*, July 2015. doi: 10.48550/arXiv.1507.06033.
Cited on page 18.

[53] Rüdiger Scheibl et al. Coalescence and flow in ultrarelativistic heavy ion collisions. *Phys. Rev. C*, 59(3):1585–1602, March 1999. ISSN 2469-9993. doi: 10.1103/PhysRevC.59.1585.
Cited on pages 19, 20, 23, 29, and 30.

[54] ALICE Collaboration et al. Centrality dependence of pion freeze-out radii in Pb-Pb collisions at $\sqrt{s_{NN}} = 2.76$ TeV. *Phys. Rev. C*, 93(2):024905, February 2016. ISSN 2469-9993. doi: 10.1103/PhysRevC.93.024905.
Cited on page 20.

[55] ALICE Collaboration et al. Two-pion femtoscopy in p-Pb collisions at $\sqrt{s_{NN}} = 5.02$ TeV. *Phys. Rev. C*, 91(3):034906, March 2015. ISSN 2469-9993. doi: 10.1103/PhysRevC.91.034906.
Not cited.

[56] ALICE Collaboration et al. Charged kaon femtoscopic correlations in pp collisions at $\sqrt{s}$=7 TeV. *Phys. Rev. D*, 87(5):052016, March 2013. ISSN 2470-0029. doi: 10.1103/PhysRevD.87.052016.
Cited on page 20.

[57] M. Hillery et al. Distribution functions in physics: Fundamentals. *Phys. Rep.*, 106(3): 121–167, April 1984. ISSN 0370-1573. doi: 10.1016/0370-1573(84)90160-1.
Cited on page 21.

[58] S. E. Koonin. Proton Pictures of High-Energy Nuclear Collisions. *Phys. Lett. B*, 70: 43–47, 1977. doi: 10.1016/0370-2693(77)90340-9.
Cited on page 25.

[59] S. Pratt et al. Detailed predictions for two-pion correlations in ultrarelativistic heavy-ion collisions. *Phys. Rev. C*, 42(6):2646–2652, December 1990. doi: 10.1103/PhysRevC.42.2646.
Cited on page 25.

[60] D. L. Mihaylov et al. A femtoscopic correlation analysis tool using the Schrödinger equation (CATS). *Eur. Phys. J. C*, 78(5):394–15, May 2018. ISSN 1434-6052. doi: 10.1140/epjc/s10052-018-5859-0.
Cited on pages 27 and 28.

[61] ALICE Collaboration et al. One-dimensional pion, kaon, and proton femtoscopy in Pb-Pb collisions at $\sqrt{s_{NN}} = 2.76$ TeV. *Phys. Rev. C*, 92(5):054908, November 2015. doi: 10.1103/PhysRevC.92.054908.
Cited on page 27.

[62] ALICE Collaboration. Common femtoscopic hadron-emission source in pp collisions at the LHC. *arXiv*, November 2023. doi: 10.48550/arXiv.2311.14527.
Cited on page 28.

[63] M. Kachelrieß et al. Alternative coalescence model for deuteron, tritium, helium-3 and their antinuclei. *Eur. Phys. J. A*, 56(1):4–12, January 2020. ISSN 1434-601X. doi: 10.1140/epja/s10050-019-00007-9.
Cited on pages 29 and 70.

[64] Tom Reichert et al. Energy dependence of light hypernuclei production in heavy-ion collisions from a coalescence and statistical-thermal model perspective. *Phys. Rev. C*, 107(1):014912, January 2023. doi: 10.1103/PhysRevC.107.014912.
Cited on page 30.

[65] E. Colomés et al. Comparing Wigner, Husimi and Bohmian distributions: which one is a true probability distribution in phase space? *J. Comput. Electron.*, 14(4):894–906, December 2015. ISSN 1572-8137. doi: 10.1007/s10825-015-0737-6.
Cited on page 30.

[66] Lamek Hulthén, Masao Sugawara, et al. *Structure of Atomic Nuclei / Bau der Atomkerne*. Springer, Berlin, Germany. ISBN 978-3-642-45872-9. URL https://link.springer.com/book/10.1007/978-3-642-45872-9.
Cited on page 33.

[67] S. Mrowczynski. On the neutron proton correlations and deuteron production. *Phys. Lett. B*, 277:43–48, 1992. doi: 10.1016/0370-2693(92)90954-3.
Cited on page 33.

[68] Roderick V. Reid. Local phenomenological nucleon-nucleon potentials. *Annals of Physics*, 50:411–448, 1968. URL https://api.semanticscholar.org/CorpusID:123231724.
Cited on page 34.

[69] J. R. Bergervoet et al. Phase shift analysis of all proton-proton scattering data below T_{lab}=350 MeV. *Phys. Rev. C*, 41(4):1435–1452, April 1990. doi: 10.1103/PhysRevC.41.1435.
Cited on pages 34 and 43.

[70] R. B. Wiringa, R. A. Smith, and T. L. Ainsworth. Nucleon-nucleon potentials with and without $\Delta(1232)$ degrees of freedom. *Phys. Rev. C*, 29:1207–1221, Apr 1984. doi: 10.1103/PhysRevC.29.1207. URL https://link.aps.org/doi/10.1103/PhysRevC.29.1207.
Cited on page 35.

[71] D. R. Entem, R. Machleidt, and Y. Nosyk. High-quality two-nucleon potentials up to fifth order of the chiral expansion. *Phys. Rev. C*, 96:024004, Aug 2017. doi: 10.1103/PhysRevC.96.024004. URL https://link.aps.org/doi/10.1103/PhysRevC.96.024004.
Cited on page 37.

[72] M. Garçon et al. The Deuteron: Structure and Form Factors. In *Advances in Nuclear Physics*, pages 293–378. Springer, Boston, MA, Boston, MA, USA, 2001. ISBN 978-0-306-47915-1. doi: 10.1007/0-306-47915-X_4.
Cited on page 39.

[73] Eite Tiesinga, Peter Mohr, David Newell, and Barry Taylor. Codata recommended values of the fundamental physical constants: 2018. (93), 2021-06-30 04:06:00 2021. doi: https://doi.org/10.1103/RevModPhys.93.025010. URL https://tsapps.nist.gov/publication/get_pdf.cfm?pub_id=931443.
Cited on page 39.

[74] V. V. Glagolev et al. The deuteron D-state probability. *Z. Phys. A: Hadrons Nucl.*, 356 (1):183–186, December 1996. ISSN 0939-7922. doi: 10.1007/BF02769215.
Cited on page 39.

[75] Alessandro Lovato et al. Density-dependent nucleon-nucleon interaction from Urbana UIX three-nucleon force. *J. Phys. Conf. Ser.*, 336(1):012016, December 2011. ISSN 1742-6596. doi: 10.1088/1742-6596/336/1/012016.
Cited on page 40.

[76] Laura E. Marcucci et al. The Hyperspherical Harmonics Method: A Tool for Testing and Improving Nuclear Interaction Models. *Front. Phys.*, 8:516145, April 2020. ISSN 2296-424X. doi: 10.3389/fphy.2020.00069.
Cited on page 40.

[77] The ALICE Collaboration et al. The ALICE experiment at the CERN LHC. *J. Instrum.*, 3(08):S08002, August 2008. ISSN 1748-0221. doi: 10.1088/1748-0221/3/08/S08002.
Cited on page 48.

[78] The ALICE Collaboration. Performance of the ALICE experiment at the CERN LHC. *Int. J. Mod. Phys. A*, 29(24):1430044, September 2014. ISSN 0217-751X. doi: 10.1142/S0217751X14300440.
Cited on page 48.

[79] P. Hauser et al. New precision measurement of the pionic deuterium s-wave strong interaction parameters. *Phys. Rev. C*, 58(4):R1869–R1872, October 1998. doi: 10.1103/PhysRevC.58.R1869.
Cited on page 49.

[80] Francesco Giacosa et al. A simple alternative to the relativistic Breit–Wigner distribution. *Eur. Phys. J. A*, 57(12):336–24, December 2021. ISSN 1434-601X. doi: 10.1140/epja/s10050-021-00641-2.
Cited on page 49.

[81] STAR Collaboration et al. Hadronic resonance production in $d+$Au collisions at $\sqrt{s_{NN}} = 200$ GeV measured at the BNL Relativistic Heavy Ion Collider. *Phys. Rev. C*, 78(4):044906, October 2008. doi: 10.1103/PhysRevC.78.044906.
Cited on page 49.

[82] K. Werner, Iu. Karpenko, T. Pierog, M. Bleicher, and K. Mikhailov. Event-by-Event Simulation of the Three-Dimensional Hydrodynamic Evolution from Flux Tube Initial Conditions in Ultrarelativistic Heavy Ion Collisions. *Phys. Rev. C*, 82:044904, 2010. doi: 10.1103/PhysRevC.82.044904.
Cited on pages 52 and 67.

[83] K. Werner, B. Guiot, Iu. Karpenko, and T. Pierog. Analysing radial flow features in p-Pb and p-p collisions at several TeV by studying identified particle production in EPOS3. *Phys. Rev. C*, 89(6):064903, 2014. doi: 10.1103/PhysRevC.89.064903.
Cited on pages 52 and 67.

[84] Volodymyr Vovchenko and Horst Stoecker. Thermal-FIST: A package for heavy-ion collisions and hadronic equation of state. *Comput. Phys. Commun.*, 244:295–310, November 2019. ISSN 0010-4655. doi: 10.1016/j.cpc.2019.06.024.
Cited on pages 54, 69, and 74.

[85] Ekkard Schnedermann et al. Thermal phenomenology of hadrons from 200A GeV S+S collisions. *Phys. Rev. C*, 48(5):2462–2475, November 1993. doi: 10.1103/PhysRevC.48.2462.
Cited on page 54.

[86] S. Acharya et al. Multiplicity dependence of π, K, and p production in pp collisions at TeV. *Eur. Phys. J. C*, 80(8):693–20, August 2020. ISSN 1434-6052. doi: 10.1140/epjc/s10052-020-8125-1.
Cited on page 54.

[87] Björn Schenke et al. (3+1)D hydrodynamic simulation of relativistic heavy-ion collisions. *Phys. Rev. C*, 82(1):014903, July 2010. doi: 10.1103/PhysRevC.82.014903.
Cited on page 55.

[88] Björn Schenke et al. Elliptic and Triangular Flow in Event-by-Event D $= 3+1$ Viscous Hydrodynamics. *Phys. Rev. Lett.*, 106(4):042301, January 2011. doi: 10.1103/PhysRevLett.106.042301.
Not cited.

[89] Jean-François Paquet et al. Production of photons in relativistic heavy-ion collisions. *Phys. Rev. C*, 93(4):044906, April 2016. doi: 10.1103/PhysRevC.93.044906.
Cited on page 55.

[90] WASA-at-COSY Collaboration et al. Abashian-Booth-Crowe Effect in Basic Double-Pionic Fusion: A New Resonance? *Phys. Rev. Lett.*, 106(24):242302, June 2011. doi: 10.1103/PhysRevLett.106.242302.
Cited on page 55.

[91] J. Weil et al. Particle production and equilibrium properties within a new hadron transport approach for heavy-ion collisions. *Phys. Rev. C*, 94(5):054905, November 2016. doi: 10.1103/PhysRevC.94.054905.
Cited on page 56.

[92] H. Albrecht et al. Observation of antideuteron production in electron-positron annihilation at 10 GeV center of mass energy. *Phys. Lett. B*, 157(4):326–332, July 1985. ISSN 0370-2693. doi: 10.1016/0370-2693(85)90675-6.
Cited on page 59.

[93] A. Drescher et al. The argus electron-photon calorimeter III. Electron-hadron separation. *Nucl. Instrum. Methods Phys. Res., Sect. A*, 237(3):464–474, July 1985. ISSN 0168-9002. doi: 10.1016/0168-9002(85)91055-1.
Cited on page 59.

[94] S. Schael et al. Deuteron and anti-deuteron production in e+e- collisions at the Z resonance. *Phys. Lett. B*, 639(3):192–201, August 2006. ISSN 0370-2693. doi: 10.1016/j.physletb.2006.06.043.
Cited on page 59.

[95] Martin Wolfgang Winkler. Cosmic ray antiprotons at high energies. *J. Cosmol. Astropart. Phys.*, 2017(02):048, February 2017. ISSN 1475-7516. doi: 10.1088/1475-7516/2017/02/048.
Cited on pages 61 and 83.

[96] M. G. Albrow et al. Search for stable particles of charge $\geqslant 1$ and mass $\geqslant$ deuteron mass. *Nucl. Phys. B*, 97(2):189–200, October 1975. ISSN 0550-3213. doi: 10.1016/0550-3213(75)90030-9.
Cited on page 62.

[97] Jaroslav Adam et al. Enhanced production of multi-strange hadrons in high-multiplicity proton-proton collisions. *Nature Phys.*, 13:535–539, 2017. doi: 10.1038/nphys4111.
Cited on page 63.

[98] Fred Cooper et al. Single-particle distribution in the hydrodynamic and statistical thermodynamic models of multiparticle production. *Phys. Rev. D*, 10(1):186–189, July 1974. ISSN 2470-0029. doi: 10.1103/PhysRevD.10.186.
Cited on page 67.

[99] S. A. Bass et al. Microscopic models for ultrarelativistic heavy ion collisions. *Prog. Part. Nucl. Phys.*, 41:255–369, January 1998. ISSN 0146-6410. doi: 10.1016/S0146-6410(98)00058-1.
Cited on page 67.

[100] M. Bleicher et al. Relativistic hadron-hadron collisions in the ultra-relativistic quantum molecular dynamics model. *J. Phys. G: Nucl. Part. Phys.*, 25(9):1859, September 1999. ISSN 0954-3899. doi: 10.1088/0954-3899/25/9/308.
Cited on page 67.

[101] Shreyasi Acharya et al. Multiplicity dependence of light-flavor hadron production in pp collisions at $\sqrt{s} = 7$ TeV. *Phys.Rev.C*, 99(2), 2019. doi: 10.1103/PhysRevC.99.024906.
Cited on page 68.

[102] M. Kachelrieß et al. On nuclear coalescence in small interacting systems. *Eur. Phys. J. A*, 57(5):167–9, May 2021. ISSN 1434-601X. doi: 10.1140/epja/s10050-021-00469-w.
Cited on page 70.

[103] Sukanya Sombun et al. Deuteron production from phase-space coalescence in the UrQMD approach. *Phys. Rev. C*, 99(1):014901, January 2019. ISSN 2469-9993. doi: 10.1103/PhysRevC.99.014901.
Cited on page 71.

[104] Constantino Tsallis. Possible generalization of Boltzmann-Gibbs statistics. *J. Stat. Phys.*, 52(1):479–487, July 1988. ISSN 1572-9613. doi: 10.1007/BF01016429.
Cited on page 71.

[105] BRAHMS Collaboration et al. Rapidity dependence of deuteron production in central Au + Au collisions at $\sqrt{s_{\mathrm{NN}}} = 200$ GeV. *Phys. Rev. C*, 83(4):044906, April 2011. doi: 10.1103/PhysRevC.83.044906.
Cited on page 77.

[106] L. A. Dal et al. Alternative formation model for antideuterons from dark matter. *Phys. Rev. D*, 91(12):123536, June 2015. doi: 10.1103/PhysRevD.91.123536.
Cited on page 78.

[107] S. Acharya et al. Study of the Λ–Λ interaction with femtoscopy correlations in pp and p–Pb collisions at the LHC. *Phys. Lett. B*, 797:134822, October 2019. ISSN 0370-2693. doi: 10.1016/j.physletb.2019.134822.
Cited on page 78.

[108] I. V. Moskalenko and A. W. Strong. Production and Propagation of Cosmic-Ray Positrons and Electrons. *Astrophys. J.*, 493(2):694, February 1998. ISSN 0004-637X. doi: 10.1086/305152.
Cited on page 79.

[109] Fu-Hu Liu. Unified description of multiplicity distributions of final-state particles produced in collisions at high energies. *Nucl. Phys. A*, 810(1):159–172, September 2008. ISSN 0375-9474. doi: 10.1016/j.nuclphysa.2008.06.014.
Cited on page 80.

[110] T. Anticic et al. Inclusive production of protons, anti-protons and neutrons in p+p collisions at 158 GeV/c beam momentum. *Eur. Phys. J. C*, 65(1):9–63, January 2010. ISSN 1434-6052. doi: 10.1140/epjc/s10052-009-1172-2.
Cited on page 83.

[111] Daniela Ruggiano. Two-particle angular correlations of identified particles in pp collisions at $\sqrt{s} = 13$ TeV with ALICE. 11 2023.
Cited on page 88.

[112] A. D. Brandt et al. Measurement of the $2S_{1/2} - 8D_{5/2}$ Transition in Hydrogen. *Phys. Rev. Lett.*, 128(2):023001, January 2022. doi: 10.1103/PhysRevLett.128.023001.
Cited on page 90.

[113] Adam Kisiel et al. Pion, kaon, and proton femtoscopy in Pb-Pb collisions at $\sqrt{s_{NN}} =$ 2.76 TeV modeled in (3+1)D hydrodynamics. *Phys. Rev. C*, 90(6):064914, December 2014. doi: 10.1103/PhysRevC.90.064914.
Cited on page 91.

[114] I. Angeli et al. Table of experimental nuclear ground state charge radii: An update. *At. Data Nucl. Data Tables*, 99(1):69–95, January 2013. ISSN 0092-640X. doi: 10.1016/j.adt.2011.12.006.
Cited on page 100.

[115] Hidekatsu Nemura et al. Study of Light Λ- and ΛΛ-Hypernuclei with the Stochastic Variational Method and Effective ΛN Potentials. *Prog. Theor. Phys.*, 103(5):929–958, May 2000. ISSN 0033-068X. doi: 10.1143/PTP.103.929.
Cited on page 105.